DEVELOPMENT OF FLAT FLAME BURNERS FOR INDUSTRIAL HEAT TRANSFER APPLICATIONS

VÍCTOR EDUARDO CASTAÑEDA GUTIÉRREZ OTERO

School of Engineering
College of Physical Sciences and Engineering
Cardiff University

Supervisors:

Dr. Agustín Valera Medina
Dr. Richard Marsh
Dr. Philip Anderson

Thesis submitted in fulfillment of the requirements for the degree of
Doctor of Philosophy in Engineering

December 2019

ABSTRACT

Several industrial processes involve the heating of long and thin strips. One such process is the decarburising annealing of electrical steel. Published research suggests that rapid heating of up to $100°C/s$ during the decarburising annealing process significantly improves the magnetic properties of these steels. In this investigation, it was shown that the currently used technology of radiant tube burners was not optimal for the heating of these type of products. Therefore, the main objective of this project was to develop a novel type of burner that produced a flat wall attached flame by means of the Coanda effect. Due to its unique flame geometry, the burner achieved the required heating rates.

The behaviour and fundamental characteristics of isothermal and reacting Coanda flows were investigated. A combination of laser diagnostics, temperature measurements and visual observations were used to obtain information about the flow. A precessing vortex core that contributes to the flat flow profile was identified. A hysteresis behaviour between different flow states was observed. Critical factors that affect the onset and stability of the Coanda flame were determined; being the most relevant ones the applied swirl intensity, the flow rate, the relation between plate height and the nozzle outlet, the equivalence ratio and the nozzle geometry.

Subsequently, the experimental results were used to validate numerical simulations. The numerical simulations were used to conduct a parametric analysis for the burner geometry optimisation. The optimised burner was compared to a radiant tube burner via CFD simulations. It was found that the Coanda burner had lower radiant heat flux than the radiant tube burner. However, this downside was compensated by an increase in the total radiating area in the furnace. The use of the proposed Coanda burner in the decarburising annealing process had the potential to cause an increase in heating rate, a reduction in energy requirement, a reduction in NO_x emissions, a reduction in heating time, an increase in temperature homogeneity of the load, and a reduction in volume furnace with the consequential reduction in start-up times. Thus, the proposed technology has the potential to reduce the energy intensity of the annealing process and, because of the increased heating rate, improve the magnetic properties of the final product.

PUBLICATIONS

[1] Castaneda, V. et al. "Identification of the complex nature of coherent structures in Open and Coanda Jet flows via 2D3C-PIV." In: *19th International Symposium on Applications of Laser and Imaging Techniques to Fluid Mechanics*. Lisbon, 2018.

[2] Castaneda, V. and Valera-Medina, A. "Coanda flames for development of flat burners." In: *Energy Procedia*. Vol. 158. Elsevier Ltd, 2019, pp. 1885–1890.

The important thing is not to stop questioning.
Curiosity has its own reason for existing.
One cannot help but be in awe when he contemplates the mysteries
of eternity, of life, of the marvelous structure of reality.
It is enough if one tries merely to comprehend a little of this mystery every
day.

— Albert Einstein

ACKNOWLEDGMENTS

Firstly, I would like to express my sincere gratitude to my PhD supervisor Dr Agustin Valera-Medina. Thank you for all the guidance and support you gave me across these years. Thank you for all the suggestions and feedback in all my research outputs, presentations and thesis writing. Without your help and support, this project would not have been possible.

To Cogent Power Ltd and in particular Dr Fiona Robinson, Mr Mark Cichuta and Mr Dominic Power for answering my questions and providing me with the necessary information to give this project a practical focus.

To the technical team at Cardiff University Mechanical Engineering workshop especially Mr Malcom Seaborne, Mr Andrew Rankmore and Mr Paul Malpas. Thank you for helping me solve the diverse technical problems that appeared through the development of this investigation.

To Dr Maarten Vanierschot thank you for receiving me at KU Leuven, reviewing my conference paper manuscript and for all the help with my numerical simulations.

To all the amazing friends I was fortunate to make in Cardiff. Hector, Claudia, Edith, Haydee, Barbara, Roberto and my housemates Maria and Mariana, without you the experience would definitely not have been the same. You made Cardiff feel like a second home.

To my parents Victor and Sonia, I am here thanks to all the effort you have made. This achievement is as much mine as it is yours.

And most important of all, to my wife, Martha. Thank you for starting and finishing this PhD journey alongside me. Thank you very much for all your encouragement and understanding during the tough moments. And also for the joy and cheers during the good ones. But especially, thank you for all your love.

CONTENTS

LIST OF FIGURES

LIST OF TABLES

ACRONYMS

AFR   Air/Fuel Ratio

BSF   Backward Stabilised Flame

CFD   Computational Fluid Dynamics

CGO   Conventional Grain Oriented

CJF   Closed Jet Flow

CoJF   Coanda Jet Flow

CoVB   Coanda Vortex Breakdown

CRZ   Central Recirculation Zone

CSF   Coanda Stabilised Flame

DNS   Direct Numerical Simulation

DOE   Design of Experiments

ERZ   External Recirculation Zone

FAR   Fuel/Air Ratio

FFT   Fast Fourier Transform

FVM   Finite Volume Method

GCI   Grid Convergence Index

GHG   Greenhouse Gas

INTRODUCTION

1.1 CLIMATE CHANGE AND ENERGY PANORAMA

The latest report by the Intergovernmental Panel on Climate Change (IPCC) states that it is undeniable that human activities are responsible for global climate change [1]:

> "Human influence on the climate system is clear, and recent anthropogenic emissions of greenhouse gases are the highest in history. Recent climate changes have had widespread impacts on human and natural systems." [1]

In the last few decades, climate change has had an impact on natural and human systems. Hydrological systems have been affected by climate change. Changes in precipitation and melting of ice and snow have affected the quality and quantity of the water resource. Species have modified their geographical distribution areas, seasonal activities and migration patterns. Crop yields have had an overall negative impact due to climate change. Climate-related extremes such as heatwaves, droughts, floods, cyclones, and wildfires have revealed the vulnerability of ecosystems and human systems to climate variability [1].

The biggest contributor to climate change is Greenhouse Gas (GHG) emissions. From this, CO_2 from the burning of fossil fuels and industrial processes contributes to 78% of the total GHG emissions. Without additional efforts to reduce the GHG emissions, an increase in these gases is expected in the future due to the increase in population and economic activity. Reference scenarios developed by the IPCC estimate an increase in surface temperature in the range of 3.7°C to 4.8°C by 2100 in comparison to pre-industrial levels (Figure 1.1). To limit the increase in temperature to 2.0°C target considered acceptable by the IPCC, large scale improvements in energy efficiency in the process industry are required [2].

1.2 EMISSIONS AND ENERGY CONSUMPTION IN THE PROCESS INDUSTRY

The industry sector accounts for around 29% of final energy use and their emissions represent 30% of the global GHG emissions [3]. Industrial CO_2 emissions in 2010 accounted for 13.14 $GtCO_2$ of which 40.1% were from direct energy-related emissions, 40.0% from indirect emissions related to electricity and heat production, 19.7% from process emissions, and 0.2% from waste/wastewater. The industries that account for the most of the total process emissions are cement production (53.3%), production of chemicals (18.4%), lime production (9.4%), and ferrous and non-ferrous metals production (8.0%). In the United Kingdom,
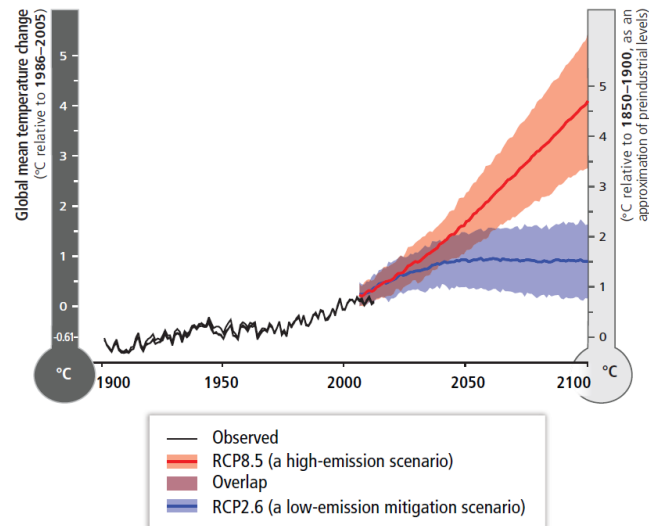
Figure 1.1: Increase in average global surface temperature with high- and low-emission scenario [1].

industrial emissions represented 2% of its total GHG emissions of 451.1 $MtCO_2$ in 2018. The main source of emissions for this sector were the cement, lime, iron and steel production [4]. For the iron and steel industry, more than two-thirds of the total energy consumption of the industry is used to provide heat, mainly by burning fossil fuels [5]. Most of the manufacturing industrial CO_2 emissions arise due to fossil fuel combustion used to provide the intense heat that is required for the conversion of raw materials into industrial products. An opportunity exists within the aforementioned industries to reduce emissions/energy intensity through technological changes (e.g., changes in product mix, adoption of energy-efficient technologies, etc.) [2].

1.3 FLAT FLAME BURNER CONCEPT

Several processes within the iron and steel industry involve the heating of long and thin strips (refer to Section 2.5 for an overview of some of these processes) which currently is accomplished by the use of radiant tubes (refer to Section 2.4 for an overview of the operation and types of radiant tubes). The efficiency of such heating devices is not optimal for heating iron/steel strips as half of the radiating area of the tube faces towards the walls of the furnace leading to a waste of direct heat radiation. Additionally, the radiant tubes are subject to space constraints due to the need of having the tubes sufficiently spaced apart to avoid excessive radiation between them. It is argued in the present work that a radiating flat surface would be a better approach because it would not be subject to space constraints and the radiating area would be greatly increased. More so, a greater radiating area would have the additional benefit of providing a faster heating rate which, for some type of products such as electrical steel, would improve the product quality (refer to Section 2.5.4 for more details).

Figure 1.2: Radiant tubes inside an electrical steel annealing furnace.
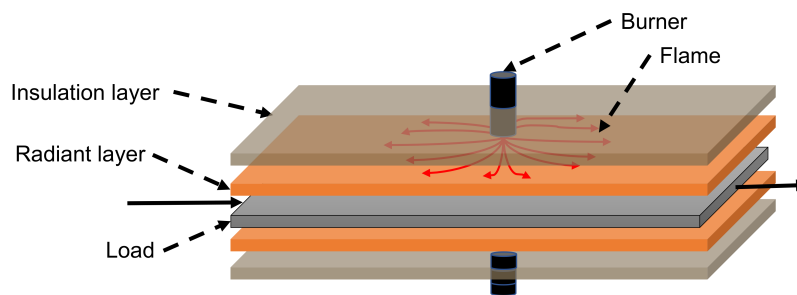
Figure 1.3: Coanda burner concept.

The present work proposes the use of the Coanda effect to produce a flat wall attached flame as an alternative to currently used industrial heat-treating technologies commonly used in the iron and steel industry. The Coanda effect refers to the hydrodynamic effect where a fluid jet exiting an orifice get deflected and attaches to an adjacent flat or curved surface. This effect is a consequence of a modification in the pressure field of the jet by the adjacent surface. A more detailed explanation of the effect is given in Section 2.3 of this thesis. A diagram of the proposed concept is shown in Figure 1.3. The burner would consist of two radiant plates placed at the top and bottom of the load. The radiant plates are in turn heated by the Coanda burner. Everything is encased within and insulated by the furnace walls. If required, the same concept could be used for direct flame heating by removing the radiant plate. The final aim would be to increase the heat flux to the load and temperature homogeneity by having a bigger radiating area, reduce furnace volume by having the radiant source closer to the load, and overall lower fuel consumption and reduced emissions.

1.3.1 *Fundamental calculations*

The fundamental reasoning behind the proposal comes from the radiative heat transfer equation:

$$\dot{q}_{1\rightarrow2} = \sigma A_1 F_{1\rightarrow2}\left(T_1^4 - T_2^4\right)$$

$$F_{12} = \frac{1}{\pi} \tan^{-1} \frac{b}{a}$$

If $b \gg a$

$$F_{12} = 0.5$$

$$F_{12} = \sqrt{1 + \left(\frac{h}{w}\right)^2} - \frac{h}{w}$$

If $w \gg h$

$$F_{12} = 1$$
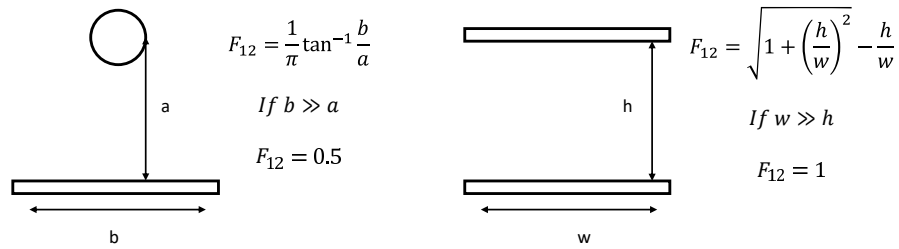
Figure 1.4: View factor for a radiative cylinder to a load plate and a radiative plate to a load plate.

where $\dot{q}$ is the radiative heat flux from the radiative source to the load, σ is the Stefan-Boltzmann constant, A is the radiative area, F is the view factor between the two surfaces, and T the temperature of the surface. From the above equation, it is possible to deduce that a change in the radiation source from a cylinder (i.e. radiant tube) to a plate would yield an increase in the view factor from 0.5 to 1.0. The increase in the view factor would have as a consequence an increased direct heat flux from the radiative source to the load. A schematic of the increase in view factor between the geometries is shown in Figure 1.4.

1.4   THESIS AIMS AND OBJECTIVES

The aim of this thesis was the development of a burner that uses the Coanda effect to produce a flat wall attached flame. The proposed burner would potentially replace radiant tubes used inside steel annealing furnaces. The burner would reduce overall fuel consumption, emissions, and improve product quality. To meet this aim, several interim objectives needed to be met:

- Understand the fluid mechanics behind an isothermal Coanda jet flow and the differences it has with normal open jets, specifically: the general characteristics, the coherent structures present in the Coanda flow, and the effect the geometry has on its onset.

- Understand the flame behaviour of a confined and unconfined Coanda flame, specifically: the possible flow patterns it can have; the stability of a Coanda flame in relation to a variation in flow rate, equivalence ratio and geometry; and the viability of having a confinement surrounding the flame.

- The data generated will be used to validate Computational Fluid Dynamics (CFD) models. CFD simulations will then be conducted to optimise the proposed burner by make changes in geometry and operating conditions. The optimised burner will then be compared with a generic radiant tube.

- A case study of an electrical steel annealing furnace will be made to assess the viability of substituting the currently used radiant tubes by the concept Coanda burner.

1.5 SUMMARY OF CHAPTERS

Chapter 1 introduces the rationale behind using the Coanda effect and its potential for the development of a burner that produces a flat wall attached flame. It proceeds to outline the thesis aims and methodology. Chapter 2 reviews previous scientific research on the Coanda effect. It also summarizes general combustion principles, characteristics of swirl burners, common types of radiant tube burners, and gives an overview of the electrical steel production process. Chapter 3 describes the tools for analysing the flow, both experimentally and numerically. For the experimental part, the laboratory devices and the experimental measurement techniques used are described. The post-processing techniques are explained. Following, the numerical setup, numerical models, discretization schemes, and grid analysis are described.

In Chapter 4, the results of the isothermal experiments on the swirl burner are presented. Time-averaged results for the two different flow patterns, Open Jet Flow (OJF) and Coanda Jet Flow (CoJF), at different flow rates are discussed followed by the spectral analysis of the flow fields. Then, the principal modes of the flow obtained by proper orthogonal decomposition and the coherent structures present in the flow are identified and described. Finally, the results for experiments involving a change in geometry and its effect on the flow pattern are presented.

In Chapter 5, the results of combustion experiments on a swirl burner are presented. An overview of the identified flame flow patterns is made. Following, a description of the effect variations in geometry has on the flame stability in an unconfined combustion is given. Finally, results of a confined Coanda flame are presented, which include confinement wall temperatures, flue gas temperatures, and general remarks on the operation of the burner.

In Chapter 6, the results of the numerical simulations are presented. Simulations are made for the isothermal and combustion cases. Their result is compared to the experimental data obtained in the previous chapters to validate the chosen turbulence and combustion models. Areas on which the current design can be improved are identified.

In Chapter 7, a parametric analysis on the burner geometry and operating conditions is conducted to optimise the burner. Then, the proposed configuration is scaled-up via simulations and compared to a radiant tube burner. Finally, a case study of an electrical steel annealing furnace where the radiant tubes are replaced for radiant plates heated by a Coanda flame is presented. The feasibility of the implementation of the proposed design is discussed.

Chapter 8 gives a general discussion of the results presented in this thesis and compares them with research available in the literature. Finally, in Chapter 9, the conclusions of this study are given, as well as, suggestions for future research.

LITERATURE REVIEW

This chapter covers the literature review on swirl burners and the Coanda effect. Additionally, it gives an overview of combustion theory, typical industrial heating devices, and the production of electrical steel. This chapter is structured as follows, first Section 2.1 gives an overview of the theory behind combustion, including the chemistry, flame characteristics and undesirable emissions. Then, Section 2.2 reviews the research that has been conducted on swirl burners, including the flow patterns and structures present in the flow that aid in the flame stability. Section 2.3 presents a definition of the Coanda effect, a review of the fluid dynamics behind it, and the research that has been done around it. Section 2.4 describes the principle of operation of radiant tubes and the common designs that exist. Finally, Section 2.5 introduces the characteristics of electrical steel, its production process and expands on the description of the furnace that will be used in the last chapter of this thesis as a case study.

2.1 COMBUSTION PRINCIPLES

The objective of this section is to give a brief overview of the different elements that a combustion process comprises and to define certain concepts that will be mentioned in this thesis. For an in-depth study of the subject, many books exist [6–9]. A combustion process involves a combination of chemical reactions, thermodynamics, heat transfer and mass transport. It is an important concept in diverse engineering fields as its a key part of internal combustion engines, aircraft engines, power plants, heating inside furnaces, and other processes.

2.1.1 *Mass and energy conservation*

In every chemical reaction, mass is neither created nor destroyed. In other words, mass is conserved. For example, in the reaction between methane and oxygen, the chemical reaction is as follows:

$$CH_4 + 2O_2 \rightarrow CO_2 + 2H_2O \tag{2.1}$$
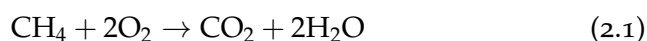
The subscript refers to the number of atoms in each molecule. The antecedent number refers to the number of molecules for the given chemical compound. In this case, one molecule of methane reacts with two molecules of oxygen to produce one molecule of carbon dioxide and two molecules of water. The equation is balanced, this means that the number of atoms in each side is the same, even though the molecular species have changed. Because of the very small weight of each molecule, it is not a practical unit to work with; instead, the unit mole is used.

A mole is defined as 6.02×10^{23} molecules. Moles can be converted to mass by multiplying them by their respective atomic weight.

Like mass, energy is neither created nor destroyed. Energy is stored in the chemical bonds of the molecules. If the stored energy in the products of a chemical reaction is higher than the stored energy in the reactants, the reaction requires energy to happen. These reactions are called endothermic reactions. On the contrary, if the products have lower energy than the reactants, heat is released. These reactions are called exothermic reactions. By definition, fuels are chemical compounds that produce heat when reacting with oxygen. The energy released can be calculated by the difference of the standard enthalpy of formation of the products and reactants. The standard enthalpy of formation of a compound is the energy required to form 1 mol of that compound from its component elements at 1 bar and 25°C. For example, for the reaction between methane and oxygen:

$$\Delta H^\circ_{rxn} = \left[\Delta H^\circ_f \left(CO_{2\,(g)} \right) + 2\Delta H^\circ_f \left(H_2O_{(l)} \right) \right]$$
$$- \left[\Delta H^\circ_f \left(CH_{4\,(g)} \right) + 2\Delta H^\circ_f \left(O_{2\,(g)} \right) \right] \quad (2.2)$$

$$\Delta H^\circ_{rxn} = [-393.5 + 2\,(-285.8)] - [-74.84 + 2\,(0)] = -890.4 \text{kJ}/\text{gmol}$$

where ΔH°_f is the standard enthalpy of formation for the specific compound. Each compound needs to be taken from the standard state of 1 bar and 25°C to the conditions at which the reaction is taking place in order to obtain the total change in enthalpy. This is done by using the specific heat capacity of the compound.

$$\Delta H = nC^\circ_p \Delta T \quad (2.3)$$

where n is the number of moles, C°_p is the specific heat capacity, and ΔT is the change in temperature. The change in enthalpy for any non-reacting components in the mixture needs to be also taken into account (e.g. nitrogen).

For fuels, a practical way of expressing the energy released is by the Lower Heating Value (LHV) and Higher Heating Value (HHV). LHV assumes that the combustion exit gases are sufficiently hot that the water vapour from the combustion process does not condense, i.e. the heat stored in the water vapour is not recovered. HHV considers that the combustion gases are cold enough so that the water is condensed. Tables exist for the LHV and HHV. Both values are usually reported in energy per unit mass (e.g. kJ/kg) instead of energy per unit mole (e.g. kJ/kmol). Using the heating value tables mostly avoids the need to calculate the heat of reaction. However, care needs to be taken when choosing between the two, as the appropriate one will depend on the process. For an in-depth explanation of mass and energy balances, refer to the book by Himmelblau [10].

2.1.2 *Equivalence ratio and flammability limits*

In internal combustion engine processes, it is common to employ the Air/Fuel Ratio (AFR) (Equation 2.4) to describe the conditions of the mixture. Another possibility is the inverse relationship, the Fuel/Air Ratio (FAR) (Equation 2.5), which is commonly used in the gas turbine industry. However, both the AFR and the FAR fail to describe how much excess of fuel (or air) is being used. This is because the amount of air needed to react will vary depending on the fuel.

$$AFR = \frac{m_{air}}{m_{fuel}} \tag{2.4}$$

$$FAR = \frac{m_{fuel}}{m_{air}} \tag{2.5}$$

A better alternative is using the air–fuel equivalence ratio (λ) (Equation 2.6) or fuel–air equivalence ratio (ϕ) (Equation 2.7). Both of these divide the AFR or the FAR by, respectively, the air/fuel stoichiometric ratio or the fuel/air stoichiometric ratio. The stoichiometric ratio is the ratio at which all the reactants are consumed without any excess of either of them. The advantage of using either of these methods is that it takes into account (and is therefore independent of) the type of fuel and units of measurement used. The equations for each are:

$$\lambda = \frac{\text{oxidizer-to-fuel ratio}}{(\text{oxidizer-to-fuel ratio})_{st}} = \frac{m_{ox}/m_{fuel}}{\left(m_{ox}/m_{fuel}\right)_{st}} = \frac{n_{ox}/n_{fuel}}{\left(n_{ox}/n_{fuel}\right)_{st}} \tag{2.6}$$

$$\phi = \frac{\text{fuel-to-oxidizer ratio}}{(\text{fuel-to-oxidizer ratio})_{st}} = \frac{m_{fuel}/m_{ox}}{\left(m_{fuel}/m_{ox}\right)_{st}} = \frac{n_{fuel}/n_{ox}}{\left(n_{fuel}/n_{ox}\right)_{st}} \tag{2.7}$$

where m represents the mass, n represents the number of moles, and the suffix *st* stands for stoichiometric conditions. With either of these methods, it is possible to quickly see if the process is using the exact amount of fuel (or oxidizer), or if there is an excess or lack of it. In the case of the air–fuel equivalence ratio (λ) a value of $\lambda < 1$ indicates a fuel-rich (lack of oxidizer) mixture and a value of $\lambda > 1$ indicates a fuel-lean (excess of oxidizer) mixture. In the case of the fuel–air equivalence ratio (ϕ) a value of $\lambda > 1$ indicates a fuel-rich (lack of oxidizer) mixture and a value of $\lambda < 1$ indicates a fuel-lean (excess of oxidizer) mixture. In this thesis, the fuel–air equivalence ratio (ϕ) is used.

There are air and fuel mixture ratios at which the combustion can occur. These limits are called Lower Flammability Limit (LFL) and Upper Flammability Limit (UFL). The LFL indicates the minimum amount of fuel possible in the mixture for the combustion to be possible. A concentration of fuel below this limit makes the mixture too fuel-lean for the combustion to occur. While the UFL indicates the highest possible amount of fuel. A concentration of fuel above this limit makes the mixture too fuel-rich for the combustion to occur. The ideal mixture would be the stoichiometric ratio. However, because it is not possible
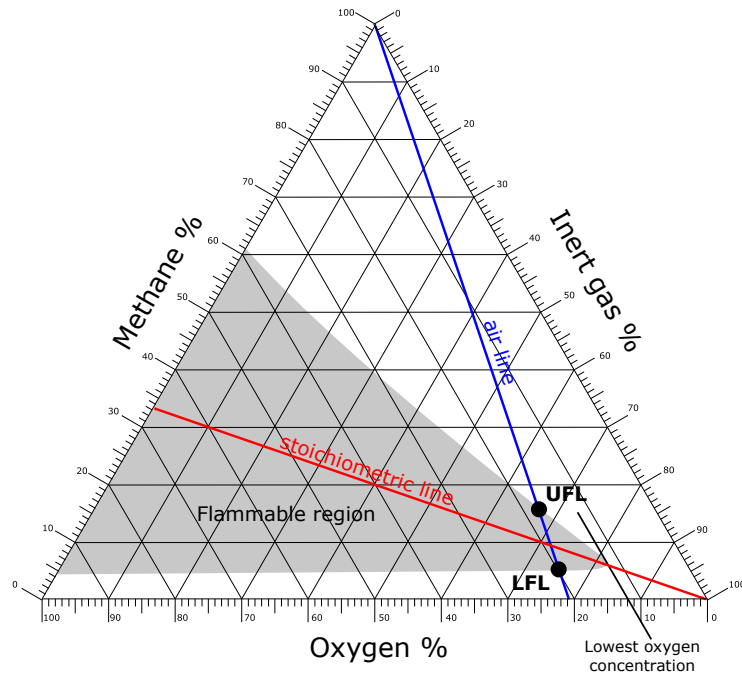
Figure 2.1: Flammability limits of methane with oxygen [12].

to perfectly mix the fuel and air, in practice an excess air of $\sim$ 3% is used in order to ensure a complete combustion. Theoretical flammability limits are related to the physicochemical properties of the fuel–air mixture. However, experimental flammability limits are also a function of the heat losses from the system, mixture of the chemical species, and fluid dynamics of the device making the real flammability limits device-dependent [7, 11]. The flammability limit can be increased by using higher concentrations of oxygen than those present in the air. Figure 2.1 shows the flammability limits of methane with oxygen. For methane, the LFL and UFL limits with air are 5% and 15%, respectively.

2.1.3 *Flame properties*

A flame is the intense luminous region that is typically produced during a combustion process. A flame can be defined as a small layer of fluid (also called the flame front) where changes in chemical species, concentration of species, and temperature occur. A related characteristic is the ignition temperature of the fuel, which is the temperature required for the combustion to take place. Once the gas mixture is ignited, there is usually enough energy for the reaction to be self-sustained, this means that the reaction fuel is providing enough energy to ignite the surrounding molecules. If the ignition temperature is not high enough, or if sufficient energy is extracted, the fuel cannot continue burning. Another factor that influences the flame is the hydrodynamic effects that are produced by the particular device used, which play an important role in the flame stability [13]. Following, some relevant characteristics of flames will be described.
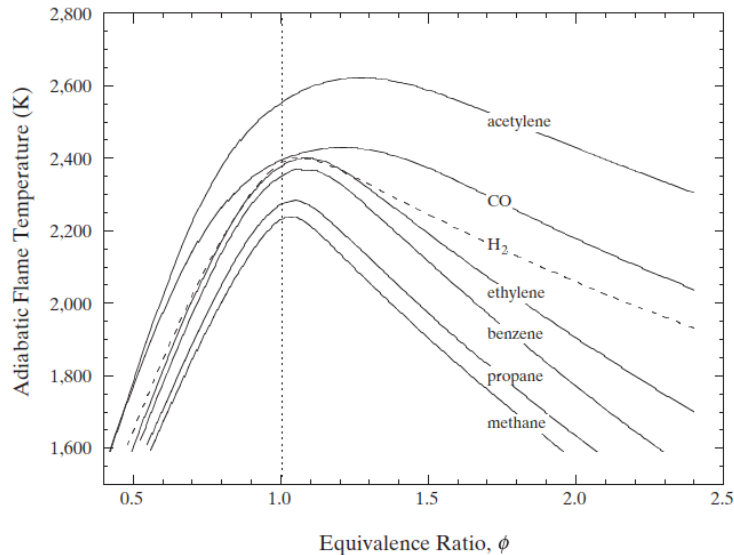
Figure 2.2: Adiabatic flame temperature as a function of fuel equivalence ratio, ϕ, for several fuel–air mixtures at standard temperature and pressure. Image reproduced from Law [9].

2.1.3.1 *Temperature*

The maximum temperature a flame can reach in ideal conditions is called the adiabatic flame temperature. Ideal conditions mean the assumption that all the energy contained in the fuel is used to heat the reacting gas mixture (along with any inert gases present in the mixture). The adiabatic flame temperature is highly dependent on the equivalence ratio, initial temperature and pressure. The adiabatic temperature is directly related to the amount of energy the specific fuel contains, i.e. the higher the energy density of the fuel, the higher the adiabatic temperature is going to be. Figure 2.2 shows the adiabatic flame temperature of various fuels with air as an oxidizer and as a function of their equivalence ratios. In practice, the flame temperature is lower than the adiabatic temperature due to several factors, mainly, heat losses with the surroundings and combustion inefficiencies. However, the adiabatic flame temperature remains a useful quantity to take into account in combustion-related calculations [13].

2.1.3.2 *Flame velocity*

The speed at which a flame propagates is an important characteristic that needs to be taken into account in a combustion process as it can influence the stability of the flame. It is usually reported as the laminar flame speed, S_L, for each particular fuel. The laminar flame speed is related to the kinetics of the flame and the molecular diffusivity of the species in the mixture, that is, how fast the fuel and oxidizer can react and pass the energy to the adjacent unreacted mixture. The laminar flame speed is measured by having the reactants perfectly mixed in ideal proportions and with no influence from the surroundings or hydrodynamic effects (usually by having a simple injection method and a very

big confinement). In this way, in laminar flames, the flow conditions do not alter the chemical kinetics nor the rate of heat release. Turbulence changes this dependence [14]. However, laminar flame velocity remains an important factor in determining the turbulent flame speed.

In turbulent flames, the flame speed is no longer a function only of the fuel, but also of the flow conditions. A flame in a turbulent regime increases the mixing rate of the reactants at a molecular level which increases the rate of consumption and, in turn, flame speed. Turbulent flame velocity, S_t, can be defined as the velocity at which unburned mixture enters the flame zone in a direction normal to the flame [15]. This definition assumes that the flame surface is represented by a time-averaged quantity. The turbulent flame velocity can be expressed as [7]:

$$S_t = \frac{\dot{m}}{\overline{A} \rho_u} \tag{2.8}$$

where $\dot{m}$ is the reactant flow rate, ρ_u is the unburned gas density, and $\overline{A}$ is the time-averaged flame area. It is complicated to determine the flame area experimentally which can lead to uncertainty in the flame speed measurements.

2.1.3.3 *Premixed turbulent flame regimes*

The effect that turbulence has on the flame thickness is dependent on the length scale of the turbulent effects. Turbulent effects cascade through a system at distinct lengths and time scales. The lengths are classified by the size of their eddies as l_0 (largest eddies, integral length scale), l_λ (average eddy size, Taylor microscale) and l_k (smallest scale, Kolmogorov scale). Energy gets transferred from the largest to the smallest scales where it is ultimately dissipated as heat [16, 17]. The structure of a turbulent flame is governed by the relationships of l_k and l_0 to the laminar flame thickness, δ_L. The laminar flame thickness is the thickness of the reaction zone that is controlled by molecular heat and mass transport. Efforts have been dedicated to the creation of combustion regime diagrams that map the turbulent flame structure based on a given set of variables. The first such diagram was created by [18]. The diagram relates the Reynolds, Damköhler and Karlovitz numbers to the flame regime. These numbers are defined as [8]:

$$\text{Re} = \frac{\text{turbulent viscosity}}{\text{laminar viscosity}} = \frac{u' l_0}{\nu} \tag{2.9}$$

$$\text{Da} = \frac{\text{eddy turnover time}}{\text{laminar flame time}} = \frac{\tau_{\text{flow}}}{\tau_{\text{chem}}} = \frac{l_0/u'}{\delta_L/S_L} = \frac{l_0 S_L}{u' \delta_L} \tag{2.10}$$

$$\text{Ka} = \frac{\text{laminar flame passage time}}{\text{time for flame stretching}} = \frac{\delta_L \nu}{S_L l_k^2} \tag{2.11}$$

where u' is the fluctuating velocity based on Reynolds decomposition, l_0 is the integral length scale, ν is the kinematic viscosity, S_L is the laminar flame speed, δ_L is the laminar flame thickness, and l_k is the
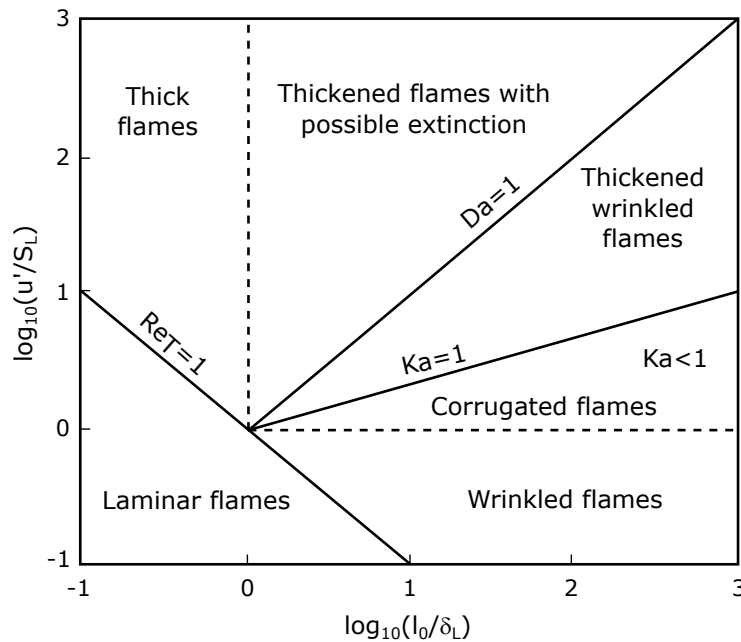
Figure 2.3: Borghi diagram. Image reproduced from [8].

Kolmogorov length scale. The Borghi diagram is shown in Figure 2.3. The diagram shows the regions with the different flow regimes [8]:

- Wrinkled Flame Regime ($u' < S_L$): occurs when turbulence intensity is low while all length scales, including the Kolmogorov length scale l_k, are larger than δ_L. In this case, the flame is much smaller than any turbulent scale which means that for the turbulence the flame is infinitely thin. Thus, the low turbulence level has only a wrinkling effect on the flame front and no turbulent mixing happens inside the flame.

- Corrugated flames ($u' > S_L, \mathrm{Ka} < 1$): occurs when the turbulent intensity is high. The flame remains infinitely small in comparison with the turbulent scales. However, due to the higher turbulent intensity pockets of fresh or burned gases can appear which produces a corrugated structure on the flame front.

- Thickened flames ($\mathrm{Ka} > 1, \mathrm{Da} > 1$): the Kolmogorov length scale l_k is much smaller than the flame thickness δ_L. Everything is mixed by turbulence and the mixture no longer has a flamelet-type small-scale structure. Flames typically extinguish in this regime.

- Thickened wrinkled flames ($u' > S_L, \mathrm{Ka} > 1, \mathrm{Da} < 1$): there is turbulent mixing in the preheat region of the flame, but the reaction zone retains the structure of a laminar flame.

2.1.3.4 *Combustion instabilities*

A stable flame is one that is anchored at a desired location in the burner. Two instabilities related to the flame speed and turbulent flow speed are the flame lift-off and flashback.

Lift-off of the flame occurs when the operating conditions and fuel produce fast flow timescales, τ_{flow}, and slow chemical timescales, τ_{chem}. In these conditions, the reactants move at a velocity that exceeds the flame speed. Thus, the flame is not able to propagate upstream at a velocity that is faster than the flow. This causes the condition known as lift-off, where the flame loses its anchor point at the burner nozzle and detaches from it. This could lead to flame extinction (blow-off) if the flame is carried to a region downstream of the burner where it is diluted by combustion products (or ambient air) below the LFL [19].

Flashback of the flame occurs when the operating conditions and fuel produce slow flow timescales, τ_{flow}, and fast chemical timescales, τ_{chem}. In this case, the flame propagates upstream faster than the flow moves downstream. In the case of premixed fuel and oxidizer, the flame can propagate inside the burner and damage the equipment by getting in contact with parts that are not able to withstand high temperatures. Flashback usually propagates at areas with local reduced velocity such as shear layers [20]. There are different mechanisms that lead to flashback in a premixed flame. Flashback due to flame propagation in the core flow can occur if there is an increase in turbulent burning velocity due to changes in fuel composition or a decrease in the flow velocity due to changes in burner power. Another type of flashback mechanism is the boundary layer flashback. This type of flashback is a consequence of the reduced velocity of the reactants near the wall due to the no-slip wall boundary condition. Finally, combustion-induced vortex breakdown flashback is specific to swirl-stabilized burners. In this case, the combustion process can move the vortex-breakdown bubble that stabilises the flow from downstream the nozzle to deep within the burner. A review of each of these mechanisms is made in the book by Benim and Syed [21].

Two common methods for flame stabilization are bluff-body stabilization and swirling flows. A review of bluff-body flame stabilization is made by Shanbhogue et al. [22] and a review of swirl stabilized flames is made by Huang and Yang [23]. Both methods rely on creating recirculation zones that stabilize the flame. A bluff body is any non-streamlined shape inserted into the flow field. The bluff-body works by obstructing part of the flow and creating a strong recirculation zone behind the flameholding device. The flame stabilization point lies close to the edge of the flameholder. Swirl stabilization creates recirculation zones by introducing a swirl component to the flow. Further discussion of swirling flows and their characteristics is presented in Section 2.2.

2.1.4 *Emissions*

During a combustion process, several undesired contaminants can be produced depending on the type of fuel and the combustion conditions. The most relevant contaminants in a combustion process are CO_2, CO, NO_x, and SO_x due to their impact on the greenhouse effect, acid rain and smog formation [24].

2.1.4.1 *Carbon dioxide*

It is present in the atmosphere at concentrations of ~ 400 ppm. It acts as a greenhouse gas. The concentration of CO_2 in the atmosphere has been steadily increasing since the industrial revolution. Efforts have been made to develop technologies that can capture and store CO_2 or by use of alternative fuels such as hydrogen [25].

2.1.4.2 *Carbon monoxide*

Carbon monoxide results from an incomplete combustion process due to insufficient oxidizer, poor mixing or low temperature. High CO levels indicate a loss of efficiency in the combustion process. CO is an indirect GHG, as is it can react with OH radicals. OH radicals help reduce the concentration of strong GHG such as methane [24].

2.1.4.3 *Nitrogen oxides*

NO_x contributes to the formation of ground-level ozone. Ground-level ozone can have health impacts on sensitive population (e.g. asthmatics). NO_x also contributes to the formation of smog and acid rain. The major source of NO_x is fossil fuel combustion where it is produced in small quantities measured in parts per million. A typical industrial combustion process would produce NO_x in the range of 100 to 200 ppm. Environmental guidelines typically regulate NO_x emissions to levels below 30 ppm. In a combustion process NO_x is usually produced via three main pathways [26]:

- Thermal NO_x: occurs when there is a direct reaction between nitrogen and oxygen ($N_2 + O_2 \rightarrow NO + O$). High temperatures are required to dissociate molecular nitrogen. Thus, thermal NO_x becomes a special concern at temperatures greater than $\sim 1600°C$.

- Fuel NO_x: occurs when nitrogen is part of the fuel molecule (e.g. coal). NO_x is formed by rapid pyrolysis of the fuel which produces intermediate cyanide radicals ($C_xH_yN \rightarrow HCN + CN + \cdots$). Cyanide radicals are oxidized by oxygen to produce nitric oxide ($HCN + CN + O_2 \rightarrow NO + \cdots$). In regions with strict NO_x limits, nitrogen is typically removed from the fuel before the combustion process.

- Prompt NO_x: is similar to fuel NO_x with the exemption that nitrogen comes from molecular nitrogen. Molecular nitrogen then reacts with the fuel to form the same cyanide radicals at the fuel NO_x path. This pathway usually occurs in fuel-rich conditions.

NO_x formation is dominated by its thermal formation mechanism, thus, by the flame temperature. In turn, flame temperature depends on the fuel composition, the temperature of the combustion air, and the relative thermal loading of the burner. The two main strategies for NO_x reduction are flue gas recirculation and staged combustion. The first one

consists on diluting the combustion process by the addition of a nonreactive medium, usually flue gases from the combustion process. This reduces the maximum flame temperature and therefore NOx formation. The second strategy consists on igniting the fuel-air mixture in stages by limiting either the air or the fuel, i.e. first a portion of the fuel-oxidizer mixture is combusted, then, further downstream additional air or fuel is supplied (depending on whether the first stage was fuel-rich or fuel-lean). This technique splits the available energy of the fuel over different sections of the burner which results in a lower flame temperature than that of a single combustion stage [26].

2.1.4.4 *Sulphur oxides*

Sulphur oxides are of special concern in a combustion process. The largest source of atmospheric SO_x is the burning of fossil fuels by power plants. Sulphur oxides easily react with water in the atmosphere and result in acid rain which has a detrimental effect on crops, can corrode structures and has an impact on human health [24].

2.2 SWIRL BURNERS

As mentioned Section 2.1.3, applying swirl to the combustion reactants is a way to produce recirculation zones within the flame which help on its stabilisation [27]. A schematic of a swirling flow is shown in Figure 2.4. Huang and Yang [23] provide a review of swirl-stabilised combustion. Large-scale effects of the swirl on the jet are well known: improved flame stability in the combustion chamber by forming a central recirculation zone, reduction in flame length accompanied by an increase in flame width, and increase in flow mixing caused by entrainment of surrounding gases in the shear layer region. These effects increase with increased swirl [28, 29]. In addition to the increase in flame stability, swirling flows have been of interest due to their potential of reducing NO_x emissions [30, 31]. Following, some of the flow patterns present in swirling flows will be discussed. The main structures present in the flow are the vortex breakdown-induced central recirculation zone downstream of the nozzle and the precessing vortex core surrounding the central recirculation zone.

2.2.1 *Characteristics of swirling flows*

2.2.1.1 *Vortex breakdown*

Vortex breakdown has been extensively studied as it is considered one of the most important characteristics in swirling flows. An extensive review of this subject has been made by Lucca-Negro and O'Doherty [32]. Vortex breakdown can be divided into six different types of which only two are observed for high Reynolds numbers: axisymmetric (bubble) breakdown and spiral break-down [33]. Vortex breakdown in annular swirling flows occurs due to the tangential velocity component of the
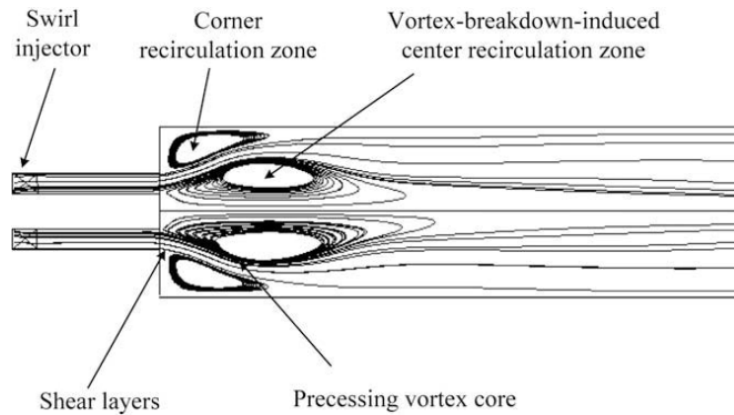
Figure 2.4: Flow patterns for a flame with inlet swirl. Image reproduced from [23].

flow exiting the nozzle. In the case of strong swirl, an adverse pressure gradient is created, which is large enough that results in a reversed flow along the axis. This leads to the creation of a Central Recirculation Zone (CRZ). The region where the CRZ occurs is the main responsible for the flame stabilisation mechanism due to the internal stagnation points and reversed flows that are created. The reversed flows help with the recirculation of hot products and, consequently, the residence times of the reacting species [34].

2.2.1.2 *Precessing vortex core*

The Precessing Vortex Core (PVC) is a three-dimensional unsteady asymmetric coherent flow structure that is characterised by a periodical off-axis precession of the centre of rotation [23]. The PVC is related to the vortex breakdown phenomenon and the associated recirculation zone. This structure has been commonly reported in turbulent swirling flow devices [35–39]. A comprehensive review of the literature available was made by Syred [40]. Syred and Beér [41] determined that the PVC is situated in the boundary of the reverse flow zone between the zero velocity and zero streamline. More recently, Oberleithner et al. [42] and Terhaar et al. [43] have shown that the PVC is caused by global hydrodynamic instabilities of the mean flow which produce oscillations at the base of the flow, resulting in vortex shedding in the shear layer. The PVC can be characterised by the Strouhal number where the frequency of precession depends on the swirl number and chamber configurations and increases linearly with the flow rate [40].

In reacting swirling flows the PVC has been shown to have a strong effect on the flame stabilisation [44]. The PVC can improve combustion efficiency by enhancing the fuel–air mixing [45, 46], enhancing mixing of burned and unburned gases [47], and modifying the local reaction zones by stretching or quenching [47, 48]. However, it might also produce undesirable phenomena like thermoacoustic oscillations of the flame [40].
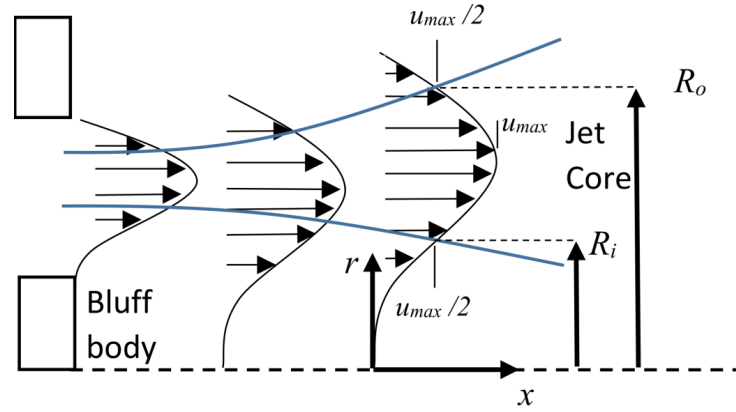
Figure 2.5: Jet core boundary defined by half-width assumption. Image reproduced from [50].

2.2.2 *Swirl number definition*

The definition of the swirl number is geometry dependent. In this thesis, the definition by Beer and Chigier [28] is used with the simplification for the pressure term made by Sheen et al. [49]. The definition denotes the ratio of tangential momentum flux to axial momentum flux on an annular jet core:

$$S_w = \frac{\int_{Ri}^{R_o} 2\pi\rho\bar{u}.\bar{w}r^2 dr}{R_o \int_{Ri}^{R_o} 2\pi\left(\rho\bar{u}^2\right)rdr} \tag{2.12}$$

where u and w are the instantaneous axial and tangential velocities and the overbar denotes time-averaged velocity components. The choice of the location of the upper and lower radius limits is important to consistently define the swirl number [50], especially in cases where there is a change of diameter or where obstructions are present. In this thesis, the radius of the inner (R_i) and outer (R_o) shear layer of the jet are defined starting from the central axis of the swirling jet. The radii are calculated using the half-width assumption where the jet core boundaries are assumed to be at the location where the axial velocity is half of the maximum velocity of the jet core. Figure 2.5 shows the boundary of the jet using such assumption.

2.3 COANDA EFFECT

The first description of the Coanda effect was made by Thomas Young in 1800. However, the effect takes its name from engineer Henri Coanda, who developed the first practical application by building the world's first jet-propelled aircraft [51–53]. Henri Coanda described the effect as:

> "The tendency of a jet of fluid emerging from an orifice to follow an adjacent flat or curved surface and to entrain fluid from the surroundings so that a region of lower pressure develops."

Coanda flows have been of interest in a diverse set of fields because of the characteristics it presents, mainly, enhanced turbulence levels and entrainment compared with those of round jets. These characteristics have been attributed to the additional rate of strain caused by the convex streamline curvature of the flow [54]. Additionally, in the particular case of axisymmetric Coanda flows, these characteristics are further enhanced by flow divergence [55]. Despite the interest of the Coanda effect in various fields, and probably because of the assorted nature of the applications, no comprehensive technical review of the literature exists. Good overviews on the topic have been made [51, 56–58]. In this section, a brief highlight of the applications and research where the Coanda effect is used will be made, followed by a simplified explanation of the physics behind it, and a review of literature that is relevant to the application developed in this thesis.

2.3.1 *Applications*

In the last 25 years, the Coanda effect has resurfaced in several applications. A compilation of the applications has been made by Reba [59], with a more recent review made by Lubert [60]. Use in home appliances includes its use in bladeless fans. For example, Li et al. [61] evaluated the flow field at different Reynolds numbers produced by a bladeless fan that uses the Coanda effect. In industry, it has been used in reaction turbines, swirl atomizers [62, 63], and cooling of cylinders [64]. The Coanda effect is perhaps most studied in the aeronautic and aerodynamic field where it is found in circulation-control aerofoils and wings [65, 66]. Also, in applications related to circulation-control, it has been used to increase lift [67] and thrust vectoring [68]. More recently, in the European Union Project ACHEON (Aerial Coanda High Efficiency Orienting-jet Nozzle) it is used to develop a nozzle for Vertical Short-Take-Off and Landing vehicles [69, 70].

Energy-related applications of the Coanda effect in the industry seem to be limited to waste gas flares. British Petroleum developed gas flares that used the Coanda effect in the 1960's. Due to their advantages over traditional flare systems, these flare systems gained widespread attention in the 1980s and 1990s and are still commonly used in offshore installations. As described by Desty et al. [71], the advantages of having a Coanda effect on these type of flares is that they produce a flame that is not easily deflected by crosswinds, while at the same time, producing a smoke-less combustion with increased combustion efficiency and decreased thermal radiation, when compared to other types of flare devices. Another advantage is that the flare can be rotated and angled to move the flame away from point locations where radiation is a concern. The history of the development of these flares can be read in the work by Desty [72]. Since their development, further research has been conducted. Carpenter and Green [73] studied the aerodynamics and aeroacoustics of a supersonic jet adhering to a tulip-shaped body typically used in flares. The authors note that there is a risk in flame separation from the surface if the curvature of the surface is too great and/or the operating

pressure too high. In a follow-up paper [56], the same authors focus on the design of flare systems that reduce the acoustic noise of Coanda supersonic jets noting that noise is not of great concern, as Coanda flares often have reduced noise levels in comparison to other types of flares. Lubert et al. [74] investigated noise production in a Coanda flare burner with a two-dimensional axismmetric super-sonic flow, particularly the identification of the location downstream the nozzle where the first shock cell forms. Two non-flare related studies by Fox and Sarkar [75] and Fox and Stewart [76] demonstrated the potential of a Coanda flow for increased heat transfer through a wall in a slot burner.

2.3.2   *Coanda effect theory*

An explanation of the mechanism behind the Coanda effect for a two-dimensional incompressible jet of air exiting through a nozzle into an atmosphere of stationary air will be given in the following paragraphs [77]. It should be noted that the geometries studied in the present thesis differ from the ones provided in the explanation that will follow. The geometry studied in this work has a backplate, does not have a side boundary and the flow is modified by swirl (refer to Section 3.1 for an explanation and schematic of the test burner). However, this explanation is the one that is typically used to explain the Coanda effect and is kept here for simplicity. For a detailed and quantitative explanation of the Coanda effect in three-dimensional swirling flows, the reader is referred to the work by Vanierschot and Van den Bulck [78].

Let us consider a jet of air exiting at high speed from an orifice into a stagnant atmosphere. In this scenario, as the jet exits the orifice it entrains the stagnant air from its surroundings. This produces a low-pressure zone around the jet (Figure 2.6a). The low-pressure zone is equal around the jet circumference making the jet travel in a straight line. If a solid surface is brought close to one of the sides of the jet (Figure 2.6b) the balance of forces is now altered. The jet will continue to try to entrain fluid from its surroundings. However, the stagnant air that was getting replaced when no wall was present can no longer be replenished because the wall is in the way. Thus, there will be a larger pressure drop near the wall surface. This makes the jet deviate towards the wall (Figure 2.6c) producing the Coanda effect. If a small step is added (Figure 2.6d) the Coanda effect is enhanced by the created recirculation bubble [51].

2.3.3   *Relevant research*

Most of the already given examples focus on applications of the Coanda effect considerably different to the one proposed in this work. For instance, the flows in aeronautical applications have a considerably different geometry and flow conditions (higher non-swirling flows emanating from a squared nozzle). It is the same case with flares, where the flow exits a nozzle with a tulip-like structure placed on top

(a) Flow pattern of a jet with no wall near it.

(b) Flow pattern in the jet as a straight wall is brought closer to it.

(c) Coanda effect takes place and the jet attaches to the nearby wall.

(d) Flow pattern with Coanda effect in the presence of a straight but offset wall.
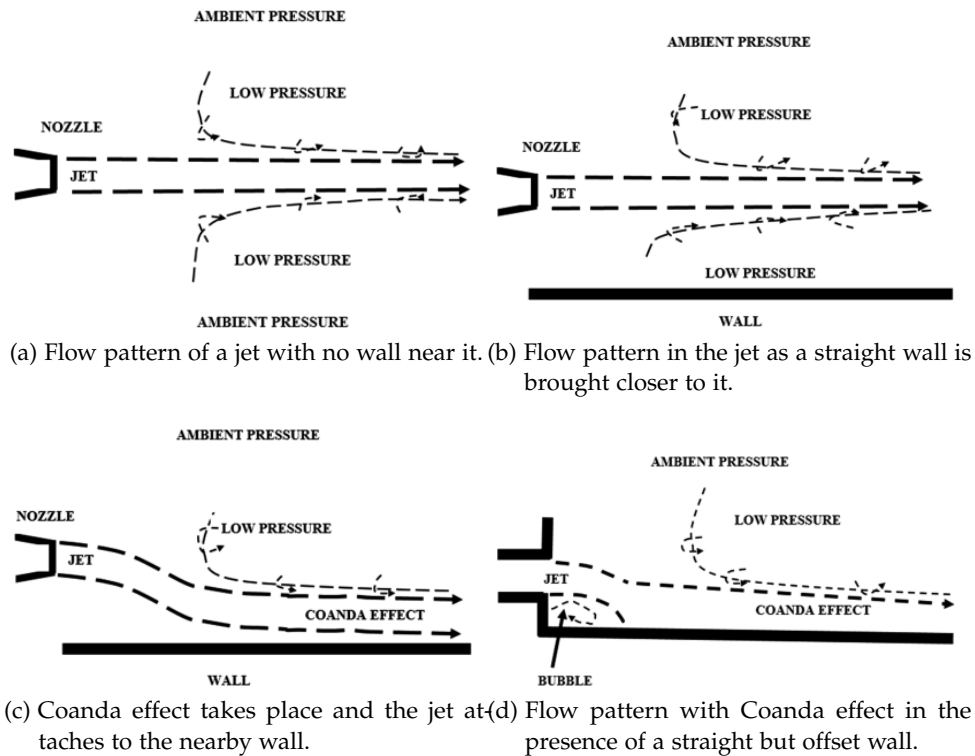
Figure 2.6: Coanda effect. Images reproduced from [77].

of where the combustion takes place. In this following paragraphs, a review of the literature relevant to the application developed in this thesis is presented.

The earliest mention of a Coanda like flame in an industrial burner appears to be by Leuckel [79], and Beer and Chigier [28][80]. The researchers mention the existence of a highly unstable sunflower-like flame exiting a coal-fired swirl burner which required high swirl and a 45° opening angle at the nozzles. The majority of the recent research on a swirling Coanda flame exiting from a circular nozzle and attached to a centred flat plate has been conducted mainly by Vanoverberghe et al., Vanierschot et al., Valera-Medina et at. and a few others. Some of their research and findings will be reviewed here.

Vanoverberghe et al. [81] reported the existence of multi-flame patterns in a confined swirl driven partially premixed combustion of an air-natural gas mixture and presented the transition pathways between the different flame states. The setup consisted of a quartz glass octagonal combustion chamber as a confinement. A variable swirl generator was used to impose a swirl velocity to the reactants. A fixed stoichiometric ratio of 1.1 was used throughout the study. Swirl intensity (0 to 1.12) and the degree of premix of the natural gas-air mixture (0 to 1) were varied. The authors identified a total of five different flame states (Figure 2.8a) which showed hysteresis between them depending on the swirl intensity applied. At zero swirl two different flame states were obtained, the Pinched Jet Flame (PJF) and the Backward Stabilised Flame (BSF). The PJF was a long trumpet-like flame with a narrow body near the nozzle that expanded downstream. The BSF was a flame attached to the
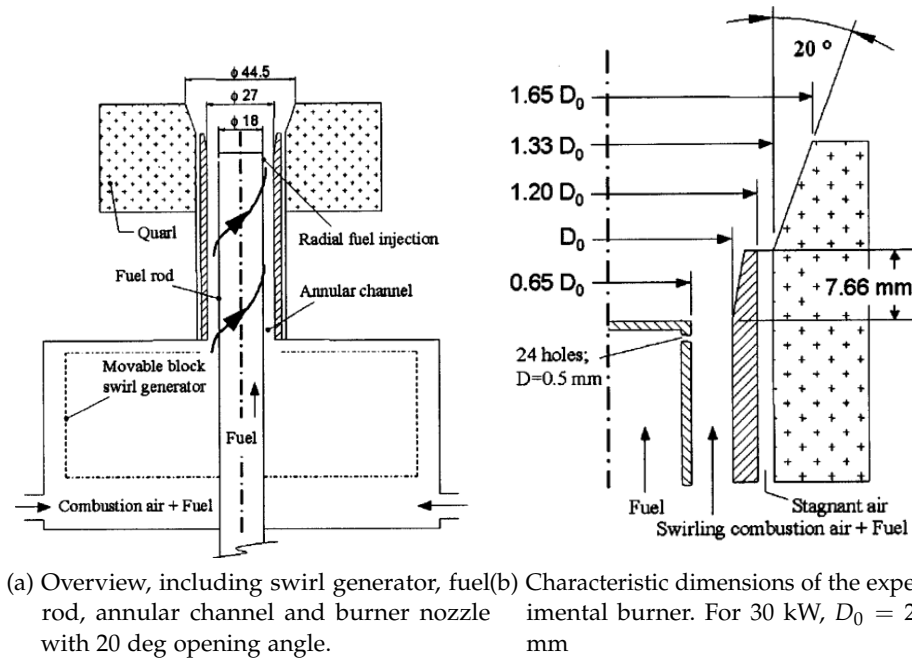
(a) Overview, including swirl generator, fuel rod, annular channel and burner nozzle with 20 deg opening angle.

(b) Characteristic dimensions of the experimental burner. For 30 kW, $D_0 = 27$ mm

Figure 2.7: Experimental 30 kW burner used by Vanoverberghe. Images reproduced from [81, 86].

outlet of the confinement as a result of blow-off. With an increase in swirl the BSF transitioned to a PJF. A further increase in swirl yielded a Nozzle Stabilised Flame (NSF) or a Swirl Stabilised Flame (SSF). The NSF is a flame attached to the nozzle mouth while the SSF is a ring-shaped flame that is lifted at some distance from the nozzle. The last identified flame was a Coanda Stabilised Flame (CSF). Such flame is attached to the bottom of the combustion chamber and produces a large flat flame surface. The NSF and SSF have been previously reported by many others [82–85]. The transition maps obtained by the authors as a function of the degree of premix are shown in Figure 2.8.

In a follow-up study using the same geometry Vanoverberghe et al. [87] investigated the mechanism of attachment of the Coanda flame to the base plate. The authors state that the forces between the outgoing jet and the recirculating backward flow do not balance out. Therefore, there must be an additional force keeping the CSF stable. The authors suggest that a low-pressure region must exist between the region where the jet bends and the burner nozzle. However, no direct observation or description of this low-pressure region is made. An additional objective was to evaluate the effect of the confinement geometry and size on the Coanda flame. First, the backwall stopper (top part of the confinement) was removed, which did not cause any apparent change in the behaviour of the flow. Then the authors proceeded to reduce the diameter of the confinement. The base case was 255 mm. They noted that the confinement can be varied between 200 and 400 mm. Below 200 mm the flame impinges in the walls of the confinement. Above 400 mm the Coanda flame becomes unstable. The authors speculate that the low pressure in the centreline and the External Recirculation Zone (ERZ) in the corner of
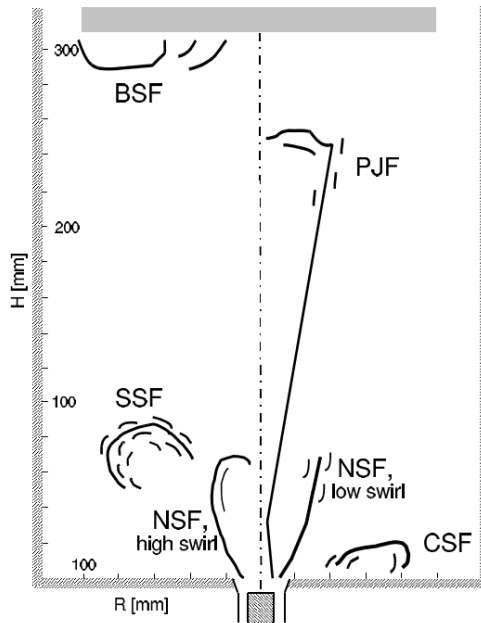
(a) Schematic view of the different flames observed by Vanoverberghe.
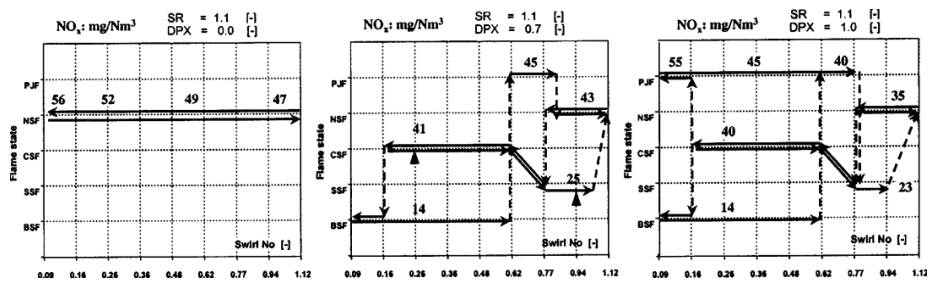
(b) Transition map obtained by Vanoverberghe as a function of degree of premix (DPX) and applied swirl.

Figure 2.8: Experimental results of Vanoverberghe in a 30 kW burner. Images reproduced from [81, 86].

the confinement plays a role in flame stabilisation. Additionally, they indicated that the central fuel rod acts as a bluff body and has an effect on the stability of the Coanda flame. Moving the fuel rod inside the burner's body makes it impossible to obtain a Coanda flame.

Vanierschot and Van den Bulck conducted several follow up studies on the same geometry using isothermal flows [88–91]. In the first study [88], the authors identified four different flow patterns with hysteresis between them by using a fixed turbulent Reynolds number of 10,650 with variations in the applied swirl number. A schematic of the flow states is shown in Figure 2.9. The terminology used by Vanierschot and Van den Bulck to name these flow states is used in this thesis. With zero swirl and up to a swirl of $\sim$ 0.4 the authors obtained a Closed Jet Flow (CJF). CJF is an annular jet without vortex breakdown. With a swirl number higher than 0.4 and lower than 0.6 an Open Jet Low Swirl Flow (OJF-LS) was obtained. In this state vortex breakdown takes place and a CRZ appears. The jet remains detached from the opening step nozzle. With swirl number higher than 0.6 an Open Jet Low High Flow (OJF-HS) was obtained. In this case, the CRZ moved upstream and widened, the jet attached to the opening step nozzle, and a corner recirculation zone appeared between the walls of the nozzle and the corner of the opening angle. The azimuthal velocity, the sub-pressure in the CRZ, and the turbulence levels decreased. Because of hysteresis present in the flow, the OJF-HS state remains stable even at values lower than the transition point required for the change from OJF-LS to OJF-HS ($S = 0.6$). When the swirl reaches $S = 0.5$, the jet transitions to CoJF where the jet bends close to 90 degrees, attaches to the horizontal wall, and a radial jet is formed. In this state, the recirculation zone widens and sub-pressure, tangential velocity and turbulent kinetic energy drop to zero close to the flow centreline. The CoJF remains stable even when no swirl is applied to the flow.

A numerical study by the same authors was conducted based on the previous results [89] where two turbulence models were tested, the Standard $\kappa - \epsilon$ and the Reynolds Stress Model (RSM). Overall, both tested turbulence models predicted the velocity profiles reasonably well. The authors mention that it is particularly interesting how well the Standard $\kappa - \epsilon$ turbulence model predicted the flow fields and hysteresis as it is known that the model does not perform with highly swirling flows (for an overview of the characteristics of each turbulence model refer to Section 3.6.1). A transition map between the flow states for the experiments and simulations is shown in Figure 2.10. Gritskevich et al. [92] used the SST $\kappa - \omega$ model on the same setup and obtained similar results. In another related numerical study by Ogus et al. [93], the authors reproduced the same observed flow states in the same setup using a laminar flow. Singh and Ramamurthi [94] conducted experiments and computations on a geometry where the flow exited a sharp-edged nozzle without a central rod. The nozzle was fitted with a flat plate. Flow rates and the degree of the swirl was varied. The authors concluded that the formation of the wall-attached jet is influenced by both Reynolds number and swirl number of the swirled
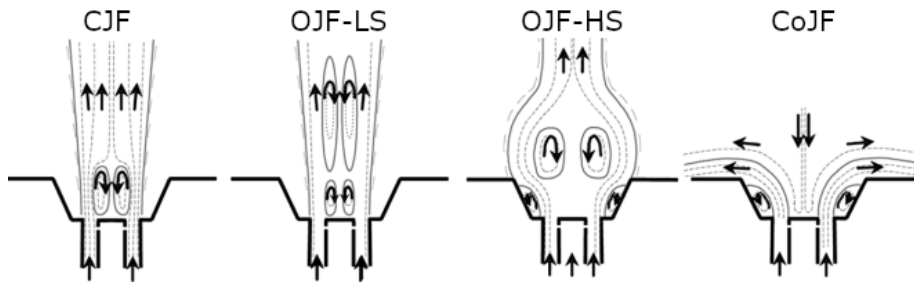
Figure 2.9: Schematic view of the different jet patterns obtained by Vanierschot and Van den Bulck together with the large scale recirculation zones. Image reproduced from [90].
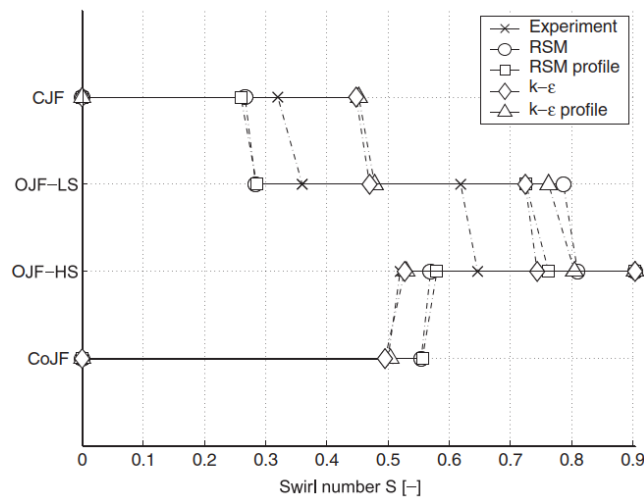
Figure 2.10: Transition map of the jets observed by Vanierschot and Van den Bulck as a function of S. Experimental and simulation results are shown. Image reproduced from [89].

gas jet. The swirl number at which a Coanda jet was formed increased monotonically as Reynolds number increased, this was true for both laminar and turbulent flows.

In a follow-up study, Vanierschot and Van den Bulck [90] studied the effect of the nozzle geometry on the hysteresis of the identified flow patterns. This was done by conducting a parametric study where the influence of the step size, opening angle, and axial length had on the flow pattern. For a fixed nozzle length of 38.3 mm and an opening angle of 30° and changing only the size of the step, the authors reported that for a small step size of 3 mm it was not possible to obtain the CoJF. With an increase of the step to 7 mm, the CoJF pattern was stable even at zero swirl. For a step size of 14 mm, the CoJF was no longer stable a zero swirl. Finally, for 18 mm the OJF-HS did not occur and the CoJF was only possible with high swirl numbers greater than 0.8. In regard to the interaction between the opening angle, step size, and swirl; the authors reported that the higher the opening angle the less swirl is required to change from an OJF-HS to a CoJF. For a given opening angle, the bigger the step size the more swirl is required to obtain a CoJF. The length of the opening angle and the step have the following interaction, if the ratio

between the opening angle / length is small the Coanda effect occurs at lower swirl numbers and if the ratio is large the Coanda effect occurs at higher swirl numbers. Some of the results are shown in Figure 2.11 and Figure 2.12. On a related study, the authors generated a method for controlling the transition from a CJF to OJF-HS and then from OJF-HS to CoJF without the need to alter the swirl by means of a secondary radial air injection [91].

A study by Valera-Medina and Baej [95] using the same swirl burner used for the present thesis investigated the transition of a reacting and isothermal flows between OJF and a CoJF. The authors conducted Particle Image Velocimetry (PIV) measurements on the flow and successfully identified some coherent structure in the flow. A theory on the transition between the two flow states in relation to the identified coherent structures was made.

Other relevant studies are the ones by Falese et al. [96] and Kwark et al. [97]. Falese et al. [96] explored multiple flame states by also changing the swirl number. In this case, the geometry was more complex. The configuration corresponds to an aeronautical liquid fuel injector. It consisted of a pilot injection system surrounded by two counter-rotating axial swirlers and a multipoint injection system, surrounded by a radial swirler. The authors kept the inner and outer swirl numbers constant at S = 0.12 and S = 0.4, respectively. The radial swirl number was varied between two values S = 0.76 and S = 0.84. The authors observed similar flow states with hysteresis as the ones reported by Vanierschot and Van den Bulck [88]. Kwark et al. [97] studied an isothermal and reacting flow using a nozzle with a curved opening with changes in the applied swirl. Similar results to the already mentioned studies were obtained with the isothermal flow. In the reacting flow, the authors observed that for the Coanda flame a higher swirl number produced a lower local flame temperature which they expected will lead to a decrease in NO_x emissions. Additionally, the maximum temperature moved to the edge of the measurement area with an increase in the swirl number. The temperature gradient along the radial direction decreased with an increased swirl. The authors speculate that a flame like this would be suitable for an industrial application where homogeneous radiation heating is required because of the flame spread.

2.4 RADIANT TUBES OPERATING PRINCIPLE AND TYPES

Radiant tubes are mainly used within the industry in heat treatment applications where the products to be heat treated (load) need to be in a protective gas atmosphere (e.g. annealing of certain types of metals) or where there is a risk of the products igniting / getting damaged by the open flame (e.g. paper drying, wood drying, curing ink on paper, plastics curing, setting dyes in textile and carpet production, etc.).
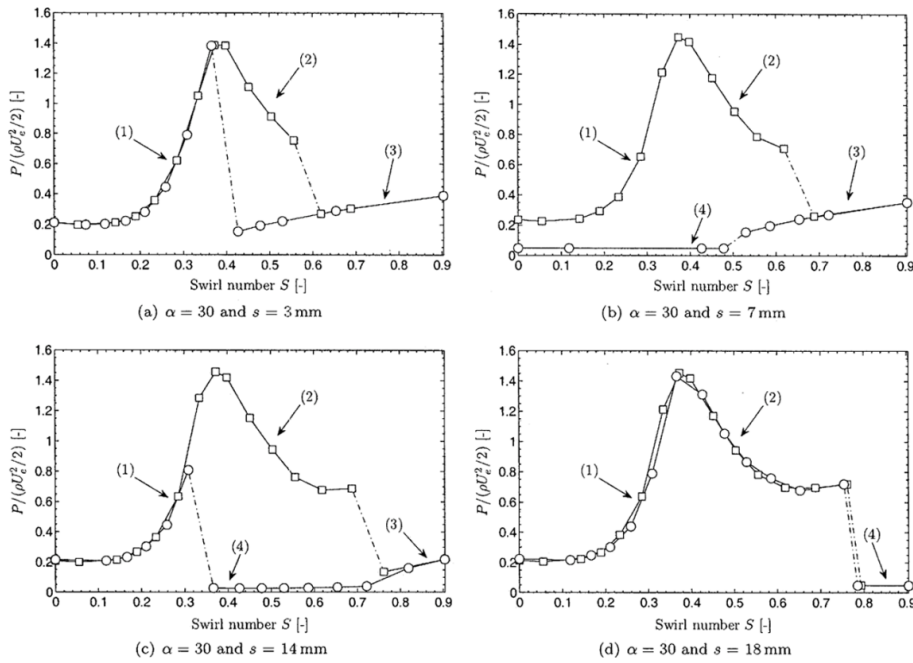
Figure 2.11: Sub-pressure measurements for combinations of angle (α) and step size obtained by Vanierschot and Van den Bulck. Region 1: CJF, region 2: OJF-LS, region 3: OJF-HS, and region 4: CoJF. Image reproduced from [90].
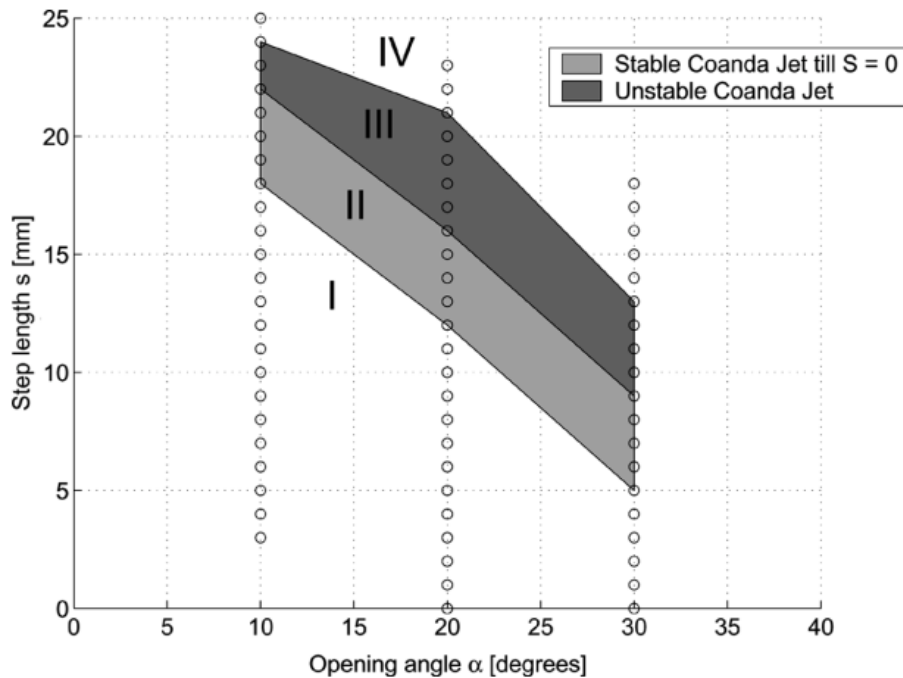
Figure 2.12: Area of stable and unstable CoJF. Dots indicate experimental points obtained by Vanierschot and Van den Bulck. Image reproduced from [90].

2.4.1   *Radiant tube operating principles*

Radiant tube burners operate by first heating a solid surface, usually by burning hydrocarbons (usually natural gas), which in turn radiates infrared (IR) energy to the load (in comparison, in open-flame burners, the radiation emitted by the flame and the gases heated by it are responsible for heating the load) [98].

One of the important features in radiant tubes is the maximum heat transferred, by radiation, from the hot tube wall to the furnace and load. Because radiation heat transfer is proportional to the fourth power of the temperature of the body, important characteristics for radiant tubes are the maximum tube temperature and temperature uniformity. Another important feature is efficiency within the radiant tube, which is related to the temperature of the flue gases. The lower the flue gas temperature the more energy that is transferred to the load through the tube wall and the higher the efficiency of the combustion system. A common way to increase the efficiency in radiant tubes is to preheat the combustion air with technologies like plug-in recuperators, recuperative and regenerative burners. Other important aspects are NO_x and CO emissions, the lifetime of radiant tubes, and maintenance costs. Radiant tubes need to be made of heat resistant alloys that usually have an operating temperature of between 900-1100°C. If a higher temperature is required, ceramic radiant tubes can be used with operating temperatures of up to 1250°C. However, ceramic tubes are more prone to breakage due to the material brittleness and difference in thermal expansion. An alternative to radiant burners are electric radiant heaters, however, their operating cost might be higher depending on the local price of natural gas and electricity [99, 100].

2.4.2   *Types of radiant tubes*

Radiant tubes can be classified by different criteria. One such classification is by the number of passes of the combustion gases.

In non-recirculating tubes, the combustion products make a single pass through the tube. Non-recirculating tubes are usually named by their shape, Figure 2.13a shows some of the designs. The simplest design is the I-tube, which is a straight tube that goes from one wall of the furnace to the opposite wall. In this case, the burner is at one end of the tube with the exhaust gases from the burner travelling through the tube and exiting at the other end. This tube requires connections on both sides of the furnace, the supply gases are on one side while the connections for the exhaust gases are on the other side. Two other designs exist, U-tube and W-tube, that allow for an increase in radiating surface area with the added advantage of having the connections on only one side of the furnace. The disadvantage of these tubes lies in its manufacturing, as it is challenging to make a single monolithic U-tube (or W-tube) that avoids the need for the 180° degree elbow where leaks and failures may occur. Another difficulty is that as the length of the radiant tube increases there is a greater potential of deviation in the temperature along the length

(a) No flue gas recirculation.   (b) Flue gas recirculation.
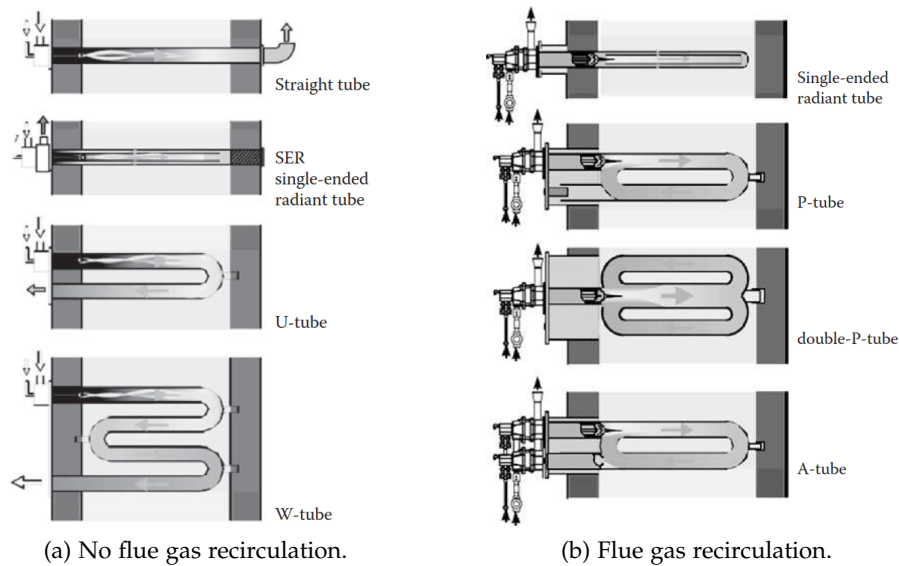
Figure 2.13: Different types of radiant tubes. Image reproduced from [99].

of the radiant tube. Non-recirculating types of tubes are not commonly used as they do not provide an adequate temperature uniformity which can lead to overheating of the tube material. In addition, it is difficult to seal them to the furnace walls because of their constant thermal expansion and contraction. They are not energy efficient by having a high flue gas temperature at the flue gas outlet. A design that mostly overcomes the mentioned limitations is the single-ended radiant tube. This type of tube has an inner tube that forms an annulus with the outer tube and the end opposite to the burner is blocked. The burner ignites the fuel inside the inner tube and the hot flue gases flow through it and then flow back through the annulus between the inner tube and outer tube. This produces a better temperature uniformity across the outer tube wall. Additionally, the burner and exhaust are located on the same side of the tube allowing for a simpler installation and maintenance [99, 100].

In recirculating tubes, a portion of the combustion products is recirculated and combined into the fresh air and fuel stream. To do this, high-velocity burners are used to entrain the combustion products from the exhaust leg of the radiant tube. Adding the recirculated products reduces the peak temperature of the burner's flame and, therefore, the potential for tube hot spots. A side consequence of reducing the flame temperature is the drastic reduction in NO_x formation. Additionally, due to high recirculation ratios within the tube, an improvement of the gas temperature uniformity and corresponding uniform tube wall temperatures is possible. These improvements aside on the temperature uniformity within the furnace and the lifetime of the radiant tubes. As in the case of non-recirculating tubes, several geometries exist and are named according to their shape. Figure 2.13b shows some of the designs [99].

(a) W-type radiant tube with recuperator.   (b) W-type radiant tube with regenerative burners.
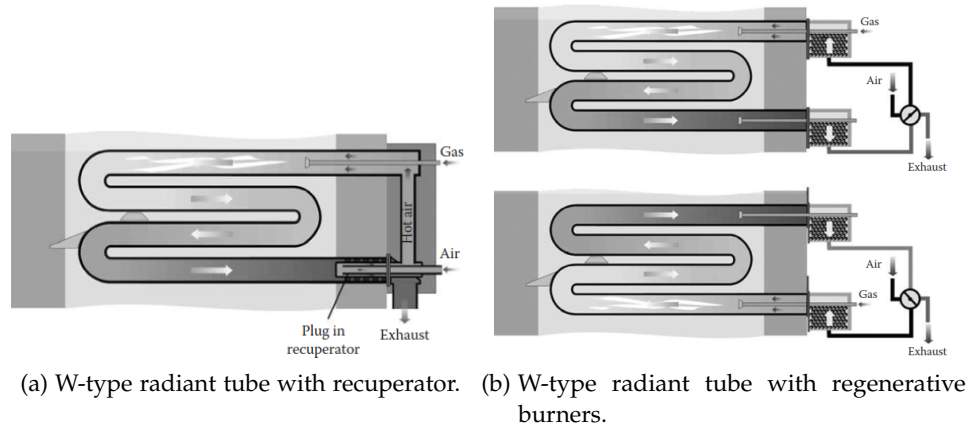
Figure 2.14: Recuperative and regenerative radiant tubes. Image reproduced from [99].

2.4.3   *Energy efficiency and emission control*

The efficiency of the radiant tube burners depends on the amount of energy that is provided to the system (i.e. the fuel) and the energy that is leaving the system (i.e. the radiant walls and the hot flue gases). It should be obvious that a way of quantifying the efficiency of the device is by measuring the temperature of the flue gases; the lower the temperature, the more energy that was transferred to the furnace and the load. Two main alternatives exist for increasing the efficiency of the burner, recuperators and regenerators. Both work by extracting energy from the flue gases and use it to preheat the incoming air. Recuperators are, in essence, counter-current heat exchangers. Figure 2.14a shows an example of a W-type radiant tube with a recuperator. Recuperators can be either part of the radiant tube (usually called self-recuperators) or an external device. Each option has advantages and disadvantages. If the recuperator is part of the tube, external space requirements and ambient air losses are minimised but a limitation on internal space exists. Efficiencies for self-recuperative burners range in the 65 to 72% on an HHV-available-heat basis. If the recuperator is an external device, external space requirements increase and external insulation for the recuperator is required. Efficiencies for external recuperators range in the 50 to 65% on an HHV-available-heat basis. Regenerative radiant tube burners require the radiant tube too have two distinct tube ends like in the case of A-, U-, and W-type radiant tubes. Regenerative radiant tubes function by having two burners, one at each end of the tube, and a heat storage regenerator containing ceramic balls. The burners operate in pairs, one burner fires while the other burner exhausts. Combustion air is preheated by the regenerator of the firing burner and the flue gases give up heat to the regenerator in the exhausting burner. Efficiencies for regenerative burners range in the 75 to 85% in an HHV-available-heat basis. Figure 2.14b shows an example of a W-type radiant tube with a regenerator [101, 102].

Typical NO_x emission reduction techniques can be applied in radiant tube burners, such as the already mentioned (see Section 2.1.4), staged combustion or flue gas recirculation. External emission control, such as selective catalytic reduction [103], can also be applied to radiant tubes. However, it can prove to be challenging as it requires an exhaust collection system that is designed and maintained to eliminate in-leakage of ambient air in order to keep emission post-treatment device at a minimum size [102].

2.5 OVERVIEW OF GRAIN-ORIENTED ELECTRICAL STEEL PRODUCTION PROCESS

2.5.1 *Grain-oriented electrical steel*

Grain-oriented electrical steel (also called silicon steel) is a type of specialised alloy typically used in transformer cores due to its high permeability, low magnetostriction, low coercive force, and low core loss [104, 105]. A typical composition of this type of alloy consists of a mixture, by weight, of Fe 96.7%, Si 3.2%, C 0.03%, Mn 0.06-0.10%, and S 0.02% [105]. The use of this material has allowed the construction of transformers that are over 99% efficient, but this has not always been the case. In the 1880s, the first electrical transformer cores were built with high-grade wrought-iron cores. However, this material made the transformers very inefficient as it had a high core loss. It was not until the work of Hadfield was published in the early 1900s that the technology of electrical steels began to develop. Hadfield discovered that by adding a small amount of silicon to iron the magnetic losses [106]. The next major material science breakthrough came in the 1920s when Honda et al. [107] found out the magnetic anisotropy of iron. In the 1930s, Goss put the discovery of Honda and Kaya to use by inventing the manufacturing process for grain-oriented electrical steel [108]. The process consisted on a combination of rolling and heat-treating the silicon-iron steel, which produced a sheet with (110)[001] texture (also called Goss texture) that had outstanding magnetic properties in the direction of the rolling. The use of this material in the transformer core allowed for an increase of 50% in saturation, a drop of hysteresis losses by a factor of four, and a fivefold increase in permeability [109]. The final major breakthrough came in 1968 with the development of a High permeability Grain Oriented (HGO) electrical steel (or HI-B as a trading name) by the Nippon Steel Corporation [110]. Since the introduction of HGO, grain-oriented types of electrical steel have been broadly classified in Conventional Grain Oriented (CGO) (average misorientation of 7 degrees from the [001] axis) and HGO (average misorientation of 3 degrees from the [001] axis) types; being the later the preferred one for use in transformer cores [111–113]. Figure 2.15 shows the decrease in core loss due to improvement in materials and manufacturing processes. For a detailed review of the historical developments refer to the review by Moses [114].
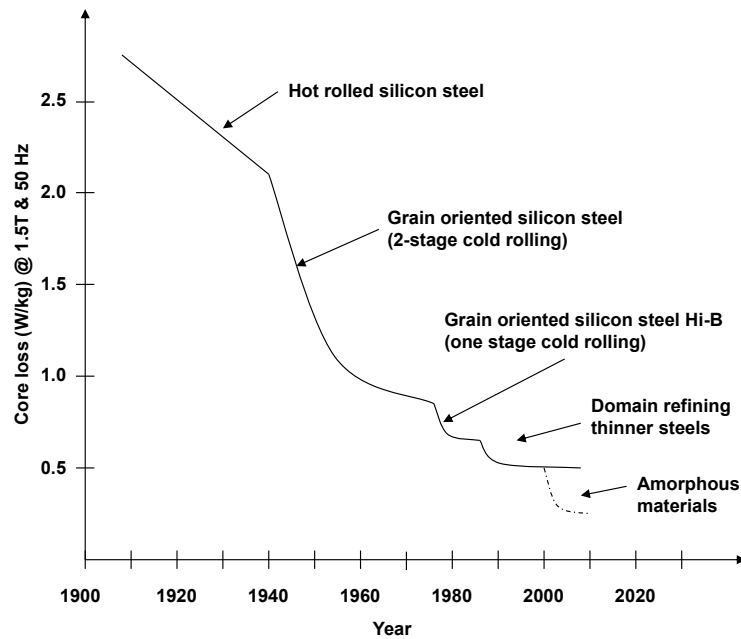
Figure 2.15: Historical reduction in transformer core loss. Images taken from [114].

The principal characteristic of grain-oriented electrical steel, as its name suggests, is the orientation of the grains that conform the metal and also the exceptional high crystal grain size which is in the order of 10 mm. Grains in polycrystalline materials are usually randomly oriented which results in their properties being isotropic. The manufacturing process developed by Goss achieved anisotropy in polycrystalline metals via plastic deformation, specifically, by rolling the metal sheet. When the sheet is rolled, most of the grains acquire a specific crystallographic plane (110) that is aligned parallel (or nearly parallel) to the surface of the sheet and a direction [001] plane that lies parallel (or nearly parallel) to the rolling direction. This means, that the electrical steel sheets used in transformer cores are fabricated in a way such that the direction which the sheet was rolled is aligned parallel to the direction of the applied magnetic field [104].

Despite the state-of-the-art transformer core materials allowing for an efficiency of over 99%, continuous improvements in material quality are being made. It is estimated that about 5% of the total electricity generated in the UK is lost due to transformer core losses [114]. The major variables affecting core loss are [105]:

- **composition**: addition of silicon decreases core loss due to a decrease in magneto-crystalline anisotropy, ability of eliminating impurities, and increased electrical resistivity.

- **impurities**: C, S, N and O are kept below 0.01% as they distort the lattice and impede domain wall motion.

- **grain orientation**: is critical for reducing core losses, for 3.15% Si-Fe, a $1°$ smaller average misorientation would improve the total core loss at 1.5 T/60 Hz by 5%.

- **grain size**: core loss goes to a minimum with a grain size of ~ 0.5 mm.

- **thickness**: a decrease in thickness leads to a decrease in loss due to a reduction in the eddy-current effects. However, at very small thicknesses core loss raises due to surface pinning.

- **surface condition**: a smooth surface leads to lower losses due to a decrease in rough spots that, in turn, decreases surface pinning.

2.5.2 *Production process*

The typical production process for grain-oriented electrical steel is shown in Figure 2.16. The process is as follows [105, 115]:

1. The metal is cast with an approximate composition of 96.7% Fe, 3.2% Si, 0.03% C, 0.06-0.10% Mn, and 0.02% S by weight. MnS is of particular importance as it acts as an inhibitor for the grain growth during the primary recrystallisation. The use of MnS is considered essential for the formation of a good (110)[001] texture.

2. The cast metal is the hot-rolled at $\sim 1300°$C to a thickness between 1.5-2.5 mm.

3. The hot-rolled coil is side trimmed in order to remove any side defects.

4. The oxide scale is annealed and de-scaled with acid.

5. The coil is then cold-rolled to its final thickness of between 0.25-0.35 mm.

6. The coil is annealed and decarburised at $\sim 840°$C in a moist H_2-N_2 atmosphere which reduced the carbon content in the steel to $\sim 0.003\%$ C. A primary recrystallisation occurs in this stage, i.e. the strain induced in the cold rolling stage is released and leads to the grow of new strain-free grains. At this stage, the grains are very small in size with a diameter of approximately 150 microns and have a very low orientation in the rolling direction.

7. The coil is then coated with MgO which combines with the Si to form an insulating glass-like layer of magnesium silicate. MgO acts as a separator of the different steel sheets in the next part of the process.

8. The coil is batch annealed at ~ 1100-$1200°$C in a dry H_2-N_2 for about 24 hours. In this part of the process, the secondary recrystallisation occurs which forms the (110)[001] texture. Also in this stage of the process, the MnS inhibitor reacts with the H_2-N_2 atmosphere and reduces to Mn and H_2S gas. The Mn stays in the solid solution with iron and increases the resistivity of the metal. Removing MnS in the alloy is important because it can inhibit domain wall movement.
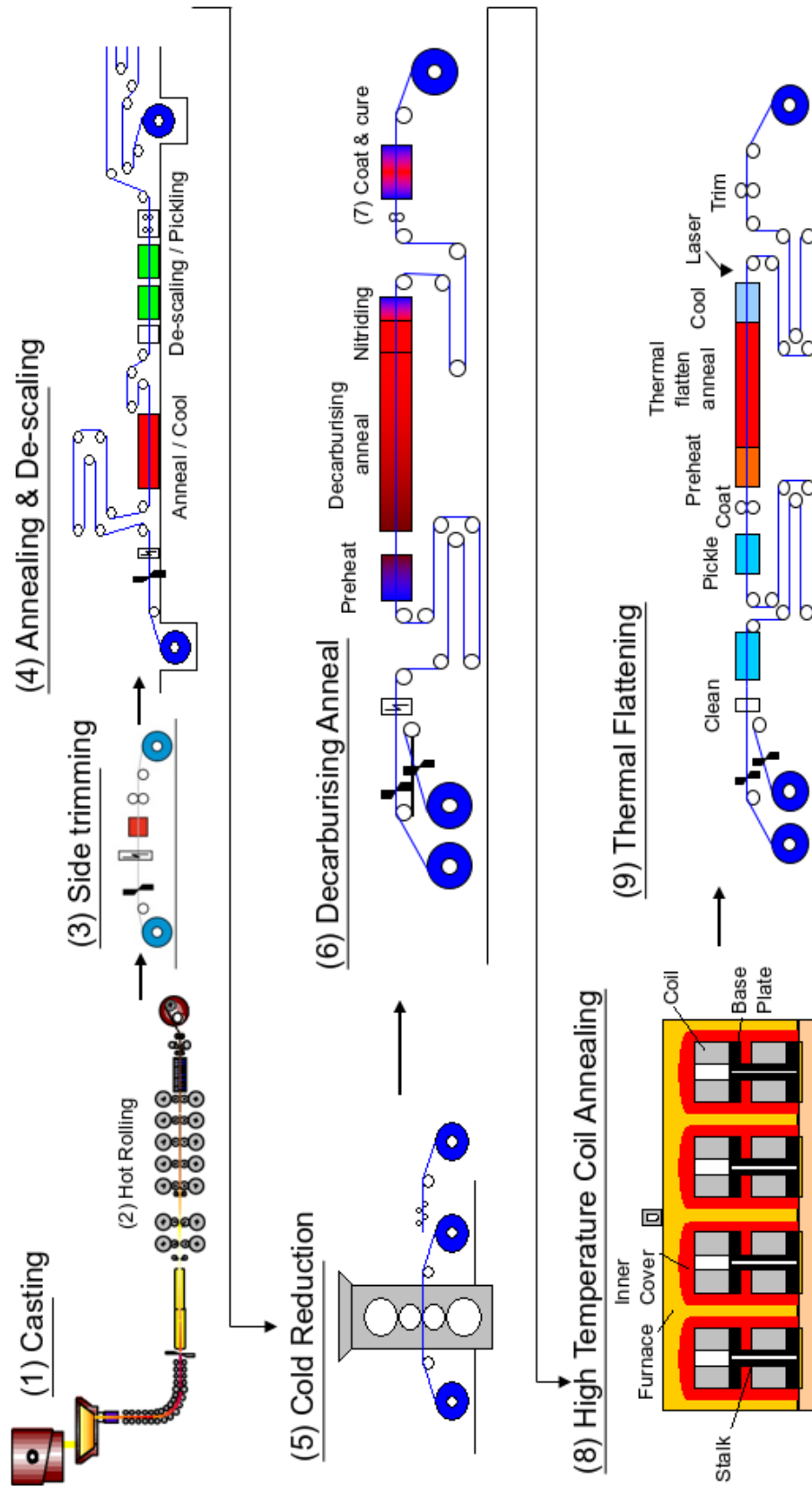
Figure 2.16: Grain-oriented electrical steel production process. Image reproduced from [116].

2.5.3 *Decarburising anneal process*

2.5.3.1 *Process description*

The process is of a semi-batch type nature where the electrical steel strip coming from the cold-rolling process is initially coiled. The strip is uncoiled and is transported through the process by a series of horizontal rollers. The strip is first passed through a burn-off furnace with open-fired burners. The purpose of this step is to clean the strip by removing any oil-based lubricant that remains from the cold rolling and to pre-heat the strip. Afterwards, the strip enters the decarburisation furnace where it is annealed in a moist H_2-N_2 atmosphere at $\sim 840°C$. The decarburisation and primary recrystallisation takes place in this part of the process. The percentage of carbon in the strip is decreased to about $\sim 0.003\%$ C which reduces magnetic losses and increases resistance to magnetic ageing. Carbon is removed by the following chemical reactions with the wet H_2-N_2 atmosphere [117]:

$$C_{(s)} + H_2O_{(g)} \rightarrow CO_{(g)} + H_{2(g)} \tag{2.13}$$

$$C_{(s)} + 2H_{2(g)} \rightarrow CH_{4(g)} \tag{2.14}$$
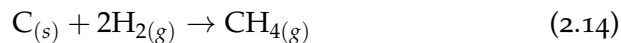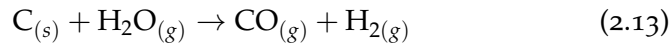
After the decarburisation anneal, a coating of MgO is applied to the surface of the strip. The coating will eventually react with the Si in the steel in order to create a glass-like film of magnesium silicate during the high-temperature batch anneal.

2.5.3.2 *Furnace description*

The decarburising furnace at TATA Steel Cogent Power consists of a tunnel of about approximately 130 m in length, 1.44 m in width and 1.33 m in height. The walls are made of 40 cm thick refractory firebrick. The atmosphere within the furnace consists of a mixture of moist H_2-N_2. A diagram of each zone is shown in Table 2.1. The furnace is split into 18 zones, each with its own temperature control. The decarburisation process occurs in zones 1 to 16. There is no physical separation between these zones, i.e. they consist of a continuous tunnel. A separating wall exists between zone 16 and 17. The nitriding process occurs in zones 17 and 18. Heating of the electrical steel strip is done via radiant tubes which are either gas fired or electrically heated. Zones 1 to 5 are gas heated and are where the ramping up of the temperature of the strip occurs. Zones 6 to 18 are electric heated and are where the temperature soaking takes place. A summary of each zone is shown in Table 2.2, which includes the furnace length, amount of radiant tubes, and total gross heating capacity of the zone.

Table 2.1: Decarburising anneal furnace gas and electric zones.

Decarburising anneal furnace																	
Gas zones						Electric zones											
1	2	3	4	5	6	7	8	9	10	11	12	13	14	15	16	17	18
Heating zones						Decarburising							Soaking zones				Nitrading

Table 2.2: Characteristics of each zone in the decarburising anneal furnace.

Zone	1	2	3	4	5	6	7	8	9	10	11	12	13	14	15	16	17	18
Heating power (kW)	490	490	665	665	420	230	116	116	116	116	116	116	116	116	116	116	116	38
Length (m)	3.0	4.0	5.8	5.8	5.2	5.5	8.2	8.2	8.2	8.2	8.2	8.2	8.2	11.0	11.0	11.0	9.8	1.2
No. RT	14	14	19	19	12	36	18	18	18	18	18	18	18	24	24	24	24	2
No. RT top	8	8	10	9	6	18	9	9	9	9	9	9	9	12	12	15	12	1
No. RT bottom	6	6	9	10	6	18	9	9	9	9	9	9	9	12	12	12	12	1
Volume (m³)	6.1	7.9	11.5	11.5	10.3	11.0	16.3	16.3	16.3	16.3	16.3	16.3	16.3	21.9	21.9	21.9	19.5	2.4

2.5.4 *Effect of heating rate during primary recrystallisation on product quality*

Some studies have suggested that a faster heating rate during the primary recrystallisation (i.e. during the initial heating in the decarburising anneal process) has a crucial role on obtaining the desired (110)[001] texture in the final product.

Park et al. [118] tested two samples of non-oriented electrical steel with different composition and initial grain size. The first sample had a composition of 98.46% Fe, 1.0% Si, 0.0050% C, 0.26% Mn, 0.0026% P, 0.27% Al, and 0.0025% N and an initial average grain size after hot-rolling of 40 μm. The second sample had a composition of 97.44% Fe, 2.0% Si, 0.0030% C, 0.24% Mn, 0.0018% P, 0.31% Al, and 0.0020% N and an initial average grain size after hot-rolling of 115 μm. The samples were cold-rolled to a final thickness of 0.5 mm which resulted in a reduction of 75%. Each sample was annealed at three distinct heating rates of 5°C/s, 10°C/s, and 30°C/s to induce the primary recrystallisation. The authors found that the heating rate had an effect on the resulting grain size during the primary recrystallisation. The slowest heating rate resulted in a final average grain size of $\sim$ 85 μm in both the sample with the initial coarse grain size (115 μm) and the initial fine grain size (40 μm). At the heating rates of 10°C/s and 30°C/s the grain size was considerably reduced to $\sim$ 30 μm for the coarse-grained samples and to $\sim$ 25 μm for the fine grained samples. A higher heating rate was also associated with an increase in Goss-oriented grains as a consequence of the reduced grain size.

Park et al. [119] tested a grain-oriented electrical steel with an initial composition of 96.72% Fe, 3.1% Si, 0.06% C, 0.1% Mn, and 0.02% P. The samples were prepared by vacuum-melting the alloy, hot-band annealing to a thickness of 2.0 mm, and subsequently cold rolling to its final thickness of 0.30 mm. The sample was then heated to a temperature of $\sim$ 700°C at two different heating rates, 20°C/s and 150°C/s. Samples were extracted at different holding times. The grain size, distribution, fraction of Goss-oriented grains, and texture of the samples were determined by optical microscopy, X-ray pole figures, and orientation image mapping. The authors found that the heating rate had no effect on the Goss-oriented grain size. However, there was an effect of the heating rate on the fraction and distribution of the Goss-oriented grains. Higher heating rates had a larger fraction of Goss-oriented grains and had a similar distribution in the surface and middle layers Figure 2.17a. In contrast, lower heating rates had less homogeneous distribution between the surface and middle layers Figure 2.17b. The result indicates that the rapid-heating promotes the creation of Goss-oriented grains inside the material.

Hou and Tzeng [120] studied the effect of heating rate and decarburisation temperature during the primary annealing on the microstructure and magnetic properties of grain-oriented electrical steels. The tested material had an initial composition of 96.52% Fe, 3.25% Si, 0.052% C, 0.14% Mg, and 0.0065% S, 0.024% Al, and 0.0079% N. The sample was

(a) Rapid-heated (150°C/s)   (b) Normal-heated (20°C/s)
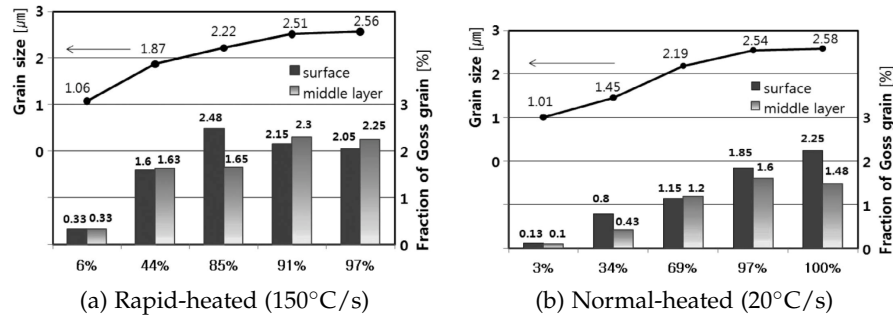
Figure 2.17: Average grain size and fraction of Goss-oriented grains at different heating rates and recrystallisation fractions. Images reproduced from [119].

prepared by hot-rolling the material in two steps to a thickness of 2.3 mm, followed by a cold-rolling to 0.35 mm. For the primary recrystallisation, three heating rates were tested, 5°C/min, 20°C/min and 300°C/s, and the annealing temperature set at 700, 750, 800 and 850°C. The samples were nitrated and coated. Finally, the secondary recrystallisation annealing was carried out in an H_2-N_2 atmosphere with a heating rate of 60°C per hour until the annealing temperature of 950°C was reached and soaked 12 hours. The authors found that the oxide layer thickness increases with decarburisation temperature and decreases with a decreased heating rate, nitrogen content decreased with increasing decarburisation temperature and increased with increasing heating rate, and primary grain size increased with increasing decarburisation temperature and decreased with increasing heating rate. These observations are of relevance because they influence the grain growth during the secondary recrystallisation. Too many nitrogen precipitate will cause abnormal grain growth to never occur, while too little cannot impede normal grain growth. Initial grain size is the driving force for grain growth during the secondary recrystallisation, i.e. big grain size do not have enough driving force to promote grain growth. Flux density and core loss are closely related to the percentage of grain growth in the secondary recrystallisation, with a higher percentage of grain growth resulting in better magnetic properties. The maximum flux density resulted when the material was heated at 300°C/s and the decarburisation annealing temperature was 850°C. Overall, magnetic flux density increases with increased temperature (Figure 2.18) and core loss decreased with increased temperature and increased heating rate (Figure 2.19).

2.6   CHAPTER SUMMARY

The literature review for the work presented in this thesis was made. First, an overview of the concepts required to understand what will be discussed in the following chapters was made. Basic combustion concepts such as stoichiometry, mass balance, energy balance were presented made. Characteristics of flames were explained as well as some of the undesirable emissions that are produced in a typical combustion
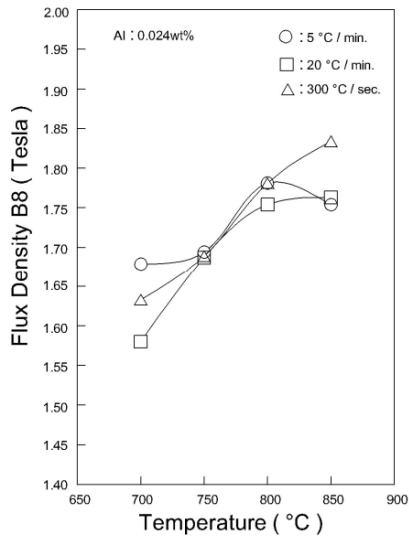
Figure 2.18: Electrical steel flux density after final annealing. Image reproduced from [120].
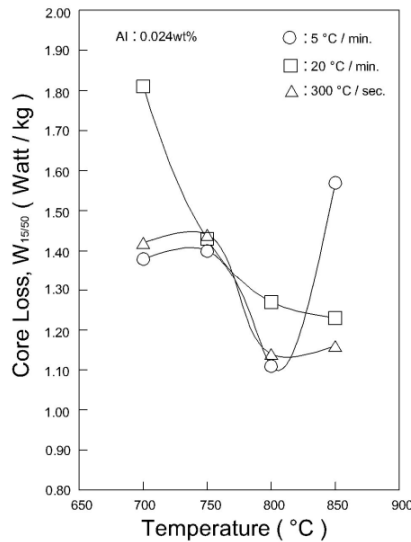
Figure 2.19: Electrical steel core loss after final annealing. Image reproduced from [120].

process. Two of the main flow phenomena that are present in swirling flows were explained. The Coanda flow was introduced and a conceptual explanation of how it occurs was provided. Some of the applications where the Coanda flow has been used were given. An in-depth review of the relevant literature was made, making special emphasis on research that is directly related with the application proposed in this thesis. An overview of what are radiant tubes and where are they used was presented in order to give an insight into the technology that the proposed burner aims to replace and improve upon. Finally, the electrical steel annealing process was shown. This process will be used as a case study to assess the potential of the proposed flat flame burner concept.

MEASUREMENT EQUIPMENT AND ANALYSIS TECHNIQUES

This chapter covers the laboratory setup, the experimental measurement techniques, post-processing methods, and the numerical approach used for the simulations. This chapter is structured as follows, first Section 3.1 presents the laboratory equipment and setup for the isothermal and combustion experiments. Section 3.2 introduces the main experimental method for this thesis. Then, in Section 3.3, 3.4 and 3.5 the employed post-processing methods are described. The numerical methods, solver setup and error estimation are introduced in Section 3.6.

3.1 LABORATORY TEST RIG DESCRIPTION

3.1.1 *Burner*

A modular swirl burner constructed from stainless steel was used in the present thesis to perform experiments under an isothermal air flow (Chapter 4) and under a reacting flow with different mixtures of air and methane (Chapter 5). A schematic of the burner is shown in Figure 3.1 and consists of the following parts:

- A swirl chamber that has a single lateral inlet with a diameter of 20 mm that is placed off-centre. The swirl chamber itself has a diameter of 56 mm and a height of 49 mm.

- A secondary inlet with an inner diameter of 9.2 mm. The desired gas is injected axially at the start of the nozzle.

- Three tangential swirl generators were available for the experiments with geometrical swirls of 0.85, 1.04 and 1.47. The dimensions of the swirl generators are shown in Figure 3.2.

- Two different sets of nozzles were used. The first set consisted of three nozzles with a diameter of $D = 28.0$ mm and nozzle opening angles of $\alpha = 30°$, 45° and 60°. The second set consisted of three nozzles with an opening angle of $\alpha = 45°$ and nozzle diameters of $D = 19.5$, 24.0 and 28.0 mm.

- A flat plate fitted to the nozzle exit.

3.1.2 *Confinement*

A squared confinement was manufactured from stainless steel and used for some of the reacting flow experiments presented in Chapter 5. A schematic of the confinement is shown in Figure 3.3. The overall
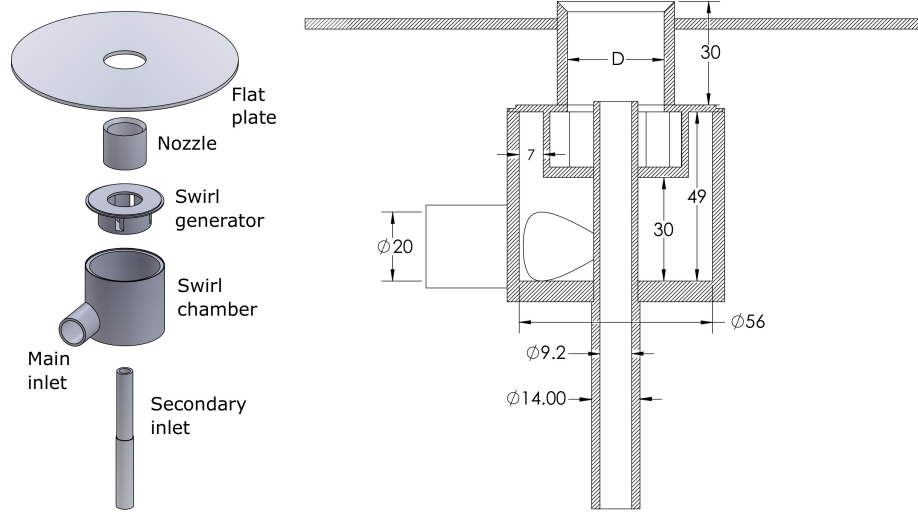
Figure 3.1: Exploded view of modular swirl burner (left) and cross-section view (right). Dimensions in millimetres.
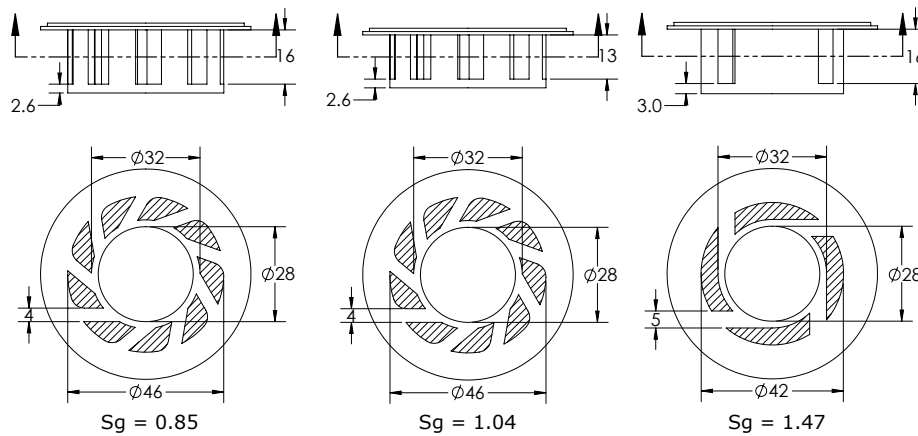
Figure 3.2: Tangential swirl generators used in the experiments. Geometrical swirl numbers are 0.85, 1.04 and 1.47 respectively. Dimensions in millimetres.

inner dimensions of the squared volume were $488 \times 488 \times 56$ mm^3. The bottom plate had a single inlet with a diameter of 32 mm that allowed for a snug fit of the burner nozzle. Along the edges of the bottom plate, there were four rectangular outlets of size 20×400 mm^2. The top plate had a lid with a diameter of 95 mm positioned at the centre of the plate that allowed the ignition of the gas mixture. This same lid allowed access to the interior of the confinement in order to change the flame flow pattern. One of the lateral walls of the confinement had a window of size 65×30 mm^2 covered by a quartz which allowed the observer to view the behaviour of flame.

3.2 PARTICLE IMAGE VELOCIMETRY

PIV is a non-intrusive optical method used for flow visualisation that provides instantaneous velocity measurements in a cross-section of a flow. The main components in a PIV system are a camera, a laser sheet, a timing device, and an image acquisition capture software. The principle of operation of the PIV method consists on seeding the flow with tracer particles. Particles are then illuminated by two subsequent laser sheet pulses. A camera is used to capture each light pulse in separate image frames. For the velocity calculation, the recorded images are divided into a grid of small areas, called Interrogation Area (IA). The average particle displacement ($\Delta \bar{x}$) is obtained by cross-correlating, pixel-by-pixel, the IAs for each image frame followed by the localisation of the correlation peak. It is probable that the correlated particle might fall totally or partially in the neighbouring IA. A way to deal with this inconvenience is to overlap IAs. Velocity components for each IA are then calculated by dividing the average particle displacement in each direction by the known time between each image frame Δt, yielding the equation $\bar{v} = \Delta \bar{x}/\Delta t$ [121]. The total number of vectors per field that are obtained is directly dependent on the camera resolution, the size of the IA, and the amount of overlapping between IAs.

Seeding plays an important role in the accuracy and reliability of the PIV technique, as the principle behind it is to determine the particle velocity instead of a direct measurement of the fluid velocity. Care must be taken when selecting the type of seeding and particle size. Particles must be small enough so that they track the flow accurately and must be large enough to scatter the required amount of light. Additionally, the seed must be uniformly distributed in the flow field and agglomeration of particles should be avoided in order to obtain accurate flow fields. As a rule of thumb, 10 to 25 particles for each resolved vector must be present in each IA [123]. Ultimately the properties, particle size, and seed volume will be dependent on the particular flow studied. A good review of tracer particles for PIV systems is found in [124].

The standard and most simple setup of a PIV system consists on acquiring images using a single CCD or CMOS camera positioned perpendicular to the measured plane. This allows the measurement of two velocity components in a plane (2D2C). However, if the flow is highly three-dimensional, the loss of the out-of-plane velocity component can
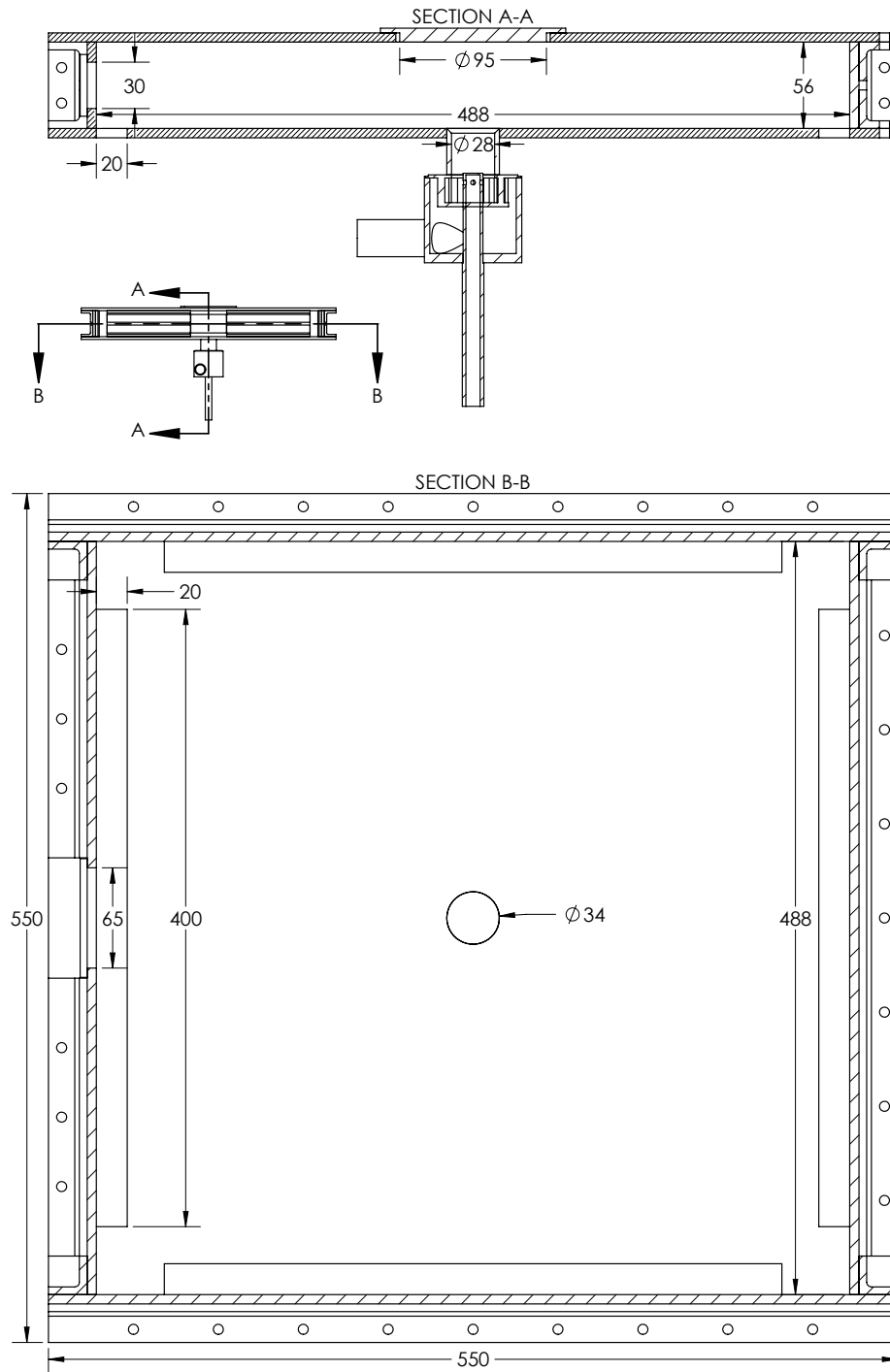
Figure 3.3: Vertical (top) and transversal (bottom) cut views of confinement. Dimensions in millimetres.
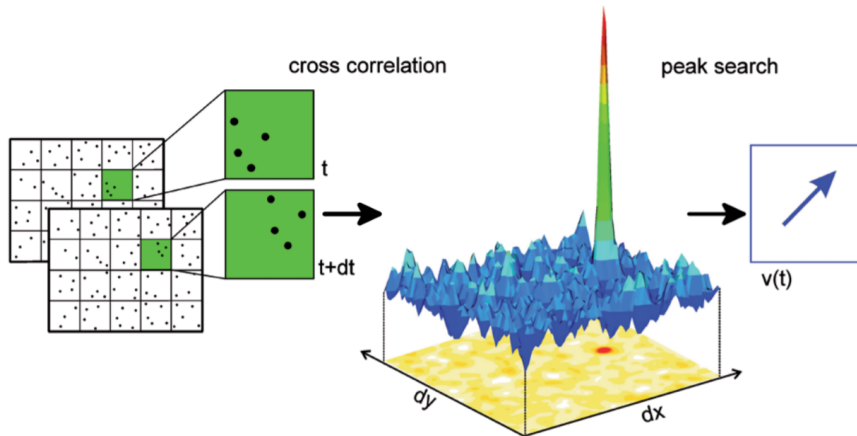
Figure 3.4: Cross-correlation process [122].
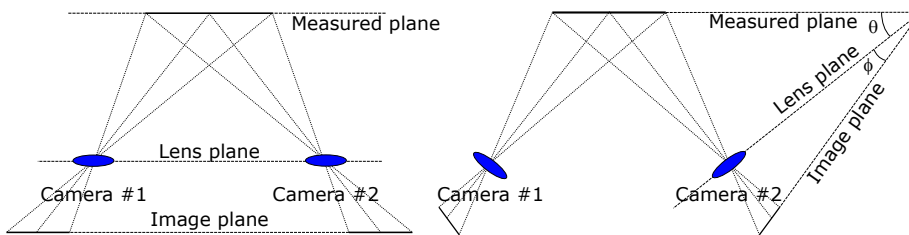
Figure 3.5: Stereo PIV configurations: (left) lens translation method, (right) angular method with tilted back plane [121].

lead to substantial measurement errors of the local velocity vector [125]. This error is due to the in-plane velocity vector projection on the viewing direction of this vector and its out-of-plane velocity component [126]. To eliminate this error, the third velocity component needs to be measured. This can be done by using Stereo Particle Image Velocimetry (S-PIV). This method consists of adding a second camera to record the flow from different positions [127]. Two different stereoscopic approaches can be used, (1) the angular method, where cameras are no longer positioned perpendicular to the measured plane, but at an angle; (2) the translational method where the cameras are perpendicular to the measured plane but are offset from the centre. In this case, the stereoscopic effects are directly related to the distance between the optical axes of the cameras [121]. The schematic of both methods can be seen in Figure 3.5. The out-of-plane velocity component can then be obtained by correlating the two measured vector fields. In this study, the angular method is used.

3.3 PROPER ORTHOGONAL DECOMPOSITION

The analysis of turbulent flows often requires the extraction of the stochastic fluctuation of a given quantity from its expected value. This forms the basis for various subsequent analyses. One way to do this is by performing a Reynolds decomposition on the flow quantity of interest. For example, for a given flow quantity of interest, x, the decomposition would be:

$$x\left(\mathbf{r}, t_k\right) = \overline{x}\left(\mathbf{r}\right) + x'\left(r, t_k\right)$$

where $\mathbf{r}$ is the spatial coordinate on the domain and t_k is the kth time step. Over-bar denotes the time average and x' is the fluctuating component. This is accurate to do if the only source of fluctuations is turbulence. However, this is not the case for the flows considered in this thesis, i.e. turbulent swirling flows. These type of flows often present different flow features like vortex shedding and coherent structures like the PVC which, as described in Chapter 2, have a periodic pattern in time. Because of this, a slightly more complex decomposition of the flow that differentiates between turbulent and periodic phenomena is required. An adequate decomposition for this case was introduced by Hussain and Reynolds [128]:

$$x\left(\mathbf{r}, t_k\right) = \overline{x}\left(\mathbf{r}\right) + x'_{prec}\left(\mathbf{r}, t_k\right) + x'_{turb}\left(\mathbf{r}, t_k\right)$$

where x'_{prec} is the coherent fluctuation of the velocity component and x'_{turb} is the turbulent fluctuation. However, distinguishing between the two types of fluctuations is non-trivial. One such method that can separate the turbulent fluctuations from the coherent fluctuations is the Proper Orthogonal Decomposition (POD). This method is based on the hierarchical decomposition of flow data into an orthogonal basis of spatially and temporally correlated modes. It was first applied in the context of fluid mechanics by Lumley [129, 130]. Several variations of the POD method have been proposed, the most appropriate one for the type of data presented in this work is the snapshots POD method proposed by Sirovich [131]. In the snapshots method, each instantaneous PIV measurement is considered to be a snapshot of the flow. The first step in the snapshots method [132, 133] consists in arranging the data at each t_k time into a single tall column vector:

$$\mathbf{x}\left(\mathbf{r}, t_k\right) = \begin{bmatrix} x\left(r_{1,1}, t_k\right) & x\left(r_{1,2}, t_k\right) & \cdots & x\left(r_{1,p}, t_k\right) \\ x\left(r_{2,1}, t_k\right) & x\left(r_{2,2}, t_k\right) & \cdots & x\left(r_{2,p}, t_k\right) \\ \vdots & \vdots & \ddots & \vdots \\ x\left(r_{q,1}, t_k\right) & x\left(r_{q,2}, t_k\right) & \cdots & x\left(r_{q,p}, t_k\right) \end{bmatrix} \tag{3.1}$$

$$\Rightarrow \mathbf{x}_k = \begin{bmatrix} x\left(r_{1,1}, t_k\right) \\ x\left(r_{2,1}, t_k\right) \\ \vdots \\ x\left(r_{1,2}, t_k\right) \\ \vdots \\ x\left(r_{q,p}, t_k\right) \end{bmatrix} = \tag{3.2}$$

The vector $\mathbf{x}_k \in \mathbb{R}^n$ is called a snapshot of data. The size n of a snapshot depends on the size of the vector field and the number of variables of interest. The snapshot vector can be arranged in a data matrix $\mathbf{X}$:

$$\mathbf{X} = \begin{bmatrix} | & | & | & | \\ \mathbf{x}_1 & \mathbf{x}_2 & \cdots & \mathbf{x}_m \\ | & | & | & | \end{bmatrix} \tag{3.3}$$

If more than one flow variable is of interest, each variable will be arranged as Equation 3.3 and the matrices will be stacked on top of each other. For example, for a three-dimensional PIV data set, matrix $\mathbf{X}$ would take the form of:

$$\mathbf{X} = \begin{bmatrix} u\left(r_{1,1}, t_1\right) & u\left(r_{1,1}, t_2\right) & \cdots & u\left(r_{1,1}, t_k\right) \\ \vdots & \vdots & \ddots & \vdots \\ u\left(r_{q,p}, t_1\right) & u\left(r_{q,p}, t_2\right) & \cdots & u\left(r_{q,p}, t_k\right) \\ v\left(r_{1,1}, t_1\right) & v\left(r_{1,1}, t_2\right) & \cdots & v\left(r_{1,1}, t_k\right) \\ \vdots & \vdots & \ddots & \vdots \\ v\left(r_{q,p}, t_1\right) & v\left(r_{q,p}, t_2\right) & \cdots & v\left(r_{q,p}, t_k\right) \\ w\left(r_{1,1}, t_1\right) & w\left(r_{1,1}, t_2\right) & \cdots & w\left(r_{1,1}, t_k\right) \\ \vdots & \vdots & \ddots & \vdots \\ w\left(r_{q,p}, t_1\right) & w\left(r_{q,p}, t_2\right) & \cdots & w\left(r_{q,p}, t_k\right) \end{bmatrix}$$

In fluid systems, the size of n is typically much larger than the number of snapshots m, making the matrix $\mathbf{X}$ tall and skinny. The POD modes can be calculated by taking the Single Value Decomposition (SVD):

$$\mathbf{X} = \mathbf{U\Sigma V}^* \tag{3.4}$$

However, this is would be computationally very demanding, as it would involve autocorrelating all the vectors in all the time instants. Here is where the practicality of the snapshots method comes into play. It is possible to construct a correlation matrix $\mathbf{X}^*\mathbf{X}$ from the inner products of the columns of $\mathbf{X}$ by doing its eigendecomposition, resulting in a matrix of size $m \times m$:

$$\mathbf{X}^*\mathbf{X} = \mathbf{V\Sigma U}^*\mathbf{U\Sigma V}^* = \mathbf{V\Sigma}^2\mathbf{V}^* \tag{3.5}$$

$$\Rightarrow \mathbf{X}^*\mathbf{X}\mathbf{V} = \mathbf{V\Sigma}^2 \tag{3.6}$$
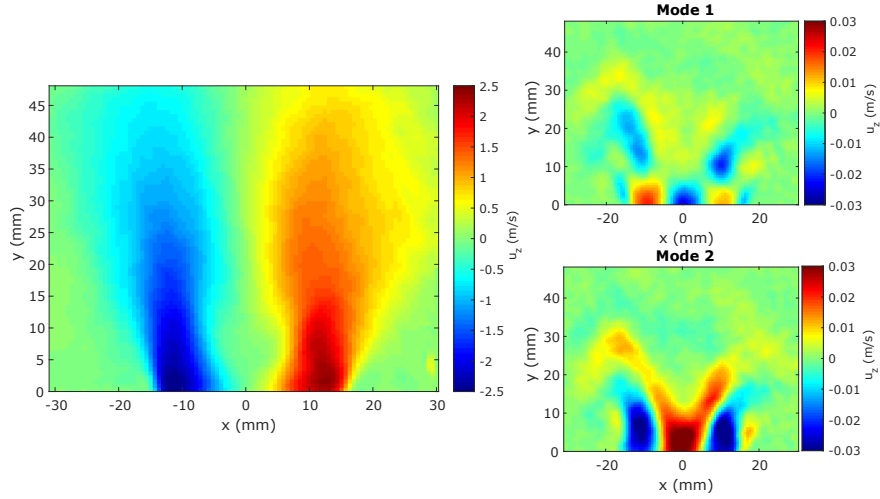
Figure 3.6: An example velocity field (left) and first 2 POD modes for that flow field (right).

the values for $\mathbf{V}$ and $\boldsymbol{\Sigma}$ can then be calculated. It is now possible to construct the POD modes matrix $\mathbf{U}$ by:

$$\mathbf{U} = \mathbf{X}\mathbf{V}\boldsymbol{\Sigma}^* \tag{3.7}$$

where matrix $\mathbf{U}$ contains the spatial correlations of data and matrix $\mathbf{V}$ the temporal information. Analysis of certain elements of the flow fields can be done by reconstructing the fields using only some of the POD modes $\mathbf{U}$, corresponding eigenvalues $\boldsymbol{\Sigma}$, and temporal eigenvectors $\mathbf{V}$. This is explained in more detail in the following paragraphs. The reconstructed data matrix $\widetilde{\mathbf{X}}$ can be calculated by using only the desired k POD modes:

$$\widetilde{\mathbf{X}} = \mathbf{U}\boldsymbol{\Sigma}\mathbf{V}^* \tag{3.8}$$

A relation exists between the magnitude of the eigenvalues captured in the diagonal matrix $\boldsymbol{\Sigma}$ and the kinetic energy captured by the corresponding k^{th} POD mode [134]. By sorting the eigenvalues by their magnitude as $\Sigma_1 \geq \Sigma_2 \geq \cdots \geq \Sigma_i = 0$ it is possible to hierarchically reconstruct vector fields with respect to the turbulent kinetic energy contained in each mode [131, 135]. By doing this, the low energy random motions of in the flow are eliminated. For example, Figure 3.6 shows mean flow field and its first two POD modes.

Further characterisation of the flow can be done by looking at the temporal information stored in matrix $\mathbf{V}$. Any phenomena that repeats in time, as is the case of coherent structures, will be identifiable in this matrix if the temporal acquisition resolution was adequate. Thus, the information in matrix $\mathbf{V}$ effectively allows the separation of the fluctuating component $x'\left(r, t_k\right)$ into a fluctuations due to coherent temporal phenomena $x'_{prec}\left(\mathbf{r}, t_k\right)$ and random fluctuations produced by turbulence
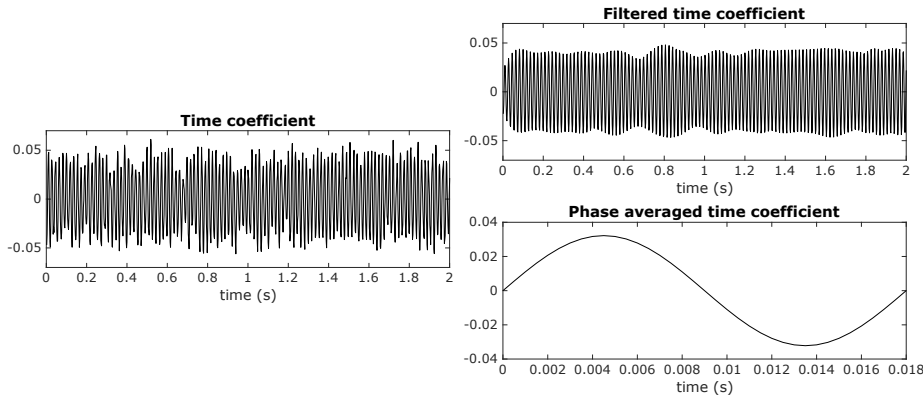
Figure 3.7: Temporal coefficient filtering and phase averaging for the sample flow field shown in Figure 3.6. The temporal signal (left), band-pass filtered signal with cutoff frequency = 55.6 ± 1 Hz (top right) and phase average of a single period (bottom right).

$x'_{turb}(\mathbf{r}, t_k)$. A good starting point is to do a Fast Fourier Transform (FFT) on the vectors of the most energetic modes and look for frequencies that are in line with the expected phenomena. Once the frequencies of interest are identified, the temporal eigenvectors can be further filtered with a low-pass or band-pass filter with a cut-off frequency equal to the frequency of interest, followed by phase averaging. The result of this would be a set of phase averaged fields free of random fluctuations above and below the cut-off frequency. The obtained fields would reveal any underlying coherent structures present in the flow.

An example of the filtering and phase averaging of one of the temporal eigenvectors of the previous example is shown in Figure 3.7. In this example, the temporal coefficient shows an apparent random behaviour. However, after applying a band-pass filter and further phase averaging, a clear temporal oscillating behaviour is seen. If the original dataset is partially reconstructed with Equation 3.8 using only the relevant filtered and phase averaged temporal coefficients, a clear visualisation of the behaviour of the temporal phenomena of interest can be obtained.

3.4 VORTEX IDENTIFICATION

The coherent structures identified in the swirling flows with the POD are meant to be visualised. Coherent structures are big scale vortices or eddies that move with the flow. Several methods for vortex identification exist, mainly the Q criterion [136], the Δ criterion [137], the λ_{ci} criterion [138], and the λ_2 criterion [139]. The methods offer a robust criterion that allows them to discriminate against shear motions in favour of vortex cores. All these methods are based on the velocity gradient tensor D_{ij}. This is a second-order tensor that can be decomposed into a symmetric and an antisymmetric part $D_{ij} = S_{ij} + \Omega_{ij}$. S_{ij} is known as the rate-of-strain tensor, and Ω_{ij} is the vorticity tensor. An eddy is defined as the location where vorticity magnitude dominates the strain rate. In this thesis, for vortex visualisation in the 2D PIV measurement plane, the λ_{ci} criterion is used. The λ_{ci} criterion is also known as the swirling strength
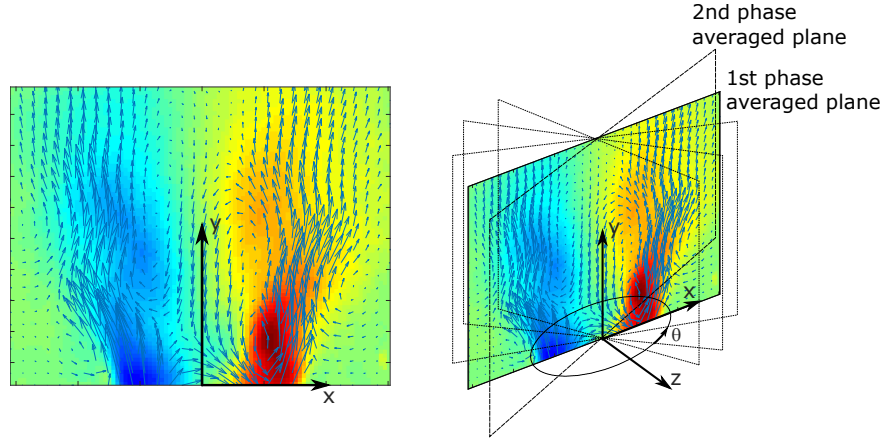
Figure 3.8: Visualisation of the rotating procedure for 3D reconstruction

criterion. A derivation of the criterion can be found in [140]. The λ_{ci} criterion for each point in the 2D flow field can be computed as:

$$\lambda_{ci} = \frac{1}{2}\sqrt{-4\left(\frac{\partial u}{\partial y}\frac{\partial v}{\partial x} - \frac{\partial u}{\partial x}\frac{\partial v}{\partial y}\right) - \left(\frac{\partial u}{\partial x} + \frac{\partial v}{\partial y}\right)^2} \qquad (3.9)$$

3.5   3D RECONSTRUCTION OF THE FLOW FIELD

The swirling flows examined in this thesis have large out of plane components which can be captured by the S-PIV method that was explained in Section 3.2. However, the visualisation and understanding of their impact on the flow behaviour are somewhat difficult if limited to a 2D space, especially when coherent structures like the PVC are to be analysed. A method for the approximate reconstruction of the 3D flow field from the planar three-component flow fields is described in this section [50, 141]. First, the acquired S-PIV data must be processed as described in Section 3.3. That is, decompose the flow with the POD method, identify the relevant POD modes of the phenomena to be analysed by looking at the frequencies in the temporal eigenvectors, reconstruct the flow with the relevant modes, and phase average the reconstructed fields. The scalar quantities of interest (e.g. a relevant vortex identification criterion) must also be calculated for each one of the phase averaged fields. Then, the 2D fields are placed in a 3D space with an angle of rotation θ between them. The angle of rotation is calculated as $\theta_{plane} = 2\pi f_p / f_s$, where f_p is the precessing frequency and f_s is the S-PIV sampling frequency of the 2D fields. The rotation procedure is exemplified in Figure 3.8.

The vector components need to be re-calculated for each θ step rotation. The axial velocity component v and any calculated scalar quantities do not change with rotation. The out of plane component w and radial component u need to be translated to the new 3D location by using the following equations:

$$u_{real} = u_{PIV}\cos\left(\theta_{plane}\right) + w_{PIV}\sin\left(\theta_{plane}\right)$$

and

$$w_{real} = u_{PIV} \sin\left(\theta_{plane}\right) + w_{PIV} \cos\left(\theta_{plane}\right)$$

Finally, velocity vectors and calculated scalar quantities can be interpolated into the 3D grid.

3.6 NUMERICAL APPROACH

Numerical simulations constitute the final part of this thesis. Their overall aim is to test changes in the burner geometry investigated in the first chapters and to estimate the overall viability in an industrial application of the flat flame concept burner that is proposed in this thesis. The commercial software Ansys Fluent 18.2 is used for solving the incompressible Navier-Stokes equations (Equation 3.10, 3.11 and 3.12). The equations can be solved in both, a stationary or instationary manner, depending on the characteristics and behaviour of the flow.

$$\frac{\partial u_i}{\partial x_i} = 0 \tag{3.10}$$

$$\frac{\rho \partial u_i}{\partial t} + \frac{\partial \rho u_i u_j}{\partial x_j} = -\frac{\partial p}{\partial x_i} + \frac{\partial \tau_{ij}}{\partial x_j} \tag{3.11}$$

$$\tau_{ij} = \mu \left(\frac{\partial u_i}{\partial x_j} + \frac{\partial u_j}{\partial x_i} \right) - \frac{2}{3} \mu \frac{\partial u_l}{\partial x_l} \delta_{ij} \tag{3.12}$$

where u_i is a velocity component, μ the viscosity, ρ the density, p the pressure, and τ_{ij} represents the viscous stress.

The solver uses the Finite Volume Method (FVM) which consists of first dividing the domain into discrete control volumes. The governing equations are integrated over these control volumes and are then substituted to finite difference type approximated equations. This effectively yields a set of algebraic equations that represent the fluxes entering and exiting the control volume. The reduction of the partial differential equations to simplified approximated algebraic equations is called discretisation. The discretised equations are then solved in an iterative manner [142]. The numerical quality of the solution is determined by the finite volume partitioning (grid), the discretisation method, and the iterative solution method. The physical accuracy of the results is dependent on the numerical quality of the solution, the boundary conditions chosen and the adequate selection of any models (e.g. turbulence).

The Reynolds number of the flows studied in this thesis is in the turbulent regime. Theoretically, all turbulent flows can be simulated by numerically solving the Navier-Stokes equations. However, this is prohibitive and not practical for industrial flow applications as it would require a computing power many orders of magnitude higher than what is generally available. As a practical alternative, CFD simulations employ turbulence models. Turbulence models allow the calculation of the mean flow without calculating the full time/space dependent flow field. For many engineering applications, this is enough as it is unnecessary to solve the turbulent fluctuations and calculate the

complete turbulent flow pattern as a function of time. In the present work, this approach will suffice as the main objective of the numerical simulations is to identify overall trends and change in behaviour of the flow with different burner geometries that will shed light into the design of future burner prototypes.

Turbulence models can be classified depending on the turbulent scales they choose to model and the scales they choose to simulate by solving the unsteady Navier-Stokes. Ranging from most detailed to least detailed, the most common approaches for turbulence modelling are:

- Direct Numerical Simulation (DNS): this method does not model the turbulent flow, instead it directly solves the Navier-Stokes equations to simulate all the scales of turbulence. However, this requires a grid size sufficiently fine to solve the Kolmogorov scales and a time step small enough to solve the fastest fluctuations. In addition to this, the simulation must be run for long periods of time to ensure that the obtained solution that is statistically stationary and is no longer affected by the boundary conditions used to start the computation. These make this method unfeasible for solving even simple engineering problems [143].

- Large Eddy Simulation (LES): this method solves the smallest turbulent scale that the computational grid allows for. Any sub-grid turbulence phenomena are modelled. As it was the case with DNS, LES computations are highly unsteady and must run for long periods of time to ensure that the obtained solution is statistically stationary and is no longer affected by the boundary conditions used to start the computation. This method requires much less computational resources than LES, however, the requirements are still considerable. Some engineering problems have started to be addressed by this method, especially for small geometries [143].

- Reynolds-averaged Navier-Stokes (RANS): the model focuses on the mean flow and the effect of turbulence on the mean flow properties. The model uses a single turbulent length scale that characterises the entire turbulent spectrum. Before numerically solving the Navier-Stokes equations, the equations are time-averaged. By doing this, an extra term appears in the equations due to the interactions between turbulent fluctuations. This term is modelled with classical turbulence models, of which the most popular one are the k–ε model and the RSM. Of all the methods this one requires the least computational resources to do the calculations. Because of this, RANS has been the most popular approach for engineering flow calculations [142].

The combustion process is governed by the same transport equations for fluid flow and heat transfer. Additionally, all the parameters and phenomena described in Section 2.1 come into play. Additional models are required for the combustion chemistry and kinetics. As was the case with the turbulence modelling, several possible modelling approaches can be taken with the combustion process, reaction mechanism, and

kinetics. Ranging from most detailed to least detailed, the most common approaches for modelling the reaction kinetics are:

- Detailed mechanisms: a chemical reaction never takes place in one single step, tens or hundreds of intermediate reactions might be occurring in between the initial reactants and final product. For example, the reaction between methane and air involves 325 reactions and 53 species [144]. CHEMKIN [145] is a widely used software for estimating the reaction kinetics of for large systems of chemical equations. The reaction kinetics can then be incorporated into the CFD software. However, each chemical species adds an additional partial differential equation to be solved. This potentially makes the simulation unnecessarily complicated and computationally expensive as it might not be in the interest of the researcher everything that happens in all these reactions.

- Reduced mechanisms: reduced reaction mechanisms have been developed that involve fewer reactions but still predict major and important minor species. For example, a methane-air reaction mechanism has been derived that consists of 39 reactions and 17 chemical species [146]. The degree of reduction in the reaction mechanism is a trade-off between the computational cost and the accuracy required.

- Simple Chemical Reacting System (SCRS): this approach assumes that chemical reactions are infinitely fast and any intermediate reactions are ignored leading to a one-step global reaction. This approach is adequate if the only concern is the global nature of the combustion process (e.g. amount of energy released, final temperature reached, etc.) and the final concentrations of the major species. A clear advantage of this approach is that it has a much lower computational cost as only one additional partial differential equation is required [142].

3.6.1 Models used for simulations

3.6.1.1 Turbulence modelling

In the present work, the RANS modelling approach is chosen due to its lower computational resource requirements and high computational solution turnaround. For this approach, the Navier-Stokes equations conserve their general form, but now the velocities represent the ensemble-averaged values [147]:

$$\frac{\partial \rho}{\partial t} + \frac{\partial}{\partial x_i}\left(\rho u_i\right) = 0 \tag{3.13}$$

$$\frac{\partial \rho}{\partial t}\left(\rho u_i\right) + \frac{\partial}{\partial x_i}\left(\rho u_i u_j\right) =$$
$$-\frac{\partial p}{\partial x_i} + \frac{\partial}{\partial x_j}\left[\mu\left(\frac{\partial u_i}{\partial x_j} + \frac{\partial u_j}{\partial x_i} - \frac{2}{3}\delta_{ij}\frac{\partial u_l}{\partial x_l}\right)\right] + \frac{\partial}{\partial x_j}\left(-\rho\overline{u_i' u_j'}\right) \tag{3.14}$$

As mentioned earlier, an additional term appears $-\rho\overline{u'_i u'_j}$. This term represents the effect of turbulence in the flow field and must be modelled in order to close Equation 3.14. Several models exist and are available in Fluent, detailing each of them is outside of the scope of the present work and the reader is referred to the many available books on the subject [142, 148, 149]. However, a brief overview of the models used in this thesis is given in Table 3.1.

3.6.1.2   Combustion modelling

For the combustion simulations in this thesis, the reduced reaction mechanisms approach is chosen using a 2-step reaction in order to provide a better degree of accuracy in the production of emissions [152, 153].

The species transport model provided in Fluent is used. The model solves mixing and transport of chemical species by solving conservation equations describing convection, diffusion, and reaction sources for each component species. The convection-diffusion equation has the following form for species i^{th} [154]:

$$\frac{\partial}{\partial t}\left(\rho Y_i\right) + \nabla \cdot \left(\rho \vec{v} Y_i\right) = -\nabla \cdot \vec{J}_i + R_i + S_i \tag{3.15}$$

where Y_i is the local mass fraction, R_i is the net rate of production, S_i is the rate of creation by addition from the dispersed phase, and J_i is the diffusion flux. Fluent models the diffusion flux with a modified Fick's law for turbulent flows:

$$\vec{J}_i = -\left(\rho D_{i,m} + \frac{\mu_t}{Sc_t}\right) \tag{3.16}$$

where $D_{i,m}$ is the mass diffusion coefficient, $D_{T,i}$ is the thermal diffusion coefficient, and Sc_t is the turbulent Schmidt number. The turbulent Schmidt number is defined as $Sc_t = \frac{\mu_t}{\rho D_t}$ where μ_t is the turbulent viscosity and D_t the turbulent diffusivity. The reaction rates of Equation 3.15 can be computed in Fluent with one of two alternatives. The first one is with the direct use of finite-rate kinetics. In this case, the effect of turbulent fluctuations on kinetics is ignored and the reaction rate is determined by calculating the finite-rate chemistry directly. The net creation/destruction of chemical species i is then calculated as the sum of the reactions the species participates in:

$$R_i = M_{w,i} \sum_{r=1}^{N_R} \hat{R}_{w,i} \tag{3.17}$$

where $M_{w,i}$ is the molecular weight and $\hat{R}_{w,i}$ is the molar rate of creation/destruction of species i in reaction r.

The second modelling alternative is eddy-dissipation model proposed by Magnussen and Hjertager [155] which assumes that the reaction rate is controlled by turbulence, ignoring the chemistry timescales and Arrhenius chemical kinetic calculations. The net creation/destruction of

Table 3.1: Turbulence models highlights [142, 150, 151].

Model	Advantages	Disadvantages
Standard $\kappa - \epsilon$	- only initial boundary conditions need to be supplied. - good performance for many industrially relevant flows. - most validated turbulence model.	- more expensive than mixing length model (two extra PDEs). - performs poorly on relevant cases: (i) some unconfined flows (ii) flows with large extra strains (e.g. curved boundary layers, swirling flows) (iii) rotating flows (iv) flows where anisotropy of normal Reynolds stresses domains (e.g. fully developed flows in non-circular ducts) (v) separating flow prediction
Realizable $\kappa - \epsilon$	- substantial improvements over the standard $\kappa - \epsilon$ model in cases where the flow presents strong streamline curvature, vortices, flow separation and/or rotation.	- produces non-physical turbulent viscosities when the computational domain contains both rotating and stationary fluid zones.
SST $\kappa - \omega$	- accurate and robust prediction of problems with flow separation. - useful for modelling near the wall flow. - lower length scales near wall.	- can over predict separation - very sensitive to initial conditions - has issues with free stream flows.
Reynolds Stress Model	- most general of all classical turbulence models. - only initial boundary conditions need to be supplied. - accurate calculation of mean flow properties and Reynolds stresses for simple and complex flows.	- seven extra PDEs make the model very computationally expensive. - not as widely validated as $\kappa - \epsilon$ models. - similar poor performance as the $\kappa - \epsilon$ model in flows with axisymmetric jets or with unconfined recirculating flows.

Table 3.2: 2-step methane combustion parameters.

Reaction	Rate expression	Pre-exponential factor	Activation energy
$CH_4 + 2O_2 \rightarrow CO_2 + 2H_2O$	$k\,[CH_4]^{0.7}\,[O_2]^{0.8}$	5.012×10^{11}	2.0×10^8
$CO + \frac{1}{2}O_2 + H_2O \rightleftharpoons CO_2 + H_2O$	$k\,[CO]\,[O_2]^{1/4}\,[H_2O]^{1/2}$	2.239×10^{12}	1.7×10^8

chemical species i due to reaction r is given by the smaller value of the following two expressions:

$$R_{i,r} = v'_{i,r} M_{w,i} A \rho \frac{\varepsilon}{\kappa} \min_{\Re} \left(\frac{Y_{\Re}}{v'_{\Re,r} M_{w,\Re}} \right) \qquad (3.18)$$

$$R_{i,r} = v'_{i,r} M_{w,i} A B \rho \frac{\varepsilon}{\kappa} \left(\frac{\sum Y_P}{\sum v'_{j,r} M_{w,j}} \right) \qquad (3.19)$$

where Y_P is the mass fraction of any product species P, $Y_{\Re}$ is the mass fraction of a reactant $\Re$, A is an empirical constant equal to 4.0, and B is an empirical constant equal to 0.5.

For combustion reactions, fuels burn quickly, and the overall rate of reaction is controlled by turbulent mixing. Upon first inspection, it appears that the best model would be the eddy-dissipation because the reaction rate is very fast and is controlled mainly by the mixing of the reactants. However, choosing the finite-rate model would lead to unrealistic results. In the premixed flame cases studied in this thesis, this model would cause the reactants to burn as soon as they enter the computational domain, upstream of the flame stabiliser. A third modelling alternative is provided in Fluent where both models are used so that the net reaction rate is taken as the minimum of the two rates. The finite-rate kinetic model acts as a switch, preventing the reaction raking place before the flame stabiliser [156]. This last approach is the one used for all the reaction modelling in this thesis.

3.6.1.3 Radiation modelling

Due to the high temperatures present in this study, it is necessary to consider the effects of radiation. For this, the P-1 model provided in Fluent is used [157]. The radiation flux q_r is described by:

$$q_r = -\frac{1}{3\,(a + \sigma_s) - C\sigma_s} \nabla G \qquad (3.20)$$

where a is the absorption coefficient, σ_s is the scattering coefficient, G is the incident radiation, and C is the linear-anisotropic phase function coefficient. The expression can by simplified by defining the parameter:

$$\Gamma = \frac{1}{3\,(a + \sigma_s) - C\sigma_s} \qquad (3.21)$$

Which yields:

$$q_r = -\Gamma \nabla G \tag{3.22}$$

The transport equation for G is:

$$\nabla \cdot (\Gamma \nabla G) - aG + 4an^2 \sigma T^4 = S_G \tag{3.23}$$

where n is the refractive index of the medium, σ is the Stefan-Boltzmann constant and S_G is a user-defined radiation source. Combining Equation 3.22 and Equation 3.23 yields the following equation:

$$-\nabla \cdot q_r = aG - 4an^2 \sigma T^4 \tag{3.24}$$

which can be directly substituted into the energy equation to account for radiation heat sources (or sinks).

3.6.1.4 *Heat transfer at the walls*

For the confined combustion cases studied in this thesis, it is necessary to account for convective and radiative heat transfer through the wall boundaries of the computational domain. Fluent models convective transfer with the equation:

$$q = h_{ext} (T_{ext} - T_w) \tag{3.25}$$

where h_{ext} is the external heat transfer coefficient, T_{ext} is the external heat-sink temperature, and T_w is the surface temperature of the wall. Radiative heat transfer is modelled with the equation:

$$q = \varepsilon_{ext} \sigma \left(T_\infty^4 - T_w^4 \right) \tag{3.26}$$

where ε_{ext} is the emissivity of the external wall surface, σ is the Stefan-Boltzmann constant, T_w is the surface temperature of the wall, and T_∞ is the temperature of the radiation source or sink on the exterior of the domain. Combining Equation 3.25 and Equation 3.26 yields:

$$q = h_{ext} (T_{ext} - T_w) + \varepsilon_{ext} \sigma \left(T_\infty^4 - T_w^4 \right) \tag{3.27}$$

For some of the cases presented in this work, it is necessary to estimate the value of the convective heat transfer coefficient h_{ext}. This was done by following the methodology outlined in Lienhard, IV and Lienhard, V [158]. The formula to calculate the Nusselt number for an upward-facing horizontal heated plate proposed by Raithby and Hollands [159] was used:

$$\overline{\mathrm{Nu}}_L = 0.14 \mathrm{Ra}_L^{1/3} \left(\frac{1 + 0.0107 \, \mathrm{Pr}}{1 + 0.01 \, \mathrm{Pr}} \right), \quad 0.024 \leq \mathrm{Pr} \leq 2000 \tag{3.28}$$

where Nu is the Nusselt number, Ra is the Rayleigh number, and Pr is the Prandtl number. The Rayleigh number is calculated as:

$$\mathrm{Ra} = \mathrm{GrPr}$$

where Gr is the Grashof number. Grashof and Prandtl numbers are calculated as:

$$\text{Gr} = \frac{g\beta\rho^2 \left|T_\infty - T_w\right| L^3}{\mu^2}$$

$$\text{Pr} = \frac{c_p\mu}{k}$$

where g is the gravity and L is the characteristic length of the horizontal plate. L is calculated as $L = area\,of\,plate\,/\,perimeter\,of\,plate$. The remaining variables correspond to the fluid properties of the external heat-sink. β is the coefficient of thermal expansion, ρ is the density, μ is the viscosity, and k the thermal conductivity. All properties must be evaluated at $\overline{T} = \left(T_\infty + T\right)/2$. The heat transfer coefficient can be calculated as:

$$h_{ext} = \frac{\overline{\text{Nu}_L}k}{L} \tag{3.29}$$

3.6.2 *Solver details*

In addition to the models used, a choice needs to be made regarding the discretisation scheme for the partial differential equations. In all the numerical simulations in the present work, the Quadratic Upstream Interpolation for Convective Kinematics (QUICK) is used for the momentum, turbulence, species, and energy discretisation. The QUICK scheme is a higher-order discretisation scheme that provides a third-order truncation error when used in structured girds, which are the grids employed in all the simulations in this study. The use of a high order scheme greatly reduces the numerical diffusion errors present in lower-order truncation schemes, increasing the numerical accuracy of the solution [142, 148].

An additional decision needs to be made on how the pressure term in the Navier-Stokes equations is going to be solved. All the flows analysed in the present work can be considered incompressible, this arises several problems. Pressure gradients appear in the Navier-Stokes equations, thus, a way for calculating the pressure gradient is needed to fully solve them. More so, the momentum equations and the continuity equation are strongly coupled with every velocity component appearing in each momentum equation and in the continuity equation. If the flow was compressible, the continuity equation could be used as the transport equation for density alongside the energy equation to obtain the pressure by using the equation of state $p = p\left(\rho, T\right)$. This is evidently not the case for an incompressible flow because the density is constant. However, pressure appears in all three momentum equations and the velocity field must satisfy the continuity equation. This gives a set of four equations with for four variables. A way to couple the pressure and velocity is needed. The Semi-Implicit Method for Pressure Linked Equations (SIMPLE) algorithm by Patankar and Spalding [160] is used to do this pressure-velocity coupling as it is effective and has a

low computational cost. The SIMPLE algorithm is a predictor-corrector method that works by first looking at the initially calculated pressure field, then looking at the cell and determining if continuity is satisfied or not. If continuity is not satisfied, the pressure in the cell is adjusted to increase/decrease the pressure relative to the neighbouring cells [142, 148].

3.6.3 *Grid generation and convergence*

Grid generation was done in ICEM CFD 18.2. All the grids that were generated for the present work are made from fully structured hexagonal cells. This allows for using the SIMPLE algorithm with minimum discretisation error and for a third-order truncation error using the QUICK scheme. The details of each grid are described in the relevant sections of Chapter 6.

A grid independence study was carried out in order to calculate the discretisation error between different grid sizes and minimise the impact this has on the solution. For this, mean values and swirl numbers of converged solutions on three grids with different element count were compared using the Grid Convergence Index (GCI) method proposed by Roache [161]. The GCI is a measure of the error percentage of the computed value in relation to the asymptotic numerical value which is an indication of how much the solution would change with further grid refinement. The GCI for two finest consecutive grids is defined as:

$$GCI_{21} = \frac{F_s\,|e_{21}|}{r^p - 1} \times 100\%$$ (3.30)

where e_{21} is the error of a variable of interest g between two consecutive grids and is calculated as:

$$e_{21} = \frac{g_2 - g_1}{g_1} \times 100\%$$ (3.31)

r is the grid refinement ratio and is calculated as:

$$r_{12} = \left(\frac{number\,of\,elements\,in\,grid\,1}{number\,of\,elements\,in\,grid\,2} \right)^{1/dimension\,of\,grid}$$ (3.32)

According to Roache [161], the grid refinement ratio r should be no less than 1.1 so that the change in discretisation error is greater than any possible numerical noise in the solution. The next element p is the observed order of convergence and is calculated as:

$$p = \left[\ln\left(\frac{g_3 - g_2}{g_2 - g_1} \right) + p \right] / \ln(r)$$ (3.33)

Note that the observed order of convergence will likely be lower than the theoretical order of convergence, i.e. the one the CFD numerical algorithm will provide (third-order, or $p = 3$, in case of the QUICK scheme), due to boundary conditions, numerical models, and the grid. Similarly, the calculation is repeated for the two coarsest grids:

$$GCI_{32} = \frac{F_s \, |e_{32}|}{r^p - 1} \times 100\%$$ (3.34)

Finally, if the relation:

$$GCI_{32} = r^p GCI_{21}$$ (3.35)

is close to each other, it can be concluded that the grids are in the asymptotic range. An overall error of the variable of interest can be calculated by means of the Richardson extrapolation by using the two finest grids:

$$g^* = \frac{r_{12}^p g_1 - g_2}{r^p - 1}$$ (3.36)

This value is the one that would be obtained if the grid was infinitely refined. An estimate of the discretisation error can then be obtained by comparing the results from the different grids to the one of the Richardson extrapolation:

$$e_1^* = \frac{g_1 - g^*}{g^*} \times 100\%$$ (3.37)

3.7   CHAPTER SUMMARY

The methods and devices used for the study of the flow in this thesis were presented. The experimental laboratory equipment was described. These consisted in a modular swirl burner constructed from stainless steel that is used in the isothermal and combustion experiments. The burner can be fitted with nozzles of different diameters (D = 19.5, 24.0 and 28.0 mm) and opening angles (α = 30°, 45° and 60°). Three tangential swirl generators with geometrical swirl numbers of 0.85, 1.04 and 1.47 were available for the experiments. A squared confinement with overall inner dimensions of $488 \times 488 \times 56$ mm^3 was manufactured from stainless steel for the combustion experiments. Afterwards, an overview of the S-PIV was given. The principle behind the measurement of the vector field was described, as well as the possible sources of error that need to be considered. Afterwards, the main post-processing methods were shown. These were: the POD method which allows for the decomposition of the velocity vectors into their principal modes, the λ_{ci} criterion for vortex identification, and a method for the approximate reconstruction of the 3D flow field from the planar three-component PIV flow fields.

An overview of the numerical methods used in the thesis is described. first, a description of the available turbulence models is made. The RANS modelling approach was chosen due to its lower computational resources and high computational solution turnaround. A brief description of the advantages and disadvantages of the RANS turbulence models was given. For the reaction modelling the species transport model with the finite-rate/eddy-dissipation using a 2-step methane-air reaction was chosen in order to provide a better degree of accuracy in the emissions

production and keep the required computational resources low. The QUICK discretisation scheme was chosen to provide third-order accuracy in order to account for the strong gradients in the Coanda flow. For the pressure-velocity coupling, the SIMPLE algorithm was used. The GCI criteria was described and was used in the relevant sections of this thesis to ensure accurate grid resolution in the numerical solutions.

4

ISOTHERMAL EXPERIMENTS

This chapter covers the results of isothermal experiments on a swirl burner. The aim of the experiments is to identify, visualise and compare the coherent structures that are present in two different flow patterns, OJF and CoJF. As mentioned in Section 2.2.1, extensive research exists on the behaviour of coherent structures present in OJF, specifically for the PVC. In OJF, the PVC characteristics make it an adequate mechanism for chemical mixing whilst being a detrimental component for thermoacoustic stabilisation. Because of this, and in line with the aim of this thesis - developing a flat flame burner that uses the Coanda effect - it is critical to know if a similar structure to the PVC is present in a Coanda flow and if it has similar characteristics to the one present in OJF, as this might have a role on the stabilisation of a Coanda flame. More so, the experimental results will serve as a basis for validating the numerical simulations of Chapter 6. The fundamental idea of the research is based on first having a particular geometry at which the system would present both flow patterns under the same inlet flow conditions, to be able to identify and compare the coherent structures present in each of the flow patterns. Afterwards, another geometry was used at which the system will now present one or the other flow pattern, thus allowing the study of the flow field at the point of transition. For that aim, High-Speed Stereo PIV was used to produce time-resolved data, subsequently, proper orthogonal decomposition was used to identify the coherent modes in the flow. Swirl strength (λ_{ci}^2) analysis was conducted on the coherent modes to establish quantitative and qualitative results and to produce a 3D visualisation of the coherent structures in an OJF and CoJF.

This chapter is structured as follows, the first two sections, 4.1 and 4.2 present an introduction to the experimental setup and an overview of how the data was processed and analysed. Subsequently, Section 4.3, presents the results of the experiments: first, in Section 4.3.1, the time-averaged flow patterns for the two different flow patterns are discussed. Then a spectral analysis of the flow fields in made in Section 4.3.2. Afterwards, in Section 4.3.3, the principal modes of the flow are obtained by proper orthogonal decomposition. The coherent structures present in the flow are identified and described in Section 4.3.4. Finally, the results of the second part of the experimental trials are presented in Section 4.3.5, where the effect the geometry has on the flow pattern is studied with a single flow rate.
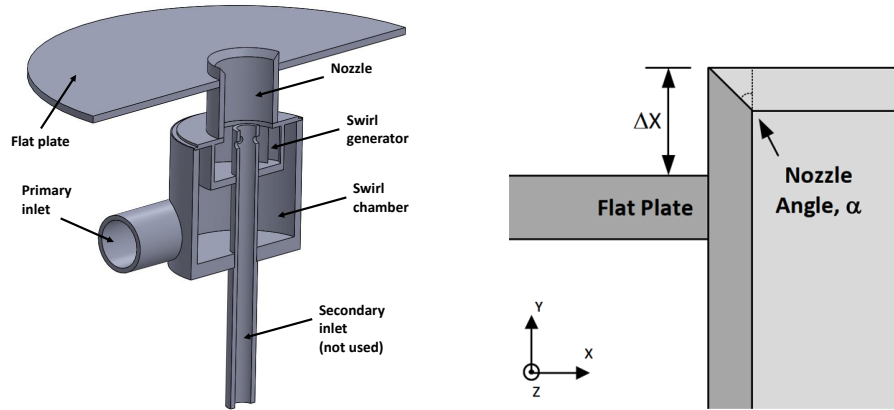
Figure 4.1: Normalised plate height schematic.

4.1   EXPERIMENTAL SETUP

4.1.1   *Swirl burner configuration*

The swirl burner detailed in Section 3.1.1 was used to examine the transition behaviour under atmospheric conditions (1 bar, 293 K). The system was fed using compressed air through flexible hoses and variable area rotameters for flow rate control. Isothermal conditions were evaluated for these trials. Two sets of experiments were carried out. For the first one, the flow rate was set at 4.2, 6.5, 9.4 and 13.5 m^3/hr to give a Reynolds Number of $\sim$ 4300, $\sim$ 6700, $\sim$ 9600, and $\sim$ 13900 respectively at the burner nozzle. The nozzle diameter was $D = 28$ mm with an opening angle $\alpha = 45°$. The burner was fitted with a tangential swirl generator providing a geometrical swirl number (Sg) of 0.85. A flat plate was fitted to the nozzle and kept at a normalised height $\Delta X/D = 0$, being ΔX the distance between the flat plate and the tip of the nozzle outlet; a schematic of this can be seen in Figure 4.1. For the second set of experiments, a single flow rate was used at $\sim$ 11000 Re. A higher swirl was imposed to the flow via a tangential swirl generator with a constant geometrical swirl number (Sg) of 1.04. The increase in swirl number allowed for the observation of a clear transition between the Coanda and Open jet flow as the $\Delta X/D$ was varied. Different nozzle angles α of 30°, 45° and 60° were studied to observe their impact on the flow for time-resolved analyses. Only these angles were analysed as previous trials on this same burner showed the greatest variance in flow conditions during their transition [95]. The flat plate was used to change the height of the nozzle with respect to the plate, thus allowing the superimposition of the airflow as a CoJF or OJF. Different normalised heights $\Delta X/D$ were used from 0.000 to 0.203.
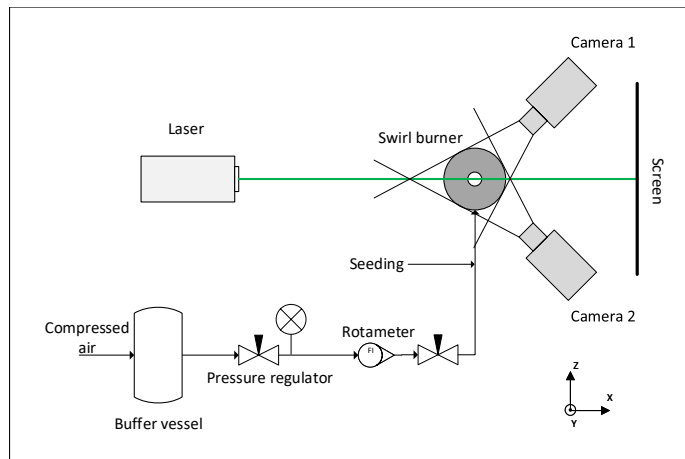
Figure 4.2: Experimental setup.
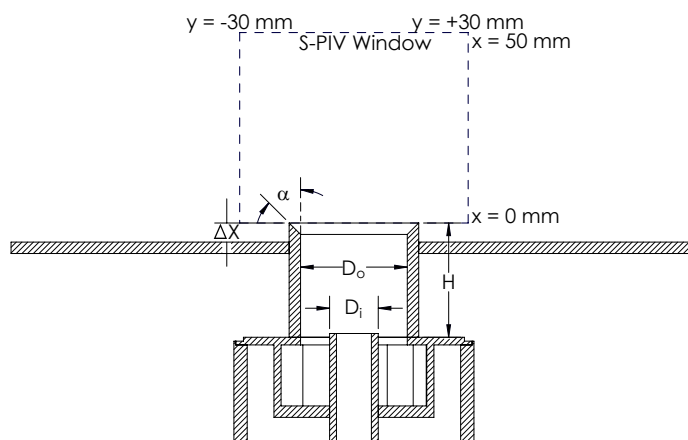
Figure 4.3: Area of PIV window.

4.1.2 *PIV setup*

An S-PIV system was employed for measurement purposes. A diagram of the experimental setup is shown in Figure 4.2. The S-PIV system consists of a dual cavity Nd:YLF high-speed laser of 527 nm wavelength. Laser sheet optics were used to convert the laser beam into a 1 mm thick sheet. To record the images a pair of HighSpeedStar 5 CMOS cameras were used. 60 mm Nikon lenses were utilised for resolution purposes, which allowed a field of view of approximately 60×60 mm (Figure 4.3), with a resolution of 5.35 pixels per mm and a depth of view of 1.5 mm. The inlet air was seeded using a liquid nebuliser positioned ~ 2 m upstream of the burner inlet. For the first set of experiments, the repetition rate was set at 500, 750, and 1000 Hz with no phase locking. For the second set of experiments, the repetition rate was set at 125 Hz as there was no interest in analysing the temporal behaviour. In order to reduce the parallax error, focusing was achieved using a 3D calibration plate and correcting the position of the lens (Scheimflug correction). The line of view of the camera was positioned exactly in the middle of the nozzle.

After the acquisition of the Stereo PIV data, a frame-to-frame adaptive correlation technique was carried out with a starting interrogation area of 64×64 pixels going to a final size of 24×24 pixels. Time-averaged flow fields were calculated using 1024 pairs of frames. Axial-radial velocity maps were created over the ranges of the minimal and maximal velocities. The vector fields were also used to determine vortical structures and swirling strength values (λ_{ci}^2) during both stable flow patterns (i.e. CoJF or OJF). The data was post-processed using Matlab R2018b with the PIVMat toolbox [162]. The snapshots method was used to obtain the POD for each flow case to identify coherent structures within each flow pattern [163] (refer to Section 3.3 for details). To isolate the fluctuations in the flow and differentiate between processing fluctuations and fluctuations due to turbulence, a triple velocity decomposition was done (refer to Section 3.3 for details).

To obtain a better visualisation of the coherent structures within the flow, a 3D reconstruction was done by phase averaging the POD modes that correspond to the precessing motion. Then, to place the values in a 3D space, the 2D fields were rotated using an angle of rotation $\theta = 2\pi f_p / f_s$, where f_p is the precessing frequency and f_s is the sampling frequency of the 2D fields. The vector components are then recalculated for each θ step rotation. Finally, velocity vectors and calculated scalar quantities were interpolated in the 3D grid (refer to Section 3.5 for details).

4.3   RESULTS

4.3.1   *Time-averaged flow patterns*

Time-averaged results were produced for various flow rates with the flat plate at a normalised height such that both CoJF and OJF coexisted. For the current burner setup, this happened at $|\Delta X/D| = 0.000$ with a nozzle opening angle of $45°$. Vector fields of the in-plane time-averaged velocity components u_x and u_y and contours of the out of plane velocity component u_z are shown in figure Figure 4.4. The u_z velocity component was scaled by dividing by the mean velocity magnitude for each case to allow a comparison of the different Reynolds numbers. The vector fields show the expected velocity profile: a vertical jet core with a CRZ for the OJF (top row of Figure 4.4) and a horizontal jet core with a downward velocity at the centre of the nozzle (bottom row of Figure 4.4). For the Coanda flow pattern, a slight decrease in the jet angle at the nozzle outlet can be observed as the flow rate is increased, this is especially evident in the axial velocity plots shown in Figure 4.5. As is shown afterwards, this increased inclination is related to a stronger attachment of the jet core to the flat plate by a vortical structure in the outer shear layer of the jet.
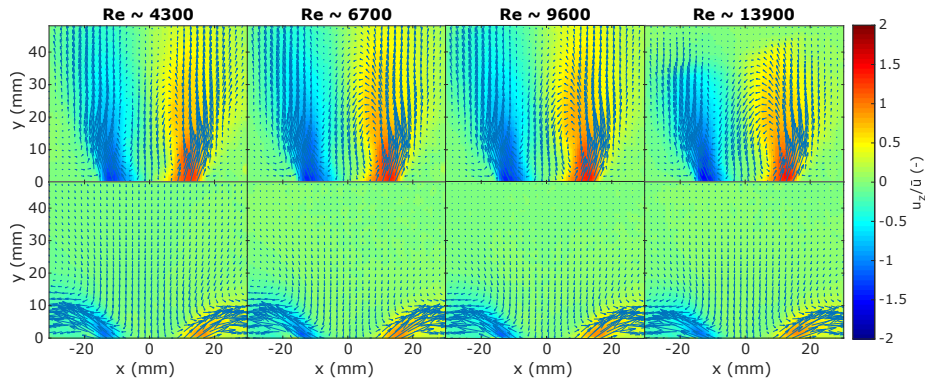
Figure 4.4: Time-averaged velocity fields at different flow rates with contours of scaled out of plane velocity component. Velocities are scaled by the mean velocity magnitude of each case.
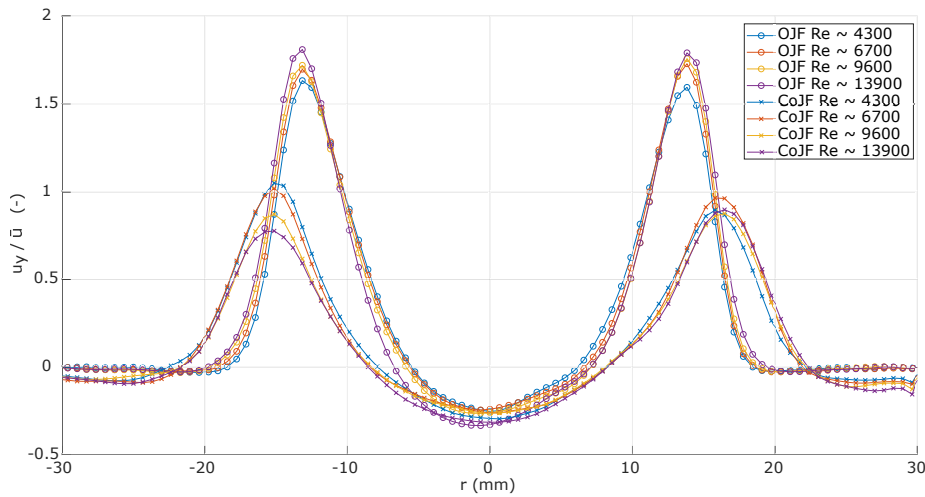
Figure 4.5: Scaled mean axial velocity with $|\Delta X/D| = 0.000$ and $\alpha = 45°$ nozzle for different flow rates. Velocities are scaled by the mean velocity magnitude of each case.
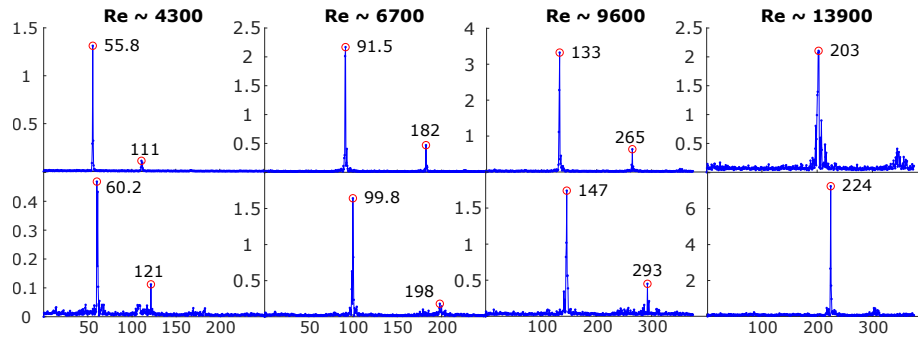
Figure 4.6: Power spectra of OJF (top row) and CoJF (bottom row). 500 Hz sampling rate for Re~ 4300 & 6700 and 750 Hz for Re~ 9600 & 13900.
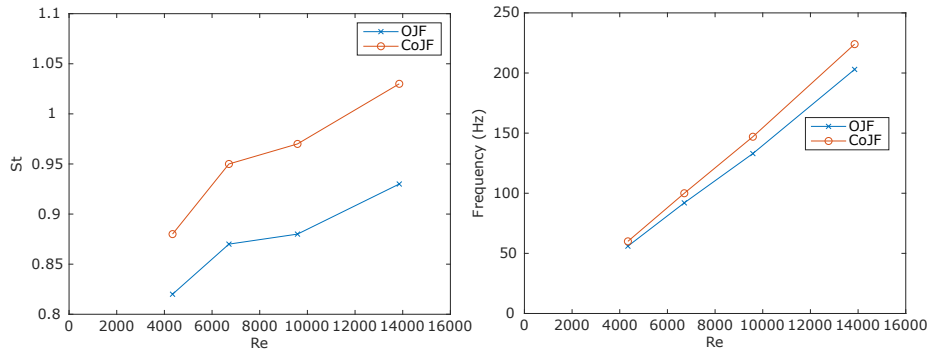
Figure 4.7: Strouhal vs Reynolds (left) and frequency vs Reynolds (right).

4.3.2 *Temporal power spectrum analysis*

Power spectra were extracted from the regions with high Root Mean Squared (RMS) value. The sampling rate for the Re $\sim$ 4300 and $\sim$ 6700 flow rates was 500 Hz, and a sampling rate of 750 Hz was used for the Re $\sim$ 9600 and $\sim$ 13900 flow rates. To discard any possible aliasing, experiments were repeated with a sampling rate of 1000 Hz yielding the same results as the experiments with lower sampling rates. The power spectrum for each flow rate is shown in Figure 4.6. As shown in the next sections, this frequency is related to the PVC. A plot of Strouhal number vs Reynolds number is shown in Figure 4.7. The precessing frequencies and Strouhal numbers for the OJF case are comparable to the ones reported in the literature [40]. The linear behaviour between the Strouhal and Reynolds numbers has been previously reported for an OJF [32]. The CoJF shows an increase in Strouhal number of $\sim$ 8.5% with respect to the OJF that is consistent across all the tested flow rates as is shown in Figure 4.7. It is speculated that the higher frequency in the CoJF is a consequence of its stagnation to the bottom surface, or alternatively because another coherent structure with higher frequency has appeared in the field. This behaviour has been previously reported [95].
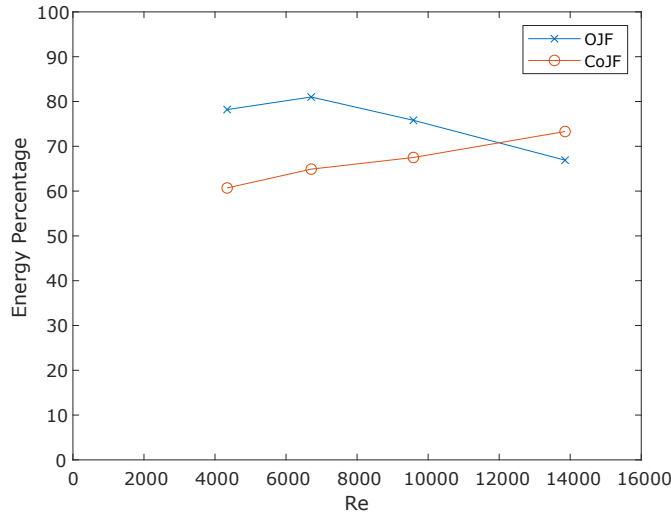
Figure 4.8: Reynolds number vs Energy percentage of first two POD modes.

4.3.3   *Proper orthogonal decomposition*

Proper orthogonal decomposition was applied to both flow patterns. Spectral analysis of the temporal POD coefficients was performed for the first 10 POD modes. Energy content and frequency of the temporal POD coefficients of each mode are shown in Table 4.1 and Table 4.2. The frequency of the first two POD modes for all flow patterns and flow rates coincide with the frequency identified in the previous section. This indicates that the first two POD modes represent the flow phenomena associated with the Precessing Vortex Core or another similar structure in the case of the CoJF. Additionally, most of the energy is contained in the first two POD modes. Figure 4.8 shows the change in energy content of the addition of the first two POD modes as the flow rate is increased. For the OJF the energy content of the first two modes ranges from $\sim 81\%$ to $\sim 67\%$ decreasing as the flow rate is increased. For the CoJF the energy content of the first two modes ranges from $\sim 61\%$ to $\sim 73\%$ and increases as the flow rate is increased. This higher energy content can be related to the experimental observations where spontaneous transitions from a CoJF to OJF occurred at low flow rates, whereas spontaneous transitions occurred from OJF to CoJF at the highest flow rate.

4.3.4   *Principal modes reconstruction and flow dynamics*

Snapshots of the OJF and CoJF were reconstructed using the first two POD modes and subsequently phase averaged. To allow for a better temporal resolution the reconstruction shown in this section corresponds to the lowest evaluated Reynolds number (Re ~ 4300). However, the same general flow behaviour and coherent structures were observed for the higher flow rates. Triple velocity decomposition RMS values of both flow patterns are shown in Figure 4.9. Precessing RMS fluctuations indicate the region of coherent vortex shedding with $\sim 65\%$ and $\sim 55\%$ of

Table 4.1: Frequency and energy content of POD modes for OJF.

REYNOLDS	~ 4300		~ 6700		~ 9600		~ 13900	
MODE	FREQUENCY	ENERGY	FREQUENCY	ENERGY	FREQUENCY	ENERGY	FREQUENCY	ENERGY
1	55.8	45.90%	91.5	45.60%	132.8	41.80%	203.3	35.80%
2	55.8	32.30%	91.5	35.40%	132.8	34.00%	203.3	31.10%
3	7.8	2.70%	3.4	2.60%	13.9	3.90%	14.7	5.50%
4	111.1	1.60%	182.5	1.50%	69.7	2.50%	1.5	3.60%
5	0.5	1.30%	32.3	1.40%	13.9	2.00%	346.4	2.70%
6	111.1	1.20%	182.5	1.20%	264.9	1.80%	347.8	2.20%
7	111.1	1.10%	182.5	0.90%	264.9	1.20%	347.1	1.90%
8	2.9	1.10%	47.0	0.90%	264.9	0.90%	103.5	1.40%
9	16.1	0.90%	182.5	0.80%	264.9	0.90%	51.4	1.30%
10	20.5	0.70%	58.7	0.70%	29.4	0.80%	25.0	1.00%
Total		88.7%		90.8%		89.7%		86.5%

Table 4.2: Frequency and energy content of POD modes for CoJF.

REYNOLDS	~ 4300		~ 6700		~ 9600		~ 13900	
MODE	FREQUENCY	ENERGY	FREQUENCY	ENERGY	FREQUENCY	ENERGY	FREQUENCY	ENERGY
1	60.2	31.30%	99.8	34.70%	146.8	36.80%	223.8	40.90%
2	60.2	29.40%	99.8	30.20%	146.8	30.70%	223.8	32.40%
3	13.7	10.30%	18.1	10.70%	18.3	8.90%	25.7	7.10%
4	6.8	5.90%	1.0	4.90%	292.8	4.30%	304.5	3.30%
5	121.3	4.60%	198.1	3.40%	292.8	4.10%	304.5	3.20%
6	121.3	4.00%	198.1	2.90%	292.8	3.30%	301.6	2.50%
7	13.7	2.20%	26.4	2.60%	38.9	2.60%	302.3	2.10%
8	47.0	1.70%	80.2	1.50%	112.3	1.50%	244.4	1.30%
9	7.8	1.40%	18.6	1.30%	115.2	1.20%	23.5	1.00%
10	4.4	1.00%	2.0	0.90%	283.3	0.70%	294.3	0.70%
Total		91.6%		93.1%		94.0%		94.5%
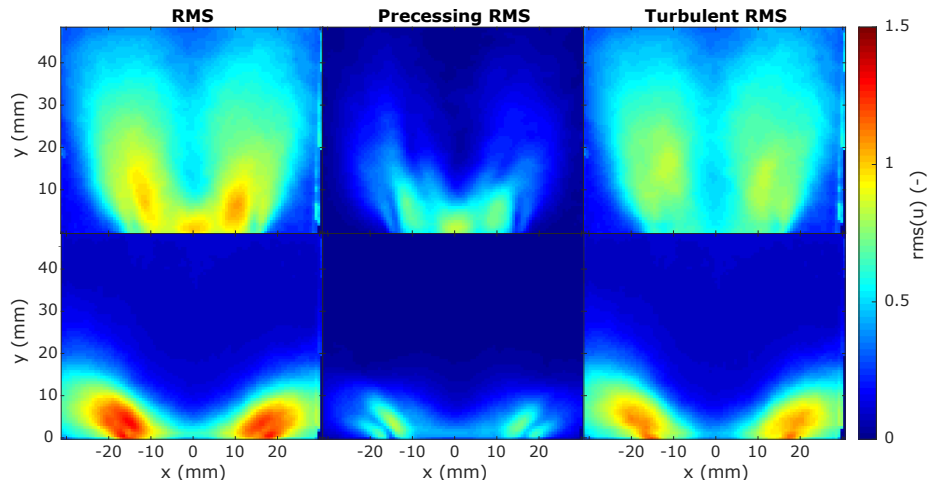
Figure 4.9: Scaled triple velocity decomposition time-averaged RMS fields for OJF (top) and CoJF (bottom) at Re $\sim$ 4300 with $|\Delta X/D| = 0.000$ and $\alpha = 45°$ nozzle.

the fluctuations attributed to the processing phenomena for OJF and CoJF, respectively. The phase averaged reconstructed loops are shown in Figure 4.10 and Figure 4.11, respectively for the OJF and CoJF, with swirling strength contours for vortex identification, corresponding to a precession frequency of 56 Hz and 60 Hz respectively.

For the OJF case (Figure 4.10) two different vortical structures can be observed, the first one in the inner shear layer and a second one in the outer shear layer of the jet core. These vortices correspond to the out of plane movement of the inner and outer PVC. A strong inner shear vortex can be seen at the $1/8\,2\pi$ mark on the negative side of the x-axis with swirl strength of $\sim 140,000\ 1/s^2$. As the PVC spiral continues rotating, this vortex loses strength and moves along the y-axis until it practically disappears at the $5/8\,2\pi$ mark, reducing its swirl strength to $\sim 4,000\ 1/s^2$. At the $4/8\,2\pi$ mark, an inner shear vortex starts moving into the measured plane at the positive side of the x-axis. This vortex shows its peak strength at the $5/8\,2\pi$ mark with a swirl strength of $\sim 170,000\ 1/s^2$; as before, and as the PVC continues rotating, this vortex moves along the y-axis and loses strength almost disappearing at the $1/8\,2\pi$ mark with a swirl strength of $\sim 4,000\ 1/s^2$. Better visualisation of the PVC can be achieved by doing a 3D reconstruction of the phase average of the first two POD modes. This is shown in Figure 4.12a, the CRZ is delimited by an isosurface of axial velocity of 0 m/s (red colour); similarly, the jet core is delimited by an isosurface of axial velocity of 1.2 m/s (yellow colour). Two PVCs can be observed by delimiting an isosurface with a swirl strength of $5,000\ 1/s^2$. The first PVC is located between the CRZ and the jet core, and a second one is in the outer region of the jet core. These types of vortices have been previously reported in the literature on flows with PVC structures [164, 165]. The double helix vortical structure shown in the 3D reconstruction of Figure 4.12a has been previously observed in inviscid flows[32].

The CoJF case (Figure 4.11) also shows two different vortical structures. However, in contrast to the OJF, the strongest vortex is located between
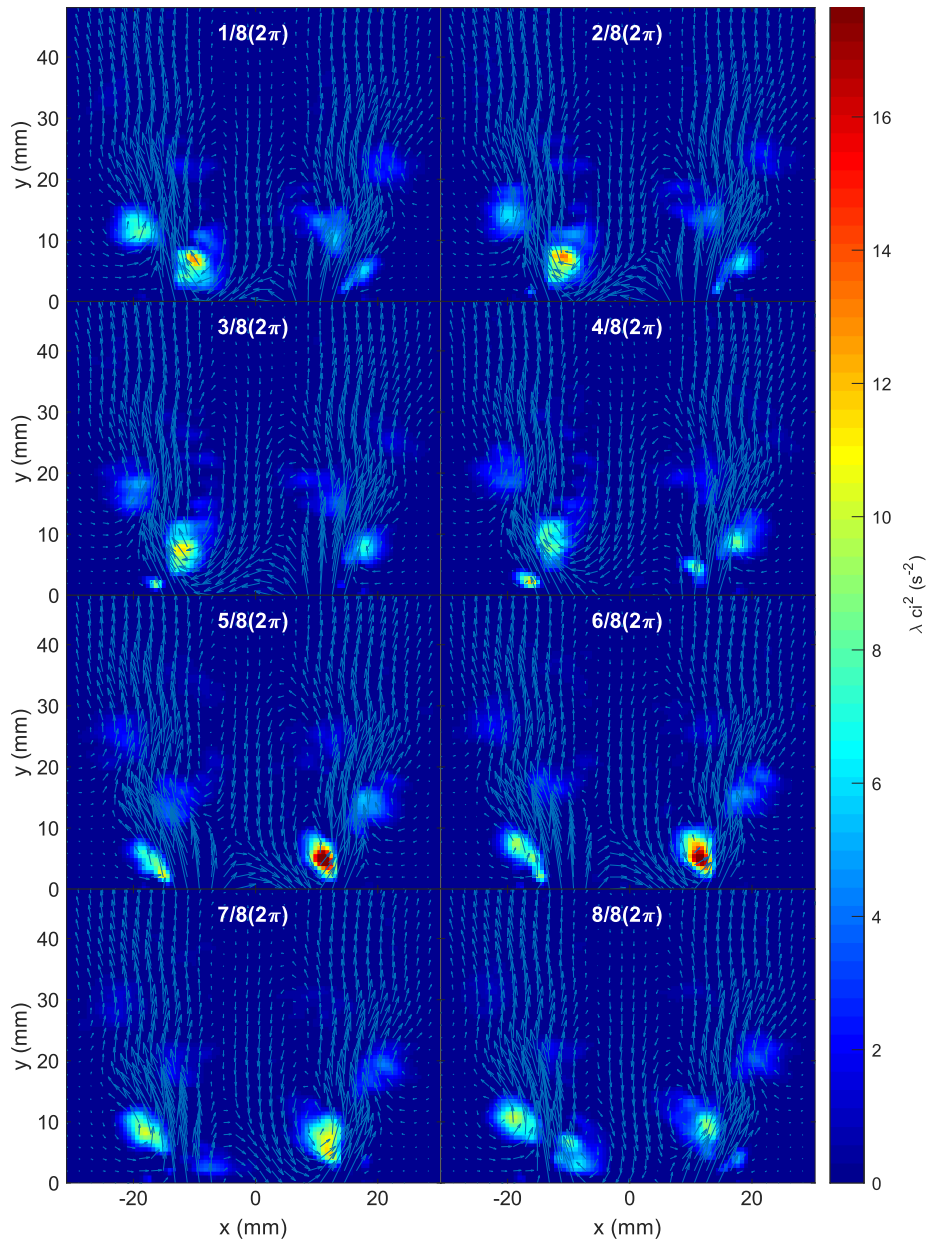
Figure 4.10: Time series of POD reconstruction of OJF with velocity vectors and swirl strength (λ_{2ci}) contours.

the plate and the jet core in the outer shear layer. This vortical structure keeps the jet attached to the bottom wall by means of the Coanda effect. This vortex has been previously identified as a Coanda Vortex Breakdown (CoVB), which is a product consequence of the pressure, recirculation and swirling motion of the flow [95]. The centre of the vortex has a pressure minimum, keeping the jet attached to the wall [88, 89]. A weaker second vortex is found in the inner shear layer and is similar to the PVC of the OJF, thus creating a CoVB pair [95]. For the outer vortex, as time passes, the vortex in the positive side of the x-axis goes from a high swirl strength of $\sim 220,000 \; 1/s^2$ at the $1/8\,2\pi$ mark to almost moving out of the measured plane at the $5/8\,2\pi$ mark. At the $4/8\,2\pi$ mark, as the structure passes through the positive side of the x-axis a vortex starts appearing. The vortex at the left-hand side of the system gets it highest swirl strength of $\sim 250,000 \; 1/s^2$ at the $5/8\,2\pi$ mark and almost disappears at the $1/8\,2\pi$ mark. When this coherent structure passes through the observed plane, the jet separates from the plate. After the structure has passed, the jet quickly reattaches to the plate. A 3D reconstruction of the phase average of the first two POD modes for the Coanda flow was also made and is shown in Figure 4.12b. In the same way, as in the OJF case, the jet core is delimited by an isosurface of the radial velocity of 1.4 m/s (yellow colour) and due to the nature of the flow, no obvious recirculation zone exists. Two vortical structures can be observed by delimiting the isosurface with a swirl strength of $5,000 \; 1/s^2$. The first one, strong vortex located between the outer shear layer of the jet and the flat plate. The second one, a PVC-like structure, can be seen in the inner shear layer.

4.3.5 *Effect of plate height on flow pattern*

Time-averaged results were produced for various plate positions. A higher swirl was imposed to the flow via a tangential swirl generator with a constant geometrical swirl number (Sg) of 1.04. The increase in swirl number allowed for the observation of a clear transition between the Coanda and Open jet flow as $\Delta X/D$ was varied. A fully developed CoJF ($|\Delta X/D| = 0.000$), a transitional flow with CoJF or OJF features ($|\Delta X/D| = 0.082$), and a fully developed OJF ($|\Delta X/D| = 0.125$) were firstly imposed using a nozzle with an angle $\alpha = 45°$. A moderate swirl under CoJF, $|\Delta X/D| = 0.000$, showed a flat velocity profile, see Figure 4.13. When looking at the radial profiles of axial velocity in Figure 4.14, the Coanda effect near the nozzle creates a large downward velocity zone near the centre. In the shear layer of this recirculation zone with the jet, high turbulence intensities can be found indicating the strong mixing between the jet and the entrained air near the centre of the burner. Lowering the flat plate of the burner decreases the Coanda effect near the nozzle outlet. Comparing Figure 4.13a and Figure 4.13b makes noticeable that the CoJF at $|\Delta X/D| = 0.082$ is less deflected towards the wall compared to the one at $|\Delta X/D| = 0.000$.

As the strength of the Coanda effect is weaker, the flow can transit to the OJF configuration as the flow detaches from the flat plate at the
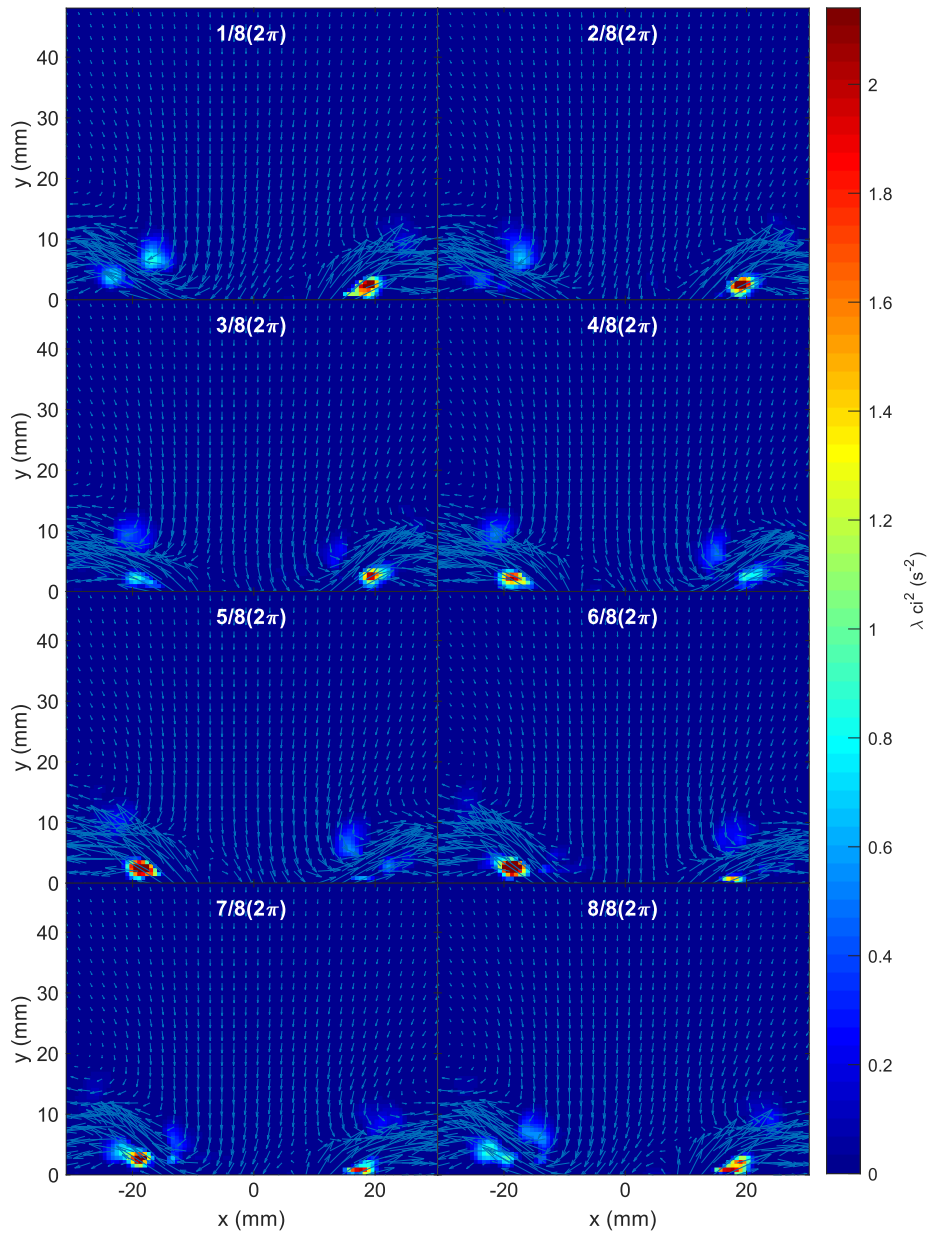
Figure 4.11: Time series of POD reconstruction of CoJF with velocity vectors and swirl strength (λ_{2ci}) contours.

(a) OJF.

(b) CoJF.
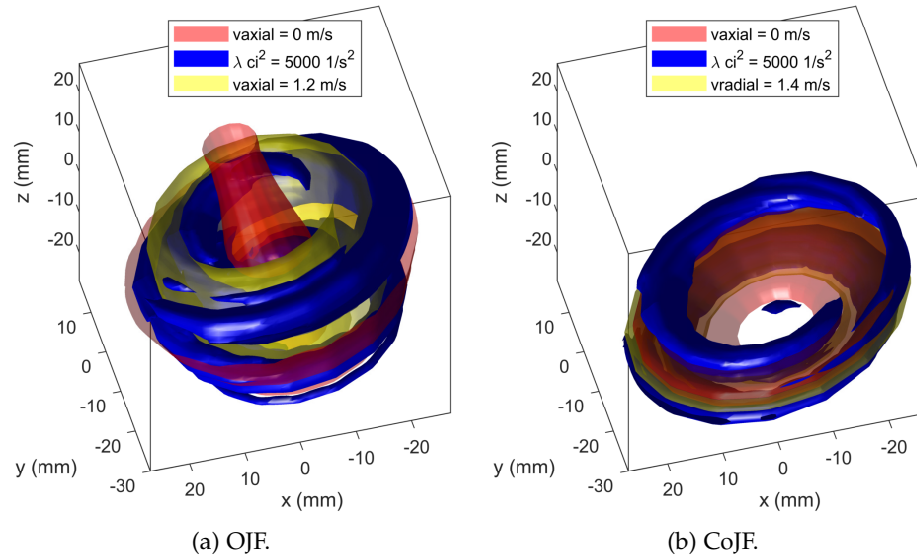
Figure 4.12: 3D Reconstruction.

same distance $|\Delta X/D| = 0.082$. Experiments indicate that the transition can be only achieved by perturbation of the outer shear layer and not the inner one. It is speculated that by physically disturbing the outer shear layer, the coherent structure trapped between the jet core and the plate (identified in the previous section) breaks down and is unable to continue anchoring the jet. Looking at the velocity fields in Figure 4.13c shows that the detachment of the jet leads to a drastic change in flow pattern downstream of the jet. A large CRZ is formed with high downward velocities near the centre and a complete open jet annihilates the CoJF, see Figure 4.13d.

Despite the great influence of the detachment of the flow on the downstream field, close to the nozzle there is very little influence in both shear layers of the jet. Moreover, it is worth noting that RMS values for all the cases remain similar and high, especially in the inner shear layer, see Figure 4.14. This shows that the turbulent nature of the phenomenon is in the same order of magnitude to average velocities but in coherence between processes.

Similar trials were performed using a nozzle with $\alpha = 30°$, the results are shown in Figure 4.15 and Figure 4.16. Average velocity profiles are $\sim$ 30% higher in magnitude for the open jets. When comparing the Coanda flow close to transition at $|\Delta X/D| = 0.125$, average velocity profiles depict a similar condition to the $\alpha = 45°$ case, compare Figure 4.14 and Figure 4.16. Note that the RMS values are very similar in both cases. This is not surprising, as the flow is redirected with a similar horizontal profile as the $\alpha = 45°$ case. Once that the flow has acquired an Open jet profile close to transition, see Figure 4.16c, it is evident that the CoJF has disappeared, and the jet has acquired a less spread, more compact and coherent shape. The initial hypothesis suggested that the flow would follow a flatter profile. However, once that the flow transits to an Open Jet the shearing flow detaches from the nozzle, showing a jet that is not
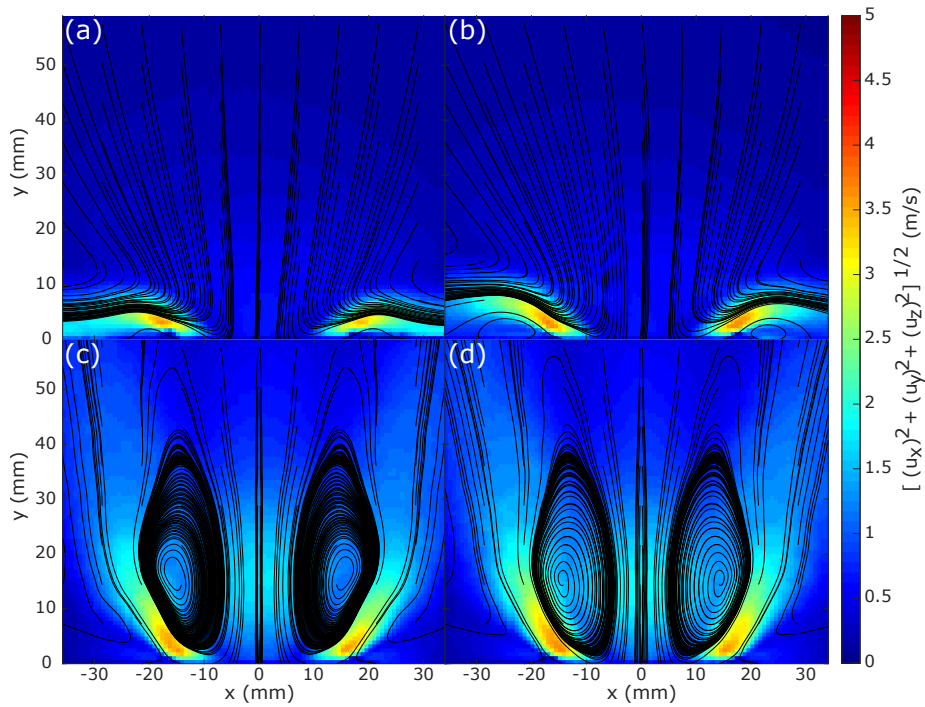
Figure 4.13: Scaled average velocity profiles. a) CoJF $|\Delta X/D| = 0.000$; b) CoJF close to transition $|\Delta X/D| = 0.082$; c) OJF close to transition $|\Delta X/D| = 0.082$; d) OJF $|\Delta X/D| = 0.125$. Re$\sim 11,100$, $\alpha = 45°$, 125 Hz. Units in [m/s].
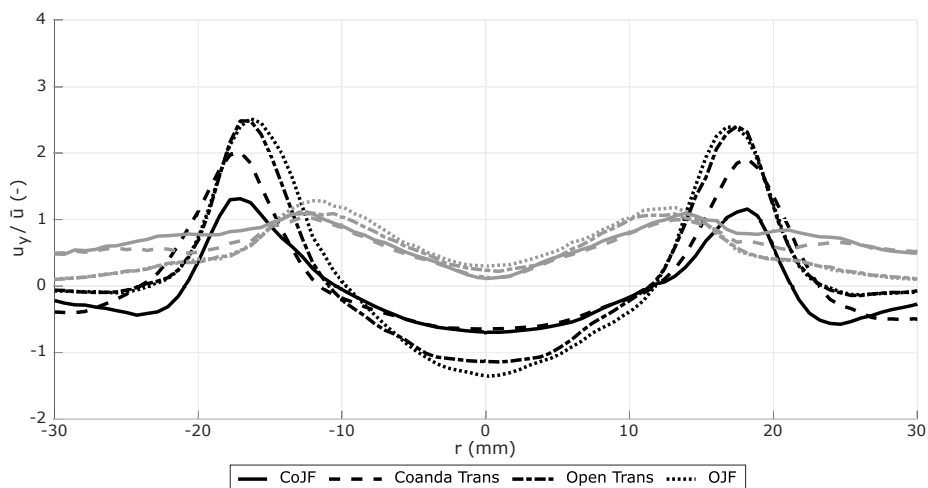
Figure 4.14: Scaled mean axial velocity (black lines) and RMS profiles (grey lines) at $X/D = 0.100$. Re$\sim 11,100$, $\alpha = 45°$, 125 Hz.
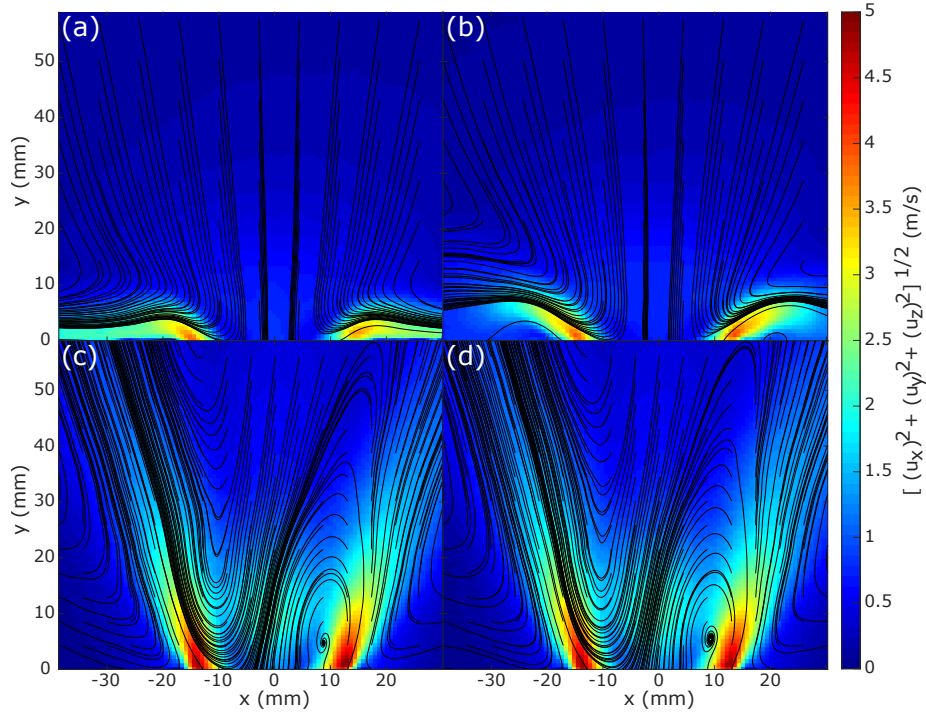
Figure 4.15: Scaled average velocity profiles. a) CoJF $|\Delta X/D| = 0.000$; b) CoJF close to transition $|\Delta X/D| = 0.121$; c) OJF close to transition $|\Delta X/D| = 0.121$; d) OJF $|\Delta X/D| = 0.204$. Re$\sim 11,100$, $\alpha = 30°$, 125 Hz. Units in [m/s].

constrained to geometrical boundaries from the burner. Axial velocity profiles are considerably higher than for the $\alpha = 45°$ case, indicating less spread of the jet. Although the total velocity remains in the same range as the 45° case, see Figure 4.14 and Figure 4.16, the increase in axial velocity confirms a lower radial contribution. Therefore, the profiles from a fully developed OJF and a flow that has just transitioned into an Open Jet are very similar.

The study using $\alpha = 60°$, showed a transient regime at $|\Delta X/D| = 0.061$. It is speculated that the strength of the CoJF underlying coherent structure has considerably increased. Since the flow needs to be bent even further than in the previous case, the only manner this can be achieved is with a stronger structure. As observed from the profiles, see Figure 4.17d, the jet angle has a similar angle to the nozzle, thus suggesting that the flow is still in contact with the burner. However, contrary to the CoJF case, this is theorised to be the remaining of the vortex produced by the shearing flow, thus a strong external recirculation zone has been created. Since the jet has now opened, the PVC is rotating across the flow [84]. This behaviour impacts the axial velocity with lower values than those obtained with 30° nozzle, see Figure 4.18.

A conclusion from all previous results is that for the establishment of the CoJF close to transition it is necessary that the flow remains in contact with the nozzle. Thus, a combination of shear and low pressure can support the coherent structures required for the existence of the CoJF. A summary of the results is depicted in Table 4.3.
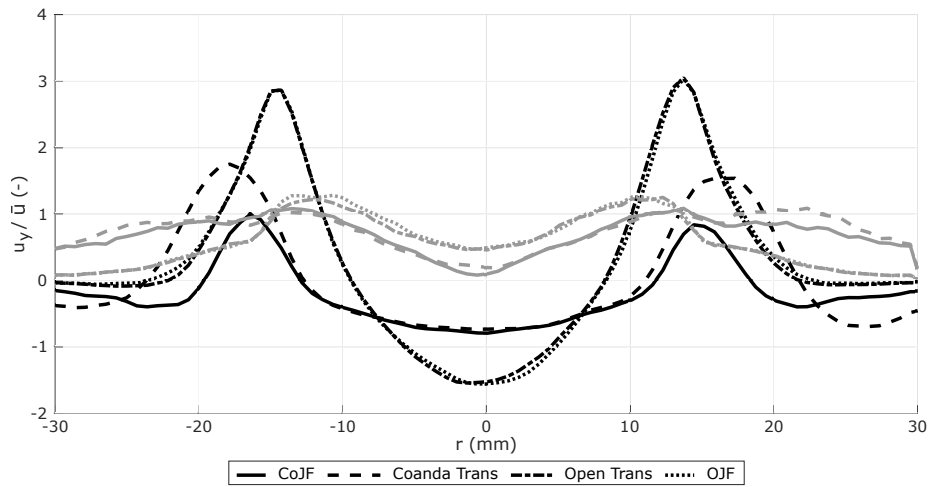
Figure 4.16: Scaled mean axial velocity (black lines) and RMS profiles (grey lines) at $X/D = 0.100$. Re$\sim 11,100$, $\alpha = 30°$, 125 Hz.
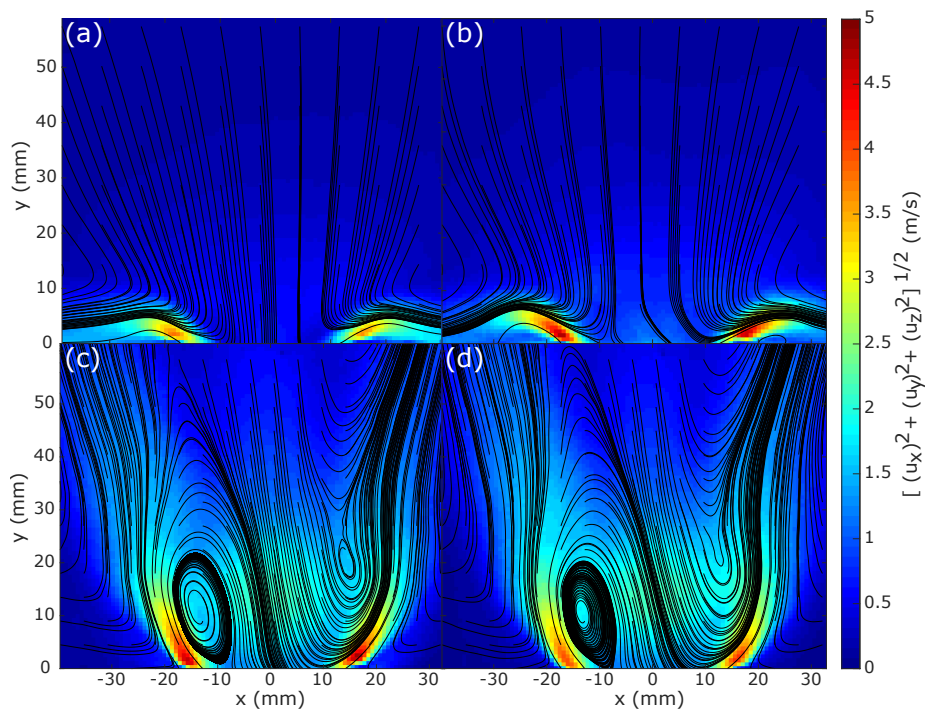
Figure 4.17: Scaled average velocity profiles. a) CoJF $|\Delta X/D| = 0.000$; b) CoJF close to transition $|\Delta X/D| = 0.061$; c) OJF close to transition $|\Delta X/D| = 0.061$; d) OJF $|\Delta X/D| = 0.161$. Re$\sim 11,100$, $\alpha = 60°$, 125 Hz. Units in [m/s].
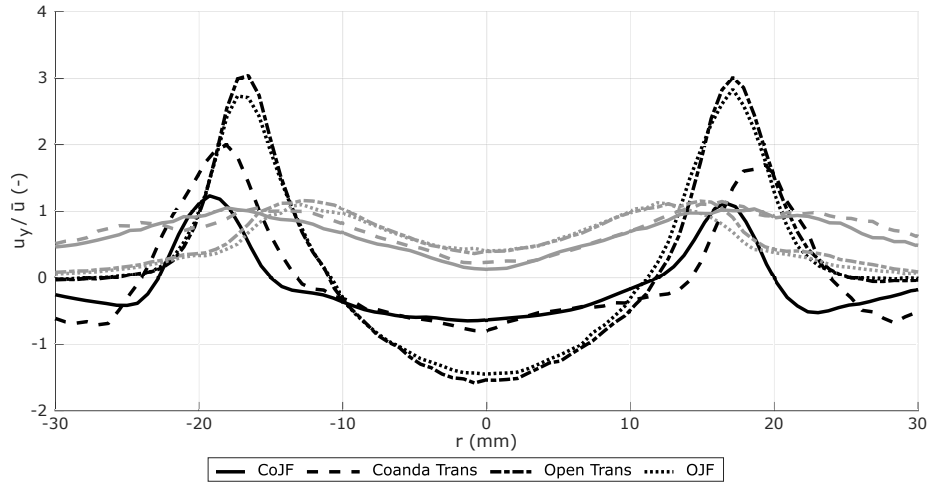
Figure 4.18: Scaled mean axial velocity (black lines) and RMS profiles (grey lines) at $X/D = 0.100$. Re$\sim 11,100$, $\alpha = 60°$, 125 Hz.

Table 4.3: Summary of results for the flow patterns obtained with a combination of flat plate position, $|\Delta X/D|$, and nozzle angle, α.

		Flat Plate Normalised Position			
α	0.000	0.061	0.082	0.121	> 0.121
		Type of Flow Pattern			
30°					
45°					
60°					

● CoJF   ● CoJF/OJF   ● OJF

4.4 CHAPTER SUMMARY

This chapter studied the flow dynamics of two flow patterns, OJF and CoJF , using 2D3C-PIV in a generic swirl burner. The measurements were conducted at different Reynolds numbers at the burner nozzle in the range from ~ 4300 to ~ 13900. A spectral analysis was conducted to identify the dominant frequencies of the flow. The combination of swirl and plate height was such that both flow patterns could coexist. Coherent flow structures were identified by POD by reconstructing the most energetic modes with matching temporal frequency. 3D reconstructions were made of the lowest evaluated Reynolds number. A Precessing Vortex Core pair was found in the inner and outer shear layer for the OJF case. For the CoJF case, a very strong vortex in the outer shear layer and a PVC in the inner shear layer was found. The vorticity of this outer vortex is twice the vorticity of the inner vortex. Hence, this strong vortex is dominant and changes the precession frequency of the PVC being lower in the OJF than in the CoJF.

The effect of the base plate with respect to the nozzle outlet was also evaluated. High-Speed PIV was used to capture the features of the mean flow from/to an OJF to/from a CoJF. It was observed that close to transition the jet bends at different angles than those of the fully developed flows. The CRZ is not entirely anchored for the transitional OJF, whilst a deflected jet is present in the transitional CoJF. Contact with the nozzle also played an important role in the establishment of the CoJF, likely a consequence of the shearing and low-pressure region established between the flow and the solid body.

COMBUSTION EXPERIMENTS

This chapter covers the results of combustion experiments on the swirl burner. The aim of the experiments is to identify regions of operation and burner geometries where a Coanda flame is stable under different mass flow rates and equivalence ratios. As mentioned in Section 2.3, some applications for the Coanda flow exist in the industry, being waste gas flares the only one that involves combustion. Therefore, it is not a surprise that the available literature is mostly limited to waste gas flares. It is believed that unexplored potential applications exist that take advantage of the flat flow profile that the Coanda effect produces, especially on industrial processes that involve the heat treating of flat surfaces. Because of this, experiments need to be carried out to understand the stability and behaviour of a Coanda flame that is attached to a horizontal surface. More so, the experimental results will serve as a basis for validating the numerical simulations presented in Chapter 6. The fundamental idea of the research is based on having different burner geometries where the stability of an unconfined Coanda flame under different mass flow rates and equivalence ratios can be mapped. Once stable regions of operation are identified, additional characteristics of the flow and flame are obtained by PIV measurements. Furthermore, it is necessary to carry out additional experiments with a confined flow to be able to determine the stability of the flame and identify potential improvements to the design, as well as issues that might arise on a pilot-scale application.

This chapter is structured in two main sections, one that deals with the unconfined experiments (Section 5.1), and another one for the confined experiments (Section 5.2). The first section starts by detailing the experimental setup in Section 5.1.1; then, in Section 5.1.2 gives an overview of the flame flow patterns that were observed in the experiments. Following that, Section 5.1.3, presents the effect that variations in geometry have on the flame stability. The PIV measurements for selected operating points are given in Section 5.1.5. Finally, general remarks of the experiments are given in Section 5.1.6. The second section also starts by giving a description of the experimental setup in Section 5.2.1. Afterwards, results are shown in Section 5.2.2 of the confinement wall temperatures. Finally, general remarks for the confined experiment are given in Section 5.2.3.

5.1 UNCONFINED EXPERIMENTS

5.1.1 *Experimental setup*

The swirl burner detailed in Section 3.1.1 was used to examine the flame stability under a CoJF and an OJF pattern. A schematic of the
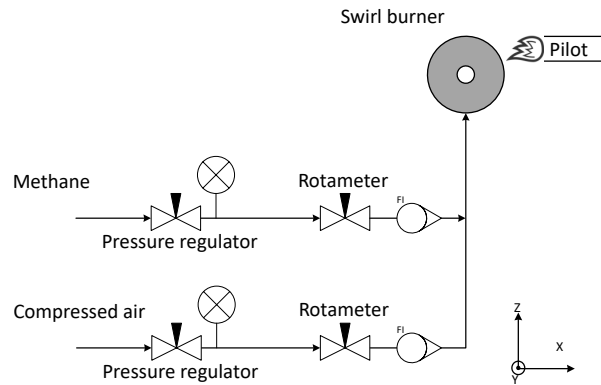
Figure 5.1: Experimental setup.

experimental setup is presented in Figure 5.1. Methane was used as fuel and air as an oxidiser. Both gases were supplied to the system through flexible hoses. Inlet gas temperature was ~ 293 K and the pressure was close to atmospheric. Three Variable Area Flow Meters (VAFM) with ranges of $1 - 12$ L/min, $6 - 50$ L/min and $40 - 440$ L/min for air at Normal Temperature and Pressure (NTP) were used to regulate the air flow. The air was split between the VAFM in such a way that operating at the limits of each flow meter was avoided. A single VAFM with a range of $1 - 18$ L/min for methane at NTP was used to regulate the methane flow. After passing through the VAFM, methane and air were combined into a single stream ~ 1 meter upstream from the burner inlet. Finally, the gas mixture went out through the nozzle burner and was ignited by a pilot light located ~ 0.3 m downstream the nozzle exit.

To examine the effect of different geometries on the flame flow pattern and on the stability limits, two tangential swirl generators (Sg = 0.85 and 1.47), three nozzle diameters ($D = 19.5$, 24.0 and 28.0 mm) and three nozzle angles ($\alpha = 30°$, $45°$ and $60°$) were used. A flat plate was fitted to the nozzle. Two different normalised plate heights were chosen, $\Delta X/D = 0.00$ and $\Delta X/D = 0.36$, being X the distance between the flat plate and the tip of the nozzle outlet (refer to Figure 4.1 for a schematic). A set of experiments was performed for each normalised height. Gas flow rate was varied from 3 L/min (~ 2 g/s) to a maximum of 12 L/min (~ 8 g/s) in incremental steps of 1 L/min (~ 0.7 g/s). For each methane flow rate, the air flow rate was increased in increments of 1 L/min until an equivalence ratio of ~ 0.75 was reached. The flow pattern was recorded for each air and gas flow rate combination. This procedure was repeated for each tangential swirl generator, nozzle diameter and nozzle angle. All experiments were performed without the use of a confinement.

For the flame length experiments, a digital single-lens reflex camera was positioned ~ 1 m from the flame. A background image without a flame was taken. Another image was taken with a calibration plate to correlate the pixels of the image with the distance. The previous three nozzle diameters were tested ($D = 19.5$, 24.0 and 28.0 mm). A set of 100 images were taken for each combination of equivalence ratio and mass flow rate. Each image of the set had the background image subtracted.

Background subtracted images were averaged and the flame length was calculated. All the image processing and manipulation was carried out using Matlab R2018b with the Image Processing Toolbox.

A PIV system was employed to acquire the general flow patterns of a Coanda flame and an open flame. The PIV system consisted of a single cavity Nd:YLF laser of 532 nm wavelength. Laser sheet optics were used to convert the laser beam into a 1 mm thick sheet. A single CMOS camera was used with 60 mm Nikon lenses, which allowed for a field of view of approximately 80×80 mm (Figure 4.3), with a resolution of 5.35 pixels per mm and a depth of view of 1.5 mm. The inlet air was seeded using a pressurised vessel at ~ 0.5 bar containing aluminium oxide with a mean particle size of 10 μm. A single equivalence ratio and mass flow rate were chosen such that both the Coanda and open flame could be obtained. The acquisition rate was set at 5 Hz with no phase locking. The line of view of the camera was positioned exactly in the middle of the nozzle. A set of 500 images were taken for each flow pattern.

5.1.2 *Flow pattern overview*

To examine the possible flame patterns, experiments were carried out with the flat plate set at the position of $\Delta X/D = 0.36$, a tangential swirl generator with Sg $= 1.47$, nozzle diameter of $D = 28.0$ and a nozzle angle of $\alpha = 45°$. This configuration served as a base case for comparison with variations in geometry. Four different states of the open jet flame were identified. For each gas flow rate with a low inlet air flow, the flame started as a stable, nozzle attached flame (Figure 5.2a). From this state, an increase in air flow could start the transition to one of two states: (1) flashback and (2) lifted flame. The transition to flashback occurred when the total mass flow rate was less than ~ 1.00 g/s. In this situation, as the air flow was increased, the outer part of the flame continued attached to the nozzle but the central part of the flame started flashbacking into the nozzle. A point was reached when full flashback occurred, and the combustion was taking place entirely inside the burner (Figure 5.2d). This flashback behaviour has been previously described in the literature as combustion induced vortex breakdown [166]. The transition to a lifted flame occurred when the total mass flow rate was more than ~ 1.00 g/s. An increase in the air flow detached the flame from the nozzle and made it transition into a lifted flame state (Figure 5.2b). From this point, the lifted flame can take two paths as air flow is increased. The first one is flashback (Figure 5.2d). The second one being a lifted flame that ends up being blown off. Figure 5.4a shows the different transition points for each state. The overall behaviour of the open jet flame is known and widely reported in the literature [7, 167].

With the flat plate at a position of $X/D = 0.00$, the four previously described flame states were also possible. As with the previous configuration, the flame started as a stable, nozzle attached flame (Figure 5.2a). With an increase in air flow, the flame transitioned to either a lifted

(a) Stable open jet flame.   (b) Lifted flame.   (c) Transition lifted flame-flashback.   (d) Flashback.
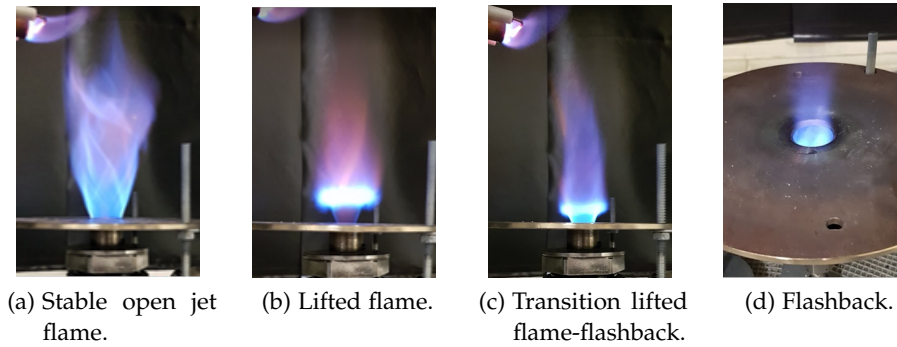
Figure 5.2: Observed flame patterns with $\Delta X / D = 0.36$, Sg $= 1.47$, $D = 28.0$ and $\alpha = 45°$.

flame or to flashback. An attempt was made to induce the Coanda flame by using a steel rod to spread the flame for each increase in gas and air flow. A mass flow rate threshold of ~ 0.50 g/s was identified, below which it was impossible to obtain a Coanda flame. If the attempt was made to spread the OJF nozzle attached flame when the mass flow rate was less than 0.50 g/s the flame immediately returned to its nozzle attached state and the Coanda state could not be induced. With a mass flow rate greater than 0.50 g/s, once the Coanda flame was established it remained attached to the plate until physically disturbed (Figure 5.3a and Figure 5.3c). From this point, with an increase in air flow rate, the flame gradually retreated to the nozzle and the combustion zone became smaller (Figure 5.3b and Figure 5.3d). This behaviour continued until the equivalence ratio reached a threshold of ~ 1.25 where the Coanda flame spontaneously detached from the plate and turned into a lifted flame that was close to a flashback condition (Figure 5.2b). The two thresholds observed for the Coanda flame suggest that there are at least two factors that are important for the onset and breakdown of the Coanda effect. The first one being the velocity of the gases at the nozzle exit that allows for the entrainment of stagnant air and the subsequent establishment of the Coanda effect. The second factor is combustion stability, more specifically the flashback point, at which the Coanda flow is no longer able to keep attached to the flat plate. Figure 5.4b shows the different transitions points for each state.

The results of these experiments agree with the ones in Chapter 4, a normalised plate height of the plate height $\Delta X / D = 0.00$ allows for the existence of a CoJF pattern, whereas a normalised height of $\Delta X / D = 0.36$ made it impossible to obtain. This is expected, as the theory behind the existence of a Coanda flow requires a horizontal surface for the flow to attach to (see Section 2.3).

5.1.3   *Stability limits*

Unless stated otherwise, all the following experiments are carried out with the same conditions as the base case presented in Section 5.1.2; this

(a) Stable Coanda flame.

(b) Transition Coanda-flashback.

(c) Stable Coanda flame.

(d) Transition Coanda-flashback.
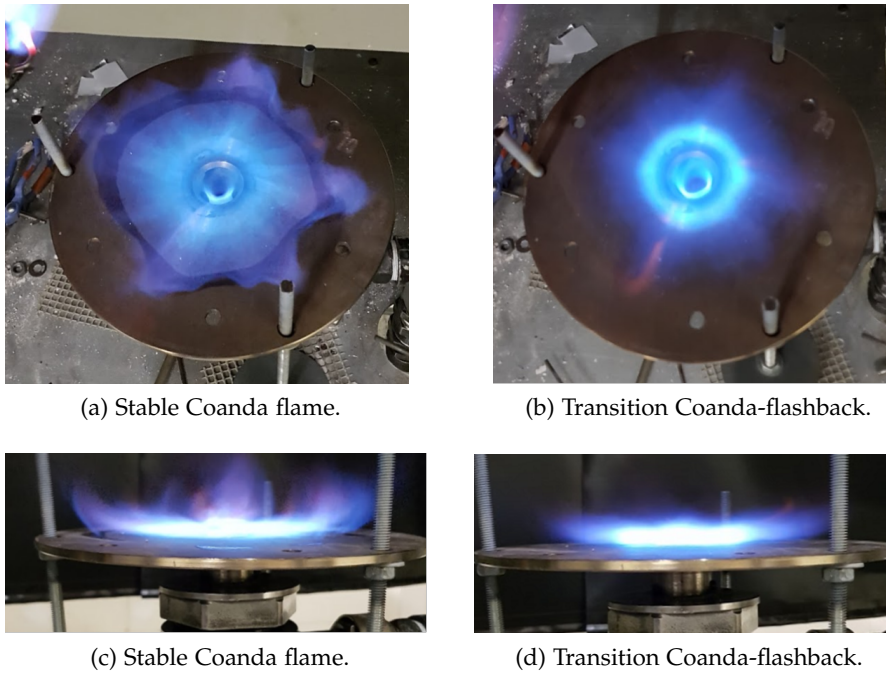
Figure 5.3: Observed flame patterns with $\Delta X/D = 0.00$, Sg $= 1.47$, $D = 28.0$ and $\alpha = 45°$.

(a) $\Delta X/D = 0.36$.
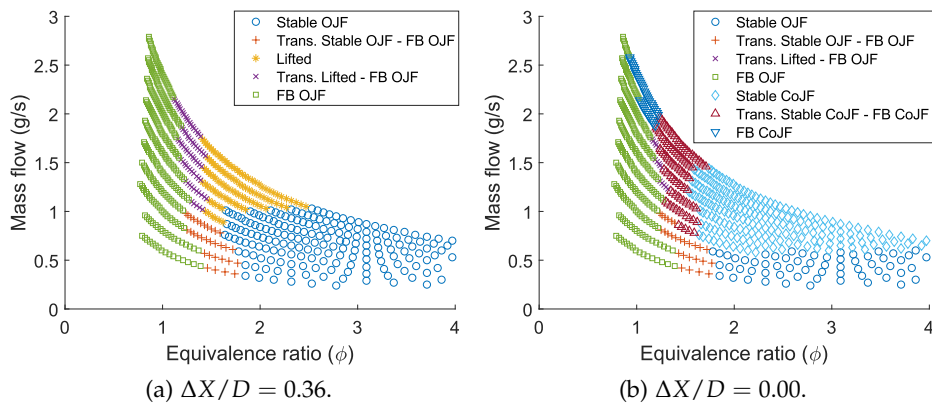
(b) $\Delta X/D = 0.00$.

Figure 5.4: Stability map with Sg $= 1.47$, $D = 28.0$ and $\alpha = 45°$.
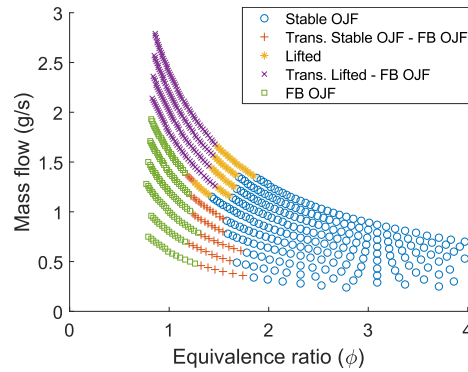
Figure 5.5: Stability map with $\Delta X/D = 0.00$, $\text{Sg} = 0.85$, $D = 28.0$ and $\alpha = 45°$.

is, flat plate set at position $\Delta X/D = 0.00$, tangential swirl generator with $\text{Sg} = 1.47$, nozzle diameter of $D = 28.0$, and nozzle angle of $\alpha = 45°$.

5.1.3.1   *Effect of swirl variation*

Using a tangential swirl generator with $\text{Sg} = 0.85$, it was not possible to produce a Coanda flame. The stability map for this configuration is shown in Figure 5.5. It is speculated that the reason for the impossibility of having a Coanda flame is that the swirl applied by the tangential swirl generator is not enough to produce a Coanda effect. As mentioned in Section 2.3.3, one of the parameters that caused the onset of the Coanda effect in isothermal flows was an increase in the swirl applied to the flow [88, 89]. Similar behaviour has been previously observed in reacting flows [81]. However, further experiments are needed to confirm that the same is happening here as the nozzle geometry is different.

5.1.3.2   *Effect of nozzle angle*

Using nozzle angles of $\alpha = 30°$ and $\alpha = 60°$, made it impossible to obtain a Coanda flame. The stability map is shown in Figure 5.6. This is different to what was obtained with an isothermal flow on Section 4.3.5, where a Coanda flow was always able to be obtained with any nozzle angle if the plate position remained at $\Delta X/D = 0.00$. Further experimentation is required to accurately explain the underlying phenomena that causes the difference between the reacting and isothermal flow.

5.1.3.3   *Effect of nozzle diameter*

Changing the nozzle diameter produced the most useful results of tested variations in geometry. Three different nozzle diameters were tested $D = 19.5$, 24.0, and 28.0 mm. For each of these diameters, two different experiments were carried out. The first one focused on the spontaneous change in flow pattern without any external disturbance. The second one investigated maximising the region were the Coanda flow can be obtained by physically disturbing the flow (i.e. trying to induce the Coanda effect with a steel rod). Results of these trials are shown in Figure 5.7. For the trials without external disturbance (left column of Figure 5.7) as the nozzle diameter is reduced, the region where a Coanda
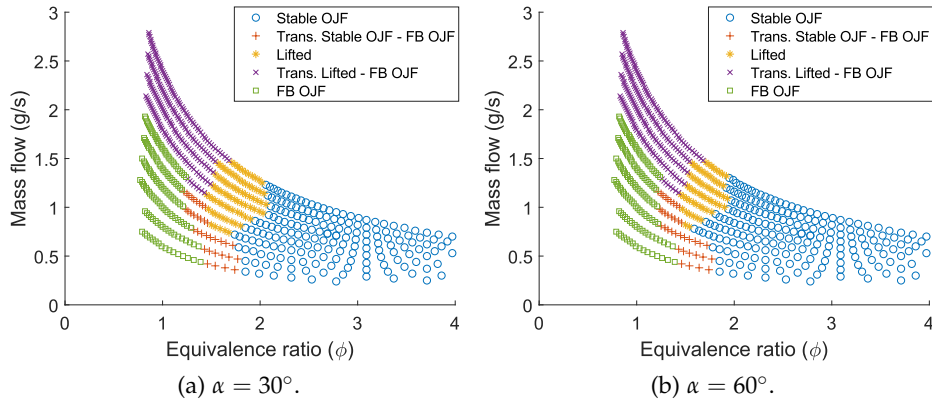
Figure 5.6: Stability map with $\Delta X/D = 0.00$, Sg $= 0.85$ and $D = 28.0$.

flame is spontaneously produced increases. This is a positive effect on the stability of the Coanda flame and is something to be expected. The reason is that as the nozzle diameter is reduced, the outlet velocity increases, which causes greater entrainment of the stagnant atmospheric air; as it was explained before (Section 2.3) this is one of the main requirements for having a Coanda effect. Looking at the results with external disturbance (right column of Figure 5.7) as the nozzle diameter is reduced, the propensity to flashback increases leading to a much bigger region of Coanda flashback. This is an undesired result, as it was observed that when the combustion area was reduced in a Coanda flame, the base plate where the flow is attached greatly increased in temperature. This could lead to damage to the equipment in the day to day operation. Thus, there is a compromise between using a smaller diameter nozzle to obtain a Coanda flame that is hotter and smaller in diameter but more stable and using a bigger diameter nozzle to obtain a Coanda flame that is bigger in diameter and cooler, but less stable.

5.1.4 *Flame length*

The effect of the mass flow rate, equivalence ratio and nozzle diameter on the Coanda flame length was evaluated. First, a set of experimental points was chosen in such a way that the different states of the Coanda flame were captured. The experimental points can be seen in Figure 5.8 and are organised in five horizontal rows. Each row corresponds to a fixed amount of air. Data was acquired for each point with each one of the three nozzle diameters.

The result of these experiments is shown in Figure 5.9 with a plot of the experimental data for each nozzle diameter. A line is fitted to the points of each air flow rate. A clear pattern can be observed from these plots; for all the cases, as the equivalence ratio is increased (i.e. more gas is added to the fixed air flow), the flame length increases. This agrees with the observations made in the previous section where the experimental points that have a lower equivalence ratio are closer to the flashback point, which will shorten the flame. However, another possible
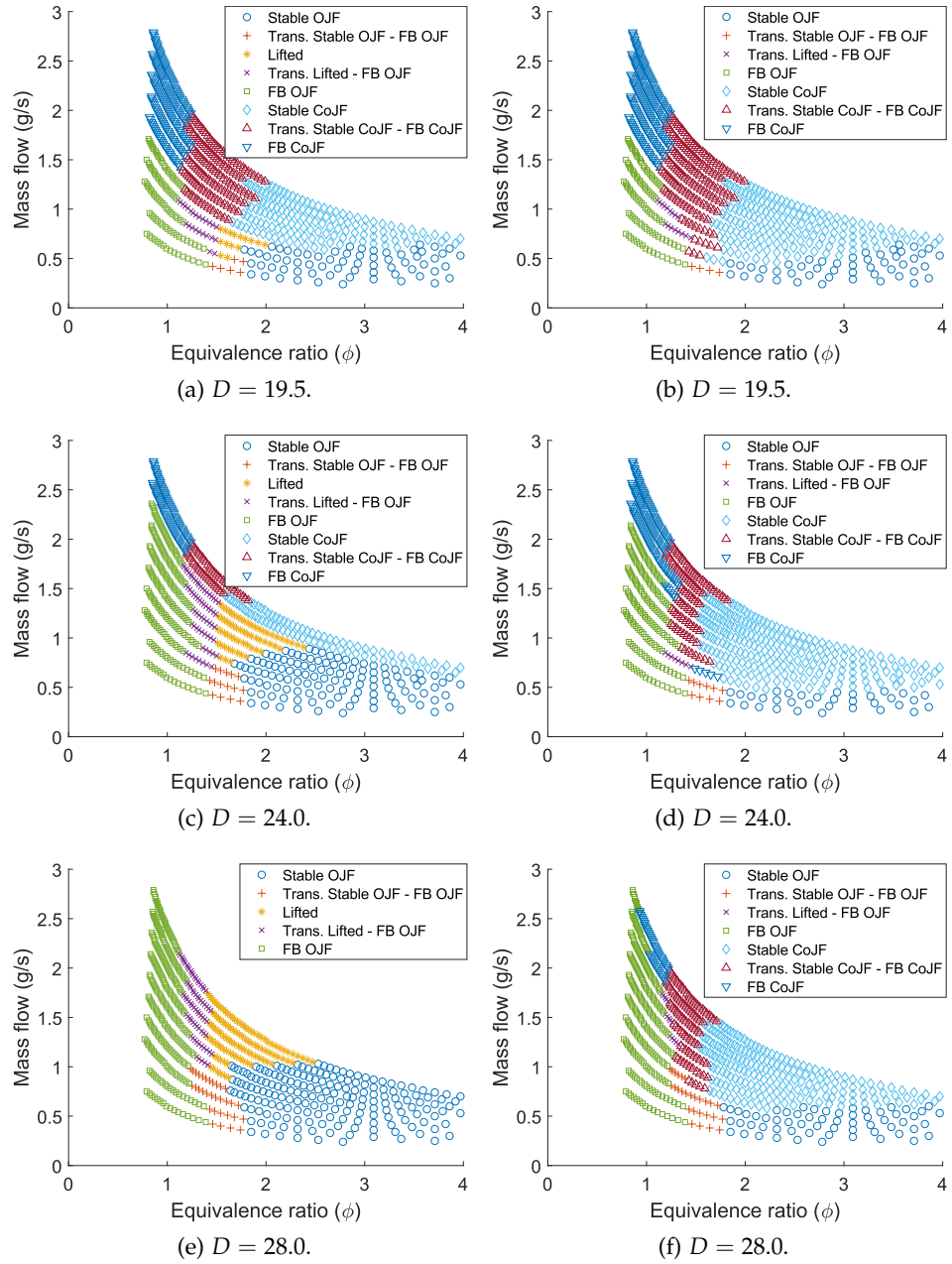
Figure 5.7: Stability map with $\Delta X/D = 0.00$, Sg $= 1.47$ and $\alpha = 45°$. Spontaneous flow pattern change (left) and flow pattern change with external disturbance (right).
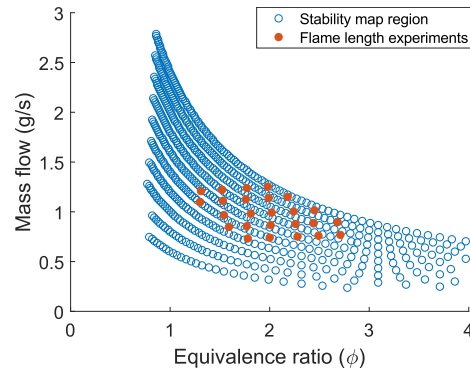
Figure 5.8: Experimental points for flame length experiments.

explanation for this observation is that, because the experiments were carried out without a confinement, the equivalence ratio is not accurate as there is effectively an unlimited supply of air. A very gas-rich flame will inevitably elongate because the gas will be mixing and reacting with the external air. Both factors, the flashback with increased airflow and the unconfined measurements, must be affecting the flame length. Confined experiments would be needed to differentiate between these effects.

A comparison between the three nozzle diameters can be seen in Figure 5.10. In this figure, the data of Figure 5.9 is plotted in a single plot and the centroid of the points of each nozzle is calculated (solid colour marker). Judging by the scatter data points and the centroid values, it appears that with an increased nozzle size there is an increase in flame length. This coincides with the observations made in the previous section where with a decrease in the nozzle diameter the flashback propensity increased.

5.1.5   *PIV measurements*

All the following experiments are carried out with the same conditions as the base case presented in Section 5.1.2, this is a flat plate set at position $\Delta X / D = 0.00$, a tangential swirl generator with Sg $= 1.47$, nozzle diameter of $D = 28.0$, and nozzle angle of $\alpha = 45°$. A single experimental point with a total mass flow rate of 0.70 g/s and an equivalence ratio of 2.50 was used. This experimental point was chosen because both, the Coanda and open flame, are possible flame flow patterns. The aim of this study was to determine general flow characteristics by looking at the mean values. The values obtained will also be used in Chapter 6 to validate the numerical simulations. The results of the PIV measurements are shown in Figure 5.11. The open flame exhibits a clear defined jet with a CRZ. The Coanda flame shows the expected horizontal velocity profile with two recirculation zones in the region where the flame detaches from the plate.

(a) $D = 19.5$ mm.

(b) $D = 24.0$ mm.

(c) $D = 28.0$ mm.
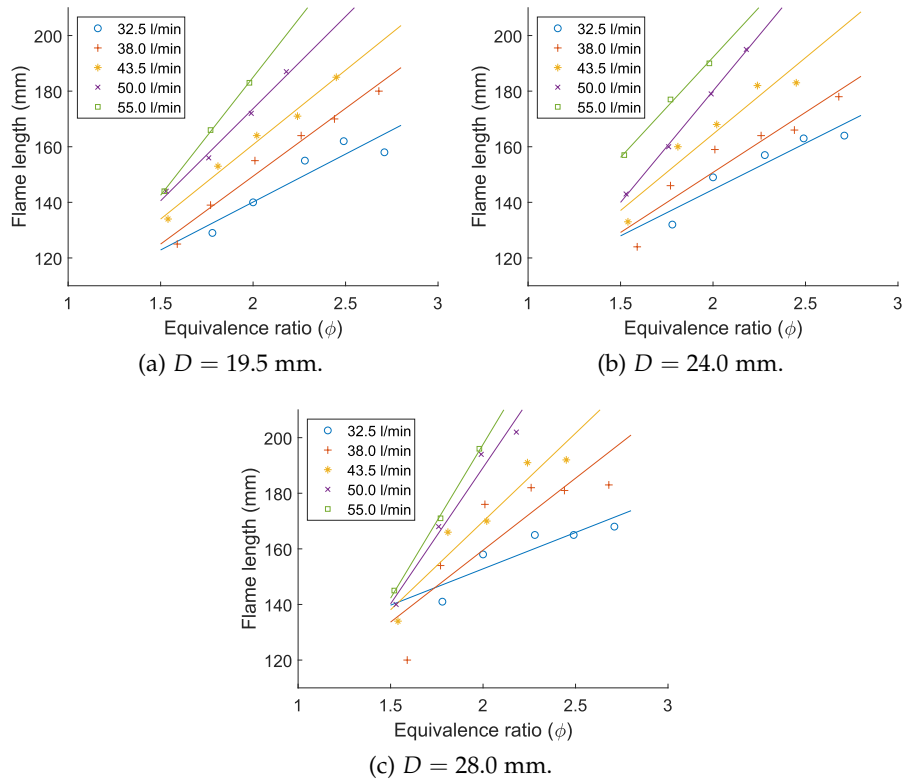
Figure 5.9: Coanda flame length with varying equivalence ratio with a constant air flow.
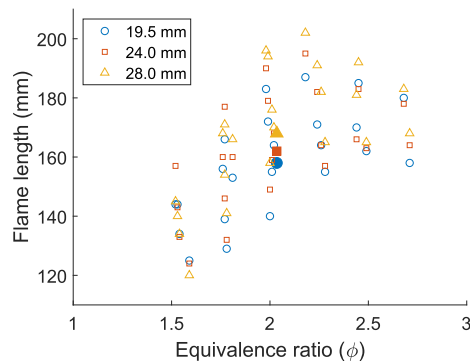
Figure 5.10: Coanda flame length with varying equivalence ratio and nozzle diameter.
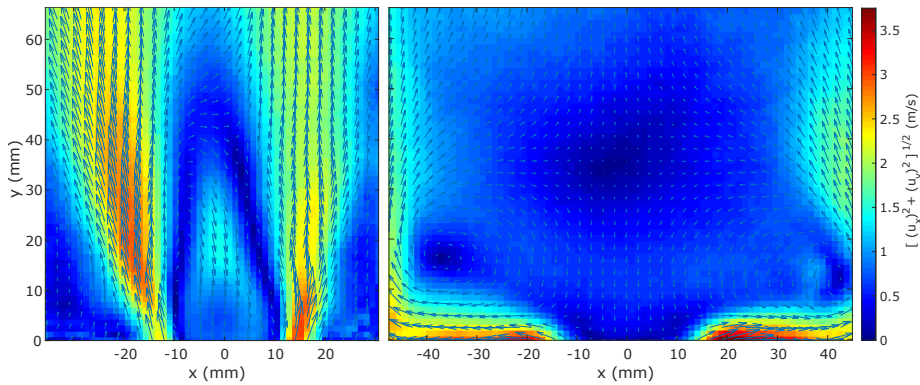
Figure 5.11: Contours of mean velocity magnitude for an open flame (left) and a Coanda flame (right) with total mass flow rate of 0.70 g/s and an equivalence ratio of 2.50.

5.1.6 *General remarks*

During these experiments, it was not possible to operate in the lower range of the flammability limit because when the air flow was increased the flame always went to flashback. The reason for this might be the high geometrical swirl number used. However, as it was pointed earlier, with a lower geometrical swirl it was not possible to obtain a Coanda flame. The effect of the high geometrical swirl number was further exacerbated with the increased air flow. This is because the tangential swirl generator had fixed vanes and additional air would increase the real swirl number of the flow. Further experiments should focus on quantifying the swirl number of the flow with an increase in air flow and correlate that with the change in flame flow pattern. A possible experimental technique to do this would be S-PIV. A related experimental approach would be testing different nozzle geometries that are not just limited to changing the nozzle angle. For example, Vanoverberghe [168], tested a nozzle that could maintain a Coanda flow pattern even with no swirl applied to it. However, the initial onset of the Coanda flow required an increase in swirl followed by a decrease in swirl applied via a variable swirl generator.

5.2 CONFINED EXPERIMENTS

5.2.1 *Experimental setup*

The swirl burner detailed in Section 3.1.1 was used with a tangential swirl generator with Sg = 1.47, nozzle diameter of $D = 28.0$, and nozzle angle of $\alpha = 45°$. A secondary air inlet for axial injection was added to the burner. The confinement described in Section 3.1.2 was fixed at a position of $\Delta X/D = 0.00$ with respect to the burner nozzle exit. A photograph of the experimental setup can be seen in Figure 5.12. A partially premix flow of 8 L/min methane and 40 L/min air was used in the main flow. The secondary axial air injection flow was set at 35 L/min, yielding an effective equivalence ratio very close to ~ 1.06 and

(a) Confinement.

(b) Confined Coanda flame.
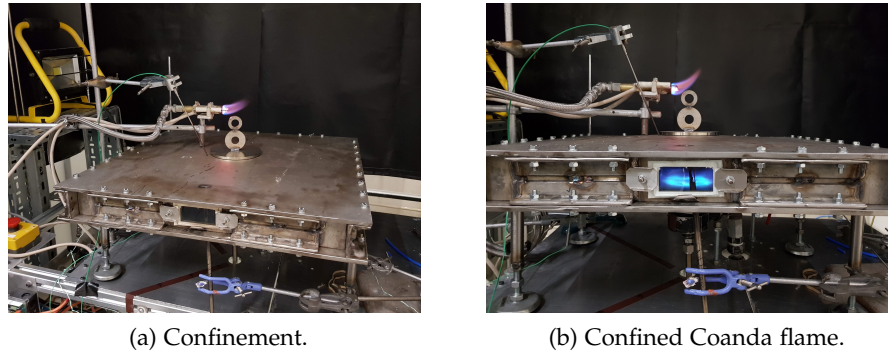
Figure 5.12: Experimental setup for a confined Coanda flame.

a total mass flow rate of ~ 1.62 g/s. All flows are at NTP and ambient temperature was $\sim 20°$C. The flame was ignited by removing a lid at the top of the confinement. After ignition, the lid was re-positioned. For temperature measurement purposes, four thermocouples were positioned at each one of the confinement outlets. The temperature of the confinement walls was registered using an Infrared (IR) camera. The IR images were post-processed using Matlab R2018b. Data gathering started when the confinement reached thermal equilibrium with its surroundings, this was judged to be when the temperature registered by the thermocouples and the IR image no longer increased.

5.2.2   *Confinement wall temperature*

The thermal image of the top plate of the confinement is shown in Figure 5.13. A first look at the image suggests that the temperature distribution along the surface is not homogeneous. To better analyse this, two plots are made from this image, one along the horizontal centre line (dotted line) and another one at a radial distance of 110 mm (dashed circle). Both plots are shown in Figure 5.14. Figure 5.14a confirms the suspicions, the temperature distribution along the length of the top plate follows a parabolic behaviour with a maximum temperature of $\sim 225°$C in the centre of the plate and a minimum temperature of $\sim 150°$C near the edges. Figure 5.14b shows that the temperature has some fluctuation at a fixed radial distance of $r = 110$ with values between 200 and 250°C and a mean temperature of $\sim 210°$C.

The thermal image of the bottom plate of the confinement is shown in Figure 5.15. The maximum temperature is $\sim 310°$C and is located just near the nozzle where the Coanda flame sits on the plate. In an actual application of a device like this, the side corresponding to the bottom plate would be insulated, which would only increase the maximum temperature. Some way of mitigating the high temperature needs to be implemented so the risk of damaging the equipment is minimised. A possible alternative would be to replace the bottom plate for a material that could withstand higher temperatures. The material in question could be a ceramic such as silicon carbide. However, the risk of breakage would need to be considered due to the brittleness of the ceramic.
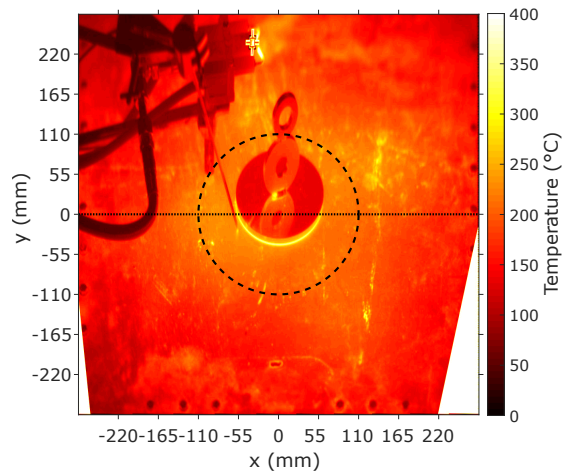
Figure 5.13: Thermal image of upper confinement plate after ~ 2 hours of operation with equivalence ratio of ~ 1.06, total mass flow rate of ~ 1.52 g/s, Sg $= 1.47$, $D = 28.0$ and $\alpha = 45°$.
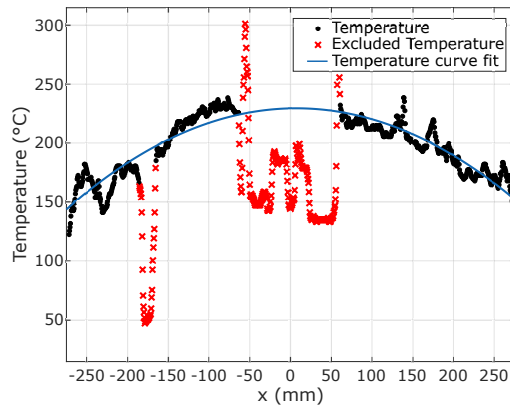
(a) Temperature plot along horizontal centre line.
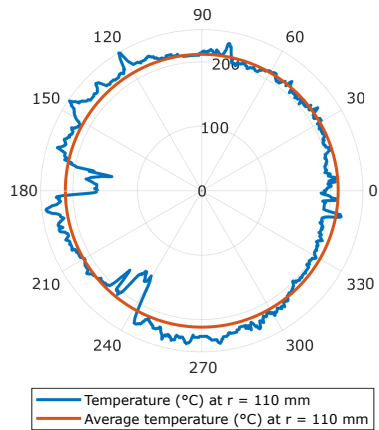
(b) Temperature plot along circle with radius 110 mm.

Figure 5.14: Temperature plots of thermal image.
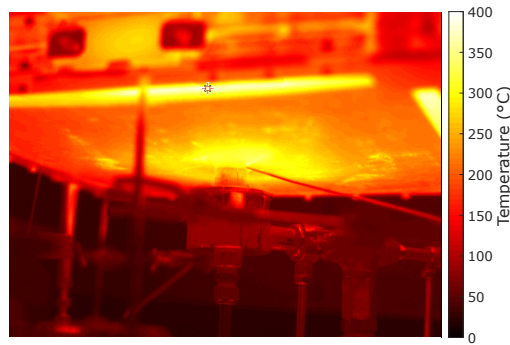
Figure 5.15: Thermal image of lower confinement plate after $\sim$ 2 hours of operation with equivalence ratio of $\sim$ 1.06, total mass flow rate of $\sim$ 1.52 g/s, Sg $= 1.47$, $D = 28.0$ and $\alpha = 45°$.

5.2.3 *General remarks*

The main question that motivated this experiment was the feasibility of having a Coanda flame inside a confinement, especially regarding the obstruction of the recirculation zone above that Coanda flame by the top part of the confinement. This experiment successfully proves that it is possible to have a confined Coanda flame, however, this was not without complications. The first issue, which was already highlighted in the previous section (5.1), is that the geometry of the burner is not optimal for the Coanda flow. This is because with the current setup it is not possible to operate within the flammability limits. To temporary remedy this in the present experiments, the secondary axial air flow was added. Nevertheless, something to be considered in future designs is better optimisation of the swirl and nozzle geometry. The second issue is the thermal deformation of the confinement, especially of the base plate where the Coanda flame is attached. As the temperature of the base plate increased, the plate curved outwards, this changed the $\Delta X/D$ of the plate with respect to the nozzle outlet. If the height of confinement was not adjusted so that the $\Delta X/D$ remained $\sim$ 0, the Coanda flame changed to a lifted flame and rapidly heated the top part of the confinement. Future designs need to take this into consideration. This could be avoided by having the nozzle and the base plate as a single piece, instead of the modular approach taken in this experiment. Another possibility would be to use a ceramic material with low expansion coefficient for the base plate. However, the added risk of the ceramic breaking would be needed to be considered.

5.3 CHAPTER SUMMARY

The flame stability under two flow patterns, Open Jet Flow and Coanda Jet Flow, was investigated using a swirl burner. The swirl burner was fitted with a flat plate and the distance between the plate and the tip of the nozzle was changed to induce one of the two flow patterns. General flame flow patterns were identified. Some flow patterns already reported in the literature were observed. For the Coanda flow pattern, newly and

yet to be reported flame behaviours were identified. The two thresholds observed for the Coanda flame suggest two factors that influence the onset and breakdown of the Coanda effect: (1) the velocity of the gases at the nozzle exit and (2) the combustion stability, specifically the flashback point, where the Coanda flow breaks down and transitions into a lifted flame close to flashback.

The flame stability of the swirl burner without confinement was mapped by changing the burner geometry. Two tangential swirl generators (Sg = 0.85 and 1.47), three nozzle diameters (D = 19.5, 24.0 and 28.0 mm) and three nozzle angles (α = 30°, 45° and 60°) were used. With the tangential swirl generator of Sg = 0.85, it was not possible to obtain a Coanda flame. The same was true for nozzle angles of $\alpha = 30°$ and $\alpha = 60°$. It is speculated that the reason for this is that the applied geometrical swirl of Sg = 0.85 is not enough for the flow to transition to a Coanda pattern. Further experiments are required to determine the reason for the impossibility of having a Coanda flow with nozzle angles of $\alpha = 30°$ and $\alpha = 60°$. For the nozzle diameter trials, it was found that by reducing the nozzle diameter the propensity of Coanda flashback increases as well as the Coanda flame stability. On the other hand, increasing the nozzle diameter leads to a less stable but more spread flame. Thus, there is a compromise between using a smaller diameter nozzle to obtain a Coanda flame that is hotter and smaller in diameter but more stable and using a larger diameter nozzle to obtain a Coanda flame that is bigger in diameter and cooler but less stable.

Combustion experiments were carried out by fitting the swirl burner with a tangential swirl generator with Sg = 1.47, nozzle diameter of $D = 28.0$, and nozzle angle of $\alpha = 45°$. A secondary air inlet for axial injection was added to the burner. The confinement was fixed at a position of $\Delta X/D = 0.00$ with respect to the burner nozzle exit. Equivalence ratio was ~ 1.00 with a total mass flow rate of ~ 1.62 g/s. After two hours of operation thermal equilibrium with the surroundings was reached. At this point, it was found that the temperature distribution along the top surface of the confinement was not homogeneous. Plotting the temperature distribution from the centre and moving outwards radially, it was found that the temperature follows a parabolic behaviour with a maximum temperature of $\sim 225°$C in the centre of the plate and a minimum temperature $\sim 150°$C near the edges. Some complications occurred during the operation of the confined burner, these were mainly related to the thermal deformation of the confinement and the stability of the Coanda flame. As the confinement thermally deformed, the $\Delta X/D$ of the plate with respect to the nozzle outlet changed. If the $\Delta X/D$ was not maintained at ~ 0, the Coanda flame transitioned into a lifted flame. Future experimental devices need to take this into account.

CFD SIMULATION MODELS VALIDATION

This chapter covers the results of CFD simulations of the swirl burner using the same geometries and operating conditions of the isothermal experiments and combustion experiments from the previous chapters. The first objective of the simulations is to validate the used turbulence, combustion, and radiation models by comparing the CFD results with parameters measured during the experiments. The second objective is to obtain additional information regarding the behaviour of the isothermal and reacting flow to be able to identify areas of opportunity on which the current burner can be improved. The models and the identified areas of opportunity will serve as the basis for the work presented in Chapter 7.

This chapter is structured as follows, the first section, Section 6.1, presents an isothermal simulation where the result is compared to the experiments conducted in Chapter 4 with the aim to validate the chosen turbulence model and simulation strategy. Section 6.2 presents a comparison between confined and unconfined reacting flow simulations, its validation with the experimental results shown in Chapter 5, and an identification of areas of opportunity upon which the current burner design can be improved.

6.1 ISOTHERMAL SIMULATIONS

6.1.1 *Simulation strategy*

The strategy for the simulations outlined in this section is shown in Figure 6.1. The numbers in between parenthesis (#) in the following paragraphs correspond to the ones used in Figure 6.1.

The first study of this section focused on simplifying the full 3D geometry of the burner into an axisymmetric 2D model in order to reduce the computational resources and simulation time required [169]. It should be noted that for all the geometries discussed below, three grids with an increasing number of elements were created and the GCI proposed by Roache [161] was used to calculate the discretisation error and ensure that the solution is grid-independent. The general procedure used to achieve this was to conduct a (1) 3D simulation on the whole burner geometry (Figure 6.2a). The flow condition just after the geometrical swirl generator was then extracted from the simulation. Afterwards, a (2) Simplified 3D geometry that started just downstream the swirl generator was created (Figure 6.2b). In other words, this new geometry had the geometrical swirl generator removed; thus, its inlet started at the annulus of the nozzle. Two different simulations were conducted on this geometry. The first one (2.1) with an equivalent swirl applied as a boundary condition and the second one (2.2) with the
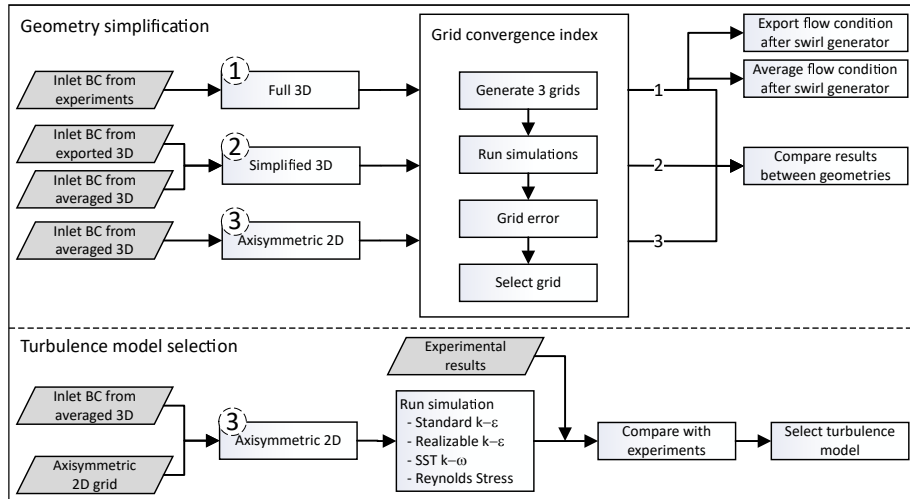
Figure 6.1: Isothermal simulation strategy.

imported velocity boundary condition obtained from (1). Similarly, an (3) Axisymmetric 2D geometry was created (Figure 6.2b). The simulation in this geometry was ran applying the equivalent swirl from (1) as a boundary condition. Finally, the simulation results from (1), (2) and (3) were compared in order to ensure that the simplified geometries behave like the full 3D geometry.

The next part of this section deals with choosing an appropriate turbulence model that accurately solves the studied flow. Flows of this type (i.e. wall attached Coanda flows) might present hysteresis as evidenced by the literature review in Chapter 2 and by the results discussed in Chapter 4. This behaviour adds an additional challenge for the CFD simulations: how to make the numerical model transition between the two states? Experimental results by Singh and Ramamurthi [94] suggest that a change in the flow pattern can be induced by increasing/decreasing the swirl applied to the flow. The same behaviour was observed by Vanierschot and Van den Bulck experimentally [88] and numerically [89]. This approach was taken in the present work. Therefore, the swirl applied to the Axisymmetric 2D geometry was gradually increased and decreased in order to produce a change from an OJF to a CoJF and vice versa. Furthermore, several turbulence models were tested: Standard $\kappa - \epsilon$, Realizable $\kappa - \epsilon$, SST $\kappa - \omega$ and RSM (refer to Table 3.1 for details on each model). The results from the various turbulence models were then compared to the experimental results from Chapter 4 to choose the one that best describes the studied flow.

6.1.2   *Grid generation*

Three grids with an increasing number of elements were created for each of the geometries studied in this section. A summary of the details of each grid is provided in Table 6.1. Due to the complexity of the geometry of the Full 3D case the grid was a polyhedral style grid. For the cases Simplified 3D and Axisymmetric 2D the grid was a full hexahedral and

(a) Full 3D geometry

(b) Simplified 3D/Axisymmetric 2D geometry
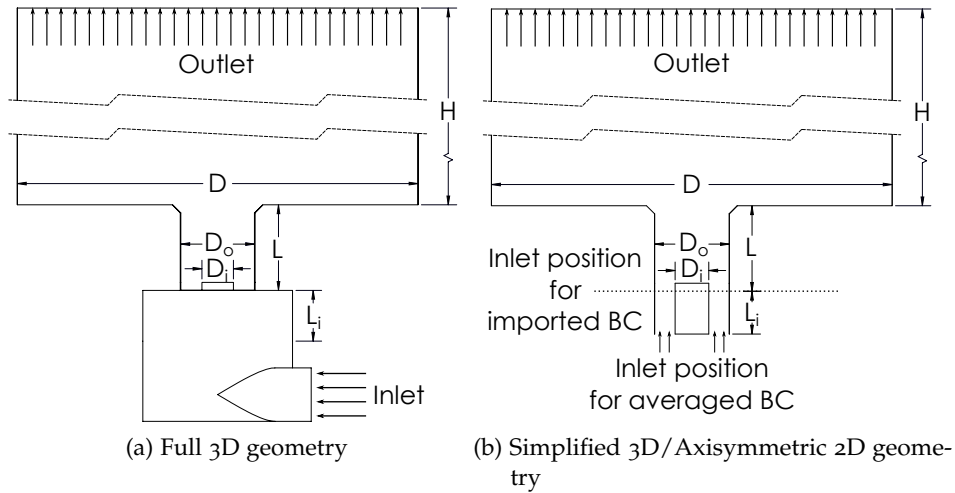
Figure 6.2: Computational domain for isothermal simulations. $H = 240$ mm, $D = 150$ mm, $D_0 = 28$ mm, $D_i = 12.8$ mm, $L = 32$ mm, $L_i = 19$ mm.

(a) Walls

(b) Cross section plane inside the flow domain
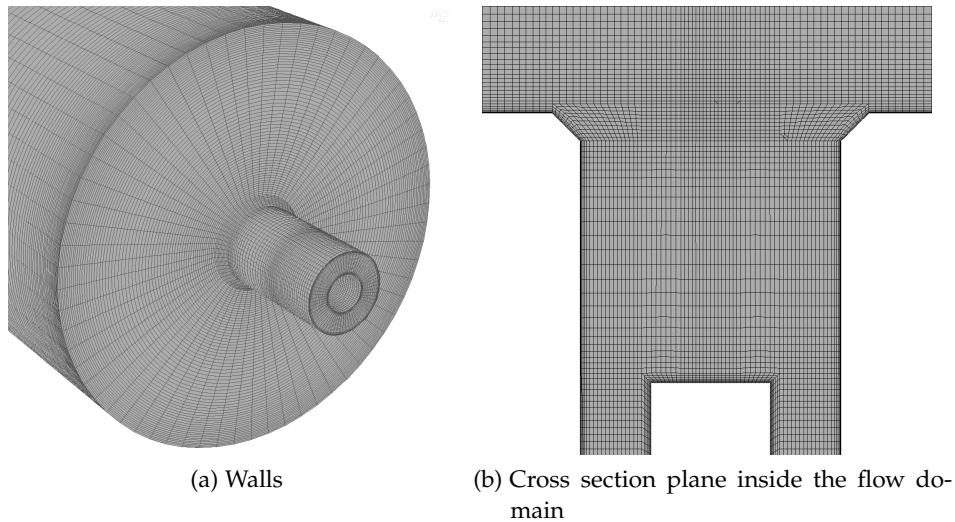
Figure 6.3: The numerical grid.

tetrahedral grid, respectively. In all cases, an inflation layer was created at the walls of the burner in order to be able to resolve the boundary layer using the Enhanced Wall Treatment option available in Ansys Fluent [170]. The grid refinement ratio r was kept greater than 1.1 so that the change in discretisation error calculated by the GCI method was greater than any noise in the solution [161]. Quality parameters for all grids were within acceptable values [171], i.e. greater than 0.20 for minimum orthogonal quality and an aspect ratio of less than 200. It should be noted that the value of the aspect ratio in Table 6.1 is at the boundary layer where large aspect ratios are acceptable as there are no strong transverse gradients. The value of the aspect ratio in regions away from the wall is much smaller. Figure 6.3 shows different views of the Simplified 3D grid.

Table 6.1: Grid sizes and quality parameters.

Geometry	Full 3D	Simplified 3D	Axisymmetric 2D
Grid size			
Grid 1 (fine)	$1,005,451$	$2,153,376$	$450,514$
Grid 2 (medium)	$662,065$	$1,233,200$	$222,719$
Grid 3 (coarse)	$443,889$	$706,112$	$109,697$
Refinement ratio			
r_{12}	1.15	1.20	1.42
r_{23}	1.15	1.20	1.42
Quality parameters			
Minimum orthogonal quality			
Grid 1 (fine)	0.32	0.40	0.70
Grid 2 (medium)	0.32	0.37	0.70
Grid 3 (coarse)	0.30	0.32	0.70
Maximum aspect ratio			
Grid 1 (fine)	41	215	174
Grid 2 (medium)	26	216	113
Grid 3 (coarse)	25	230	73

Table 6.2: Boundary conditions for geometry simplification.

Geometry	Inlet location	Velocity (m/s)	Axial (m/s)	Tangential (m/s)	Volume flow rate (m3/hr)
Full 3D	Burner inlet	5.31	normal to boundary		6
Simplified 3D	Annulus	Imported from Full 3D result			6
Simplified 3D	Annulus	-	3.42	4.11	6
Axisymmetric 2D	Annulus	-	3.42	4.11	6

Table 6.3: Axial and tangential inlet velocity boundary conditions at annulus and the corresponding swirl number.

Swirl number	0.10	0.20	0.30	0.40	0.50	0.60	0.70	0.80	0.90	1.00
Axial velocity (m/s)	3.42	3.42	3.42	3.42	3.42	3.42	3.42	3.42	3.42	3.42
Tangential velocity (m/s)	0.46	0.91	1.37	1.82	2.28	2.74	3.19	3.65	4.11	4.56

6.1.3 Boundary conditions

The computational domain and boundaries mentioned in this subsection are shown in Figure 6.2. For the cases studied in Section 6.1.4 and Section 6.1.5, the inlet boundary condition for the Full 3D case was set as a velocity inlet of 5.31 m/s (this value corresponds to a volume flow rate of ~ 6 m^3/hr which is one of the experimental points in Chapter 4). For the simplified 3D case with imported boundary condition, the values obtained from the 3D simulation at the position shown in Figure 6.2 were used as the inlet boundary condition. For the simplified 3D case with the averaged boundary condition and the simplified 2D case, the swirl number at the position shown in Figure 6.2 was calculated giving a swirl number of 0.90. This swirl number was used as the inlet boundary condition at the nozzle annulus with an axial velocity of 3.42 m/s (a value which produces a volume flow rate of ~ 6 m^3/hr). A summary of the inlet boundary conditions for each case is shown in Table 6.2

For the cases studied in Section 6.1.6, the inlet swirl was increased and decreased in order to induce a change in the flow pattern. To achieve this, the axial velocity of 3.42 m/s was kept constant at the annulus while a tangential velocity was varied. Table 6.3 shows the axial and tangential velocity boundary conditions applied and the corresponding swirl number obtained at the inlet. For each simulation with increased/decreased swirl, the result of the previous simulation was used as an initial condition of the whole domain to determine the hysteresis behaviour and the transition point between flow patterns.

For all the cases in this section, the lateral surface of the confinement that follows the nozzle was set up as a wall with no-slip boundary condition. It should be noted that this is not exactly the experimental

setup mentioned in Chapter 4, the experimental setup was that of an unconfined flow. However, this was done to reduce the computational domain and avoid prohibitively lengthy simulations. Despite this, the simulation results were still comparable with the experimental results as no significant error should have been produced because the confinement was three times that of the nozzle diameter [172]. The outlet boundary condition was set at constant atmospheric pressure.

6.1.4 *Grid convergence*

For a numerical simulation to be valid, the solution needs to be grid-independent; that is, the solution must not change with a refinement in the grid size and the discretisation error must be acceptable. To this end, a solution is obtained for each of the geometries with the three grid densities listed in Table 6.1 and the boundary conditions mentioned in Table 6.2. The Realizable $\kappa - \varepsilon$ turbulence model is used for this test. The QUICK discretisation scheme is selected in order to achieve third-order accuracy [142, 148]. Simulations are conducted using the Unsteady Reynolds-averaged Navier-Stokes (URANS) modelling approach. The grid sensitivity study is based on the GCI method [161] described in Section 3.6.3. The compared mean values are: the minimum pressure, the maximum velocity magnitude, and the minimum axial velocity at the centreline of the burner; the minimum pressure and maximum velocity magnitude at the exit of the nozzle; and the swirl number at the annulus, the middle of the nozzle and the exit of the nozzle. The error values for these variables, GCI values between the grids, observed order of convergence and check for asymptotic range of each geometry are shown in Table 6.4. In all cases the observed order of convergence for the monitored variables was within expected values, this is ~ 2 for the polyhedral meshes and ~ 3 for the hexahedral/tetrahedral meshes [161]. As mentioned in Section 3.6, the observed order of convergence will be lower than the theoretical order of convergence due to boundary conditions, numerical models, and the grid. In all the grids the obtained solution appears to be within the asymptotic range as the values of GCI_{23} and $r^{p}GCI_{12}$ are close to each other. Both the observed order of convergence and the asymptotic range check provide certainty that the obtained GCI values for the grids are accurate. The finer grids for each geometry provided a GCI below 3.3%, 1.9% and 0.3% respectively for the Full 3D, Simplified 3D, and Axisymmetric 2D geometries. In contrast, the coarser grids provided a GCI below 4.1%, 3.0% and 0.7% respectively for the geometries. Taking into account the GCI values and the computational resources for each grid, the following grids were chosen for the remaining of simulations in this section: the medium Full 3D grid (662,065 elements), the coarse Simplified 3D grid (706,112 elements), and the coarse Axisymmetric 2D grid (109,697 elements).

Table 6.4: Grid Convergence Index.

(a) Full 3D geometry

Variable	Grid 3 Coarse	Grid 2 Medium	Grid 1 Fine	GCI 2-3	GCI 1-2	Order of convergence	Asymptotic range GCI_{23}	~	$r^p GCI_{12}$
Centreline Minimum Pressure (Pa)	-18.1396	-18.0725	-18.0179	1.67%	1.36%	1.84	1.44%	≈	1.55%
Centreline Maximum Velocity Magnitude (m/s)	1.37179	1.37246	1.37335	-0.22%	-0.30%	1.82	0.19%	≈	0.34%
Centreline Minimum Axial Velocity (m/s)	-1.36864	-1.37073	-1.37241	-0.65%	-0.52%	1.92	0.59%	≈	0.63%
Nozzle Maximum Pressure (Pa)	-1.55622	-1.56847	-1.57849	-3.60%	-2.93%	1.80	3.60%	≈	3.87%
Nozzle Maximum Velocity Magnitude (m/s)	7.76710	7.83921	7.89774	-4.10%	-3.30%	1.86	3.57%	≈	3.80%
Swirl Number at Annulus	0.864820	0.866790	0.868420	-1.11%	-0.91%	1.72	0.88%	≈	0.96%
Swirl Number at Middle of Nozzle	0.932627	0.931465	0.930510	0.59%	0.48%	1.77	0.48%	≈	0.53%
Swirl Number at Nozzle Outlet	0.653395	0.652112	0.651046	0.98%	0.81%	1.68	0.76%	≈	0.84%

(b) Simplified 3D geometry

Variable	Grid 3 Coarse	Grid 2 Medium	Grid 1 Fine	GCI 2-3	GCI 1-2	Order of convergence	Asymptotic range GCI_{23}	~	$r^p GCI_{12}$
Centreline Minimum Pressure (Pa)	-16.3893	-16.3587	-16.3411	0.32%	0.18%	2.98	0.32%	≈	0.31%
Centreline Maximum Velocity Magnitude (m/s)	1.27402	1.28109	1.28538	-1.06%	-0.64%	2.69	1.06%	≈	1.05%
Centreline Minimum Axial Velocity (m/s)	-1.27365	-1.28086	-1.28522	-1.08%	-0.65%	2.71	1.08%	≈	1.06%
Nozzle Maximum Pressure (Pa)	-1.36461	-1.37756	-1.38521	-1.70%	-1.00%	2.83	1.70%	≈	1.67%
Nozzle Maximum Velocity Magnitude (m/s)	6.99340	7.09251	7.15511	-3.00%	-1.88%	2.47	3.00%	≈	2.94%
Swirl Number at Annulus	0.904177	0.908562	0.911123	-0.85%	-0.49%	2.89	0.85%	≈	0.84%
Swirl Number at Middle of Nozzle	0.974899	0.976436	0.977422	-0.35%	-0.23%	2.39	0.35%	≈	0.35%
Swirl Number at Nozzle Outlet	0.675301	0.676087	0.676551	-0.21%	-0.12%	2.83	0.21%	≈	0.21%

(c) Axisymmetric 2D geometry

Variable	Grid 3 Coarse	Grid 2 Medium	Grid 1 Fine	GCI 2-3	GCI 1-2	Order of convergence	Asymptotic range GCI_{23}	~	$r^p GCI_{12}$
Centreline Minimum Pressure (Pa)	-16.2020	-16.2965	-16.3321	-0.44%	-0.17%	2.75	0.44%	≈	0.34%
Centreline Maximum Velocity Magnitude (m/s)	1.31005	1.29864	1.29449	0.63%	0.23%	2.84	0.63%	≈	0.47%
Centreline Minimum Axial Velocity (m/s)	-1.31033	-1.29863	-1.29448	0.62%	0.22%	2.92	0.62%	≈	0.45%
Nozzle Maximum Pressure (Pa)	-1.48780	-1.48123	-1.47866	0.36%	0.14%	2.64	0.36%	≈	0.29%
Nozzle Maximum Velocity Magnitude (m/s)	7.27368	7.28866	7.29424	-0.15%	-0.06%	2.78	0.15%	≈	0.12%
Swirl Number at Annulus	0.865709	0.866031	0.866150	-0.03%	-0.01%	2.80	0.03%	≈	0.02%
Swirl Number at Middle of Nozzle	0.932724	0.935024	0.935902	-0.19%	-0.07%	2.71	0.19%	≈	0.15%
Swirl Number at Nozzle Outlet	0.647262	0.647802	0.648016	-0.07%	-0.03%	2.60	0.07%	≈	0.06%
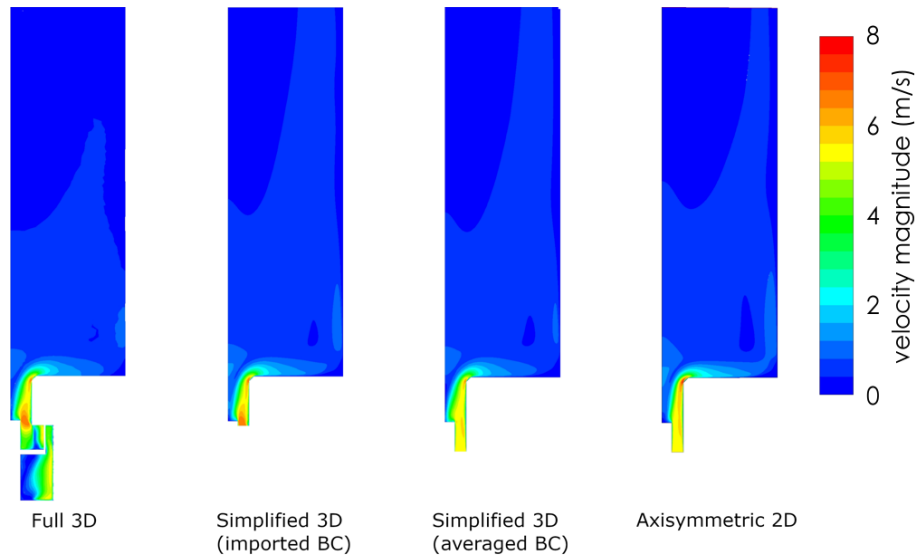
Figure 6.4: Contours of geometries tested. Only halve of the 3D contours is shown in order to allow for a better comparison with the axisymmetric 2D geometry.

6.1.5   *Geometry simplification*

Simulations on the Full 3D, Simplified 3D and Axisymmetric 2D geometries with the respective selected grid sizes were carried out with the Realizable $\kappa - \epsilon$ turbulence model in order to assess the differences in simulations results between each geometry. The boundary conditions are listed in Table 6.2. Contours for these simulations are shown in Figure 6.4 (only half of the geometry of each 3D contour is shown in order to allow for a better comparison with the axisymmetric grid). It can be seen that general flow patterns remain the same across the different geometries. However, a more detailed analysis shows some discrepancy between the cases. Figure 6.5 shows plots of axial velocity and pressure at the centreline of the computational domain for each geometry. Differences between the cases for the pressure and axial velocity profiles can be observed. The ones that stand out are in the Axisymmetric 2D case and the Simplified 3D case with imported BC showing a higher pressure and a lower axial velocity in comparison with the full 3D case. Some differences were expected given that the involved fluid dynamics are very complex and three-dimensional. However, despite the differences, this did not produce a significant discrepancy on the velocity profiles at the exit of the nozzle as is shown in Figure 6.6. All in all, the mesh simplification from 3D to 2D axisymmetric was considered as acceptable taking into account that the focus of the simplification was not on the accuracy of any individual model employed, but on the overall effectiveness of the simulation and the comparability between the studied cases that are presented in the following chapters.
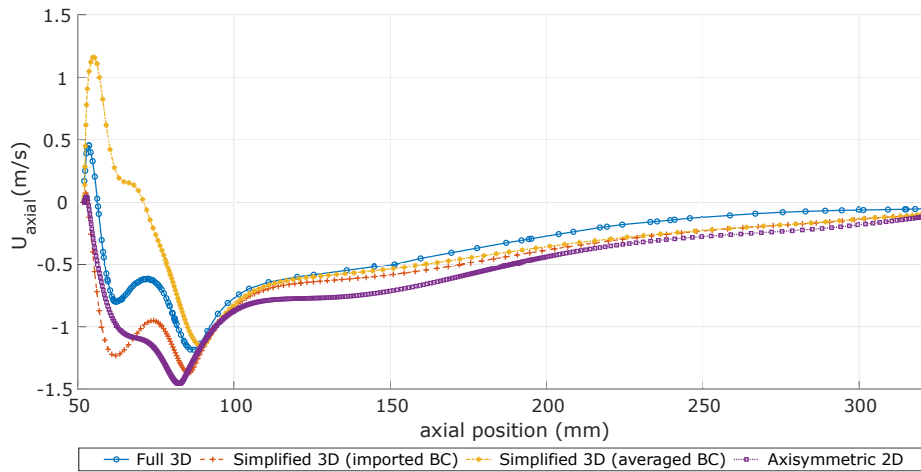
(a) Centreline axial velocity.
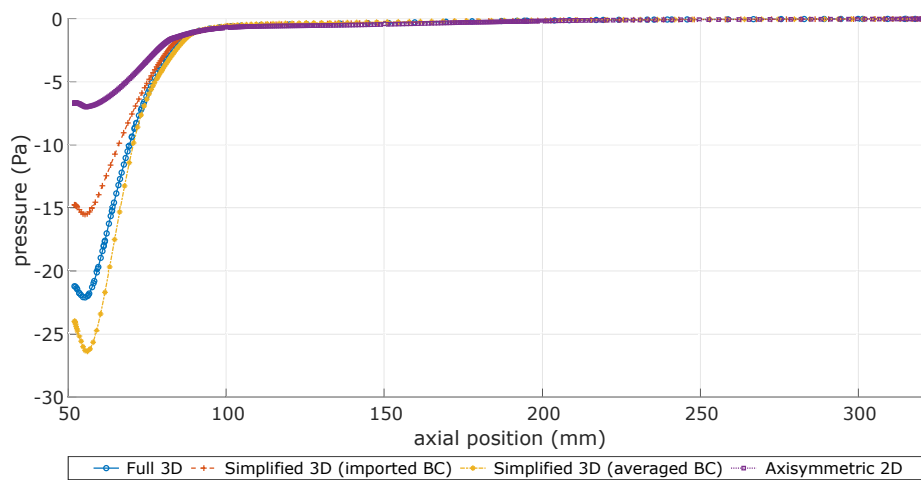
(b) Centreline pressure.

Figure 6.5: Centreline plots for the studied geometries.
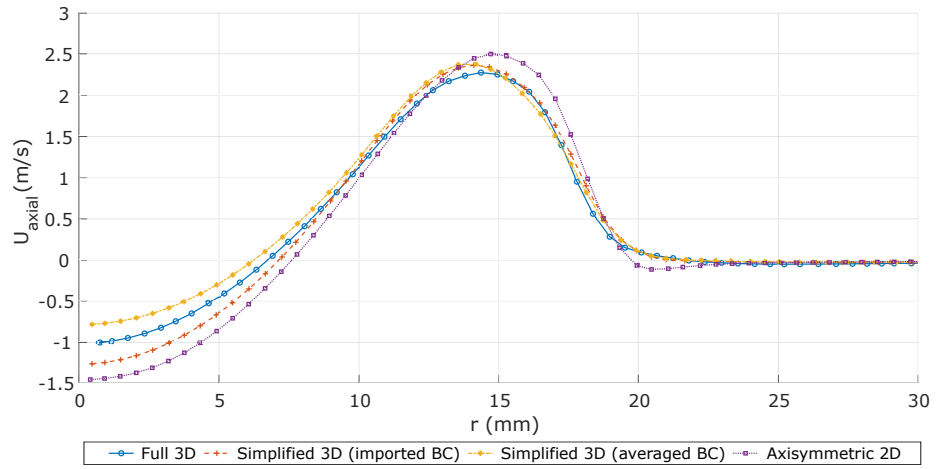
(a) Nozzle outlet axial velocity.
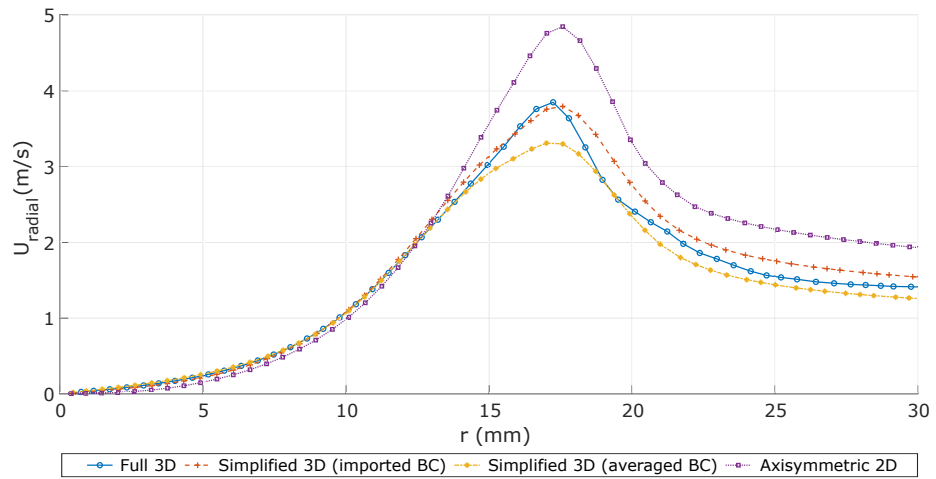
(b) Nozzle outlet radial velocity.
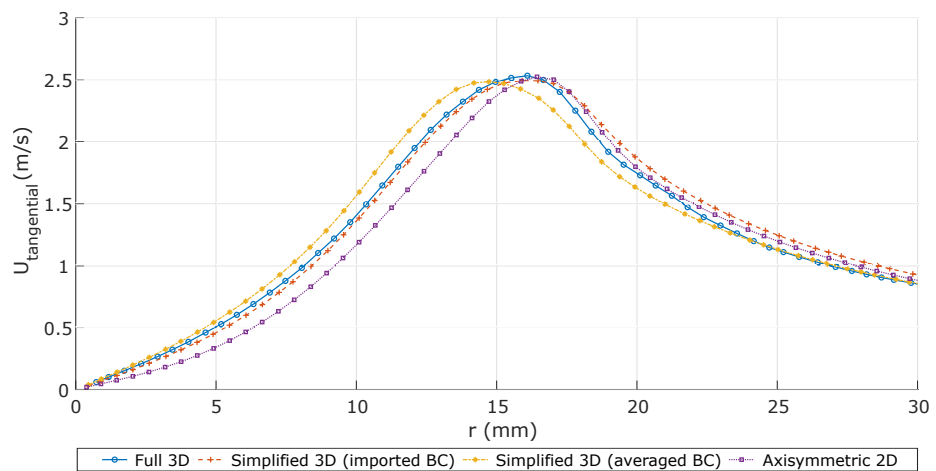
(c) Nozzle outlet tangential velocity.

Figure 6.6: Velocities at nozzle outlet for the studied geometries.

6.1.6 *Swirl variation*

Four turbulence models were tested in order to determine the one that best described the studied flow. The tested turbulence models were the Standard $\kappa - \epsilon$, Realizable $\kappa - \epsilon$, SST $\kappa - \omega$, and RSM. A brief description of the advantages and disadvantages of each model is given in Section 3.6.1. Boundary conditions were the same ones presented in Section 6.1.3. Swirl number at the inlet of the computational domain was increased and decreased with the values of Table 6.3 in order to induce a change from an OJF pattern to a CoJF pattern and vice-versa. For each simulation, the result of the previous simulation was used as an initial condition of the whole domain to determine the hysteresis behaviour and the transition point between flow patterns. Figure 6.7 to Figure 6.10 show the flow state with the applied swirl number at the inlet for each turbulence model studied. Red numbers in the figures denote the swirl number at the nozzle exit for that flow pattern and applied inlet swirl.

The Standard $\kappa - \epsilon$ turbulence model (Figure 6.7) produced three distinct flow patterns: a CJF characterised by an axial jet flow with no CRZ, an OJF characterised by an annular jet with a CRZ, and a CoJF characterised by the flat velocity profile. The transition between flow patterns was as follows. With zero swirl the flow started as a CJF. With an applied swirl of ~ 0.45, the flow transitioned into an OJF. From this state, with a further increase in the swirl to ~ 0.75 the flow transitioned into a CoJF where it remained with any increase in the swirl. From the CoJF state, a decrease in the swirl to ~ 0.55 made the flow transition back into an OJF. A further decrease in the inlet swirl to ~ 0.45 caused the flow to transition to the starting state of the CJF. Swirl numbers at the nozzle outlet for the hysteresis region range from $0.62 \rightarrow 0.66$ for the OJF and $0.68 \rightarrow 0.77$ for the CoJF.

The Realizable $\kappa - \epsilon$ turbulence model (Figure 6.8) behaved like the Standard $\kappa - \epsilon$ model. It produced the same three flow patterns: CJF, OJF, and CoJF. The transition from a CJF to an OJF occurred at an inlet swirl number of ~ 0.35. The transition from OJF to CoJF occurred at a swirl number of ~ 0.85. With swirl number higher than ~ 0.85 the flow remained as a CoJF. With a subsequent decrease in the swirl, the flow transitioned from a CoJF pattern to an OJF at a swirl number of ~ 0.45. Further decrease of the inlet swirl number made the flow transition back to a CJF at a swirl number of ~ 0.35. Swirl numbers at the nozzle outlet for the hysteresis region range from $0.53 \rightarrow 0.68$ for the OJF and $0.56 \rightarrow 0.80$ for the CoJF.

The SST $\kappa - \omega$ turbulence model (Figure 6.9) produced an additional flow pattern. This was an open jet with jets angled further away from the axial position. This pattern has been previously identified experimentally and in numerical simulations [89]. The two states of the OJF will be distinguished by the terminology OJF-LS and OJF-HS for the behaviours at low and high swirl, respectively. The flow transitioned from a CJF to an OJF-LS at an inlet swirl number of ~ 0.35. The transition from an OJF-LS to an OJF-HS occurred at an inlet swirl number of ~ 1.45. The

flow remained in this state until a very high inlet swirl of ~ 5.25 was applied and the flow transitioned to a CoJF. With swirl number higher than ~ 5.25 the flow remained as a CoJF. From a CoJF pattern, a decrease of the applied inlet swirl number leads to an OJF-HS state at a swirl number of ~ 1.45. Further decrease of the inlet swirl number leads to an OJF-LS at an applied swirl of ~ 1.35 and then to a CJF at a swirl number of ~ 0.35. Swirl numbers at the nozzle outlet for the hysteresis region range from $0.74 \to 1.06$ for the OJF and $1.12 \to 1.74$ for the CoJF.

The Reynolds Stress turbulence model (Figure 6.10) behaved like the SST $\kappa - \omega$ model producing the same flow patterns but with a lower applied inlet swirl. The transition from a CJF to an OJF-LS occurred at an inlet swirl number of ~ 0.55, the transition from OJF-LS to OJF-HS at a swirl number of ~ 1.45 and the transition from OJF-HS to CoJF at a swirl number of ~ 2.15. With swirl number higher than ~ 2.15 the flow remained as a CoJF. With a decrease in the swirl, the flow reverted to an OJF-HS with at a swirl number of ~ 1.65 and back to a CJF at a swirl number of ~ 0.45. Swirl numbers at the nozzle outlet for the hysteresis region range from $0.81 \to 0.90$ for the OJF and $0.92 \to 1.05$ for the CoJF.

6.1.7 *Simulation validation*

The most appropriate turbulence model to describe the flow studied in Chapter 4 was selected by comparing the experimental flow characteristics for the ~ 6 m^3/hr case with the results produced by the evaluated turbulence models. The turbulence model that best predicts the flow should produce swirl number values at the nozzle outlet close to the calculated experimental values of ~ 0.76 for the OJF and ~ 0.85 for the CoJF with the same inlet condition.

For the Standard $\kappa - \epsilon$ model, the highest inlet swirl number that allowed for the existence of both flow patterns (inlet swirl of ~ 0.70) produced swirl values at the nozzle outlet of ~ 0.66 and ~ 0.77 for the OJF and CoJF, respectively. Both values are below the calculated experimental values. A comparison of this turbulence model with experimental results for velocity components located 1 mm downstream the nozzle exit is shown in Figure 6.11a.

For the Realizable $\kappa - \epsilon$ model, the highest inlet swirl number that allowed for the existence of both flow patterns (inlet swirl of ~ 0.80) produced swirl values at the nozzle outlet of ~ 0.68 and ~ 0.80 for the OJF and CoJF, respectively. Similarly to the Standard $\kappa - \epsilon$, the values produced by the model under-predict the experimental results. This model is preferred to the Standard $\kappa - \epsilon$ as it has substantial improvements over the Standard $\kappa - \epsilon$ model in cases where the flow presents strong streamline curvature, vortices, flow separation and/or rotation. A comparison of this turbulence model with experimental results for velocity components located 1 mm downstream the nozzle exit is shown in Figure 6.11b.

For the SST $\kappa - \omega$ model, the swirl number that needs to be applied for a change to a CoJF pattern is particularly high at ~ 5.5 and the predicted swirl numbers at the nozzle outlet for the CoJF states are
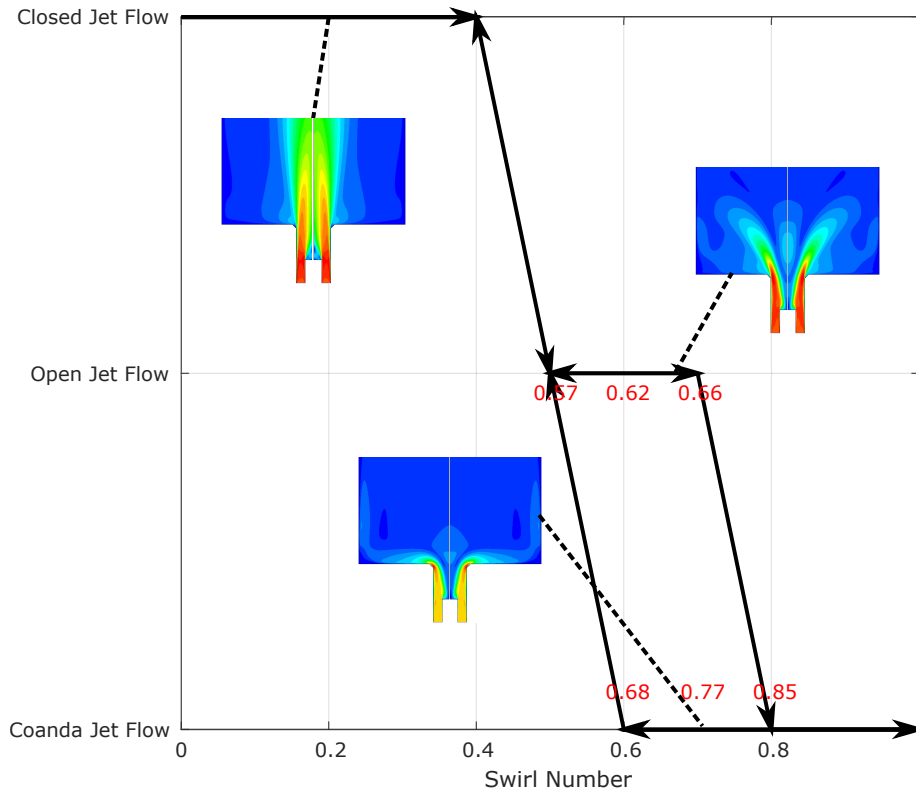
Figure 6.7: Swirl variation and flow pattern for Standard $\kappa - \epsilon$ turbulence model.
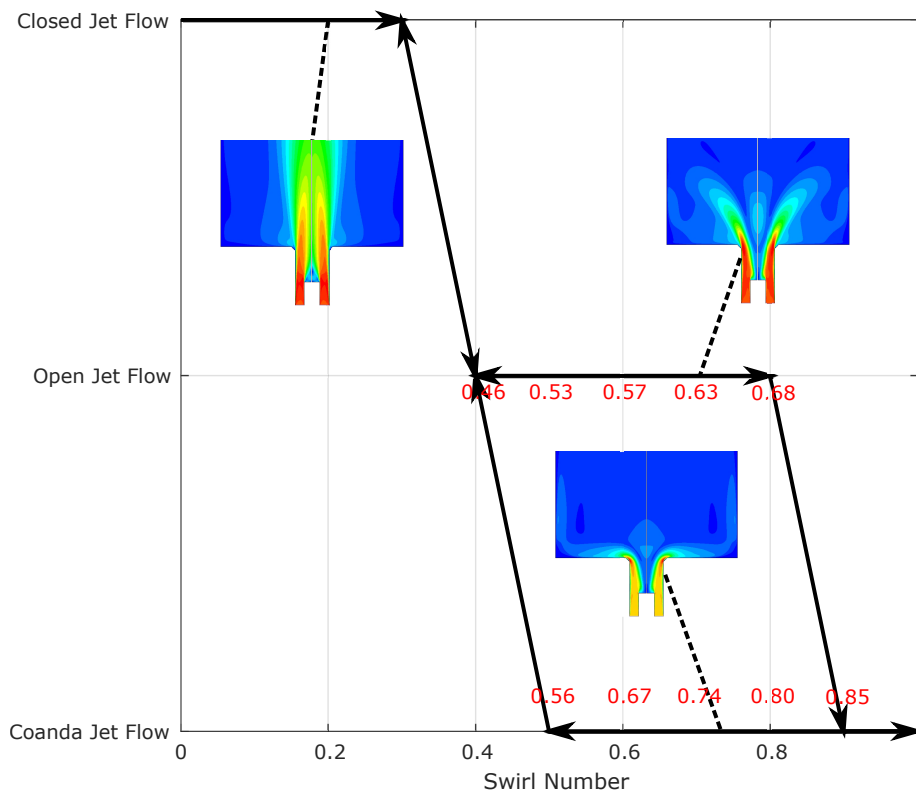
Figure 6.8: Swirl variation and flow pattern for Realizable $\kappa - \epsilon$ turbulence model.
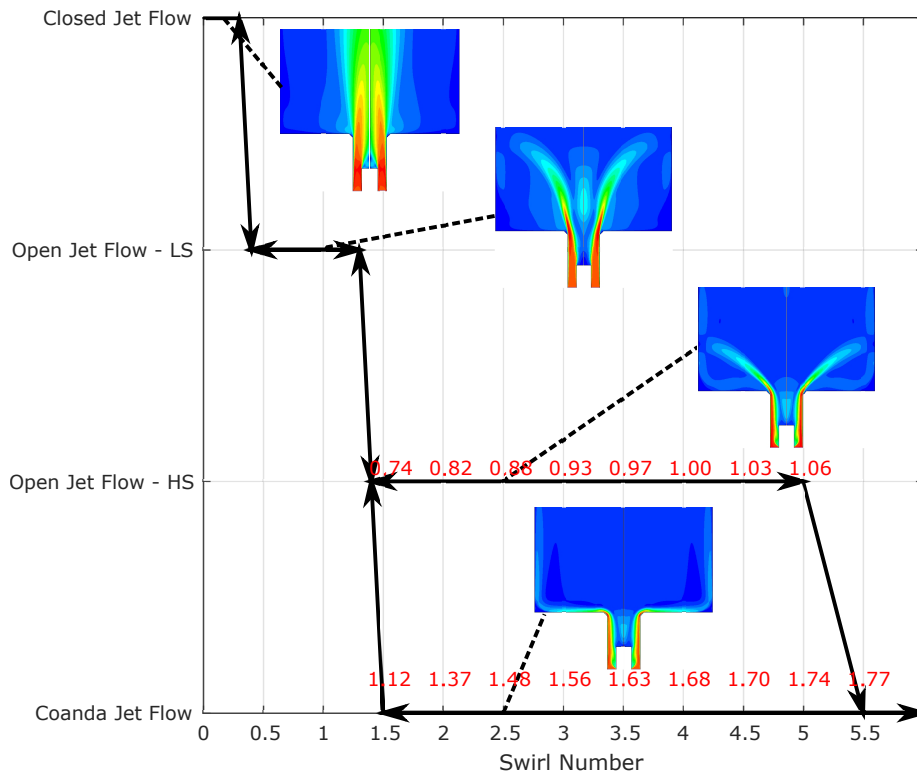
Figure 6.9: Swirl variation and flow pattern for SST $\kappa - \omega$ turbulence model.
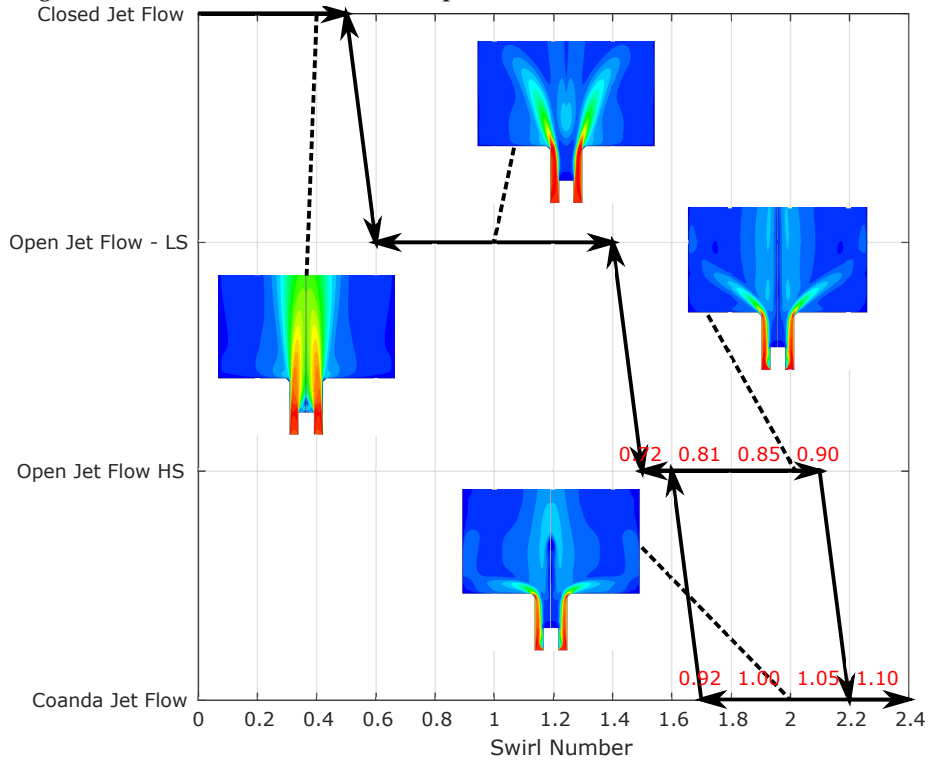
Figure 6.10: Swirl variation and flow pattern for Reynolds Stress turbulence model.

well above ~ 1.00. This behaviour could be explained by the known issues of the SST $\kappa - \omega$. Mainly that it can over-predict separation and is very sensitive to initial conditions [142]. Additionally, the overall flow pattern at the lowest possible swirl number that still presents hysteresis is considerably different from the one obtained in the experiments. A comparison of this turbulence model with experimental results for velocity components located 1 mm downstream the nozzle exit is shown in Figure 6.11c.

For the Reynolds Stress Model, the lowest inlet swirl number that allows for the existence of both flow patterns (inlet swirl of ~ 1.70) produced swirl values at the nozzle outlet of ~ 0.81 and ~ 0.92 for the OJF and CoJF, respectively. Additionally, the overall flow pattern at the lowest possible swirl number that still presents hysteresis is considerably different from the one obtained in the experiments. A comparison of this turbulence model with experimental results for velocity components located 1 mm downstream the nozzle exit is shown in Figure 6.11d.

From these results, it is concluded that the turbulence model that best described the behaviour of the studied flows was the Realizable $\kappa - \epsilon$ turbulence model. This model was chosen by taking into consideration the hysteresis plots (Figure 6.7 to Figure 6.10), the swirl number at the nozzle outlet, and the velocity component comparison between simulations and experiments (Figure 6.11a to Figure 6.11d). The Realizable $\kappa - \epsilon$ model was used for all subsequent CFD simulations in this thesis.

6.1.8 *General remarks*

The first objective of the previous simulations was to simplify the geometry from a 3D to a 2D axisymmetric. For this, three different geometries were studied: (1) Full 3D, (2) Simplified 3D, and (3) Axisymmetric 2D. A GCI was conducted on each geometry by generating three grids with an increased number of elements giving a GCI of, respectively, $< 3.3\%$, $< 1.9\%$ and $< 0.3\%$ for the finer grids of the geometries. The coarser grids provided a GCI of $< 4.1\%$, $< 3.0\%$ and $< 0.7\%$. Taking into consideration the GCI values, the medium Full 3D grid ($662,065$ elements), the coarse Simplified 3D grid ($706,112$ elements), and the coarse Axisymmetric 2D grid ($109,697$ elements) were chosen for the geometry comparison study. Three simulations were carried out using the chosen grids and the Realizable $\kappa - \epsilon$ turbulence model. The pressure and velocity components were compared between the geometries. The location of the compared values was chosen at the nozzle exit and centreline. The resulting values for each geometry yielded similar results between them. It was concluded that the simplification of the geometry from 3D to 2D axisymmetric was acceptable considering that the focus of the simulations was not on the accuracy of any individual model but on the overall effectiveness of the simulation and the comparability between the obtained results.

The second objective of the simulations was to make a comparison between turbulence models in order to choose the one that best matched the experimental results and accurately described the studied flow. The
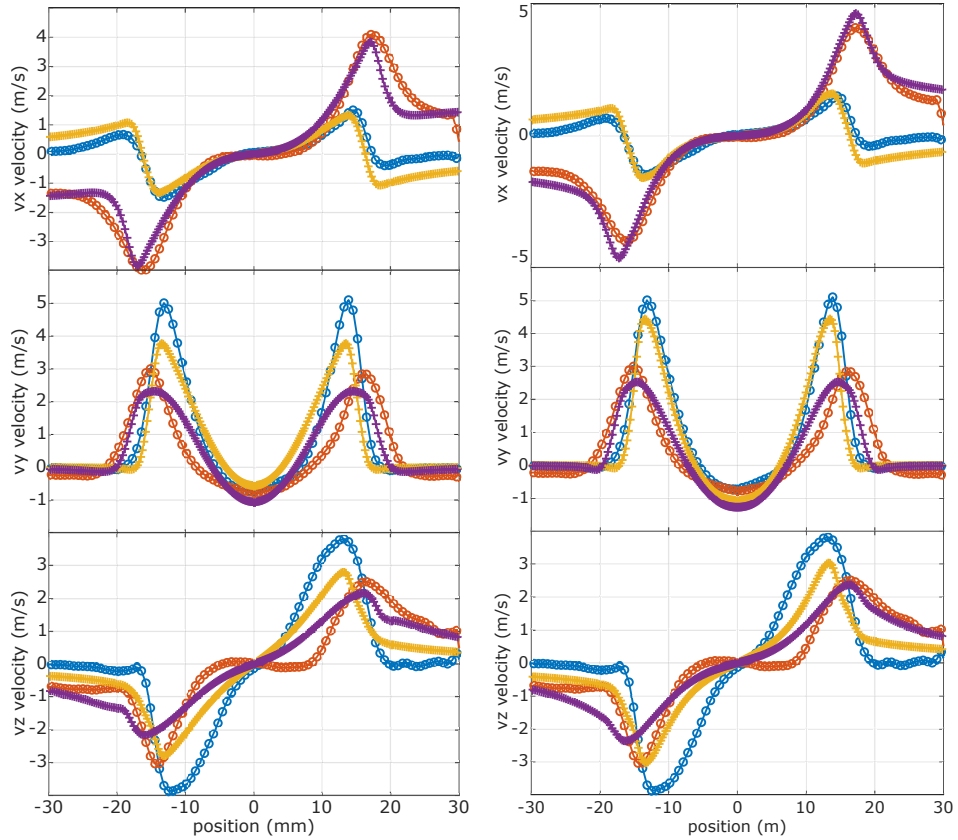
(a) Standard $\kappa - \epsilon$. Inlet swirl of ~ 0.70.

(b) Realizable $\kappa - \epsilon$. Inlet swirl of ~ 0.80.
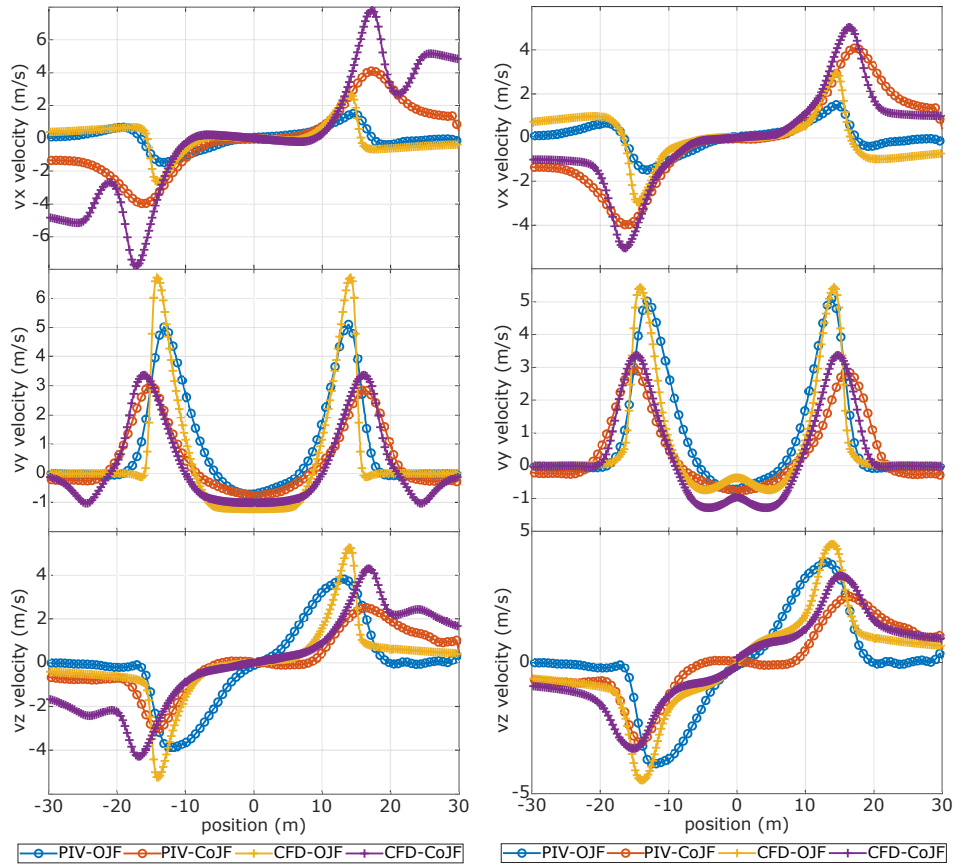
(c) SST $\kappa - \omega$. inlet swirl of ~ 1.50.

(d) RSM. Inlet swirl of ~ 1.70.

Figure 6.11: Comparison between CFD simulations and experimental data. Velocity components 1 mm downstream nozzle exit.

tested turbulence models were: Standard $\kappa - \epsilon$, Realizable $\kappa - \epsilon$, SST $\kappa - \omega$, and Reynolds Stress Model. In order to evaluate the hysteresis behaviour and transition points of the flow, the swirl boundary condition at the inlet was gradually increased for each turbulence model until a change in flow pattern was obtained. The swirl was gradually decreased after no additional change in flow pattern occurred. For each increase/decrease of the inlet swirl, the swirl number at the nozzle outlet was calculated and then compared to the experimental value. The velocity components at the nozzle outlet were also compared with experiments. The SST $\kappa - \omega$, and Reynolds Stress models greatly over predicted the transition points and the swirl number at the nozzle outlet. Additionally, the obtained overall flow pattern, at the swirl number relevant for comparison, did not match with the experimental value. The Standard $\kappa - \epsilon$ and Realizable $\kappa - \epsilon$ turbulence models produced similar transition points between them. The swirl number at the nozzle outlet and the overall flow pattern for these models were closer to the experimental results. Therefore, and considering that the Realizable $\kappa - \epsilon$ model has some advantages over the Standard $\kappa - \epsilon$ model when modelling swirling flows, the Realizable $\kappa - \epsilon$ model was selected for all subsequent CFD simulations made in this thesis.

6.2 COMBUSTION SIMULATION

6.2.1 *Simulation strategy*

The strategy for the simulations outlined in this section is shown in Figure 6.12. The numbers in between parenthesis (#) along the next paragraphs correspond to the ones used in Figure 6.12.

The first study of this section focused on the comparison between the PIV measurements of Section 5.1.5 and the 2D CFD simulations. The purpose of this is to serve as a first validation for the reacting flow simulations. The grid from the previous section, (1) Axisymmetric 2D grid (109,697 elements), is used for the comparison with some modifications. Inlet conditions for the simulation were the same as the ones used in the unconfined experiments. Parameters compared were the axial and radial velocity.

The next part of this section deals with the comparison of the confined combustion experiments with the confined CFD simulations. The purpose of this is to serve as a second validation for the reacting flow simulations to ensure that the reaction models that were used represent the experiments with a certain degree of accuracy. An additional aim is to, similarly to the approach taken for the isothermal simulations, find an Axisymmetric 2D geometry that can be comparable to the experimental values. The general procedure followed was to first conduct a (2) simplified 3D simulation with an inlet swirl boundary condition and flow rates equal to the ones used in the experiments. Similarly, an (3) Axisymmetric 2D geometry was created with a volume that matched the experimental confinement. A diagram of the computational domain is shown in Figure 6.13. It should be obvious that the Axisymmetric 2D
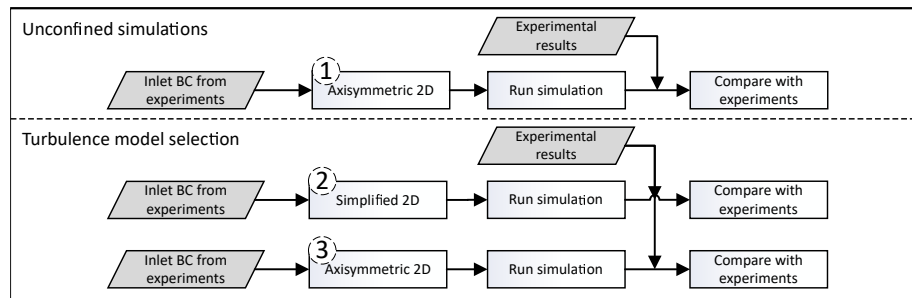
Figure 6.12: Combustion simulation strategy.
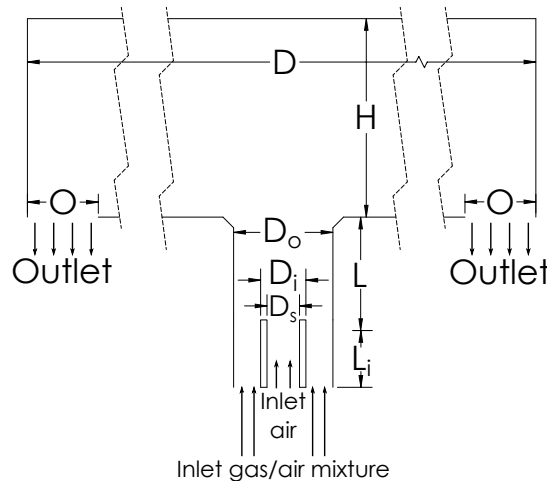
Figure 6.13: Computational domain for combustion simulations. Dimensions for the simplified 3D geometry: $H = 56$ mm, $D = 488$ mm, $D_0 = 28$ mm, $D_i = 12.8$ mm, $D_s = 9.2$ mm, $O = 20$ mm, $L = 32$ mm, $L_i = 19$ mm. Dimensions for the axisymmetric 2D geometry: $H = 56$ mm, $D = 550$ mm, $D_0 = 28$ mm, $D_i = 12.8$ mm, $D_s = 9.2$ mm, $O = 19$ mm, $L = 32$ mm, $L_i = 19$ mm.

geometry does not directly represent the experimental confinement (the experimental confinement is a cuboid and the Axisymmetric 2D is a cylinder). However, the aim was to use the 2D geometry for the parametric analysis that was conducted in Section 7.1, as it greatly reduced the computational time needed. To validate the simulation, the wall temperatures and outlet flue gas temperature were compared between the simulation results from (2), (3) and the experimental data.

6.2.2 *Grid generation*

The grids generated for the isothermal simulations (Section 6.1) were used as a basis to generate the grids shown in this section. No grid sensitivity analysis was deemed necessary as it has been previously shown that the solutions provided by the isothermal grids are grid-independent and the main flow and chemistry phenomena take place in the region encompassed by what was the isothermal geometry. Following, a brief explanation of what was done in each of the three generated grids is given.

(a) Walls

(b) Cross section plane inside the flow domain
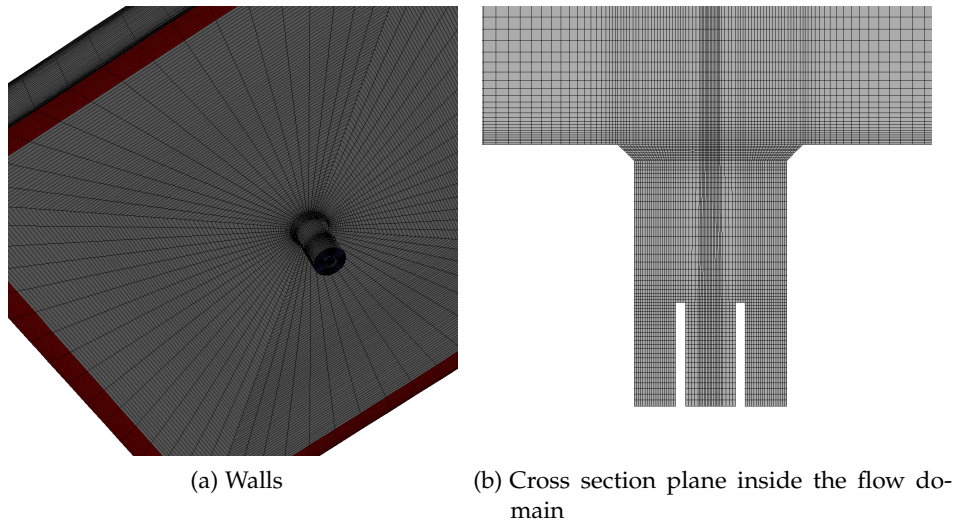
Figure 6.14: The numerical grid.

Unconfined Axisymmetric 2D: the coarse Axisymmetric 2D grid of the isothermal simulations served as a basis. The flow domain downstream of the nozzle was extended in order to allow for re-circulation of the surrounding air.

Confined 3D: the coarse Simplified 3D grid of the isothermal simulations served as a basis. The grid within the region inside the burner body remained the same. On the region downstream of the nozzle, the overall grid remained the same up to a radial distance of 2.5 nozzle diameters. Then, the grid coarsened between a radial distance of 2.5 nozzle diameters and the middle of the confinement. After the middle of the confinement length, the grid was gradually refined to be able to successfully resolve the flow behaviour at the outlet.

Confined Axisymmetric 2D: the coarse Axisymmetric 2D grid of the isothermal simulations served as a basis. The modifications were the same as the ones made for the Confined 3D grid.

Figure 6.14 shows views of the confined 3D grid.

6.2.3 *Boundary conditions*

The computational domain and boundaries mentioned in this subsection are shown in Figure 6.13. For all the simulations in this section the Realizable $\kappa - \epsilon$ was used for turbulence modelling, the Finite-Rate/Eddy-Dissipation was used for combustion modelling, and P-1 for radiation modelling.

For the unconfined cases, the inlet boundary condition was defined as a mass flow inlet with a flow rate of 0.7005 g/s with mass fractions of $CH_4 = 0.1261$, $O_2 = 0.2036$, and $N_2 = 0.6703$ which gave an effective equivalence ratio of 2.47. Inlet velocity components were 0.3511 axial and 0.9363 tangential which gave an effective swirl number of 2.00 at the inlet. All reactants entered the computational domain at 300 K. These are the same conditions used in the PIV combustion experiments from

Table 6.5: Boundary conditions for the unconfined combustion simulation.

Parameter	Value
Mass flow (g/s)	0.7005
CH4 mass fraction	0.1261
O2 mass fraction	0.2036
N2 mass fraction	0.6703
Equivalence ratio	2.47
Axial velocity component	0.3511
Tangential velocity component	0.9363
Inlet swirl	2.00

Section 5.1.5. The outlet pressure boundary condition was set at constant atmospheric pressure. A summary of the inlet boundary conditions for each case is shown in Table 6.5.

For the confined cases, the primary inlet was defined as a mass flow inlet with a flow rate of 0.9047 g/s and mass fractions of $CH_4 = 0.09751$, $O_2 = 0.2103$, and $N_2 = 0.6922$. The inlet velocity components were 0.3511 axial and 0.9363 tangential which gave an effective swirl number of 2.00 at the inlet. The secondary inlet was defined as a mass flow inlet with a flow rate of 0.6125 g/s. The mass fractions were those of pure air, i.e. mass fractions of $O_2 = 0.2300$ and $N_2 = 0.7700$. The flow entered the domain in a direction normal to the boundary. The mixture of both inlets gave an effective equivalence ratio of 1.06. All reactants entered the computational domain at 300 K. The outlet pressure boundary condition was set at constant atmospheric pressure. The wall of the confinement was defined as a thin wall with a thickness of 0.006 m, an external emissivity of 0.95 and an internal emissivity of 0.95. The temperature of the fluid and the temperature of the radiation heat-sink surrounding the computational domain were set at 293 K. The convective heat transfer coefficient was initially estimated using the methodology described in Section 3.6.1, but later set at 30 W/m²-K in order to better match the experimental results and simulation results. The need to increase the heat transfer coefficient was expected because the methodology in Section 3.6.1 is for the case of natural convection and the experimental setup had an extraction hood in place which would have increased the external air circulation. The walls of the burner were considered adiabatic. A summary of the inlet boundary conditions for each case is shown in Table 6.6.

6.2.4 *Simulation validation*

A comparison between the CFD simulations and the experimental data can be seen in Figure 6.15. Figure 6.15a shows a good agreement between experiments and simulations for the axial and radial velocities at the nozzle outlet. Figure 6.15b shows a temperature plot along the

Table 6.6: Boundary conditions for the confined combustion simulation.

Parameter	Primary inlet	Secondary inlet	Total
Mass flow (g/s)	0.9047	0.6125	1.5172
CH4 mass fraction	0.09751	-	0.05518
O2 mass fraction	0.2103	0.2300	0.2202
N2 mass fraction	0.6922	0.7700	0.7247
Equivalence ratio	1.85	-	1.06
Axial velocity component	0.3511	1.0000	-
Tangential velocity component	0.9363	0.0000	-
Inlet swirl	2.00	0.00	-

Parameter	Wall boundary
Heat transfer coefficient (W/m²-K)	30
Free stream temperature (K)	293
External emissivity	0.95
External radiation temperature (K)	293
Internal emissivity	0.95
Wall thickness (m)	0.006

horizontal centre line of the confinement plate opposite to the nozzle. It should be noted that the experimental result shows a homogeneous parabolic profile for the temperature, whereas the CFD simulations show an over-prediction at the middle section and an under-prediction at the outermost part of the plate. These over- and under-prediction can be attributed to the use of a homogeneous value for the natural convective heat transfer coefficient on the surface of the plate (i.e. the natural convective flow is the same at any given point of the plate). The real behaviour of a natural convective air flow has a local heat transfer coefficient for each section of the plate because of boundary layer separation [158]. Despite this discrepancy, the overall result shows a good agreement between the experiments and the simulations. This should suffice for the purpose of the remaining simulations in this thesis; which is, the optimisation of the flat flame burner and its comparison with a radiant tube (see Chapter 7).

6.2.5 *Observations*

Results of velocity magnitude, temperature and reaction rate for the confined CFD simulation are shown in Figure 6.16. Some opportunities for improvement were evident with the CFD/experimental confined geometry. These were mainly related to the secondary axial air injection system. The axial injection of secondary air cools the central part of the
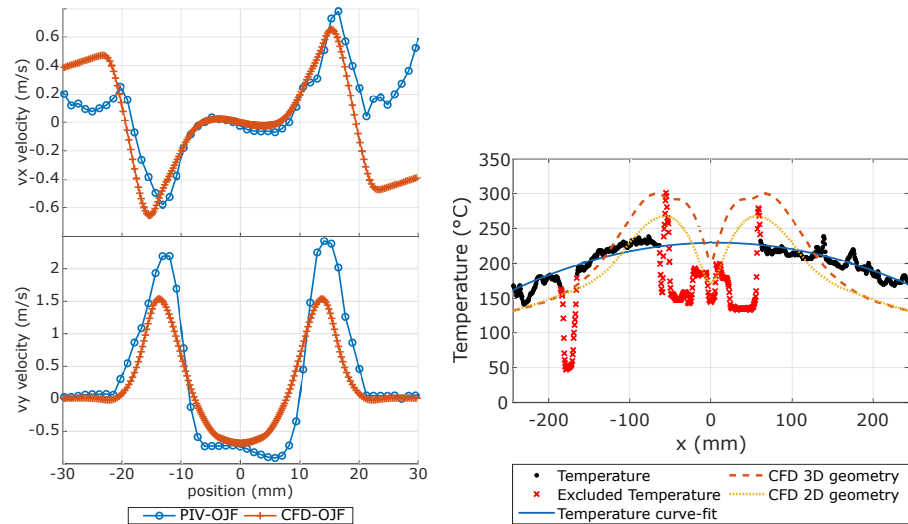
(a) Unconfined PIV experimental data and CFD simulations. Velocity components 3 mm downstream nozzle exit.

(b) Confined thermal experimental data and CFD simulations. Temperature plot along horizontal centre line.

Figure 6.15: Comparison between CFD simulations and experimental data.

plate, observe Figure 6.15b and Figure 6.16b. Also, the axial air injection concentrates the reaction at the centre of the geometry Figure 6.16c. It would have been preferable for the flame to be spread radially. Variations in geometry were studied in Section 7.1 to attempt to improve these observations.

6.2.6 *General remarks*

The purpose of the previous CFD simulations was to evaluate the accuracy of the chosen approach and the selected turbulence models by comparing them with the experimental results from Chapter 5. For these, two grids were created, a 3D grid and a 2D Axisymmetric, taking as a basis the grids tested for the isothermal simulations. It was found that the chosen models (Realizable $\kappa - \epsilon$ for turbulence, Finite-Rate/Eddy-Dissipation for combustion, and P-1 for radiation modelling) and the applied boundary conditions approximate the experiments with a good degree of accuracy. Furthermore, opportunities for improved burner design were identified. The main opportunity is related to the central axial air injection. This has two downsides; it cools down the central part of the plate and concentrates the reaction in the central region of the plate. These will be addressed in the parametric analysis presented in the next chapter.

6.3 CHAPTER SUMMARY

CFD simulations were conducted to replicate the isothermal and combustion experiments presented in the previous chapters. First, isothermal 3D simulations of the full geometry were carried out using the Realizable $\kappa - \epsilon$ turbulence model. Then, in order to reduce computation time, the
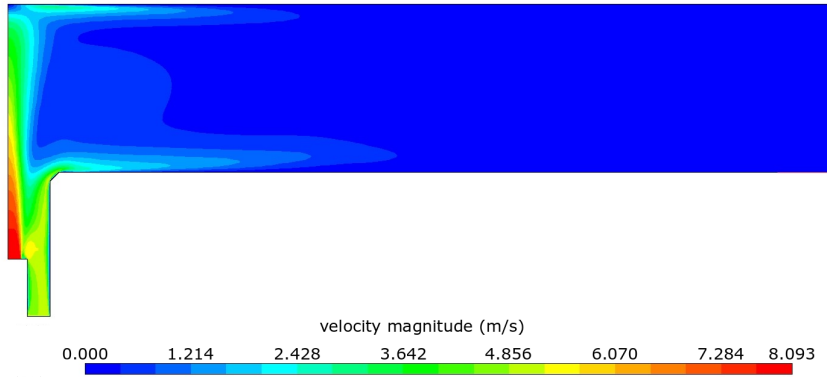
(a) Velocity magnitude contours.
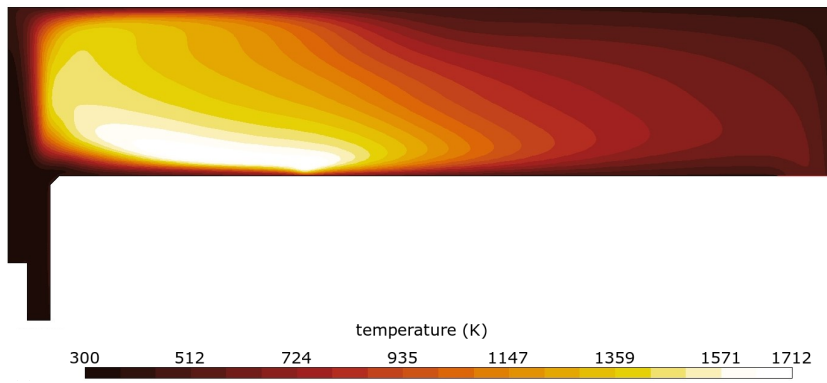
(b) Temperature contours.
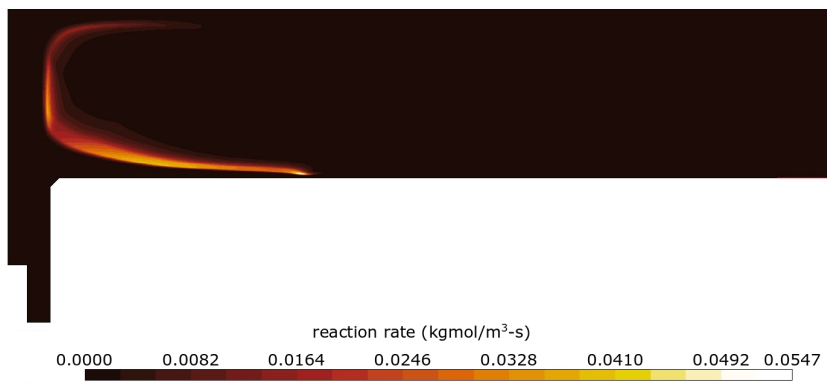
(c) Reaction rate contours.

Figure 6.16: Confined combustion simulation contours.

geometry was simplified to a 3D geometry that had the swirl generator removed (i.e. the inlet started just downstream the geometrical swirl generator). Subsequently, the dimension of the simulation was reduced to a 2D axisymmetric simulation. A GCI study was made on each of the three geometries in order to ensure the solutions obtained were grid-independent. The results of the geometries were compared between them. It was found that the simplification of the geometry from 3D to 2D axisymmetric was acceptable and did not induce a considerable error since, in the present work, the end goal of the CFD simulations is to be a tool with which the current burner design can be improved upon (see Chapter 7). In other words, the focus of the simulations was not on the accuracy of any individual model but on the overall effectiveness of the simulation and the comparability between the obtained results.

The validation of the turbulence model was made by testing different turbulence models using the 2D axisymmetric geometry and comparing the results with the experimental results from Chapter 4. The tested turbulence models were: Standard $\kappa - \epsilon$, Realizable $\kappa - \epsilon$, SST $\kappa - \omega$, and RSM. For each model, the inlet swirl was varied in order to evaluate the hysteresis behaviour and transition points of the flow. The swirl was first increased until a change in flow pattern was obtained, once this occurred the swirl was then gradually decreased. The swirl number at the nozzle outlet was calculated and compared to the PIV experiments. It was found that the overall flow pattern of the SST $\kappa - \omega$ and Reynolds Stress models did not match with the experiments. In addition, these models greatly over predicted the transition points and the swirl number at the nozzle outlet. Standard $\kappa - \epsilon$ and Realizable $\kappa - \epsilon$ turbulence models produced similar transition points between them which were closer to the experimental results. Thus, the Realizable $\kappa - \epsilon$ model was used throughout the remaining simulations in this thesis and was chosen over the Standard $\kappa - \epsilon$ model due to the advantages of the former regarding modelling flows with strong streamline curvature, vortices, flow separation, and rotation.

The validation of the combustion model and radiation model was made in two ways. The first was by comparing the unconfined 2D axisymmetric simulation results with the experimental combustion PIV data. The second was by comparing the temperature of the confinement plate opposite to the nozzle and the temperature of the combustion gases with the ones measured in the experiments. It was found that the chosen models (Realizable $\kappa - \epsilon$ for turbulence, Finite-Rate/Eddy-Dissipation for combustion, and P-1 for radiation modelling) and the applied boundary conditions approximate the experiments with a good degree of accuracy.

Finally, opportunities for the improvement of the current burner design were identified. The main opportunity was related to the central axial air injection. This had two downsides, it cooled down the central part of the plate and concentrated the reaction in the central region of the plate. These will be addressed in the parametric analysis presented in the next chapter.

7

CFD BURNER OPTIMIZATION, SCALE-UP, AND IMPLEMENTATION

This chapter covers the results of CFD simulations of the swirl burner. The objective of the simulations is to identify a burner design that can produce a homogeneous temperature profile, optimise heat transfer through the radiant surface, minimise flue gas temperature, minimise baseplate temperature, reduce emissions and provide a stable Coanda flame. Once an optimised design is identified, a scaled-up flat flame burner will be compared to a typical radiant tube burner reported in the literature. Afterwards, the results of these compared burners will be used as boundary conditions in the simulation of an electrical steel annealing furnace. The furnace simulation will serve as a case study to assess the benefits of using a Coanda flat flame burner instead of radiant tube burners.

This chapter is structured as follows, the first section, Section 7.1, shows a parametric analysis done on the laboratory scale burner. Several geometric and operating parameters of the burner were varied. Statistical analysis is made to quantify the significance of each parameter. The optimal configuration is chosen. Then, in Section 7.2 the chosen burner configuration is scaled-up and its performance is compared with a radiant tube burner reported in the literature. Finally, Section 7.3 presents a case study of an electrical steel annealing furnace where the radiant tubes are replaced for the Coanda radiant tube burner proposed in this thesis.

7.1 IDENTIFICATION OF PARAMETERS FOR BURNER OPTIMISATION

7.1.1 *Simulation strategy*

This section presents the results of an analysis conducted on the laboratory confined setup in order to optimise its design by making changes in the geometry and operating conditions. For this goal, Design of Experiments (DOE) techniques were applied to the parametric geometry CFD study to identify and rank the primary contributors to the heat transfer of the radiant plate [173–175]. A full factorial experimental design was chosen. This allowed for the identification of the main effects and possible two and three-factor interactions. Two sets of experimental designs were evaluated. The first set consisted of simulations where, in the same way as in the combustion experiments, the reactants were partially-premixed and the secondary air was injected axially through the nozzle central rod. A diagram of the computational domain can be seen in Figure 7.1a. Four parameters were varied: the nozzle diameter ($D_0 = 28$ mm and $D_0 = 24$ mm), the secondary inlet position ($P = 29$ mm and $P = 12$ mm), the confinement height ($H = 56$ mm and $H = 70$

(a) Partially-premixed   (b) Non premixed
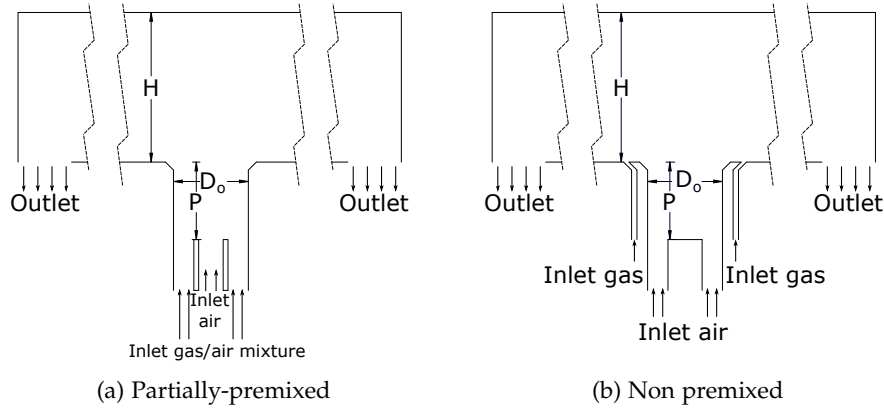
Figure 7.1: Computational domain for the parametric analysis.

mm), and the air ratio between the premixed and the air inlet ($aR = 1.3$ and $aR = 1.0$ where $aR = {}^{air\,through\,annulus\,inlet}/_{air\,through\,secondary\,inlet}$). This resulted in a total number of required simulations of $2^4 = 16$. The second set consisted of simulations where the reactants were not premixed. In this case, the totality of the air went into the domain through the nozzle annulus and the gas was added through an annulus that was positioned just downstream the nozzle exit. A diagram of the computational domain can be seen in Figure 7.1b. Three parameters were varied: the nozzle diameter ($D = 28$ mm and $D = 24$ mm), the bluff body position ($P = 29$ mm and $P = 12$ mm), and the confinement height ($H = 56$ mm and $H = 70$ mm) which give a total number of required simulations of $2^3 = 8$. A summary of the varied simulation parameters for the two experimental designs is given in Table 7.1. For both simulation sets, any geometry parameters that were not varied stayed the same as in Section 6.2. The evaluated response parameters for the experimental design were the radiative heat flux through the plate, the standard deviation of the plate's temperature, and the NO_x concentration in ppm at the outlet. All these will allow for the identification of the factors, or combination of factors, that had the biggest impact on the plate's heat transfer rate and its temperature homogeneity. The response variables were fitted to the model [173]:

$$y = \beta + \sum_{i=1}^{p} \beta_i x_i + \sum_{i=1}^{p-1} \sum_{j=i+1}^{p} \beta_{ij} x_i x_j + \sum_{i=1}^{p-2} \sum_{j=i+1}^{p-1} \sum_{k=j+1}^{p} \beta_{ijk} x_i x_j x_k + x_1 x_2 x_3 x_4 + \varepsilon$$

where y is the response variable, the β's are the unknown model coefficients calculated from the experimental data, the x's are the variables (factors), ε is a bias error within the CFD code, and p is the number of variables.

7.1.2 *Boundary conditions*

The computational domain and boundaries mentioned in this subsection are shown in Figure 7.1. For all the simulations in this section the

Table 7.1: Design of experiments for parametric analysis.

Design parameters	Unit	Level 1	Level 2
Partially-premixed			
Nozzle diameter (D_0)	mm	28	24
Secondary inlet position (P)	mm	29	12
Confinement height (H)	mm	56	70
Air ratio (aR)	-	1.3	1.0
Non-premixed			
Nozzle diameter (D_0)	mm	28	24
Bluff body position (P)	mm	29	12
Confinement height (H)	mm	56	70

Realizable $\kappa - \epsilon$ turbulence model was used. The boundary conditions that were used in this section are the same as the ones used in Section 6.2 with some exemptions which will be mentioned.

For the partially-premixed case with $aR = 1.3$ the primary inlet was defined as a mass flow inlet with a flow rate of 0.9047 g/s; mass fractions of $CH_4 = 0.09751$, $O_2 = 0.2103$, and $N_2 = 0.6922$; and a swirl number of 2.00. The secondary inlet was defined as a mass flow inlet with an air flow rate of 0.6125 g/s and a flow direction normal to the boundary.

For the partially-premixed case with $aR = 1.0$ the primary inlet was defined as a mass flow inlet with a flow rate of 0.8027 g/s; mass fractions of $CH_4 = 0.1099$, $O_2 = 0.2047$, and $N_2 = 0.6853$; and a swirl number of 2.00. The secondary inlet was defined as a mass flow inlet with an air flow rate of 0.7145 g/s and a flow direction normal to the boundary.

For the non-premixed case, the primary inlet was defined as a mass flow inlet with an air flow rate of 2.858 g/s and a swirl number of 2.00. The secondary inlet was defined as a mass flow inlet with a methane flow rate of 0.08822 g/s and a flow direction normal to the boundary.

In all cases, the mixture of both inlets gave an effective equivalence ratio of 1.06. All walls were considered adiabatic with the exemption of the plate positioned opposite to the inlets, i.e. it is assumed that the burner is perfectly insulated with the exemption of the radiant plate. A summary of the inlet boundary conditions for each case is shown in Table 7.2.

7.1.3 *Parametric analysis – 2D axisymmetric*

7.1.3.1 *Partially-premixed case*

The results for the partially-premixed case can be seen in Figure 7.2. the figure shows the percentage of variability of the selected response variable that can be uniquely attributed to each factor, or combination of factors tested. The main factor effects (Figure 7.3) appear to be the

Table 7.2: Boundary conditions for the parametric analysis.

Parameter	Primary inlet	Secondary inlet
Partially-premixed with air ratio $aR = 1.3$		
Mass flow (g/s)	0.9047	0.6125
CH_4 mass fraction	0.09751	0.0000
O_2 mass fraction	0.2103	0.2300
N_2 mass fraction	0.6922	0.7700
Partially-premixed with air ratio $aR = 1.0$		
Mass flow (g/s)	0.8027	0.7145
CH_4 mass fraction	0.1099	0.0000
O_2 mass fraction	0.2047	0.2300
N_2 mass fraction	0.6853	0.7700
Non-premixed		
Mass flow (g/s)	1.4290	0.08822
CH_4 mass fraction	0.0000	1.0000
O_2 mass fraction	0.2300	0.0000
N_2 mass fraction	0.7700	0.0000

ones that contribute the most to the variation of the response variables accounting respectively for $\sim 77\%$, $\sim 87\%$, and $\sim 62\%$ of the variability of outward plate radiation, the standard deviation of the plate temperature, and the concentration of NO_x. The greatest contributors for the variation in outward plate radiation are the nozzle diameter (D_0), the secondary inlet position (P), and the air-ratio (aR); with the confinement height (H) having a smaller contribution. A decrease in the nozzle diameter increased the outward plate radiation. A decrease in outward plate radiation occurred by having the secondary inlet position closer to the nozzle and an air ratio of 1.0. By looking into the standard deviation of the radiant plate temperature it can be seen that all main factors contribute to the variation in an amount ranging from between $\sim 20\%$ and $\sim 30\%$. The small nozzle diameter ($D_0 = 28$ mm), the large confinement ($H = 70$ mm), the secondary inlet position farther away of the nozzle ($P = -29$ mm), and having a bigger amount of air in the premixed inlet ($aR = 1.3$) leads to the reduction in standard deviation of the radiant plate temperature which translates into a more homogeneous temperature profile at the radiant plate wall. Finally, the main factors that contribute the most to the variation in NO_x emissions are the secondary inlet position, confinement height, and air ratio. In this case, the lowest emissions for each factor occur with the secondary inlet closer to the nozzle ($P = -12$ mm), the large confinement ($H = 70$ mm), and an air ratio of 1.0.
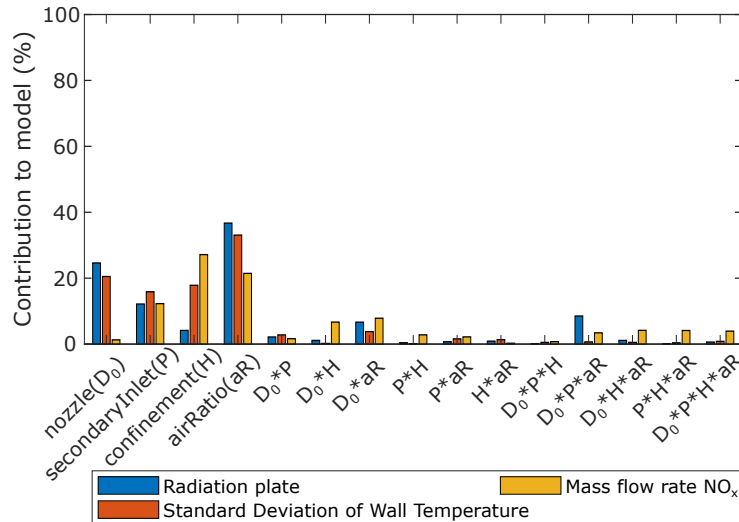
Figure 7.2: Partially-premixed simulation. Percentage of contribution for each factor or combination of factors.

Part of the previous observations of the radiation and temperature of the plate can be attributed to the increase in flow velocity produced by having a smaller primary inlet nozzle diameter. This increase in flow velocity would lead to a greater turbulence and mixing rate within the confinement that, in turn, would produce a better temperature homogeneity. In addition to this, the increase in outward radiation and temperature homogeneity produced by having an $aR = 1.3$ can be explained by the mixing of the inlet air and the position where the reaction is occurring. With an $aR = 1.0$ more air is injected axially through the secondary inlet, this would cause the reaction to occur near the centre of the confinement. In contrast, by having an $aR = 1.3$ the air goes, alongside the fuel, into the Coanda flow pattern and the heat is better distributed. The effect in NO_x reduction could be explained by a reduction in local temperature in the central part of the confinement caused by having an axial injection of cold air by the secondary inlet, in addition to having a bigger confinement that would increase the residence time (and thus, heat distribution).

The lines of the interaction plots remain mostly parallel to each other in the plots corresponding to the response of radiation output (Figure 7.4a) and standard deviation of temperature (Figure 7.4b). This indicates that the interaction effect of the varied factors on these two response variables is low. However, in the NO_x concentration plot (Figure 7.4c) there appears to be an interaction between the nozzle diameter and the other three factors.

7.1.3.2 *Non-premixed case*

The results for the non-premixed case can be seen in Figure 7.5, the figure shows the percentage of variability of the selected response variable that can be uniquely attributed to each factor (or combination of factors) tested. All the main factor effects have the same behaviour (Figure 7.6), this is, factors at a level 1 decrease output radiation, increase the stan-
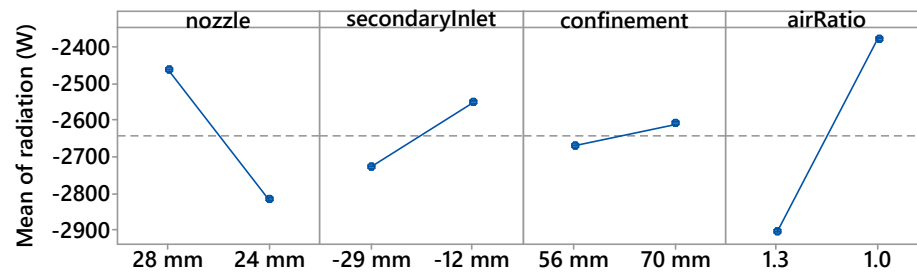
(a) Main effects plot for plate radiation.
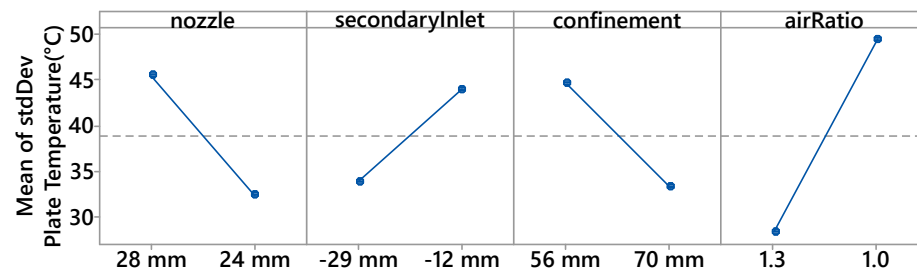
(b) Main effects plot for standard deviation of plate temperature.

(c) Main effects plot for NO_x mass flow rate.

Figure 7.3: Partially-premixed simulations. Main effect plots.

(a) Interaction plot for plate radiation.

(b) Interaction plot for standard deviation of plate temperature.

(c) Interaction plot for NO_x mass flow rate.

Figure 7.4: Partially-premixed simulations. Main effect and interaction plots.

dard deviation of temperature at the radiant surface, and increase NO_x concentration of the flue gases at the outlet. The contrary is true for the factors at a level 2. Of the main factor effects, the bluff body position (P) is the one that contributes the least to the variation of the response variables accounting respectively for $\sim 7.2\%$, $\sim 5.3\%$, and $\sim 2.5\%$ of the variability of outward plate radiation, the standard deviation of the plate temperature, and the concentration of NO_x. The confinement has the greatest impact on the outward radiation and the standard deviation of the radiant surface temperature. The nozzle size has the biggest impact on the NO_x concentration in the flue gases. Together, the main effects of the nozzle diameter (D_0) and confinement height (H) account for $\sim 80\%$ of the variability in outward radiation, $\sim 86\%$ of the change in variability deviation of the radiant plate temperature, and $\sim 74\%$ of the variability of NO_x production.

The previous observations can be attributed to the decrease in nozzle diameter and higher position of the bluff body. Both factors lead to an increase in the flow speed at the inlet and consequently to an increase in the turbulence and mixing. This provides a more homogeneous temperature across the confinement volume which, therefore, would reduce local hot zones and decrease thermal NO_x production. In addition to this, a bigger confinement would allow for a higher residence time that would tend to also homogenise the temperature. Obviously, there is a compromise, one cannot increase the volume of the confinement indefinitely because increasing the confinement size will increase the surface area of the walls. The bigger surface area would, in turn, increase the heat transfer through the walls and reduce the overall turbulence and mixing which would be detrimental for the herein proposed application.

The effect of the interaction between factors (Figure 7.7) appears to be low, with the lines of the interaction plots remaining mostly parallel to each other. The only exception being the effect the change in nozzle diameter and confinement height have in the NO_x concentration. The confinement size appears to have a bigger impact on the NO_x concentration with a nozzle diameter of 28 mm changing from ~ 0.24 to ~ 0.11 ppm respectively for a confinement size of 56 and 70 mm. The NO_x concentration for the 24 mm nozzle diameter has a smaller change from ~ 0.07 to ~ 0.04 ppm for the same confinement height values.

7.1.3.3   *Comparison between both experimental designs*

The desired configuration is that which increases the heat flux through the radiant plate, increases the temperature homogeneity, and reduces emissions. For the partially-premixed case, the combination of factors that fulfill these requirements is nozzle diameter $D_0 = 24$ mm, secondary inlet position $P = -29$ mm, confinement height $H = 70$ mm, and air-ratio $aR = 1.3$. For the non-premixed case is: nozzle diameter $D_0 = 24$ mm, bluff body position $P = -12$ mm, and confinement height $H = 70$ mm. Table 7.3 shows the relevant values of the simulation results for each one of these two cases. Figure 7.8 shows the temperature profile at the radiant layer. Figure 7.9 shows the contour plots for velocity
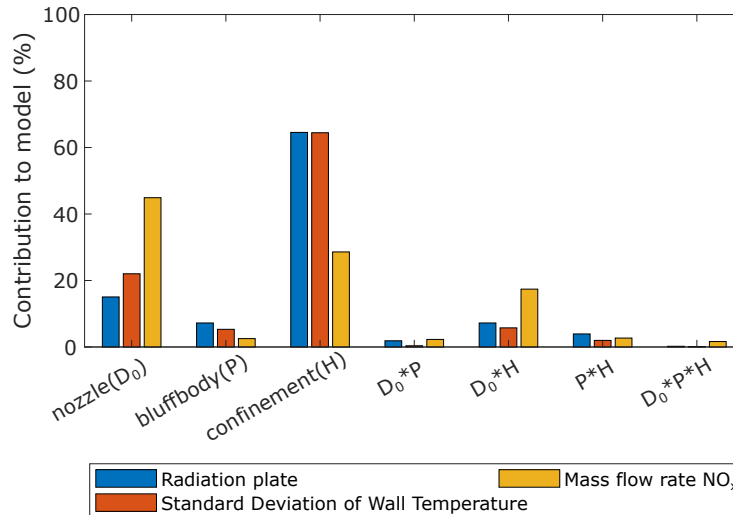
Figure 7.5: Non-premixed simulation. Percentage of contribution for each factor or combination of factors.

Table 7.3: Comparison of relevant values between selected partially-premixed case with $D_0 = 24$ mm, $P = -29$ mm, $H = 70$, $aR = 1.3$ and selected non-premixed case with $D_0 = 24$ mm, $P = -12$ mm, $H = 70$ mm.

Parameter	Partially-premixed	Non-premixed	unit
Outlet flue gas temperature	482	498	°C
NO_x at outlet	1.1527	0.0391	ppm
Radiant plate average temperature	310	309	°C
Heat flow	-3106	-3116	W

magnitude temperature. In comparison to the partially-premixed case, the outlet temperature in the non-premixed case is $\sim 3\%$ higher and the NO_x emissions are $\sim 95\%$ lower. The average temperature of the radiant plate and the heat flow remain the same between the two cases. However, looking in more detail at the radiant plate temperature profile, it is possible to see that the non-premixed case has more homogeneous temperature in the plate surface. There is a ΔT of $\sim 15°C$ between the highest and lowest temperature. In comparison, in the partially-premixed case, the ΔT is of $\sim 55°C$. The difference in temperatures is caused by how the reactants are fed into the confinement. As explained earlier, in the case of the partially-premixed case the supplementary air is injected axially. This has the following effects: first the central part of the confinement is cooled by the axial air; then, immediately downstream, the reaction takes place in a small region close to the central part of the domain which rapidly rise the temperature. In the non-premixed case, the air enters the domain and acquires a Coanda flow pattern. Then the air mixes with the fuel and starts reacting. Because the reaction is spread into a bigger area the temperature does not raise as much in the central part of the confinement. The more homogeneous temperature in the non-premixed case leads to the observed decrease in NO_x emissions.
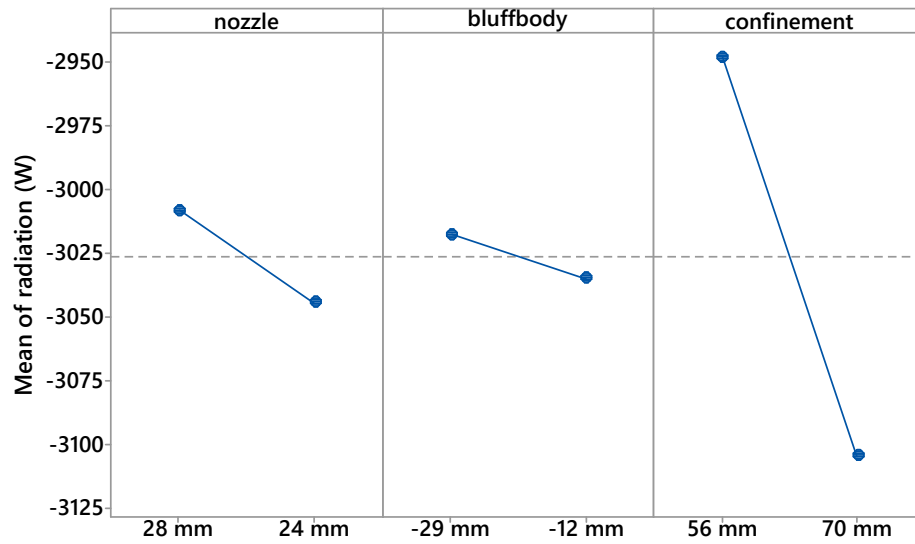
(a) Main effects plot for plate radiation.
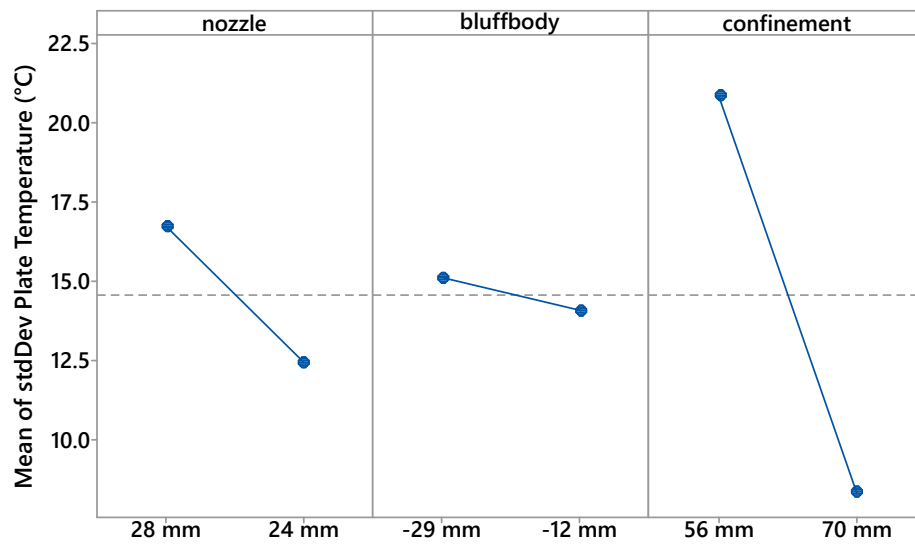
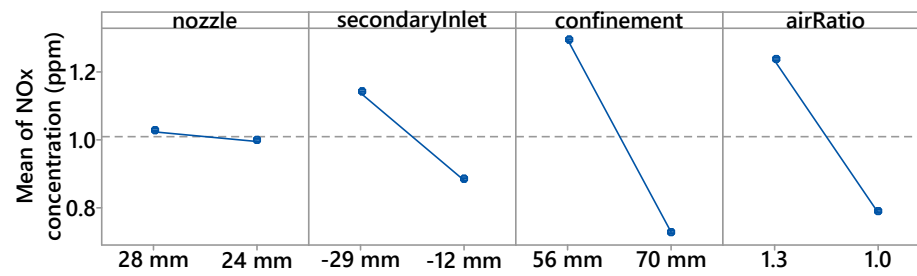

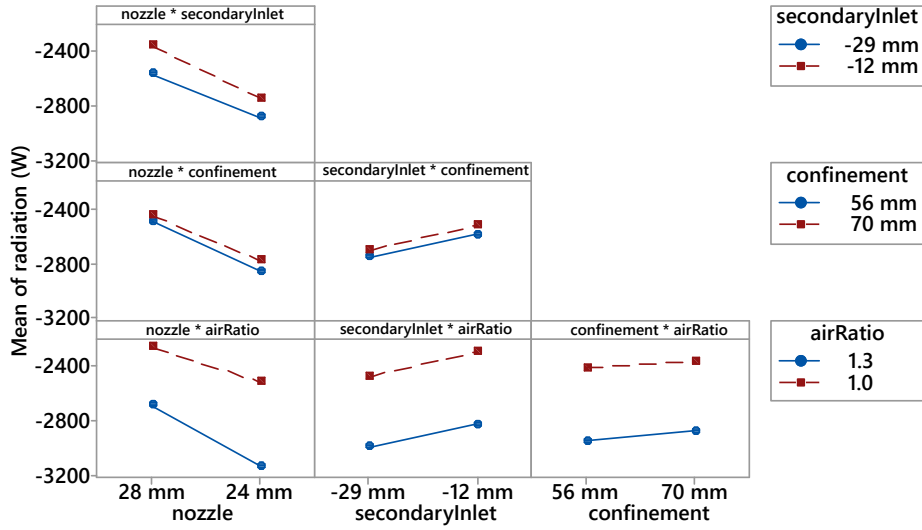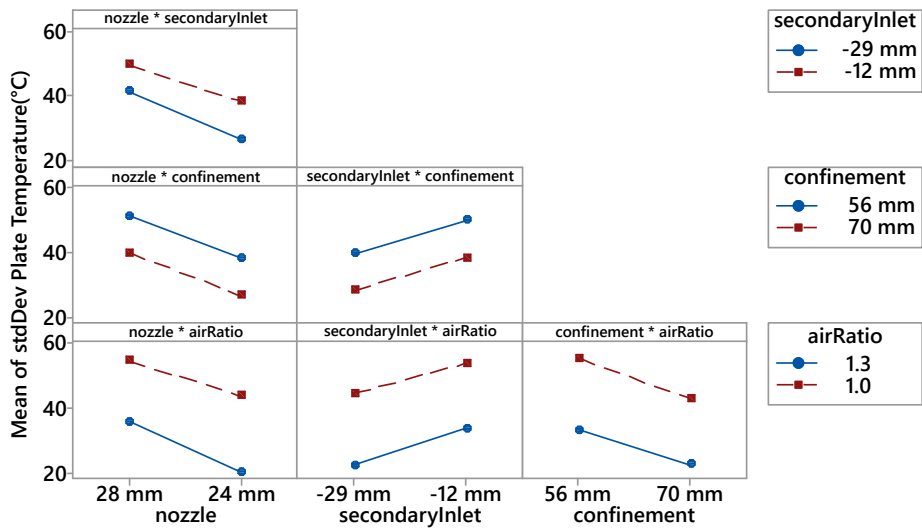(b) Main effects plot for standard deviation of plate temperature.

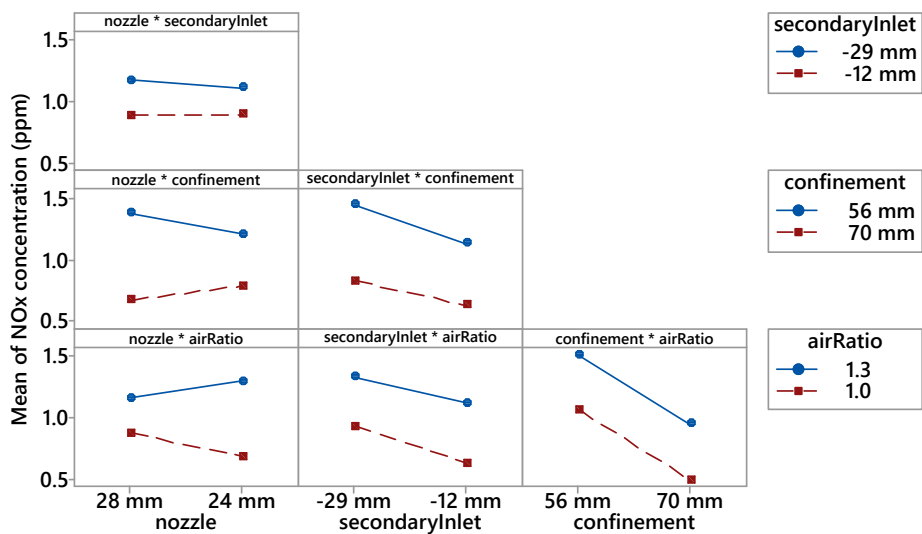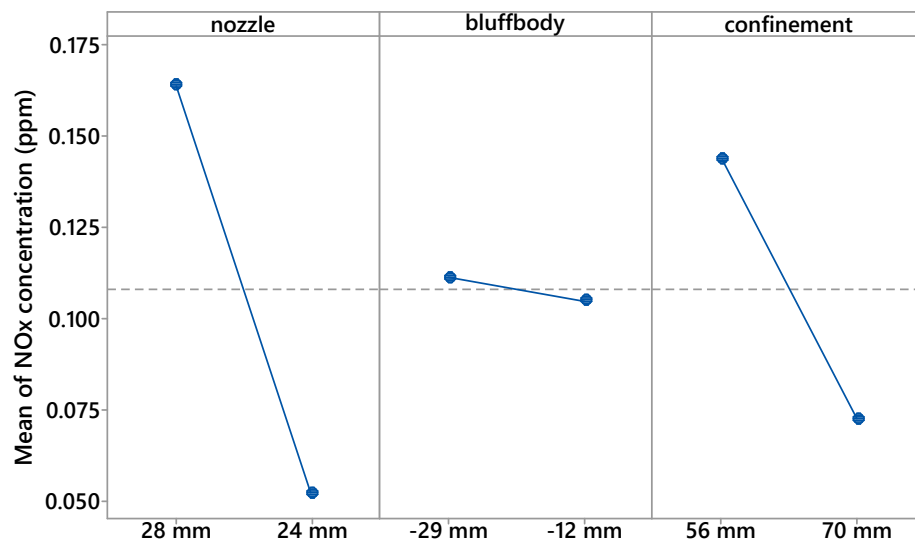(c) Main effects plot for NO_x mass flow rate.

Figure 7.6: Non-premixed simulations. Main effects plots.
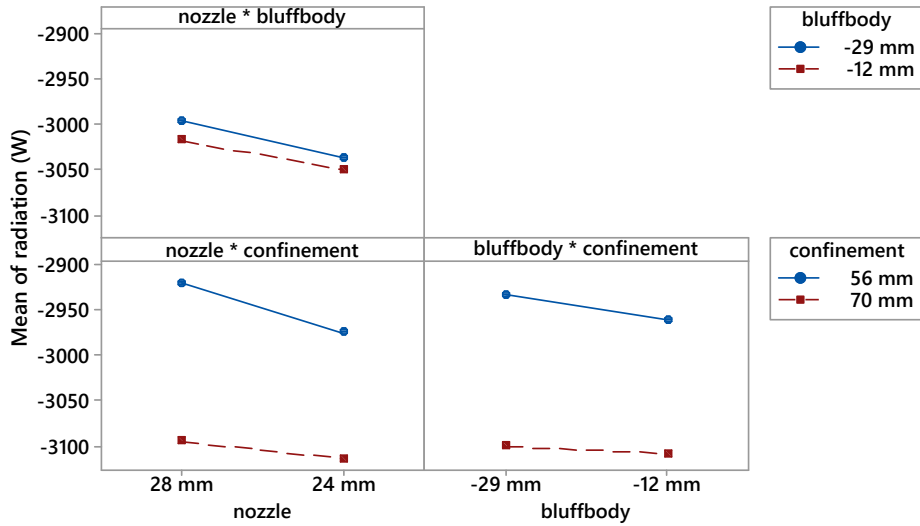
(a) Interaction plot for plate radiation.
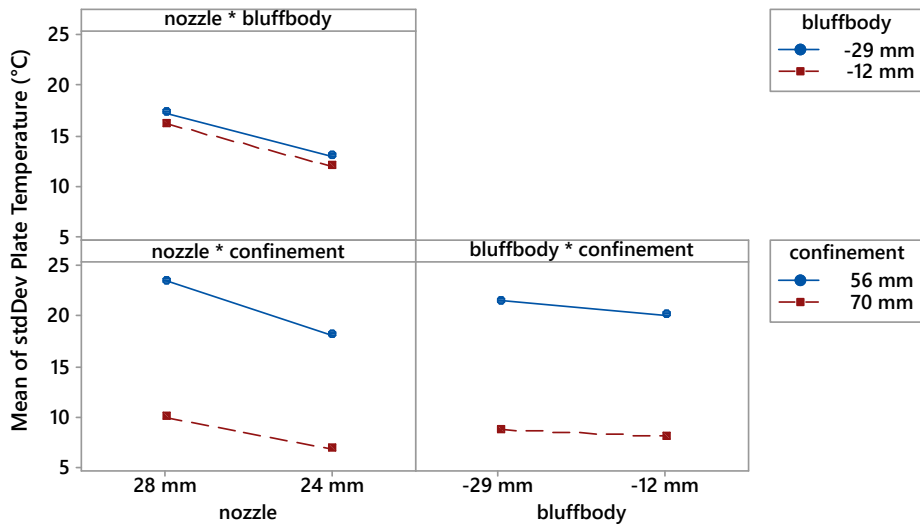
(b) Interaction plot for standard deviation of plate temperature.
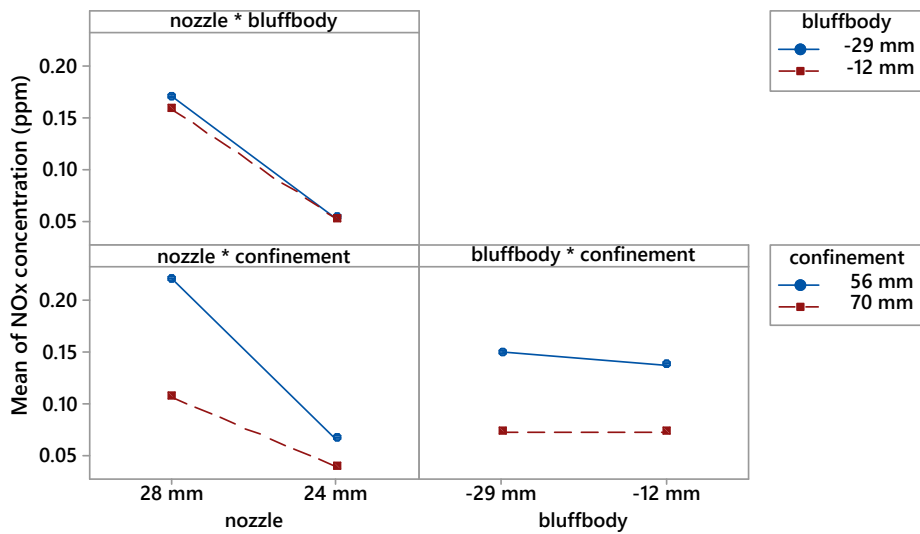
(c) Interaction plot for NO$_x$ mass flow rate.

Figure 7.7: Non-premixed simulations. Main effect and interaction plots.
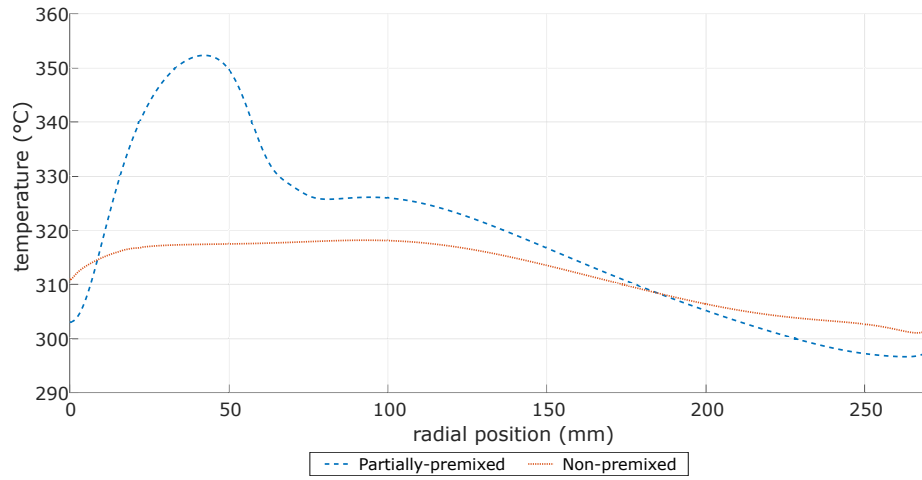
Figure 7.8: Comparison of wall temperature between selected partially-premixed case with $D_0 = 24$ mm, $P = -29$ mm, $H = 70$, $aR = 1.3$ and selected non-premixed case with $D_0 = 24$ mm, $P = -12$ mm, $H = 70$ mm.
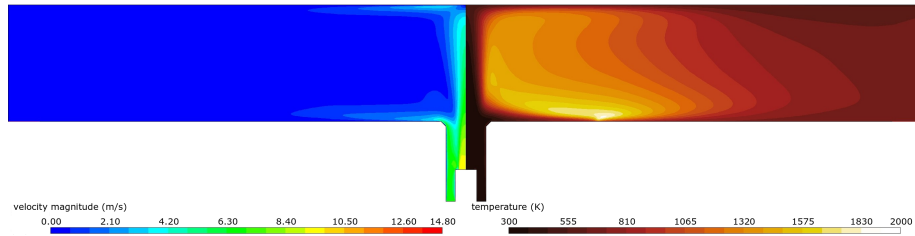
(a) Non-premixed. Velocity magnitude (left) and temperature (right) contours.
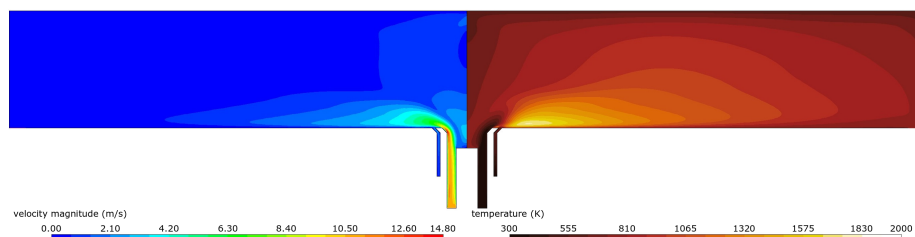
(b) Non-premixed. Velocity magnitude (left) and temperature (right) contours.

Figure 7.9: Contours of the selected partially-premixed case (top) and the selected non-premixed case (bottom).

7.1.4 *General remarks*

A parametric analysis was conducted on the confined Coanda burner with the objective of identifying a configuration that increases the heat flux through the radiant plate, increases the temperature homogeneity, and reduces emissions. Two overall geometries were evaluated. In the first one, the reactants were fed into the domain partially-premixed with an axial injection of supplementary air. In the second geometry, the reactants were fed into the domain non-premixed with the fuel injected at an angle immediately downstream the nozzle. The varied factors were: nozzle diameter ($D_0 = 28$ mm and $D_0 = 24$ mm), secondary inlet position ($P = 29$ mm and $P = 12$ mm), confinement height ($H = 56$ mm and $H = 70$ mm), and the air ratio in the premixed and air inlet ($aR = 1.3$ and $aR = 1.0$). This last one applied only to the partially-premixed case. Main factors and interaction plots were created. The best configuration for each case was identified. It was found that, overall, the partially-premixed configuration is detrimental to the stated objectives. The non-premixed case provides a much better temperature homogeneity and NO_x reduction.

7.2 SCALE-UP OF RADIANT PLATE AND COMPARISON WITH RADIANT TUBE

7.2.1 *Description of radiant tube*

The radiant tube burner presented in the papers by Tsioumanis et al. [176, 177] was used as a reference case for a performance comparison with the proposed Coanda burner. The radiant tube and boundary conditions used by the authors will be briefly described. Figure 7.10 shows a diagram of the radiant tube. The tube is of the single-ended recuperative type. All the metal components in the burner are considered to be made of Inconel-600 alloy. A ceramic fibre plug is fitted to the inner tube side that is closest to the combustion zone in order to protect the burner components in this area. The inlet cold air enters the combustion chamber through a long annulus. The air flow then reaches the recuperator section where it is pre-heated by the hot combustion products and, at the same time, the swirl is applied by a helical coil swirler in order to accelerate the flow and improve the heat transfer. At the end of the annular section, the pre-heated air passes through a step ring which slightly reduces the swirl and homogenises the circumferential flow distribution. The air is then split into a primary (inner) and secondary (outer) flow by a silicon carbide tube. The primary air flow mixes with the fuel and is ignited by the pilot burner. The swirling air-gas mixture then enters the combustion chamber where it expands and mixes with the secondary air. The combustion products exit the combustion chamber and flow back through an outer annulus into the recuperator section.

The authors conducted two CFD simulations: an isothermal and a reacting flow simulation. Both simulations were validated against exper-
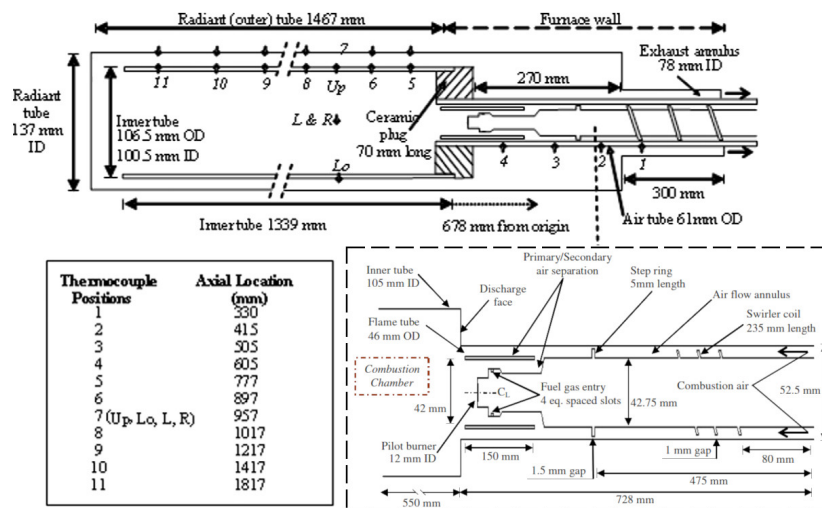
Figure 7.10: Radiant tube. Key design features, dimensions, and thermocouple locations [177].

imental data. For the isothermal flow simulation, the air was injected at the air inlet, flue inlet, and pilot inlet. The CFD velocity profiles were validated against experimental air flow velocity measurements obtained by hot-wire probes at two planes of the combustion chamber, 50 mm and 100 mm, downstream of the nozzle exit. For the reacting flow simulation, the CFD temperature at specific points (see Figure 7.10) of the inner tube and recuperator section were compared against experimental thermocouple measurements.

7.2.2 *Description of Coanda flat plate burner*

A scaled-up version of the selected non-premixed Coanda burner from Section 7.1 is shown in Figure 7.11. The burner dimensions were scaled-up by multiplying its dimensions by a factor of between ~ 2.0 and ~ 2.5, giving a nozzle diameter of $D_0 = 60$ mm, position of the bluff-body of $P = -17$ mm, and confinement height of $H = 150$ mm. The length of the burner confinement was such that the radiating area was the same as that of the radiant tube burner, i.e. a value of $R = 448$ mm, in order to have a radiating area of ~ 0.63 m². Furthermore, a return annulus for the hot flue gases was added to the burner in order to account for the recuperator in the radiant tube burner. This added recuperator section was kept with similar dimensions as the ones of the radiant tube burner. All the metal components in the burner are considered to be made of Inconel-600 alloy. A ceramic fibre plug is fitted at the nozzle outlet in order to protect the burner components in this area from the hot gases in the combustion zone.

7.2.3 *Simulation strategy*

The approach taken for these simulations was like the one taken in the previous chapter (Chapter 6). First, the radiant tube computational
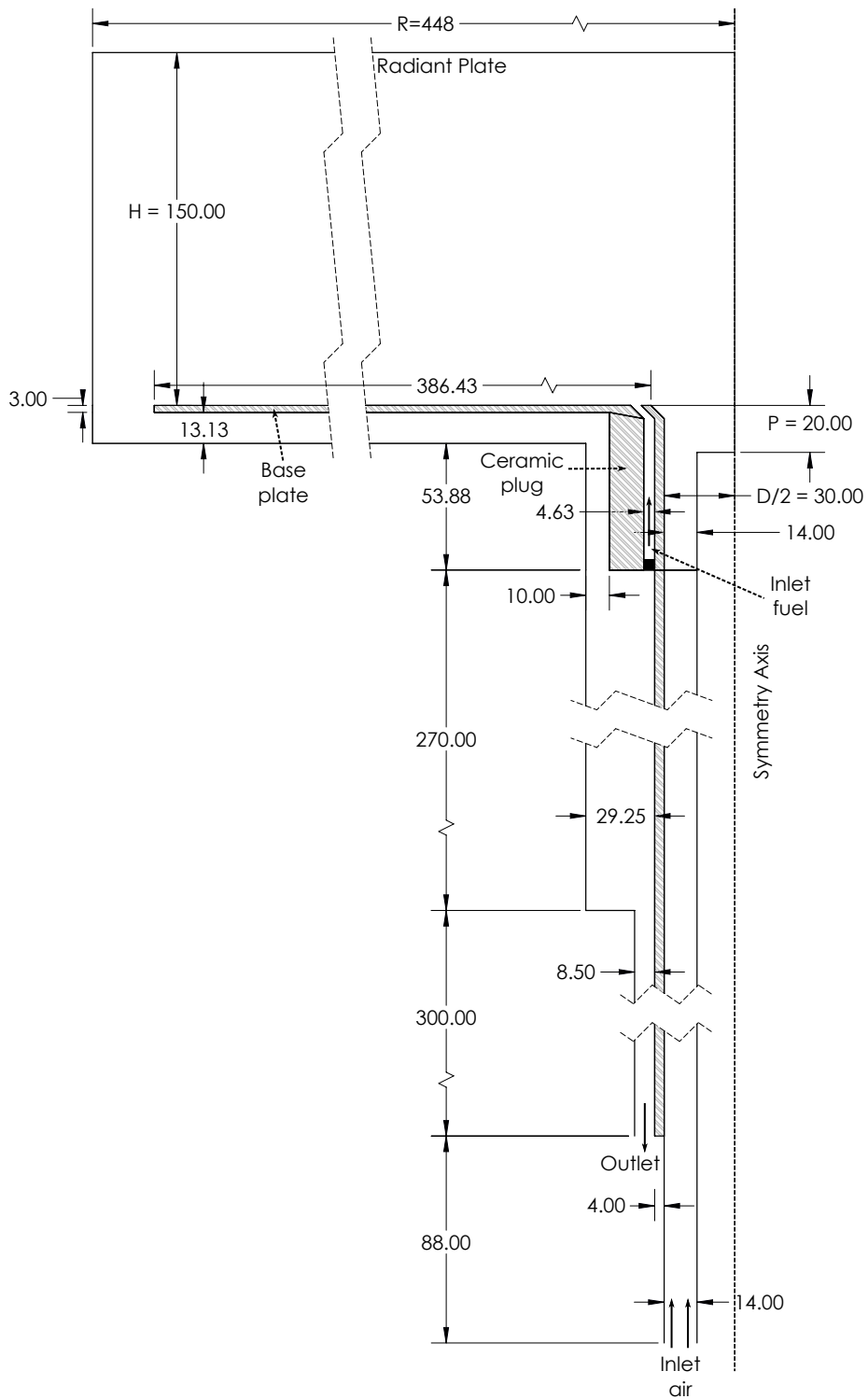
Figure 7.11: Scaled-up Coanda burner. All dimensions are in mm.

Table 7.4: Boundary conditions for the isothermal radiant tube simulation.

Inlet	Air mass flow rate (g/s)	Temperature (K)
Main	7.880	300
Fuel	0.675	300
Pilot	0.363	300

domain was created as a 2D axisymmetric geometry. Then the models used were validated against the experimental results. To do this, simulations were conducted for the isothermal and reacting flow cases. The same boundary conditions that were applied by Tsioumanis et al. are used. The results are then compared with the ones obtained in the experiments by the authors.

Once the models are validated against experiments, simulations were conducted to compare the radiant tube burner with the Coanda flat flame burner. To do this, first a change was made in the radiant tube outer wall boundary condition. The authors of the paper used a fixed temperature boundary condition which would not be useful for a comparison with the Coanda flat plate burner because one of the objectives is to compare the radiant and convective heat transfer profile between the two burners. Instead, the previously used value for the convective heat transfer coefficient of 30 W/m²-K (see Section 6.2) is set for the comparison. A simulation of the radiant tube is carried out with this change in the boundary condition. Finally, a simulation of the proposed Coanda flat plate burner is made. The total air flow rate, fuel flow rate and wall boundary conditions were kept the same between the Coanda burner and the radiant tube burner.

7.2.4 *Boundary conditions*

For all the simulations in this section the Realizable $\kappa - \epsilon$ turbulence model was used.

For the radiant tube, isothermal simulations air was used as a working fluid. The main inlet air flow rate was set at 7.880 g/s, the fuel inlet air flow was set at 0.675 g/s, and the pilot air flow inlet was set at 0.363 g/s. The temperature for all inlets was 300 K. The outlet pressure boundary condition was set at constant atmospheric pressure. A summary of the settings is shown in Table 7.4.

The boundary conditions for the radiant tube with combustion are shown in Table 7.5. As mentioned earlier, the inlet flow boundary conditions are the same for the simulation used for the validation of the radiant tube and the simulation used for the comparison with the Coanda burner. The boundary conditions are an air flow rate of 8.906 g/s through the air inlet a methane flow rate of 0.494 g/s through the fuel inlet, and a flow rate of 0.339 g/s with a mass fractions of $CH_4 = 0.05540$, $O_2 = 0.2172$, and $N_2 = 0.7273$ through the pilot inlet. The wall boundary conditions for the outer tube differ between the two simulations. The

simulation used for validation has a fixed wall temperature of 1248 K. The simulation used for comparison has a mixed convection-radiation wall boundary condition with a heat transfer coefficient of 30 W/m²-K, free stream and radiation temperature of 1073 K, internal emissivity of 0.8 and external emissivity of 0.8. All the other walls of the radiant tube were considered adiabatic.

The Coanda flat plate burner boundary conditions are shown in Table 7.5. The total air and fuel flow rates were kept the same as the radiant tube burner. However, in the case of the Coanda burner, the air and fuel corresponding to the pilot inlet were split between the main air inlet and fuel inlet. This gave a mass flow rate at the air inlet of 9.227 g/s and a methane flow rate of 0.513 g/s at the fuel inlet. The wall boundary conditions for the radiant plate were kept the same as the conditions for the outer tube of radiant tube burner with a heat transfer coefficient of 30 W/m²-K, free stream and radiation temperature of 1073 K, internal emissivity of 0.8 and external emissivity of 0.8. As before, all the remaining walls were considered adiabatic.

Several different materials are used in the simulations presented in this section. Inconel-600 alloy is used for all the metal components of the burners, silicon carbide for the tube that splits the air flow in the radiant tube burner, and ceramic fibre in the combustion zone. The physical and thermal property values of the materials are taken either as a constant or as a temperature-dependent polynomial with the form of $a + bT + cT^2 + dT^3 + eT^4$. The polynomial coefficients are shown in Table 7.6.

7.2.5 *Burner comparison*

7.2.5.1 *Radiant tube validation of the 2D model*

A comparison between the CFD simulations and the experimental data acquired by Tsioumanis et al. can be seen in Figure 7.12. Figure 7.12a and Figure 7.12b show a good agreement between experiments and simulations for axial, radial and tangential velocities at the two planes of the combustion chamber. Figure 7.12c also shows a good agreement for the temperature of the inner tube. From this, it is possible to say that the simplification to a 2D geometry does not yield much error and that the used models are within a reasonable degree of accuracy.

7.2.5.2 *Comparison of Coanda flat plate burner vs radiant tube*

A comparison between the temperature contours of the CFD simulation results of the radiant tube burner and the Coanda flat plate burner can be seen in Figure 7.13. Table 7.7 shows relevant physical dimensions and temperatures at relevant locations of the radiant tube burner and the Coanda flat plate burner. Both burners produce the same average temperature of $\sim 885°C$ at their respective radiating outer surface. This is expected, as both have the same radiating surface area and boundary conditions. However, the convective and radiative heat flux differ between both cases. The radiant tube had a total heat flux of

Table 7.5: Boundary conditions for the reacting radiant tube simulation.

Parameter	Air inlet	Fuel inlet	Pilot inlet
Radiant tube burner			
Mass flow rate (g/s)	8.906	0.494	0.339
CH_4 mass fraction	-	1.0000	0.0554
O_2 mass fraction	0.2300	-	0.2173
N_2 mass fraction	0.7700	-	0.7273
Temperature (K)	300	300	300
Coanda flat plate burner			
Mass flow rate (g/s)	9.227	0.513	-
CH_4 mass fraction	-	1.0000	-
O_2 mass fraction	0.2300	-	-
N_2 mass fraction	0.7700	-	-
Temperature (K)	700	300	-
Wall boundary	validation		comparison
Heat transfer coefficient (W/m²-K)	-		30
Free stream temperature (K)	-		1073
External emissivity	-		0.8
External radiation temperature (K)	-		1073
Internal emissivity	0.8		0.8
Wall temperature (K)	1248		-
Wall thickness (m)	0.003		0.003

Table 7.6: Physical and thermal properties of various materials used in the burners.

Coefficient	a	b	c	d	e
Density (kg/m³)					
Inconel-600 [178]	8.4700E+03				
Ceramic fibre [179]	3.0000E+03				
Silicon carbide [180]	3.1000E+03				
Specific heat (J/kg-K)					
Inconel-600 [178]	3.8235E+02	2.1249E-01			
Ceramic fibre [179]	1.0000E+03				
Silicon carbide [180]	2.6490E+02	1.9861E+00	-1.6345E-03	6.5589E-07	-9.8563E-11
Thermal conductivity (W/m-K)					
Inconel-600 [178]	1.1174E+01	1.1496E-02	3.4938E-06		
Ceramic fibre [179]	4.4338E-02	3.8571E-06	7.1429E-08		
Silicon carbide [180]	1.8642E+02	-3.3152E-01	2.8976E-04	-1.1973E-07	1.8644E-11
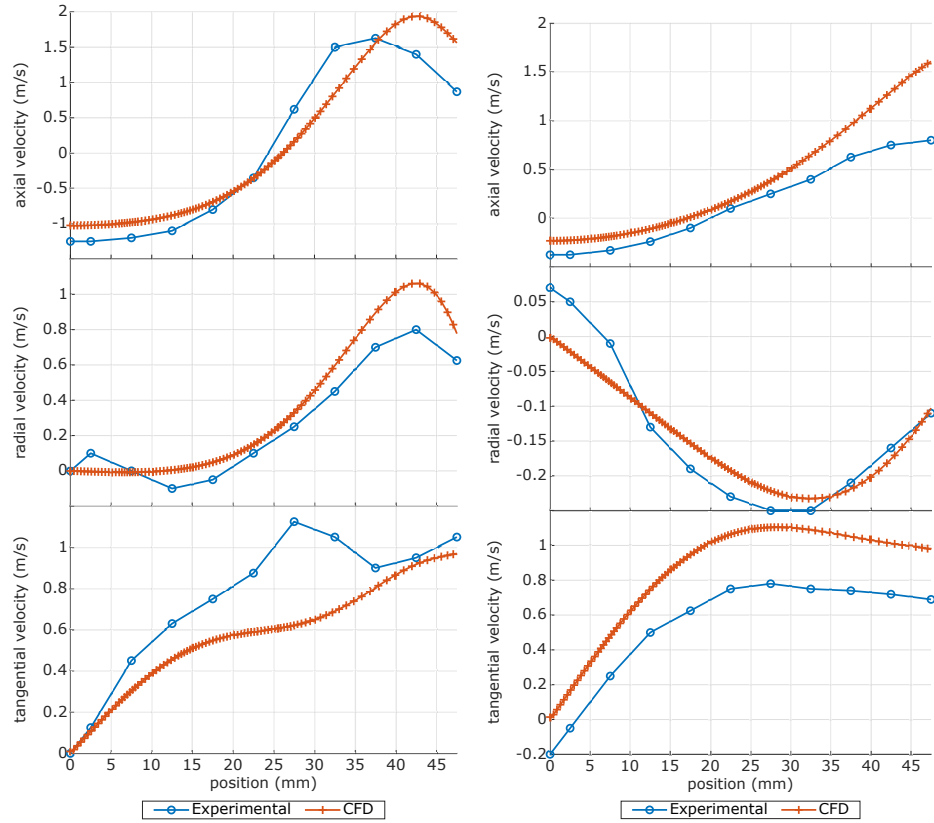
(a) Isothermal. Velocity profiles at plane 1.   (b) Isothermal. Velocity profiles at plane 2.
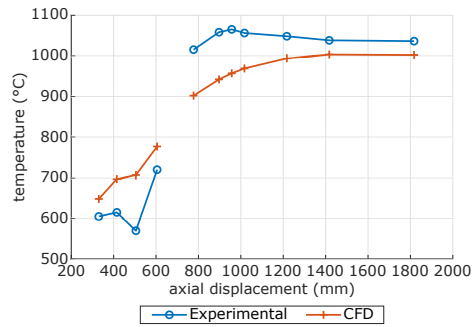
(c) Reacting flow. Temperatures at inner tube wall.

Figure 7.12: Comparison between experimental data and CFD simulations of the radiant tube burner.

$-28,041$ W/m² and the Coanda flat plate burner had a total heat flux of $-23,325$ W/m².

The difference in the heat flux can be explained by looking at the variation of the temperature profile at the radiating boundary wall of both burners (Figure 7.14). The radiant tube burner has a ΔT of 86°C between the minimum temperature (~ 832°C) and maximum temperature (~ 918°C) at the outer tube wall. The temperature is greater in the side of the tube closer to the flame (i.e. close to the nozzle). The standard deviation of the temperature is 24.01°C. The Coanda flat plate burner presents a more homogeneous profile having a ΔT of 6°C between the minimum temperature (~ 883°C) and maximum temperature (~ 886°C) at the outer plate wall, and a standard deviation of 0.99°C. The increased homogeneity for the Coanda plate burner is attributed to two related factors. The spread of the flame by the Coanda effect allows for an increased radiating surface area and the flame radiates directly to the radiant plate surface which has a bigger surface area than the inner tube of the radiant tube burner. In contrast, in the radiant tube burner, the temperature is concentrated in a smaller volume due to the need of having an inner tube and because of the overall geometry of the tube. The difference between the outward radiation of the two burners can be seen in Figure 7.13.

The better temperature homogeneity of the Coanda burner is not the only improvement. The NO_x production in the Coanda flat plate burner is almost 18 times lower than the one of the radiant tube burner. The difference in NO_x production between the two burners is attributed to the difference in volumetric temperatures between them. As mentioned before, the temperature in the radiant tube is concentrated in a smaller area, the average temperature in the combustion zone of the radiant tube is ~ 1492°C with a peak temperature of 2103°C. In comparison, the average temperature in the combustion zone of the Coanda flat plate burner is ~ 1048°C with a peak temperature of 2033°C. The previously mentioned factors that contributed to the increase in temperature homogeneity in the radiant plate burner also contribute to the decrease in temperature in the combustion zone and reduction in thermal NO_x production. An additional factor also benefits this, the nature of the Coanda flow produces a re-circulation of the "cold" combustion gases towards the flame zone which further cools the area down.

7.2.5.3 *Design considerations for the Coanda flat plate burner*

Some design considerations need to be considered once the physical device is built. The applied swirl needs to be close to the burner nozzle to avoid a reduction in the swirl velocity and be able to maintain a stable Coanda flame. Additionally, due to the nature of the Coanda flame, care must be taken with the burner components that are close to the flame. Figure 7.15a shows temperature contours for the burner walls near the ignition zone and Figure 7.15a shows the temperature plot at the radial position of the base plate. The base plate reaches a maximum temperature of ~ 965°C and has an average temperature of
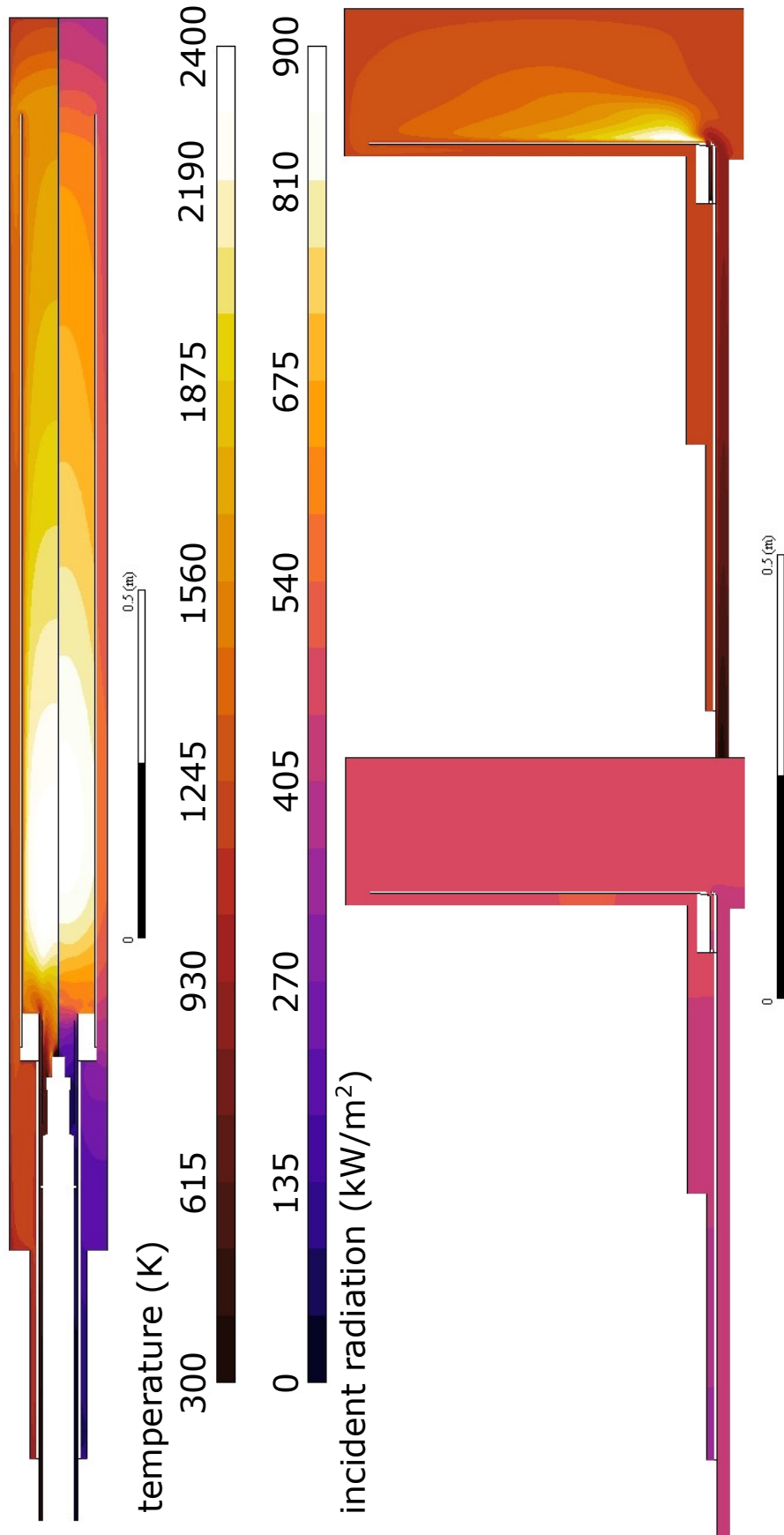
Figure 7.13: Temperature contours of radiant tube burner and Coanda flat plate burner.
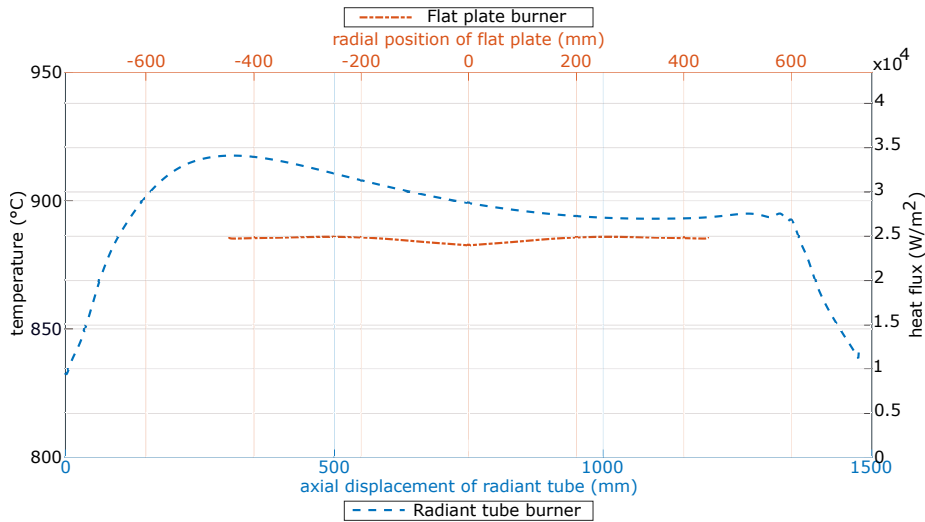
Figure 7.14: Temperature and total heat flux of radiant tube burner (blue) and Coanda flat plate burner (red) at outer wall radiating surface.

Table 7.7: Relevant physical dimensions and temperature at relevant locations of radiant tube burner and Coanda flat plate burner.

	Radiant tube	Coanda flat plate burner	Unit
Radiating area and heat flux			
Radiating area	0.63	0.63	m²
Heat flux	−28041	−23325	W/m²
Temperatures at radiating surface			
Average	885	885	°C
Maximum	918	886	°C
Minimum	832	883	°C
Standard Deviation	24.01	0.99	°C
Gas temperature at specific locations			
Inlet	27	57	°C
Outlet	714	898	°C
Pre-ignition	390	593	
Temperatures at combustion zone			
Volume	0.0113	0.0947	m³
Average	1492	1048	°C
Maximum	2103	2033	°C
Emissions			
NO_x at outlet	677	37	ppm

(a) Temperature contours at nozzle exit.

(b) Temperature plots of base plate.
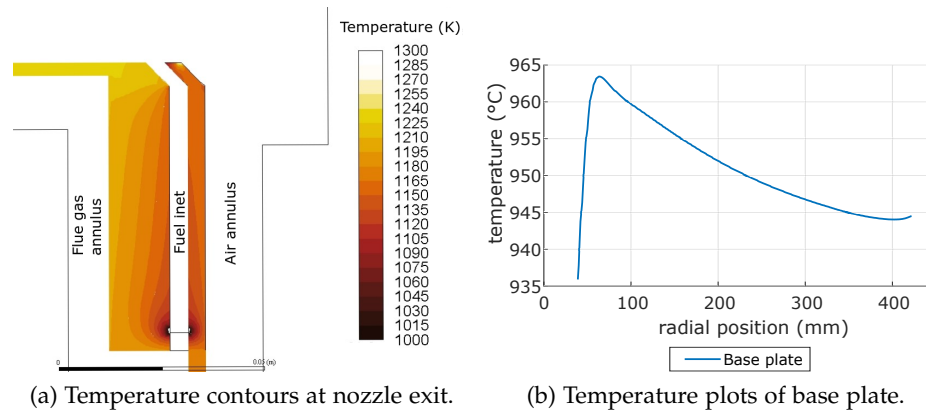
Figure 7.15: Coanda burner base plate wall temperatures.

$\sim 950°$C. The materials to be chosen for the burner need to consider these operating temperatures. Another factor that must be considered is the thermal expansion of the materials which was not taken into account in the present simulations.

7.2.6 *General remarks*

A comparison between the proposed Coanda flat plate burner and a radiant tube was done via CFD simulations. Both devices had the same radiating surface area, thermal boundary conditions, and amount of fuel. It was found that both devices had an average boundary temperature at the radiant wall of $\sim 885°$C. The radiant tube had a higher total heat flux of $-28,041$ W/m² compared to the Coanda burner with $-23,325$ W/m². However, the radiant tube had a higher variation in temperature across the length of the tube with a minimum temperature of $\sim 832°$C, a maximum temperature $\sim 918°$C, and a standard deviation of $24.01°$C. This could potentially lead to non-homogeneous heating of the load while in operation. In comparison, the Coanda flat plate burner had a much more homogeneous temperature profile across the radiant plate with a minimum temperature of $\sim 883°$C, a maximum temperature $\sim 886°$C, and a standard deviation of $0.99°$C. Regarding NO_x emissions, the Coanda flat plate burner had almost 18 times lower emission than those of the radiant tube. This was mainly because of the much higher temperatures in the radiant tube combustion zone which had an average temperature $\sim 1492°$C with a peak temperature of $2103°$C. In contrast, the Coanda flat plate burner had an average temperature of $\sim 1048°$C in the combustion zone with a peak temperature of $2033°$C. This highlights the potential of the Coanda burner of reducing emissions and providing a more homogeneous temperature.

Table 7.8: Operating conditions of the annealing furnace at Cogent Power.

Zone	1	2	3	4	5	Total
Heating power (kW)	490	490	665	665	420	2730
Length (m)	3.0	4.0	5.8	5.8	5.2	23.8
No. RT	14	14	19	19	12	78
No. RT top	8	8	10	9	6	41
No. RT bottom	6	6	9	10	6	37
Volume (m^3)	6.1	7.9	11.5	11.5	10.3	47.3
Zone temperature (°C)	840	850	880	880	880	-

7.3 CASE STUDY – ELECTRICAL STEEL ANNEALING FURNACE

7.3.1 *Overview of the current process*

As described in Section 2.5.2 one of the steps in the production of electrical steel is the continuous annealing and decarburisation process. The process needs to be carried out in a reducing atmosphere of wet H_2/N_2 mixture. As previously described in Section 2.5.4, the final quality of the electrical steel product is greatly determined by the initial heating rate of the electrical steel strip. A higher heating rate leads to better product quality.

The furnace analysed here is based on an actual furnace that was in operation at TATA Steel's Cogent Power site in Newport, United Kingdom. A detailed description of the furnace was made in Section 2.5.3, a brief recapitulation is made here. For temperature control purposes, the furnace is divided into 18 different zones. The first 5 zones have radiant tubes that are gas heated and the remaining 13 zones are electrically heated. The present work will only focus on the simulating the first 5 gas heated zones, the operating conditions and configuration for each of these zones are shown in Table 7.8. The current furnace consumes 2730 kW and has an average heating rate of ~ 27°C/s in its first 5 zones.

7.3.2 *Simulation strategy*

Tubing space constraints and the risk of the radiant tubes radiating heat to each other and produce hotspots that might damage them, make it impossible to simply add more tubes to the furnace in order to increase the heating rate of the electrical steel plate. It was expected that by using the proposed Coanda flat plate burner, the heating rate would increase mainly due to an increase in the overall radiating surface and by a decrease in the total furnace volume. Thus, the aim of the present work is not to provide a detailed simulation of the decarburisation process or the physical changes that occur in the electrical steel strip during the annealing. Instead, the present work will focus on the potential improvements that could result from changing the radiant tube burners for

the proposed Coanda flat plate burner. In particular, the improvement in the heating rate of the electrical steel strip, the reduction in furnace length and volume, the reduction in NO_x emissions, and a reduction in energy consumption. For this propose, three 2D geometries were created to conduct CFD simulations: (1) the current state of the furnace with the radiant tubes, (2) a radiant plate replacing the radiant tubes at their current position, (3) a radiant plate at half the current distance of the radiant tubes. Figure 7.16 shows the three computational domains for the simulations, where the hot radiant surfaces are coloured red, the furnace walls in black, and the electrical steel plate in blue. It was assumed that no chemical reactions take place inside the furnace.

7.3.3 *Boundary conditions*

Table 7.9 shows a summary of the boundary conditions applied to each one of the three simulations. A reference depth for the 2D domain of 1.467 meters was used. The reducing atmosphere inside the furnace was composed of a wet mixture of 75% H_2- 25% N_2 with a dew point of $\sim 65°C$ which gave an effective mixture of 60% H_2 - 20% N_2 - 20% H_2O. The Weighted Sum of Gray Gases (WSGG) model [181] was used to describe the emissivity and absorption of radiation from the H_2 - N_2 - H_2O mixture. The reducing atmosphere gas mixture entered the domain alongside the electrical steel plate at a mass flux of 0.60 kg/m²s and a temperature of 207°C. The temperature of the radiant tubes and of the Coanda flat plate burners were kept constant at a value equal to the temperature obtained in Section 7.2 ($\sim 885°C$). Emissivities of the hot radiant surfaces were set at a value of 0.8. The furnace wall was modelled as a thin wall and was assumed be made of insulating firebrick with a thickness of 0.4 m, a density of 432.7 kg/m³ [182], specific heat of 960 J/kg-K [183], thermal conductivity of 0.3548 W/m-K [182], and emissivity of 0.6 [184]. The electrical steel strip was modelled as a moving thin wall using the (Multi Reference Frame (MRF)) model available in Fluent with a specific velocity of 0.833 m/s in order to avoid the need of a dynamic mesh or a complex movement algorithm [185, 186]. This resulted in a strip mass flow rate through the furnace similar to the real value. The properties for the electrical steel were set as having a thickness of 0.3 mm, a density of 7650 kg/m³, specific heat of 600 J/kg-K, thermal conductivity of 28 W/m-K, and emissivity of 0.3 [187].

7.3.4 *Furnace comparison*

The heating rate of the three furnace configurations was compared, the results are shown in Figure 7.17. Table 7.10 shows the distance and time it took for each case to reach a temperature of $\sim 770°$ alongside the average heating rate, the total energy input, and heat flux. The current configuration with radiant tube burners took a total of 31.3 seconds to reach the target temperature and had an average heating rate of $\sim 25°C/s$. The heating rate value is close to the one of the real furnace
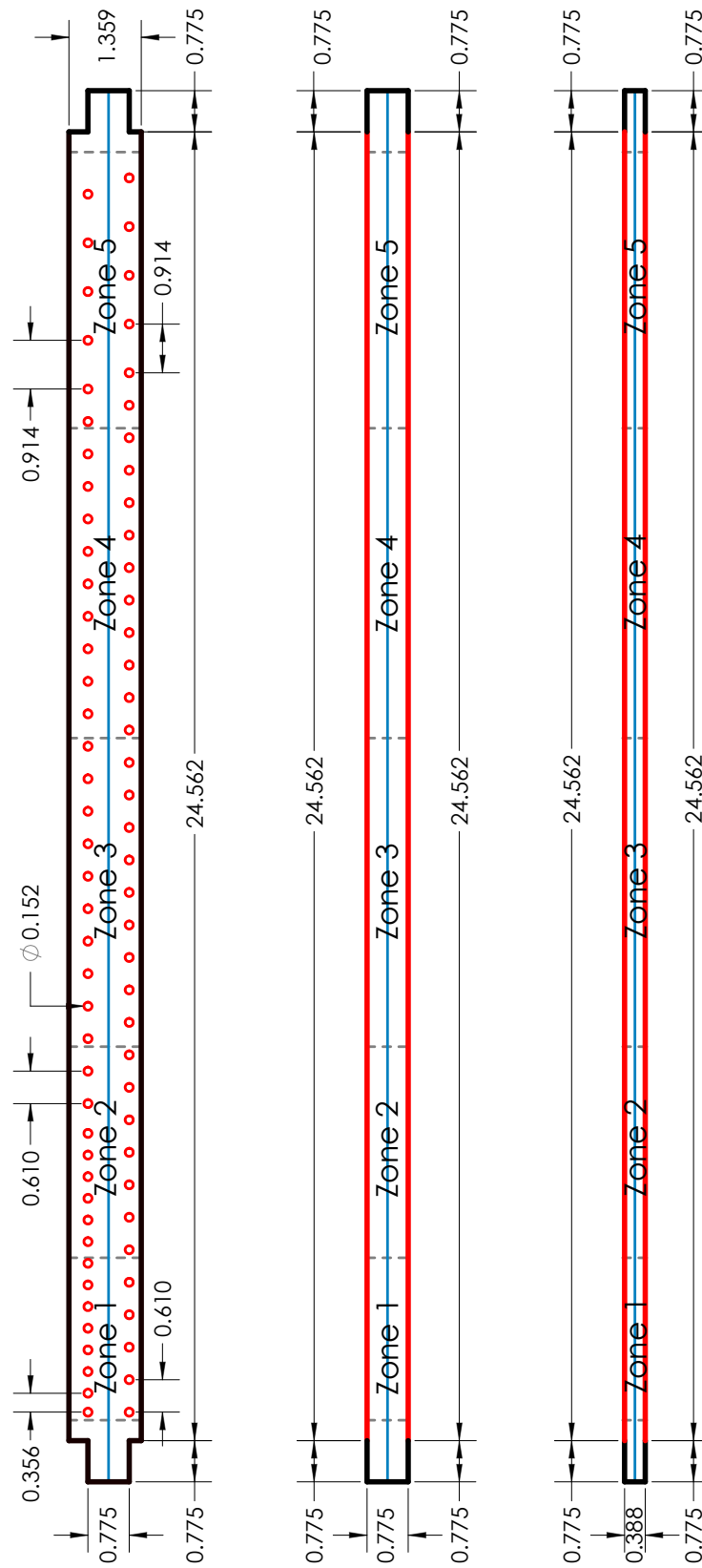
Figure 7.16: Computational domain for the furnace simulation. Dimensions are in meters.

Table 7.9: Boundary conditions, physical properties and thermal properties for the furnace simulation.

	Tubes	Plates (farther)	Plates (closer)
Furnace dimensions			
Radiant surface (m2)	54.76	72.06	72.06
Volume (m3)	48.65	29.69	14.84
Reference depth (m)		1.467	
Inlet conditions			
Inlet flow (kg/s)	1.196	0.682	0.341
Inlet temperature (°C)		207	
Composition (volume %)		60% H_2 - 20% N_2 - 20% H_2O	
Radiant surface characteristics			
Radiant surfaces temperature (°C)		885	
Emissivity		0.8	
Furnace wall characteristics			
Wall thickness (m)		0.4	
Density (kg/m3)		432.7	
Specific heat (J/kg-K)		960	
Thermal conductivity (W/m-K)		0.3548	
Electrical steel characteristics			
Strip speed (m/s)		0.833	
Strip thickness (mm)		0.3	
Density (kg/m3)		7650	
Specific heat (J/kg-K)		600	
Thermal conductivity (W/m-K)		28	
Emissivity		0.3	
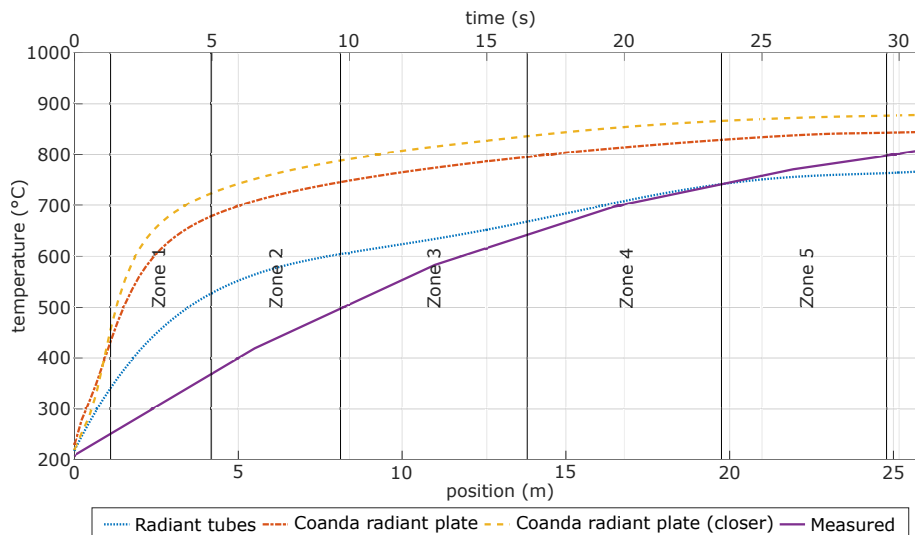
Figure 7.17: Heating rate for different furnace configurations.

at Cogent Power with a value of $\sim 27°$C/s. Both radiant plate cases performed better than the radiant tubes. The case with the radiant plates farther apart from the electrical steel strip took 12.4 seconds and had an average heating rate of $\sim 62°$C/s, while the case with the plates closer to the electrical steel strip took 7.9 seconds and had an average heating rate of $\sim 97°$C/s. These results translate into an increase in the heating rate of 148% and 288% and a decrease in heating time of 60.4% and 74.8%, respectively for the two previously mentioned radiant plates cases. In addition to the probable increase in product quality due to the increased heating rate, these results suggest that the length of the furnace could potentially be reduced.

The energy input for the case with the radiant tubes is the highest of the three cases with an energy input provided by the radiant tubes of 3098 kW. This value was close to the one of the real furnace at Cogent Power with a value of 2730 kW. The radiant plate cases performed better than the radiant tubes with an energy input of 1974 kW (decrease of 36.3%) and 1110 kW (decrease of 64.2%) respectively for the case with plates farther apart and the case with the plates closer to the electrical steel strip. The reason for this is in part because of the decreased mass flow at the inlet due to the decrease in furnace volume. It should be noted that the values provided here are just estimates and are used solely as an initial approximation to assess the potential of the proposed burner. A more complex simulation that coupled the combustion simulation of the Coanda burner with the furnace heating simulation would be required. However, such a simulation could be very computationally expensive.

7.3.5   *General remarks*

A comparison between three furnaces configurations was made via CFD simulations. The simulated cases were (1) the current state of the furnace with the radiant tubes, (2) a radiant plate replacing the radiant tubes

Table 7.10: Time and distance required to reach a temperature of $\sim 770°$, average heating rate, total energy input, and heat flux for each furnace configuration.

	length (m)	time (s)	heating rate (°C/s)	energy input (kW)	heating area (m²)	heat flux (kW/m²)
Tube	26.1	31.3	25	3098	54.8	56.6
Plate (farther)	10.3	12.4	62	1974	72.1	27.4
Plate (closer)	6.6	7.9	97	1110	72.1	15.4

at their current position, (3) a radiant plate at half the current distance of the radiant tubes. A constant temperature of $\sim 885°C$ was set as a wall boundary condition at the hot radiant tubes/plates. A gas mixture of 60% H_2 - 20% N_2 - 20% H_2O with a mass flux of 12 kg/m²s and a temperature of 207°C was set as an inlet boundary condition for the furnace. The electrical steel strip was modelled as a moving thin wall with a velocity of 0.833 m/s. The increase in the temperature of the strip through the furnace was compared between the three cases. The furnace with the radiant tube configuration performed the worst by having an average heating rate of $\sim 25°C/s$, taking 31.3 seconds to reach the final temperature of $\sim 770°$ and requiring an energy input of 3098 kW. These values are close to those of the real furnace at a value of $\sim 27°C/s$ and 2730 kW. The furnace with the radiant plates farther apart from the electrical steel strip performed the second best with a heating rate of $\sim 62°C/s$, taking 12.4 seconds to reach a temperature of $\sim 770°C$ and requiring an energy input of 1974 kW. The best performance was the case with the radiant plate closer to the electrical steel strip with a heating rate of $\sim 97°C/s$, taking 7.9 seconds to reach a temperature of $\sim 770°C$ and requiring an energy input of 1110 kW. This means that, compared to the radiant tube case, the radiant plate cases respectively had an increase in the heating rate of 148% and 288%, a decrease in heating time of 60.4% and 74.8%, and decrease in energy input of 36.3% and 64.2%. These results suggest that an increased furnace performance can be achieved by substituting the radiant tube burners for Coanda radiant plate burners.

7.4   CHAPTER SUMMARY

A parametric analysis of the Coanda burner was made using CFD simulations with the objective of identifying a configuration that increased the heat flux through the radiant plate, increased the temperature homogeneity, and reduced emissions. For this purpose, the factors that were varied were: partially-premixed or non-premixed, nozzle diameter ($D_0 = 28$ mm and $D_0 = 24$ mm), secondary inlet position ($P = 29$ mm

and $P = 12$ mm), confinement height ($H = 56$ mm and $H = 70$ mm), and the air ratio in the premixed and air inlet ($aR = 1.3$ and $aR = 1.0$ - only applicable to the partially-premixed case). The best configuration for the partially-premixed and non-premixed cases was identified and compared between them. It was found that, overall, the partially-premixed configuration was detrimental for the stated objectives and the non-premixed case provided a much better temperature homogeneity and NO_x reduction. The best configuration for the non-premixed case was that with the smaller nozzle diameter, bluff body at the position closer to the nozzle outlet, and bigger confinement height.

The best burner configuration that was identified in the parametric analysis was scaled-up by multiplying its dimensions by a factor of between ~ 2.0 and ~ 2.5. This scaled-up burner was then compared via CFD simulations with a radiant tube burner. Both devices had the same radiating surface area, thermal boundary conditions, and amount of fuel. The results showed that both devices had an average boundary temperature at the radiant wall of $\sim 885°C$. The radiant tube burner had a total heat flux of -28041 W/m², a minimum radiant tube temperature of $\sim 832°C$, a maximum radiant tube temperature $\sim 918°C$, and a standard deviation of $24.01°C$. In contrast, the Coanda burner had a lower total heat flux of -23325 W/m² but a better temperature homogeneity across the radiant surface boundary with minimum temperature of $\sim 883°C$, a maximum temperature $\sim 886°C$, and a standard deviation of $0.99°C$. The Coanda flat plate burner had NO_x emissions 18 times lower than those of the radiant tube burner, mainly due to the much higher temperatures in the radiant tube combustion zone which had an average temperature $\sim 1492°C$ with a peak temperature of $2103°C$. In comparison, the Coanda flat plate burner had an average temperature of $\sim 1048°C$ in the combustion zone with a peak temperature of $2033°C$.

Finally, a comparison between different furnaces was made by taking the results from the burner scale-up comparison as input boundary conditions. For this, three cases were considered (1) the current state of the furnace with the radiant tubes, (2) a radiant plate replacing the radiant tubes at their current position, (3) a radiant plate at a distance of half the current distance of the radiant tubes. The same boundary conditions were used for the three cases: $\sim 885°C$ as wall temperature for the hot radiant tubes/plates, mass flux inlet of 12 kg/m²s with a gas mixture composition 60% H_2 - 20% N_2 - 20% H_2O and a temperature of $207°C$. The electrical steel strip was modelled as a moving thin wall with a velocity of 0.833 m/s. The heating rate, time to reach a temperature of $\sim 770°$, and required energy input at the hot surfaces were compared between the three cases. The furnace with the radiant tube configuration had an average heating rate of $\sim 25°C/s$, taking 31.3 seconds to reach the target temperature and requiring an input of 3098 kW. These values are close to those from the real furnace at a value of $\sim 27°C/s$ and 2730 kW. The case with the radiant plates farther apart from the strip had an average heating rate of $\sim 62°C/s$, taking 12.4 seconds to reach the target temperature and requiring an input of 1974 kW. The case with the radiant plate closer to the strip had an average heating rate of $\sim 97°C/s$,

taking 7.9 seconds to reach the final temperature and requiring an input of 1110 kW. Thus, compared to the radiant tube case, the radiant plate cases respectively had an increase in the heating rate of 148% and 288%, a decrease in heating time of 60.4% and 74.8%, and decrease in energy input of 36.3% and 64.2%.

These results suggest that substituting the radiant tube burners for Coanda radiant plate burners could potentially reduce the energy consumption of the furnace, decrease the heating time, decrease the NO_x emissions, and improve the product quality of the electrical steel strip by providing a faster and more homogeneous heating rate.

DISCUSSION

The present investigation was initially motivated by the requirement of the electrical steel industry to develop a technology that could increase the heating rate of the electrical steel strip to $\sim 100°C/s$ during the primary recrystallization annealing. To achieve the required heating rate, the Coanda flat flame burner was proposed. In addition to the increased heating rate, some other benefits were expected from this development. These were a decrease in emissions, fuel consumption and furnace volume. Additionally, in the case of electrical steel, an increase in heating rate would also lead to an improvement in the magnetic properties. The proposed technology should not be solely considered for the heating of the electrical steel strip, any application that involves the heating of long flat surfaces could benefit from this development.

To develop the Coanda burner some interim objectives needed to be accomplished. The fluid mechanics behind the onset of the Coanda flow and their dependency on the burner geometry, confinement geometry and flow conditions needed to be understood. Also, the initially proposed burner needed to be optimised. Finally, an assessment of the benefits of using this burner instead of the typically used radiant tube was required in order to ensure the viability of the proposed technology. In this chapter, a summary of the results and a comparison with the available literature will be made. Each section of this chapter corresponds to one of the chapters of this thesis. The final section summarises the factors that need to considered for the development of the proposed Coanda burner and the expected benefits it would produce in the application that motivated this thesis.

8.1 ISOTHERMAL EXPERIMENTS

Two different flow patterns were identified during the isothermal experiments. The observed flow patterns could be obtained under the same geometry and flow conditions. The first flow pattern was an OJF which consisted of a vertical jet core with a CRZ. The second flow pattern was a CoJF which consisted of a radial wall attached jet core with a downward velocity profile at the centre of the nozzle. For the CoJF pattern, a higher deflection of the jet towards the base plate was observed with increased flow rate. It is theorised that the increased jet inclination is related to a stronger attachment of the jet core to the flat plate by a vortical structure in the outer shear layer of the jet. These flow patterns have been previously observed by some researchers. Vanierschot and Van den Bulck [88] reported four different flow patterns with hysteresis. The flow patterns transitioned between them by a change in the applied swirl. The obtained flow patterns were CJF, OJF-LS, OJF-HS, and CoJF. In the present work, the CJF and one of the OJF flow patterns were not

obtained. It was expected not to be able to obtain the CJF because it is only possible at a low applied swirl. Due to the difference in geometries, the question remained of whether two OJF patterns were possible with the nozzle configuration used in this work. It was not possible to answer this question because no variable swirl control was available during the experiments.

A temporal power spectrum analysis was made for the different flow rates that were studied. It was found that the Strouhal number and frequency of the OJF and CoJF increased linearly with respect to the flow rate. Additionally, the CoJF showed an increase in Strouhal number of $\sim 8.5\%$ with respect to the OJF. This observation was consistent across all the tested flow rates. The observed frequency is related to the precessing motion of the PVC. The linear increase in frequency with increased flow rate can be explained by the study made by Frederick et al. [188]. The authors showed that the PVC frequency increased with an increase in the applied swirl. In the present work, because the swirl generator had fixed vanes, any increase in flow rate would produce an increase in swirl number. However, because the swirl number upstream the nozzle exit should be the same between the two flow patterns, it is argued that the increase in Strouhal number and frequency in the CoJF with respect to the OJF is a consequence of the flow stagnation with the base plate.

The precessing and turbulence components of the flow were identified via POD. Snapshots of the OJF and CoJF were reconstructed using the first two POD modes. The reconstructed flows were subsequently phase averaged. Swirl strength values were calculated for each phase averaged flow field. Coherent structures were then visualised by projecting the flow fields into a 3D space with the appropriate angular spacing between them. The flow fields in the 3D space were then interpolated. Two helical vortices were found in both the OJF and CoJF. These helical structures are related to the PVC. In the CoJF these vortices had been previously mentioned in the literature. Vanoverberghe et al. [87] mentioned the existence of the vortex trapped between the jet core of the CoJF and the base plate. By doing a balance of forces in the jet core, the authors suggested that the low-pressure region generated by this vortex is responsible for attaching and stabilising the CoJF to the base plate. Singh and Ramamurthi [94] made a similar observation. In the present work, the precessing characteristics and their effect in the instantaneous flow behaviour were described. The precessing motion of the PVC continuously detaches and reattaches the flow jet to the base plate.

The effect of the position of the base plate with respect to the nozzle was investigated. When the base plate was aligned to the nozzle exit it was possible to obtain the CoJF irrespective of the nozzle opening angle. As the base plate was further apart from the nozzle, the flow had the possibility of being in an OJF or a CoJF. If the distance was further increased, only the OJF was obtainable. A general observation derived from the results of these experiments was that, for the CoJF close to transition, it is necessary that the flow remains in contact with the nozzle. A combination of shear and low pressure can support the

coherent structures required for the existence of the CoJF. These results highlight the importance of the adequate design of the burner geometry in order to have a stable CoJF.

8.2 COMBUSTION EXPERIMENTS

8.2.1 *Unconfined experiments*

Different flow patterns were identified during the combustion experiments. These were a stable nozzle attached flame, a lifted flame, and a wall attached Coanda flame. Transition flame states between these flow patterns with a change in flow rate and equivalence ratio were also identified. The observed flames coincide with the flames reported by Vanoverberghe et al. [81] under the names NSF, SSF and CSF. Some similarities and discrepancies in the results are worth pointing out. Some of the flames reported by Vanoverberghe et al. were not obtained in the present work (see Figure 2.8 in Section 2.3.3). These were the BSF and the PJF. The BSF is simply an effect of the combination of blow-off and flame stabilisation at the confinement outlet. The flame pattern identification in this work was done without a confinement which made impossible to obtain this flame. The PJF might have been a unique result that was dependent on the nozzle geometry used by Vanoverberghe et al. However, it is impossible to make further discussion on why this flame was not obtained in the burner studied in this work because Vanoverberghe et al. does not go into the detail of the mechanisms that produce the PJF. Another difference from the work of Vanoverberghe et al. is that in the experiments reported in this thesis, the SSF and CSF where obtained under the same flow conditions. Also, in certain limited cases, it was also possible to obtain an NSF and a CSF under the same conditions. In the experiments by Vanoverberghe et al. the NSF and CSF could not exist using the same flow conditions.

Another finding of the present work was the existence of the Coanda flashback state. It was seen that with an increase in the inlet air (i.e. decrease in equivalence ratio) the flame length decreased. The increase in flame length can be attributed to a combination of factors. First, the increased mass flow produced an increase in the effective swirl. Then, the increase in swirl pulled the reactants closer to the nozzle. Additionally, because of the fuel-rich equivalence ratios used in the experiments, the increased air allowed for a faster consumption of the reactants and avoided the need to mix additional ambient air. What made evident these observations, was the fact that with an increased air flow the base plate got much hotter just at the exit of the nozzle. Kwark et al. [97] also reported on the changes in the flame length and temperature with a change in the applied swirl. The authors mentioned that with an increase of the applied swirl the flame became wider and the temperature in the region close to the nozzle exit decreased. However, the experimental results and observations in this thesis do not completely agree with the results shown by Kwark et al. An increase in swirl would initially push the flame further outwards the nozzle.

However, a point would be reached where the flashback propensity will increase and the flame will start to get closer to the nozzle exit. Results by Singh and Ramamurthi [94] seem to confirm this observation. Using an isothermal flow, the authors observed that the recirculation bubble between the Coanda jet and the base plate got closer to the nozzle with an increase in flow rate at a fixed swirl number.

A novel contribution of the present work is the observation that the equivalence ratio affects the flow pattern. Previous research had focused on using a single flow rate. While it is true that most of the industrial applications would only use a single equivalence ratio (usually a lean flame with an excess of air of about 5%), the observation remains relevant because the flame state could be impacted by drops in pressure from either the gas flow or the air flow changing the instantaneous equivalence ratio. Due to hysteresis present in the flow, such changes in equivalence ratio might leave the flame in an undesired state. A further contribution of the present work was the finding that the nozzle diameter has a significant impact on the onset of the Coanda effect. Too big of a diameter reduces the effective region where the Coanda effect can be obtained. Too small of a diameter increased the propensity of the Coanda flashback.

A limitation of the present study should be pointed out here. The experimental device that was used had a swirl generator with a fixed swirl number. This means that a change in the mass flow rate would lead to a change in the effective swirl number. Thus, with the current experimental setup, it was impossible to completely differentiate the effect that a change in flow rate, change in the swirl, change in nozzle diameter, and change in equivalence ratio would have had in the flame flow pattern. Additionally, the flame flow pattern experiments were carried out without a confinement, so the observed equivalence ratio is not entirely accurate. Further experiments should remedy these limitations by measuring the flow velocity components in order to be able to calculate the actual swirl number of the flow. A variable swirl generator should also be used in order to capture the dynamic effect a change in the applied swirl can have in the flow pattern.

8.2.2 *Confined experiments*

One of the main questions that the confined experiments aimed to answer was the feasibility of having a Coanda flame inside a confinement. Due to the nature of the flow pattern, the Coanda effect requires a low-pressure zone above the flat flame. The obtained results successfully answer one of the initial questions that motivated this investigation. This is, the Coanda flame can indeed exist within a confinement with a relatively low height. Additionally, Vanoverberghe et al. [87] had suggested that the confinement walls play an important role in the stability of the Coanda effect by the creation of an ERZ in the corner of the confinement. The authors noted that with a confinement length longer than 400 mm the Coanda flame became unstable. The present work shows different results. The confinement used here produces the Coanda effect

with a slightly longer confinement length of 488 mm. Additionally, the confinement had the combustion gases outlet at the edges of the bottom plate. The longer confinement and the outlet position would reduce the ERZ. This indicates that the ERZ does not play such an important role in the stability of the Coanda flame.

There are additional insights obtained from the experimental results and observations presented in this thesis. The current design is not optimal for having a homogeneous temperature profile at the radiant plate. The highest temperature of the radiant plate ($\sim 225°$C) was located at its centre and the lowest temperature ($\sim 150°$C) was located at the edges. This resulted in a difference in ΔT of $\sim 75°$C. CFD simulations on the burner indicated that a different injection system for the reactants would improve the temperature homogeneity. Additionally, when the confinement was heated by the Coanda flame thermal deformation occurred. This was particularly noticeable at the base plate where the Coanda flame is attached. As mentioned previously, the distance between the nozzle exit and the base plate has a very important role in the stability of the Coanda flame. With the expansion, consequence of the increase in of the base plate, the plate curved outwards. The curvature changed the distance of the base plate with respect to the nozzle outlet. If the distance was not adjusted, the Coanda flame transitioned into a lifted flame. Further designs of a burner such as this one must remedy this by making the nozzle and the base plate a single piece of equipment or by using materials with lower thermal expansion.

8.3 CFD VALIDATION

8.3.1 *Isothermal simulations*

CFD simulations were conducted to replicate the isothermal experiments presented in the previous chapters. Flows that have hysteresis present a unique challenge for any numerical simulation. This is because the obtained result can be any of the two possible states which may cast doubt on the results. More so, different models can produce different results. To use the CFD simulations to test conceptual designs, a comparison with experimental data was required in order to validate the methods used and ensure that the obtained results are something that can will occur if experiments were made. For that purpose, in the present work, several steps were taken. First, a grid independence study was made using the GCI method. Then different turbulence models were tested. For these tests, the applied inlet swirl was increased and subsequently decreased. The obtained flow resulting from a change in the applied swirl was recorded. As the existing literature indicates, the flow pattern that can be obtained is directly dependent on the applied swirl intensity. The swirl number at the nozzle outlet was calculated and compared to the PIV experiments. It was found that the overall flow pattern of the SST $\kappa - \omega$ and RSM models did not match with the experiments. The models greatly over predicted the transition points and the swirl number at the nozzle outlet. Standard $\kappa - \epsilon$ and Realizable $\kappa - \epsilon$ turbulence models

produced similar transition points and flow patterns between them that were closer to the experimental results.

Vanierschot and Van den Bulck [89] did a similar study. Two turbulence models were tested, the Standard $\kappa - \epsilon$ and the RSM. Both tested turbulence models predicted the velocity profiles, swirl transition points and flow patterns reasonably well (see Figure 2.10 in Section 2.3.3). In their study, Vanierschot and Van den Bulck obtained four different flow patterns CJF, OJF-LS, OJF-HS, and CoJF. In this thesis, using the Standard $\kappa - \epsilon$ and Realizable $\kappa - \epsilon$ turbulence models produced only three flow patterns CJF, OJF-LS, and CoJF. Using the SST $\kappa - \omega$ and RSM models a similar flow pattern to the OJF-HS was obtained. However, the OJF-HS was not observed during the experiments. Gritskevich et al. [92] made another numerical study with the same setup used by Vanierschot and Van den Bulck. The authors used the SST $\kappa - \omega$ turbulence model. In their results, the SST $\kappa - \omega$ model did not predict accurately the velocity profiles or the swirl transition points. This agrees with the results obtained in the present investigation where the SST $\kappa - \omega$ was not able to predict the flow transition points of the experimental burner. Thus, for numerical simulations involving flows of the type studied here the SST $\kappa - \omega$ is not recommended.

One of the observations made by Vanierschot and Van den Bulck in their study is how surprisingly well the Standard $\kappa - \epsilon$ predicts the four flow structures, the transitional swirl numbers and the global hysteresis. This is despite the fact that the Standard $\kappa - \epsilon$ is known to have issues when highly swirling flows are present. A similar conclusion is drawn from the results of this thesis. Despite not having a variable swirl generator available for the experiments, the available data from the experiments indicate that the best turbulence models for these types of flows are the Standard $\kappa - \epsilon$ and Realizable $\kappa - \epsilon$. This is due to their accuracy in predicting the transition points and the relatively low computational resources that they require.

A notable difference between the results of this thesis and the study made by Vanierschot and Van den Bulck [89] and the one by Gritskevich et al. [92] is the impossibility of having the CoJF pattern at very low swirl numbers. For the Realizable $\kappa - \epsilon$ turbulence model, the lowest swirl number at which a CoJF was possible was ~ 0.5. With the burner used by Vanierschot and Van den Bulck, the CoJF was stable even at zero swirl. This suggests that the nozzle geometry plays an important role in the stability of the CoJF. The difference might be related to the corner recirculation zone formed at the nozzle step of the device used by Vanierschot and Van den Bulck which adds additional stability to the Coanda flow. The follow-up study by Vanierschot and Van den Bulck [90] confirms this. The authors tested several nozzle geometries. One such geometry did not have a step in the nozzle. In this geometry, the CoJF could not be obtained (see Figure 2.11 in Section 2.3.3). The authors mention that the presence of the step is crucial for having the CoJF. However, contrary to this observation, the CoJF was possible in the experimental and numerical setup used in this thesis even without the step. This might be due to the short nozzle expansion used which

preserves the radial velocity component. From these results, it is clear that an important design parameter for a device of this type is the nozzle geometry.

8.3.2 *Combustion simulations*

CFD combustion simulations were conducted to replicate the combustion experiments presented in the previous chapters. These simulations consider the information obtained from the isothermal simulations. The combustion simulations use the turbulence model and numerical grids that were selected for the isothermal simulations. The objective of the combustion simulations was to validate the chosen combustion and radiation models, as well as, confirming the suitability of the Realizable $\kappa - \epsilon$ for modelling the reacting flows. To do this, the results of an unconfined simulation were compared with the PIV experimental data. Additionally, a confined simulation was compared to the experimental results. For the confined simulation, the compared parameters were the radiant plate temperature and the combustion gases temperature. It was found that the chosen models and the applied boundary conditions approximate the experiments with a good enough degree of accuracy. It is challenging to pinpoint relevant literature with which the results and methods followed in this part of the investigation can be compared. However, because of the methodology that was followed (grid independency study and comparison with experimental data) and because the isothermal simulations yielded similar results to the ones available in the literature, it is possible to say that the results are accurate and the procedures followed are solid.

Furthermore, opportunities for the improvement of the experimental burner design were identified. The main opportunity was related to the central axial air injection method. This had two downsides, it cooled down the central part of the plate and concentrated the reaction in the central region of the plate. These two factors caused the current design to not have a homogeneous temperature profile across the radiant plate surface. The observations of these simulations are used for improving the design of the current burner.

8.4 CFD BURNER OPTIMISATION, SCALE-UP, AND IMPLEMENTATION

8.4.1 *Parametric study*

A parametric analysis was conducted on the confined Coanda burner. The objective was to identify a configuration that increased the heat flux through the radiant plate, increased the temperature homogeneity, and reduced emissions. The simulations used the information obtained from the isothermal and combustion simulations conducted in Chapter 6. These where mainly the selected grids and the validated turbulence, combustion, and radiations models. The use of these models and grids

ensures that the obtained results in the parametric optimisation and subsequent scale-up are accurate and will reasonably predict what would happen if the same tests were done experimentally. Two overall geometries were evaluated. In the first one, the reactants were fed into the domain partially-premixed with an axial injection of supplementary air through a central rod. In the second geometry, the reactants were fed into the domain non-premixed with the fuel injected at an angle immediately downstream the nozzle. The nozzle diameter, secondary inlet position, confinement height, and the air ratio in the premixed and air inlet were varied.

For both, the partially premixed cases and the non-premixed cases, a decrease in the nozzle diameter increased the outward plate radiation, increased the plate temperature homogeneity, and decreased the NO_x emissions. The reason for these changes can be attributed to the increase in flow velocity produced by having a smaller primary inlet nozzle diameter. This increase in flow velocity produced greater turbulence and mixing rate within the confinement which produced a better temperature homogeneity. A better temperature homogeneity decreased the local temperature peaks, therefore reduced the formation of thermal NO_x. The increase in the confinement height allowed for a higher residence time that also increased the temperature homogeneity. The greater temperature homogeneity reduced the local hot zones and decreased thermal NO_x production. Obviously, there is a compromise, one cannot increase the volume of the confinement indefinitely, as increasing the confinement size will increase the surface area of the walls causing heat losses.

Overall, it was seen from both the partially premixed cases and the non-premixed cases, that the confinement height had the greatest impact on the outward radiation and the standard deviation of the radiant surface temperature, while the nozzle size had the biggest impact on the NO_x concentration in the flue gases.

By comparing the optimal configuration of the partially premixed case against the optimal configuration of the non-premixed cases, it was clear that the non-premixed case was clearly superior. The non-premixed case greatly decreased the thermal NO_x formation, from 1.15 to 0.04 ppm, and the temperature homogeneity of the radiant plate.

It should be noted here that these simulation results suggest that a Coanda flame is possible even without any degree of air premix. In the previously mentioned study by Vanoverberghe et al. [81], the authors were not able to obtain a Coanda flame when the air and fuel were not partially premixed to some degree (see Figure 2.8 in Section 2.3.3). The difference in the results might be related to how the gas is added and the nozzle geometry. In the study by Vanoverberghe et al., the fuel was added radially through a central fuel rod. In the simulations of the present investigation, the fuel was added to the air after the onset of the Coanda flow. This might add additional stability to the Coanda effect by having the gas expansion due to the combustion taking place downstream of the structures responsible for anchoring the Coanda

flow. Further experimentation is suggested in order to validate the non-premixed geometry that resulted from the parametric analysis.

8.4.2 *Comparison between Coanda burner and radiant tube*

A scaled-up version of the optimised non-premixed Coanda burner that resulted from the parametric analysis was compared with a recuperative single-ended radiant tube burner reported in the literature [176, 177]. The burner dimensions were scaled-up by multiplying its dimensions by a factor of between $\sim$ 2.0 and $\sim$ 2.5. A return annulus for the hot flue gases was added to the burner in order to account for the recuperator in the radiant tube burner. The radiating area was kept the same between both devices. Both burners produced the same average temperature of $\sim$ 885°C at their respective radiating outer surface. This was an expected result because both burners had the same boundary conditions and radiating area. However, the temperature distribution and the heat flux varied considerably between the two burners. The radiant tube burner had a higher heat flux at $-28,041$ W/m², but it also had a greater temperature difference between the highest and lowest temperatures in the radiating surface with a $\Delta T = 86°C$ and a standard deviation of 24.01°C. The Coanda burner had a lower heat flux at $-23,325$ W/m², but had an almost negligible ΔT of 6°C and a standard deviation of 0.99°C. In addition to the better temperature homogeneity, the Coanda burner also produced NO_x emissions 18 times lower than those of the radiant tube burner. The lower NO_x emissions are a consequence of the overall lower flame temperature in the Coanda burner. The lower temperature is caused by the spread of the flame which increases the radiation of the flame to the confinement walls; and by the nature of the Coanda flow which produces a re-circulation of the "cold" combustion gases towards the flame zone which cools the area down. The explanation given here for the reduction in NO_x is confirmed by similar results obtained by Kwark et al. [97] and Vanoverberghe et al. [87]. The results of the comparison between the Coanda radiant plate burner and the radiant tube burner confirm the initial hypothesis that motivated the present investigation: the Coanda flat flame radiant burner can produce a homogeneous temperature profile while having very low NO_x emissions.

8.4.3 *CFD furnace*

A comparison between three furnace configurations was made via CFD simulations. The boundary conditions for the simulation were taken from the results of the comparison between the Coanda flat plate radiant burner and the radiant tube. The aim of the study was to assess the feasibility and expected benefits of substituting the radiant tubes for the proposed burner. The simulated cases were (1) the current state of the furnace with the radiant tubes, (2) a radiant plate replacing the radiant

tubes at their current position, and (3) a radiant plate closer to the load at half the distance of case 2.

Case 1 performed the worst by having an average heating rate of $\sim 26°\text{C/s}$, taking 31.3 seconds to reach a temperature of $\sim 770°\text{C}$ and requiring an energy input of 3098 kW. These values are close to those of the real furnace which are $\sim 27°\text{C/s}$ and 2730 kW. Case 2 performed the second best with a heating rate of $\sim 62°\text{C/s}$, taking 12.4 seconds to reach a temperature of $\sim 770°\text{C}$ and requiring an energy input of 1974 kW. Case 3 had the best best performance with a heating rate of $\sim 97°\text{C/s}$, taking 7.9 seconds to reach a temperature of $\sim 770°\text{C}$ and requiring an energy input of 1110 kW. This means that, compared to the radiant tube case, the radiant plate cases respectively had an increase in the heating rate of 148% and 288%, a decrease in heating time of 60.4% and 74.8%, and a decrease in energy input of 36.3% and 64.2%. These results suggest that an increased furnace performance can be achieved by substituting the radiant tube burners for Coanda radiant plate burners. An additional expected benefit of reducing the volume of the furnace is a decrease in start-up times which would save time and energy every time the furnace is turned back on after maintenance. These results further highlight the potential of the proposed burner as a substitute for the currently used radiant tube burners.

8.5   BURNER DESIGN CONSIDERATIONS AND EXPECTED BENEFITS

Based the information available in the literature and considering the results obtained in the experiments and simulations conducted in this investigation, any future Coanda burner that is designed for applications such as the one proposed in this thesis should:

- Have a careful design of the nozzle in order to be able to have a Coanda effect with the required flow rates and equivalence ratios.

- The burner should be fitted with a variable swirl generator.

- The air/fuel injection system must be made in such a way that the flame length is maximised.

- As an alternative for the variable swirl generator, a flow control device such as the one proposed by Vanierschot et al. [91] might be used. However, its feasibility in a reacting flow needs to be verified.

- To avoid a change in flow pattern due to changes in the flow conditions, the burner should operate in a region where the Coanda flow does not present hysteresis.

- If the previous point is not possible, a control system that monitors the state of the flame must be in place.

- The control system will detect any change in the flow pattern and make the required changes in the applied swirl in order to bring the flame back to a Coanda flow.

- The control system can be either an optical device that measures the flame luminosity or a pressure-based device such as the one used by Vanierschot and Van den Bulck [90].

- Care must be taken in the materials chosen for the nozzle and base plate, any deformation of the materials might change the surface geometry and alter the Coanda effect.

A potential downside of the proposed burner in comparison to a single-ended recuperative radiant tube burner was:

- A decrease in radiant heat flux.

However, this downside was compensated by an increase in the total radiating area in the furnace. The expected benefits of the proposed burner in comparison to a single-ended recuperative radiant tube burner are:

- Increase in heating rate.

- Reduction in energy requirement.

- Reduction in NO_x emissions.

- Reduction in heating time.

- Increase in temperature homogeneity of the load.

- Reduction in volume furnace with the consequential reduction in start-up times.

CONCLUSIONS

This investigation developed a novel burner that produces a flat wall attached flame by use of the Coanda effect. It has revealed that critical factors that affect the onset and stability of a Coanda flame are the intensity of applied swirl, the flow rate, the relation between plate height and the nozzle outlet, the equivalence ratio and the nozzle geometry. The developed burner proves to be a feasible and improved alternative to the currently used technology of radiant tubes. The use of this technology can increase the heating rate and uniformity to the load, reduce energy consumption, reduce NO_x emissions, reduce the volume of the furnace and reduce start-up times.

The major findings of this study can be summarised as:

- To obtain a Coanda flow a base plate fitted just at the nozzle outlet is required. With an adequate combination of nozzle angle and plate step size, both the OJF and the CoJF are possible. For the Coanda flow pattern, an increase in the jet angle at the nozzle outlet occurs with an increase in flow rate.

- A PVC was identified in the CoJF. The frequency of the PVC increases linearly with an increased flow rate. This behaviour had been previously reported in the literature for an OJF but not for a CoJF. The CoJF shows an increase in Strouhal number of $\sim 8.5\%$ with respect to the OJF. The increase is consistent across all the tested flow rates. The higher frequency in the CoJF is a consequence of its stagnation to the bottom surface.

- The propensity of the flow to stay at either an OJF or a CoJF pattern is correlated to the energy content of the most energetic POD modes. This is when the contained more energy than the CoJF the flow tended to spontaneously transition to the OJF and stay like that. The same was true for when the most energy was obtained by the CoJF.

- A helical precessing vortex pair was found in both the OJF and CoJF. These helical structures are related to the PVC. The vortex pair in the CoJF is located at the inner shear layer of the jet and between the outer shear layer of the jet and the plate. Phase averaged snapshots of the flow indicate that the precessing vortex structure influences the detachment and reattachment of the CoJF to the base plate. A 3D reconstruction of the flow for visualisation of the spiral vortex pair was done for both the OJF and CoJF.

- The distance of the base plate and nozzle opening angle has a direct effect on the possibility to obtain an OJF, a CoJF or both. The

base plate at a position closer to the nozzle favours the stability of the CoJF while a position farther apart from the nozzle favours the stability of an OJF. Similarly, a nozzle opening angle of 30° favours the stability of the CoJF while an angle of 60° favours the stability of an OJF.

- For a reacting flow, six possible flow states where observed. A nozzle attached flame, a lifted flame, a flame in flashback, the transition between lifted flame-flashback, a Coanda flame, and the transition between a Coanda flame-flashback Coanda flame. The state of the flame depended on the amount of swirl applied, the nozzle opening angle, the mass flow rate of the reactants, and the equivalence ratio.

- It was not possible to obtain a Coanda flame if not enough swirl was applied to the flow.

- The Coanda flame was only obtained with a nozzle opening angle of 45° and was not possible with a nozzle opening angle of 30° or 60°.

- Reducing the nozzle diameter increased the stability of the Coanda flame but it also increased the propensity of Coanda flashback. Decreasing the nozzle diameter produced a less stable Coanda flame but reduced its propensity to flashback. Thus, there is a compromise between using a smaller diameter nozzle to obtain a Coanda flame that is hotter and smaller in diameter but more stable and using a larger diameter nozzle to obtain a Coanda flame that is bigger in diameter and cooler but less stable.

- The Coanda flame length was increased with an increase in equivalence ratio. An increase in the nozzle diameter also resulted in an increase in flame length. The Coanda flame length is related to the Coanda flashback state. The closer to that state, the shorter and hotter the flame is going to be.

- Two thresholds were identified in the stability map of the Coanda flame that suggest that two factors influence the onset and breakdown of the Coanda effect. These are the velocity of the gases at the nozzle exit and the combustion stability. The Coanda combustion stability is specifically influenced by the flashback point, at this point the Coanda flow breaks down and transitions into a lifted flame close to flashback.

- The Coanda flame inside a confinement was stable when adding supplementary air axially through a secondary inlet. The confinement and the axial air injection did not break the Coanda flow pattern. When the thermal equilibrium between the confinement and the ambient temperature was reached, it was found that the temperature distribution along the top surface of the confinement was not homogeneous.

- A potential complication identified with a confined Coanda flame was the thermal expansion of the base plate and the nozzle. As the confinement thermally expanded, the $\Delta X/D$ of the plate with respect to the nozzle outlet changed. This change in $\Delta X/D$ made the Coanda flame transition into a lifted flame. This is a design factor that needs to be considered.

- For the simulations, a simplification of the full burner geometry to a two-dimensional axisymmetric geometry yielded adequate results that were comparable to the experimental measurements.

- The OJF and CoJF presented hysteresis between them, which depended on the applied swirl intensity. A higher swirl intensity made the OJF transition into a CoJF. With a subsequent decrease in swirl intensity, the CoJF could be maintained at a value lower than the one that produced its initial onset. At a certain swirl intensity value, the flow transitioned back to an OJF.

- Of the four tested turbulence models (Standard $\kappa - \epsilon$, Realizable $\kappa - \epsilon$, SST $\kappa - \omega$, and Reynolds Stress), the model that best described the flow patterns and transition points was the Realizable $\kappa - \epsilon$. This is a notable result due to the known problems that $\kappa - \epsilon$ models have when modelling swirling flows.

- The turbulence Realizable $\kappa - \epsilon$ model, combustion finite-rate/eddy-dissipation model, and radiation P-1 model adequately reproduce the experimental combustion results.

- Opportunities were identified in the current experimental combustion setup that were related to the central axial secondary air injection system. The system cooled down the central part of the plate and concentrated the reaction in the central region of the plate. This resulted in non-homogeneous heating of the confinement radiant plate.

- A parametric analysis was conducted on the laboratory Coanda burner. Two general geometries were tested, one with the reactants in a partially-premixed regime and another one with the reactants in a non-premixed regime. Additional varied factors were the nozzle diameter, the secondary inlet position, the confinement height and the air ratio. The non-premixed configuration performed better by increasing the heat flux through the radiant surface, increasing the temperature homogeneity and reducing emissions.

- The Coanda burner was scaled-up and compared to a single-ended recuperative radiant tube burner. The Coanda burner showed an improved temperature distribution in its radiant surface with a standard deviation of 0.99°C. In comparison, the radiant tube burner had a standard deviation of the temperature of 24.01°C. Emissions were 18 times lower in the Coanda burner.

- An assessment was made of the potential benefits that the implementation of the proposed Coanda burner would have in an electrical steel annealing furnace. The proposed Coanda heated radiant plates had a better performance than that of the radiant tubes. The radiant plates reduced the energy requirement by $\sim 64\%$, increased the heating rate by $\sim 288\%$, and reduced the heating time by $\sim 74.8\%$.

- A potential downside of the Coanda burner was identified. The burner had a lower radiant heat flux than the radiant tube burner. However, this downside was compensated by an increase in the total radiating area in the furnace with the Coanda burner.

- The summary of the expected benefits of the Coanda flat plate burner in comparison to a single-ended recuperative radiant tube burner are an increase in heating rate, a reduction in energy requirement, a reduction in NO_x emissions, a reduction in heating time, an increase in temperature homogeneity of the load, and a reduction in volume furnace with the consequential reduction in start-up times.

9.0.1   *Recommendations for future work*

The results obtained from this investigation indicate that the proposed novel Coanda radiant plate burner is a viable alternative to radiant tube burners. The novel burner can produce improvements in heating rate, energy efficiency and emissions. For these reasons, the suggestion is to continue with the research required for the implementation of this burner. Future efforts should focus on the testing of a scaled-up version of the burner. The recommendations for future work are:

- One of the limitations of the present investigation was the impossibility of accurately distinguishing between the effect that a change in the applied swirl, a change in flow rate, and a change in equivalence ratio would have on the stability and performance of a Coanda flame. Thus, further studies should have availability to a burner with a variable swirl generator and suitable confinement that allows for the measurement of the flow with laser diagnostic techniques. Emission analysers that halt the reaction must be fitted to the combustion gases outlet. These will allow for a better characterization of the flow and efficiency of the burner.

- As it was mentioned earlier in this work, several other researchers have made use of the Coanda effect using other nozzle geometries. For this reason, the current nozzle configuration should be compared experimentally to the other alternatives in order to choose the best one. The ideal nozzle should produce the Coanda flame while avoiding hysteresis with other flow patterns. This will avoid the accidental transition of the flow to undesired flow patterns that might damage the burner. A stability map should also be produced that shows the operating range of the Coanda burner.

- A batch furnace that replicates as close as possible the real operating conditions should be manufactured and tested. This will allow for the identification of problems that could occur at larger scales and at longer operating times. It would be useful to answer questions such as: What would happen to the Coanda flame if there was a sudden drop in pressure of one of the reactants? How can the Coanda flame be re-established? What will be an adequate way to monitor the flame state? What would be the long-term effect of the Coanda flame impingement on the burner materials? What would be the interaction between adjacent Coanda burners? How often a device of this type will need maintenance?

- For the specific application in electrical steel annealing furnaces, the effect of the heating rate and temperature homogeneity should be closely analysed. The following questions should be answered: How much will the quality of the electrical steel improve with the increased heating rate? How much product waste caused by non-homogenous heating could be avoided? Would there be any detrimental effect?

- Once the previous information is available, a cost-benefit analysis of implementing this technology should be done.

BIBLIOGRAPHY

[1]   IPCC. "Summary for Policymakers." In: *Climate Change 2013: The Physical Science Basis. Contribution of Working Group I to the Fifth Assessment Report of the Intergovernmental Panel on Climate Change*. Ed. by T. Stocker et al. Cambridge, United Kingdom and New York, NY, USA: Cambridge University Press, 2013. Chap. Summary fo (cit. on pp. 1, 2).

[2]   Fischedick, M. et al. "Industry." In: *Climate Change 2014: Mitigation of Climate Change. Contribution of Working Group III to the Fifth Assessment Report of the Intergovernmental Panel on Climate Change*. Ed. by E. O. et al. Cambridge, United Kingdom and New York, NY, USA, 2014 (cit. on pp. 1, 2).

[3]   IEA. *World Energy Balances–2013 Edition*. 2013 (cit. on p. 1).

[4]   Waite, C. *2018 UK Greenhouse Gas Emissions*. Tech. rep. Department for Business, Energy & Industrial Streategy, 2018 (cit. on p. 2).

[5]   WSP Parsons Brinckerhoff and DNV-GL. *Industrial Decarbonisation & Energy Efficiency Roadmaps to 2050 - Iron and Steel*. Tech. rep. Department of Energy and Climate Change, 2015 (cit. on p. 2).

[6]   Williams, F. A. *Combustion theory: The fundamental theory of chemically reacting flow systems, second edition*. CRC Press, Jan. 2018, pp. 1–680 (cit. on p. 7).

[7]   Turns, S. R. *An introduction to combustion : concepts and applications*. McGraw-Hill, 2012, p. 732 (cit. on pp. 7, 10, 12, 85).

[8]   Kuo, K. K. and Acharya, R. *Fundamentals of Turbulent Multi-Phase Combustion*. John Wiley and Sons, Apr. 2012 (cit. on pp. 7, 12, 13).

[9]   Law, C. K. *Combustion physics*. Vol. 9780521870. Cambridge University Press, Jan. 2006, pp. 1–722 (cit. on pp. 7, 11).

[10] Himmelblau, D. *Basic Principles and Calculations in Chemical Engineering, Eight Edition*. 7th. Prentice Hall, 2004 (cit. on p. 8).

[11] Kuo, K. K. *Principles of Combustion*. 2nd. Wiley, 2005, 760 pages (cit. on p. 10).

[12] Beyler, C. "Flammability limits of premixed and diffusion flames." In: *SFPE Handbook of Fire Protection Engineering, Fifth Edition*. Springer New York, Jan. 2016, pp. 529–553 (cit. on p. 10).

[13] Lefebvre, A. H. and Ballal, D. R. *Gas Turbine Combustion*. CRC Press, Apr. 2010 (cit. on pp. 10, 11).

[14] Dawson, J. "An investigation into naturally excited Helmholtz oscillations in a swirl burner/furnace system." PhD thesis. Cardiff University, Wales, UK, 2000 (cit. on p. 12).

[15]   Driscoll, J. F. *Turbulent premixed combustion: Flamelet structure and its effect on turbulent burning velocities*. Feb. 2008 (cit. on p. 12).

[16]   Regunath, G. S. et al. "Experimental investigation of helicity in turbulent swirling jet using dual-plane dye laser PIV technique." In: *Experiments in Fluids* 45.6 (Dec. 2008), pp. 973–986 (cit. on p. 12).

[17]   Davidson, P. A. *Turbulence : an introduction for scientists and engineers*. 2nd. Oxford: Oxford University Press, 2015, p. 630 (cit. on p. 12).

[18]   Borghi, R. "Turbulent combustion modelling." In: *Progress in Energy and Combustion Science* 14.4 (Jan. 1988), pp. 245–292 (cit. on p. 12).

[19]   Navarro-Martinez, S. and Kronenburg, A. "Flame stabilization mechanisms in lifted flames." In: *Flow, Turbulence and Combustion* 87.2-3 (Oct. 2011), pp. 377–406 (cit. on p. 14).

[20]   Eichler, C. and Sattelmayer, T. "Premixed flame flashback in wall boundary layers studied by long-distance micro-PIV." In: *Experiments in Fluids* 52.2 (Feb. 2012), pp. 347–360 (cit. on p. 14).

[21]   Benim, A. C. and Syed, K. J. *Flashback Mechanisms in Lean Premixed Gas Turbine Combustion*. Elsevier Inc., Dec. 2014, pp. 1–123 (cit. on p. 14).

[22]   Shanbhogue, S. J. et al. *Lean blowoff of bluff body stabilized flames: Scaling and dynamics*. Feb. 2009 (cit. on p. 14).

[23]   Huang, Y. and Yang, V. *Dynamics and stability of lean-premixed swirl-stabilized combustion*. Aug. 2009 (cit. on pp. 14, 16, 17).

[24]   Ehhalt, D. et al. *Atmospheric Chemistry and Greenhouse Gase*. Tech. rep. Cambridge: IPCC, 2001 (cit. on pp. 14–16).

[25]   Dunn, R. J. H. et al. "Global Climate." In: *State of the Climate in 2018*. Ed. by J. Blunden and D. S. Arndt. American Meteorological Society, 2019. Chap. Chapter 2 (cit. on p. 15).

[26]   Skalska, K. et al. *Trends in NOx abatement: A review*. Sept. 2010 (cit. on pp. 15, 16).

[27]   Gupta, A. K. et al. *Swirl flows*. Tunbridge Wells, UK: Abacus Press, 1984 (cit. on p. 16).

[28]   Beer, J. M. and Chigier, N. A. *Combustion aerodynamics*. London, UK: Applied Science Publishers, 1972 (cit. on pp. 16, 18, 21).

[29]   Park, S. H. and Shin, H. D. "Measurements of entrainment characteristics of swirling jets." In: *International Journal of Heat and Mass Transfer* 36.16 (1993), pp. 4009–4018 (cit. on p. 16).

[30]   Chen, R. H. and Driscoll, J. F. "Nitric oxide levels of jet diffusion flames: Effects of coaxial air and other mixing parameters." In: *Symposium (International) on Combustion* 23.1 (1991), pp. 281–288 (cit. on p. 16).

[31] Chen, R. H. "Some Characteristics of NOx Emission of Turbulent Nonpremixed Hydrogen-Air Flames Stabilized by Swirl-Generated Flow Recirculation." In: *Combustion Science and Technology* 110-111.1 (1995), pp. 443–460 (cit. on p. 16).

[32] Lucca-Negro, O. and O'Doherty, T. "Vortex breakdown: A review." In: *Progress in Energy and Combustion Science* 27.4 (Jan. 2001), pp. 431–481 (cit. on pp. 16, 68, 72).

[33] Leibovich, S. "Vortex stability and breakdown - survey and extension." In: *AIAA Journal* 22.9 (1984), pp. 1192–1206 (cit. on p. 16).

[34] Chen, Z. et al. "Gas/particle flow characteristics of a centrally fuel rich swirl coal combustion burner." In: *Fuel* 87.10-11 (Aug. 2008), pp. 2102–2110 (cit. on p. 17).

[35] Syred, N. et al. "The effect of hydrogen containing fuel blends upon flashback in swirl burners." In: *Applied Energy* 89.1 (Jan. 2012), pp. 106–110 (cit. on p. 17).

[36] Froud, D. et al. "Phase averaging of the precessing vortex core in a swirl burner under piloted and premixed combustion conditions." In: *Combustion and Flame* 100.3 (1995) (cit. on p. 17).

[37] Moeck, J. P. et al. "Nonlinear interaction between a precessing vortex core and acoustic oscillations in a turbulent swirling flame." In: *Combustion and Flame* 159.8 (Aug. 2012), pp. 2650–2668 (cit. on p. 17).

[38] Marques, F. and Lopez, J. M. "Precessing vortex breakdown mode in an enclosed cylinder flow." In: *Physics of Fluids* 13.6 (2001), pp. 1679–1682 (cit. on p. 17).

[39] Martinelli, F. et al. "Experimental analysis of the precessing vortex core in a free swirling jet." In: *Experiments in Fluids* 42.6 (June 2007), pp. 827–839 (cit. on p. 17).

[40] Syred, N. "A review of oscillation mechanisms and the role of the precessing vortex core (PVC) in swirl combustion systems." In: *Progress in Energy and Combustion Science* 32.2 (Jan. 2006), pp. 93–161 (cit. on pp. 17, 68).

[41] Syred, N. and Beér, J. M. "Combustion in swirling flows: A review." In: *Combustion and Flame* 23.2 (Oct. 1974), pp. 143–201 (cit. on p. 17).

[42] Oberleithner, K. et al. "Mean flow stability analysis of oscillating jet experiments." In: *Journal of Fluid Mechanics* 757 (2014), pp. 1–32 (cit. on p. 17).

[43] Terhaar, S. et al. "Key parameters governing the precessing vortex core in reacting flows: An experimental and analytical study." In: *Proceedings of the Combustion Institute* 35.3 (2015), pp. 3347–3354 (cit. on p. 17).

[44]   Oberleithner, K. et al. "Formation and flame-induced suppression of the precessing vortex core in a swirl combustor: Experiments and linear stability analysis." In: *Combustion and Flame* 162.8 (Aug. 2015), pp. 3100–3114 (cit. on p. 17).

[45]   Stöhr, M. et al. "Transient effects of fuel-air mixing in a partially-premixed turbulent swirl flame." In: *Proceedings of the Combustion Institute* 35.3 (2015), pp. 3327–3335 (cit. on p. 17).

[46]   Galley, D. et al. "Mixing and stabilization study of a partially premixed swirling flame using laser induced fluorescence." In: *Combustion and Flame* 158.1 (Jan. 2011), pp. 155–171 (cit. on p. 17).

[47]   Stöhr, M. et al. "Experimental study of vortex-flame interaction in a gas turbine model combustor." In: *Combustion and Flame* 159.8 (Aug. 2012), pp. 2636–2649 (cit. on p. 17).

[48]   Stöhr, M. et al. "Effects of Damköhler number on vortex-flame interaction in a gas turbine model combustor." In: *Proceedings of the Combustion Institute* 34.2 (2013), pp. 3107–3115 (cit. on p. 17).

[49]   Sheen, H. J. et al. "Correlation of Swirl Number for a Radial-Type Swirl Generator." In: *Experimental Thermal and Fluid Science* 12.4 (1996), pp. 444–451 (cit. on p. 18).

[50]   Ogus, G. "CFD and PIV investigation of Flow Patterns and Particle Behavior in Swirling Jets." PhD thesis. KU Leuven, 2018 (cit. on pp. 18, 50).

[51]   Wille, R. and Fernholz, H. "Report on the first European Mechanics Colloquium, on the Coanda effect." In: *Journal of Fluid Mechanics* 23.4 (1965), pp. 801–819 (cit. on pp. 18–20).

[52]   Coanda, H. *US Patent No. 1104963*. 1914 (cit. on p. 18).

[53]   Coanda, H. *US Patent No. 3261162*. 1966 (cit. on p. 18).

[54]   Hunt, I. A. and Joubert, P. N. "Effects of small streamline curvature on turbulent duct flow." In: *Journal of Fluid Mechanics* 91.4 (1979), pp. 633–659 (cit. on p. 19).

[55]   Green, P. and Carpenter, P. "Method of integral relations for curved compressible mixing layers with lateral divergence." In: *Proceedings of the 3rd International Conference on Numerical Methods in Laminar and Turbulent Flow*. Seattle, USA, 1983 (cit. on p. 19).

[56]   Carpenter, P. W. and Smith, C. "The aeroacoustics and aerodynamics of high-speed Coanda devices, part 2: Effects of modifications for flow control and noise reduction." In: *Journal of Sound and Vibration* 208.5 (Dec. 1997), pp. 803–822 (cit. on pp. 19, 20).

[57]   Trancossi, M. "An overview of scientific and technical literature on Coanda effect applied to nozzles." In: *SAE Technical Papers*. SAE International, 2011 (cit. on p. 19).

[58]   Skotnicka-Siepsiak, A. "Hysteresis of the Coanda Effect." In: *Journal of Fluids Engineering, Transactions of the ASME* 140.1 (Jan. 2018) (cit. on p. 19).

[59] Reba, I. "Applications of the Coanda Effect." In: *Scientific American* 214 (1966), pp. 84–93 (cit. on p. 19).

[60] Lubert, C. P. "On some recent applications of the coanda effect." In: *International Journal of Acoustics and Vibrations*. Vol. 16. 3. Acoustical Society of America, Feb. 2011, pp. 144–153 (cit. on p. 19).

[61] Li, H. et al. "Experimental investigation on the outlet flow field structure and the influence of Reynolds number on the outlet flow field for a bladeless fan." In: *Applied Thermal Engineering* 100 (May 2016), pp. 972–978 (cit. on p. 19).

[62] Kamplade, J. et al. "Effect of Coandă-deflection-openings on the spray behavior of pressure swirl nozzles." In: *Atomization and Sprays* 28.3 (2018), pp. 281–297 (cit. on p. 19).

[63] Musemic, E. and Walzel, P. "Swirl Atomizers with Coanda Deflection Outlets." In: *Proceedings of 12th International Conference on Liquid Atomization and Spray Systems*. Heidelberg, Germany, 2012 (cit. on p. 19).

[64] Schuh, H. and Persson, B. "Heat transfer on circular cylinders exposed to free-jet flow." In: *International Journal of Heat and Mass Transfer* 7.11 (1964) (cit. on p. 19).

[65] Wood, N. J. and Nielsen, J. N. "Circulation control airfoils as applied to rotary-wing aircraft." In: *Journal of Aircraft* 23.12 (1986), pp. 865–875 (cit. on p. 19).

[66] Zandieh, A. and Leishman, J. G. "Boundary layer and pressure measurements on a cylinder with unsteady circulation control." In: *AIAA Journal* 31.10 (1993), pp. 1769–1776 (cit. on p. 19).

[67] Nichols, J. H. and Harris, M. J. "Fixed wing CCW aerodynamics with and without supplementary thrust deflection." In: *Ames Research Center Proceedings of the Circulation-Control Workshop*. Bethesda, USA: NASA, 1987, pp. 479–489 (cit. on p. 19).

[68] Bevilaqua, P. M. and Lee, J. D. "Design of supersonic Coanda jet nozzles." In: *Ames Research Center Proceedings of the Circulation-Control Workshop*. Valencia, USA: NASA, 1987, pp. 289–312 (cit. on p. 19).

[69] Páscoa, J. C. et al. *A review of thrust-vectoring in support of a V/STOL non-moving mechanical propulsion system*. 2013 (cit. on p. 19).

[70] Trancossi, M. et al. "A new aircraft architecture based on the ACHEON Coanda effect nozzle: flight model and energy evaluation." In: *European Transport Research Review* 8.2 (June 2016) (cit. on p. 19).

[71] Desty, D. et al. "The origination, development and application of novel premixed flare burners employing the Coanda effect." In: *85th Nat. AIChE meeting*. AIChE, 1978 (cit. on p. 19).

[72] Desty, D. "No Smoke with Fire." In: *Proceedings of the Institution of Mechanical Engineers, Part A: Power and Process Engineering* 197.3 (Aug. 1983), pp. 159–170 (cit. on p. 19).

[73]   Carpenter, P. W. and Green, P. N. "The aeroacoustics and aero-dynamics of high-speed Coanda devices, part 1: Conventional arrangement of exit nozzle and surface." In: *Journal of Sound and Vibration* 208.5 (Dec. 1997), pp. 777–801 (cit. on p. 19).

[74]   Lubert, C. P. et al. "An investigation of initial shock cell formation in turbulent Coanda Wall jets." In: *International Journal of Acoustics and Vibrations* 21.2 (2016), pp. 199–208 (cit. on p. 20).

[75]   Fox, J. S. and Sarkar, F. "The influence of Coanda effect on blow-off limit." In: *Combustion Science and Technology* 6.1-2 (1972), pp. 51–53 (cit. on p. 20).

[76]   Fox, J. S. and Stewart, J. A. "The Influence of Coanda Effect on Heat Transfer from Combusting Gases." In: *Combustion Science and Technology* 19.1-2 (Nov. 1978), pp. 73–75 (cit. on p. 20).

[77]   Ahmed, N. A. *Coanda Effect: Flow Phenomenon and Applications.* 1st. CRC Press, 2019 (cit. on pp. 20, 21).

[78]   Vanierschot, M. and Van den Bulck, E. "Computation of a drastic flow pattern change in an annular swirling jet caused by a small decrease in inlet swirl." In: *International Journal for Numerical Methods in Fluids* 59.5 (Feb. 2009), pp. 577–592 (cit. on p. 20).

[79]   Leuckel, W. *Swirl intensities, swirl types and energy losses of different swirl generating devices.* Tech. rep. Ijmuiden, Holland, 1973 (cit. on p. 21).

[80]   Chigier, N. A. and Beér, J. M. "Velocity and static-pressure distributions in swirling air jets issuing from annular and divergent nozzles." In: *Journal of Fluids Engineering, Transactions of the ASME* 86.4 (1964), pp. 788–796 (cit. on p. 21).

[81]   Vanoverberghe, K. P. et al. "Multiflame patterns in swirl-driven partially premixed natural gas combustion." In: *Journal of Engineering for Gas Turbines and Power* 125.1 (Jan. 2003), pp. 40–45 (cit. on pp. 21–23, 88, 157, 162).

[82]   Mansour, M. S. "A concentric flow conical nozzle burner for highly stabilized partially premixed flames." In: *Combustion Science and Technology* 152.1-6 (2000), pp. 115–145 (cit. on p. 22).

[83]   Stöhr, M. et al. "Dynamics of lean blowout of a swirl-stabilized flame in a gas turbine model combustor." In: *Proceedings of the Combustion Institute* 33.2 (2011), pp. 2953–2960 (cit. on p. 22).

[84]   Valera-Medina, A. et al. "Central recirculation zone analysis in an unconfined tangential swirl burner with varying degrees of premixing." In: *Experiments in Fluids* 50.6 (June 2011), pp. 1611–1623 (cit. on pp. 22, 78).

[85]   Valera-Medina, A. et al. "Visualisation of isothermal large coherent structures in a swirl burner." In: *Combustion and Flame* 156.9 (Sept. 2009), pp. 1723–1734 (cit. on p. 22).

[86]   Vanoverberghe, K. et al. "Flow structure of lifted swirling jet flames." In: *Flow, Turbulence and Combustion* 73.1 (July 2004), pp. 25–47 (cit. on pp. 22, 23).

[87] Vanoverberghe, K. P. et al. "Confined annular swirling jet combustion." In: *Combustion Science and Technology* 175.3 (Mar. 2003), pp. 545–578 (cit. on pp. 22, 156, 158, 163).

[88] Vanierschot, M. and Van den Bulck, E. "Hysteresis in flow patterns in annular swirling jets." In: *Experimental Thermal and Fluid Science* 31.6 (May 2007), pp. 513–524 (cit. on pp. 24, 26, 74, 88, 100, 155).

[89] Vanierschot, M. and Van den Bulck, E. "Numerical study of hysteresis in annular swirling jets with a stepped-conical nozzle." In: *International Journal for Numerical Methods in Fluids* 54.3 (May 2007), pp. 313–324 (cit. on pp. 24, 25, 74, 88, 100, 109, 160).

[90] Vanierschot, M. and Van den Bulck, E. "Influence of the Nozzle Geometry on the Hysteresis of Annular Swirling Jets." In: *Combustion Science and Technology* 179.8 (July 2007), pp. 1451–1466 (cit. on pp. 24, 25, 27, 160, 165).

[91] Vanierschot, M. et al. "A new method for annular jet control based on cross-flow injection." In: *Physics of Fluids* 21.2 (2009) (cit. on pp. 24, 26, 164).

[92] Gritskevich, M. S. et al. "Numerical Investigation of Flow Near a Round Exhaust Channel Screened by an Annular Swirled Jet." In: *Journal of Engineering Physics and Thermophysics* 92.2 (Mar. 2019), pp. 468–476 (cit. on pp. 24, 160).

[93] Ogus, G. et al. "On the flow structures and hysteresis of laminar swirling jets." In: *Physics of Fluids* 28.12 (Dec. 2016) (cit. on p. 24).

[94] Singh, N. K. and Ramamurthi, K. "Formation of Coanda jet from sharp-edged swirl nozzle with base plate." In: *Experimental Thermal and Fluid Science* 33.4 (Apr. 2009), pp. 675–682 (cit. on pp. 24, 100, 156, 158).

[95] Valera-Medina, A. and Baej, H. "Hydrodynamics During the Transient Evolution of Open Jet Flows from/to Wall Attached Jets." In: *Flow, Turbulence and Combustion* 97.3 (Oct. 2016), pp. 743–760 (cit. on pp. 26, 64, 68, 74).

[96] Falese, M. et al. "LES of bifurcation and hysteresis in confined annular swirling flows." In: *Computers and Fluids* 89 (Jan. 2014), pp. 167–178 (cit. on p. 26).

[97] Kwark, J. H. et al. "Effect of swirl intensity on the flow and combustion of a turbulent non-premixed flat flame." In: *Flow, Turbulence and Combustion* 73.3-4 (Jan. 2005), pp. 231–257 (cit. on pp. 26, 157, 163).

[98] Baukal Jr., C. E. *Heat Transfer in Industrial Combustion.* CRC Press, May 2000 (cit. on p. 28).

[99] Flamme, M. et al. "Radiant Tube Burners." In: *Industrial Combustion Testing.* CRC Press, July 2010, pp. 511–528 (cit. on pp. 28–30).

[100] Baukal, Jr., C. E. "Heat Transfer from Burners." In: *Industrial Burners Handbook*. Ed. by C. E. Baukal, Jr. 1st. CRC Press, 2003. Chap. Chapter 6, pp. 201–254 (cit. on pp. 28, 29).

[101] Irfan, M. and Chapman, W. "Thermal stresses in radiant tubes: A comparison between recuperative and regenerative systems." In: *Applied Thermal Engineering* 30.2-3 (Feb. 2010), pp. 196–200 (cit. on p. 30).

[102] Quinn, D. E. and Newby, J. "Radiant Tube Burners." In: *Industrial Burners Handbook*. Ed. by C. E. Baukal, Jr. 1st. CRC Press, 2003. Chap. Chapter 14, pp. 485–505 (cit. on pp. 30, 31).

[103] Srivastava, R. et al. "Controlling NOx emission from industrial sources." In: *Environmental Progress* 24.2 (July 2005), pp. 181–197 (cit. on p. 31).

[104] Callister, W. D. and Rethwisch, D. G. *Materials science and engineering: An introduction, enhanced eText, 10th Edition*. Wiley-VCH, 2018 (cit. on pp. 31, 32).

[105] Luborsky, F. et al. "Magnetic properties of metals and alloys." In: *Physical Metallurgy*. Elsevier, 1996, pp. 2501–2565 (cit. on pp. 31–33).

[106] Barrett, W. *On the electrical conductivity and magnetic permeability of various alloys of iron*. Dublin: R. Dublin Soc., 1900 (cit. on p. 31).

[107] Honda, O. et al. *On the magnetic properties of single crystals of iron*. 1926 (cit. on p. 31).

[108] Goss, N. *US Patent No. 1965559*. 1934 (cit. on p. 31).

[109] Coltman, J. "The Transformer - historical overview." In: *IEEE Industry Applications Magazine* 8.1 (2002), pp. 8–15 (cit. on p. 31).

[110] Taguchi, S. and Sakakura, A. *US Patent No. 3159511*. 1964 (cit. on p. 31).

[111] Taguchi, S. et al. "New Grain-Oriented Silicon Steel with High Permeability "ORIENTCORE HI-B"." In: *IEEE Transactions on Magnetics* 10.2 (1974), pp. 123–127 (cit. on p. 31).

[112] Matsuo, M. "Texture control in the production of grain oriented silicon steels." In: *ISIJ International* 29.10 (1989), pp. 809–827 (cit. on p. 31).

[113] Xia, Z. et al. *Developments in the production of grain-oriented electrical steel*. Dec. 2008 (cit. on p. 31).

[114] Moses, A. J. "Electrical steels. Past, present and future developments." In: *IEE Proceedings A: Physical Science. Measurement and Instrumentation. Management and Education. Reviews* 137.5 (Sept. 1990), pp. 233–245 (cit. on pp. 31, 32).

[115] McCurrie, R. A. *Ferromagnetic materials : structure and properties*. Academic, 1994, p. 297 (cit. on p. 33).

[116] Cogent Power. *Grain oriented electrical steel*. 2016 (cit. on p. 34).

[117]   Block, W. F. and Jayaraman, N. "Reactions during decarbur-
        ization annealing of electrical steel." In: *Materials Science and
        Technology (United Kingdom)* 2.1 (1986), pp. 22–27 (cit. on p. 35).

[118]   Park, J.-T. et al. "Effect of Heating Rate on the Development
        of Annealing Texture in Nonoriented Electrical Steels." In: *ISIJ
        International* 43.10 (2003), pp. 1611–1614 (cit. on p. 37).

[119]   Park, N.-J. et al. "Evolution of Goss Orientation during Rapid
        Heating for Primary Recrystallization in Grain-oriented Electrical
        Steel." In: *ISIJ International* 51.6 (2011), pp. 975–981 (cit. on pp. 37,
        38).

[120]   Hou, C. K. and Tzeng, J. M. "Influence of heating rate and
        decarburization temperature on the microstructure and magnetic
        properties of grain oriented electrical steel." In: *Materials Science
        Forum*. Vol. 706-709. 2012, pp. 2622–2627 (cit. on pp. 37, 39).

[121]   Raffel, M. et al. *Particle Image Velocimetry*. Berlin, Heidelberg:
        Springer Berlin Heidelberg, 2007 (cit. on pp. 43, 45).

[122]   LaVision. *Particle Image Velocimetry*. 2018 (cit. on p. 45).

[123]   Keane, R. D. and Adrian, R. J. "Theory of cross-correlation analy-
        sis of PIV images." In: *Applied Scientific Research* 49.3 (July 1992),
        pp. 191–215 (cit. on p. 43).

[124]   Melling, A. "Tracer particles and seeding for particle image
        velocimetry." In: *Measurement Science and Technology* 8.12 (Dec.
        1997), pp. 1406–1416 (cit. on p. 43).

[125]   Jacquot, P. and Rastogi, P. K. "Influence of out-of-plane deforma-
        tion and its elimination in white light speckle photography." In:
        Optics and Lasers in Engineering 2.1 (Jan. 1981), pp. 33–55 (cit. on
        p. 45).

[126]   Arroyo, M. P. and Greated, C. A. "Stereoscopic particle image
        velocimetry." In: *Measurement Science and Technology* 2.12 (Dec.
        1991), pp. 1181–1186 (cit. on p. 45).

[127]   Prasad, A. K. "Stereoscopic particle image velocimetry." In: *Ex-
        periments in Fluids* 29.2 (Aug. 2000), pp. 103–116 (cit. on p. 45).

[128]   Hussain, A. K. M. F. and Reynolds, W. C. "The mechanics of
        an organized wave in turbulent shear flow." In: *Journal of Fluid
        Mechanics* 41.2 (Apr. 1970), pp. 241–258 (cit. on p. 46).

[129]   Lumley, J. L. "The Structure of Inhomogeneous Turbulence."
        In: *Atmospheric Turbulence and Wave Propagation*. Ed. by A. M.
        Yaglom and V. I. Tatarski. Moscow: Nauka, 1967, pp. 166–178
        (cit. on p. 46).

[130]   Holmes, P. et al. "Proper orthogonal decomposition." In: *Turbu-
        lence, Coherent Structures, Dynamical Systems and Symmetry*. Cam-
        bridge: Cambridge University Press, 1996, pp. 86–128 (cit. on
        p. 46).

[131] Sirovich, L. "Turbulence and the Dynamics of Coherent Structures Part I: Coherent Structures." In: *Quarterly of Applied Mathematics* 45 (1987), pp. 561–571 (cit. on pp. 46, 48).

[132] Kutz, J. N. et al. "Fluid Dynamics." In: *Dynamic Mode Decomposition*. Philadelphia, PA: Society for Industrial and Applied Mathematics, Nov. 2016. Chap. 2, pp. 25–38 (cit. on p. 46).

[133] Meyer, K. E. et al. "POD as tool for comparison of PIV and LES data." In: *7th International Symposium on Particle Image Velocimetry*. Rome: Faculty of Engineering, University "La Sapienza", 2007 (cit. on p. 46).

[134] Patte-Rouland, B. et al. "Flow analysis of an annular jet by particle image velocimetry and proper orthogonal decomposition." In: *Measurement Science and Technology* 12.9 (Sept. 2001), pp. 1404–1412 (cit. on p. 48).

[135] Sieber, M. et al. "Spectral proper orthogonal decomposition." In: *Journal of Fluid Mechanics* 792 (Apr. 2016), pp. 798–828 (cit. on p. 48).

[136] Hunt, J. C. R. et al. "Eddies, streams, and convergence zones in turbulent flows." In: *In its Studying Turbulence Using Numerical Simulation Databases*. NASA, 1988, pp. 193–208 (cit. on p. 49).

[137] Chong, M. S. et al. "A general classification of three-dimensional flow fields." In: *Physics of Fluids A: Fluid Dynamics* 2.5 (May 1990), pp. 765–777 (cit. on p. 49).

[138] Zhou, J. et al. "Mechanisms for generating coherent packets of hairpin vortices in channel flow." In: *Journal of Fluid Mechanics* 387 (May 1999), pp. 353–396 (cit. on p. 49).

[139] Jeong, J. and Hussain, F. "On the identification of a vortex." In: *Journal of Fluid Mechanics* 285.-1 (Feb. 1995), p. 69 (cit. on p. 49).

[140] Chen, Q. et al. "Comparison of vortex identification criteria for planar velocity fields in wall turbulence." In: *Physics of Fluids* 27.8 (Aug. 2015), p. 085101 (cit. on p. 50).

[141] Vanierschot, M. and Ogus, G. "Experimental investigation of the precessing vortex core in annular swirling jet flows in the transitional regime." In: *Experimental Thermal and Fluid Science* 106 (Sept. 2019), pp. 148–158 (cit. on p. 50).

[142] Versteeg, H. K. and Malalasekera, W. *An introduction to computational fluid dynamics : the finite volume method*. Pearson Education, 2007, p. 503 (cit. on pp. 51–55, 58, 59, 104, 113).

[143] Nichols, R. H. *Turbulence Models and Their Application to Complex Flows*. Birmingham: University of Alabama, 2010 (cit. on p. 52).

[144] Smith, G. P. et al. *GRI-MECH 3.0* (cit. on p. 53).

[145] Kee, R. et al. *CHEMKIN-III: A FORTRAN chemical kinetics package for the analysis of gas-phase chemical and plasma kinetics*. Tech. rep. Albuquerque, NM, and Livermore, CA (United States): Sandia National Laboratories (SNL), May 1996 (cit. on p. 53).

[146]   Libby, P. A. and Williams, F. A., eds. *Turbulent Reacting Flows*. Vol. 44. Topics in Applied Physics. Berlin, Heidelberg: Springer Berlin Heidelberg, 1980 (cit. on p. 53).

[147]   Ansys. "Reynolds Averaging." In: *Fluent Theory Guide*. 2018. Chap. 4.1.1 (cit. on p. 53).

[148]   Zikanov, O. *Essential computational fluid dynamics*. Wiley, 2010, p. 302 (cit. on pp. 54, 58, 59, 104).

[149]   Anderson, J. D. *Computational fluid dynamics : the basics with applications*. McGraw-Hill, 1995, p. 547 (cit. on p. 54).

[150]   Ansys. "Standard, RNG, and Realizable k-ϵ Models." In: *Fluent Theory Guide*. 2018. Chap. 4.3 (cit. on p. 55).

[151]   Ansys. "Standard, BSL, and SST k-ω Models." In: *Fluent Theory Guide*. 2018. Chap. 4.4 (cit. on p. 55).

[152]   Perry, R. H. and Green, D. W. *Perry's chemical engineers' handbook*. 5th. McGraw-Hill, 1973 (cit. on p. 54).

[153]   Poling, B. E. et al. *The properties of gases and liquids*. McGraw-Hill, 2001 (cit. on p. 54).

[154]   Ansys. "Species Transport Equations." In: *Fluent Theory Guide*. 2018. Chap. 7.1.1 (cit. on p. 54).

[155]   Magnussen, B. and Hjertager, B. "On mathematical modeling of turbulent combustion with special emphasis on soot formation and combustion." In: *Symposium (International) on Combustion* 16.1 (Jan. 1977), pp. 719–729 (cit. on p. 54).

[156]   Ansys. "Reaction Modeling." In: *Fluent Theory Guide*. 2018. Chap. 7.1.2 (cit. on p. 56).

[157]   Ansys. "P-1 Radiation Model Theory." In: *Fluent Theory Guide*. 2018. Chap. 5.3.3 (cit. on p. 56).

[158]   Lienhard, IV, J. and Lienhard, V, J. "Laminar heat transfer from inclined and horizontal plates." In: *A Heat Transfer Textbook*. 5th. Mineola, NY: Dover Publications, 2019. Chap. 8, pp. 432–435 (cit. on pp. 57, 119).

[159]   Raithby, G. and Hollands, K. G. T. "Natural Convection." In: *Handbook of Heat Transfer*. Ed. by W. M. Rohsenow et al. 3rd. New York, NY: McGraw-Hill, 1998. Chap. 4 (cit. on p. 57).

[160]   Patankar, S. and Spalding, D. "A calculation procedure for heat, mass and momentum transfer in three-dimensional parabolic flows." In: *International Journal of Heat and Mass Transfer* 15.10 (Oct. 1972), pp. 1787–1806 (cit. on p. 58).

[161]   Roache, P. J. *Verification and validation in computational science and engineering*. Hermosa Publishers, 1998, p. 446 (cit. on pp. 59, 99, 101, 104).

[162]   Moisey, F. *pivmat*. 2017 (cit. on p. 66).

[163]   Jørgensen, B. H. et al. "Low-dimensional modeling of a driven cavity flow with two free parameters." In: *Theoretical and Computational Fluid Dynamics* 16.4 (Mar. 2003), pp. 299–317 (cit. on p. 66).

[164]   Markovich, D. M. and Abdurakipov, S. S. "PIV study of vortex breakdown in low-and high-swirl flames in a model combustor." In: *10th International Symposium on Particle Image Velocimetry.* 2013 (cit. on p. 72).

[165]   Li, M. et al. "Experimental study of hydrogen addition effects on a swirl-stabilized methane-air flame." In: *Energies* 10.11 (Nov. 2017), p. 1769 (cit. on p. 72).

[166]   Sommerer, Y. et al. "Large eddy simulation and experimental study of flashback and blow-off in a lean partially premixed swirled burner." In: *Journal of Turbulence* 5 (Oct. 2004) (cit. on p. 85).

[167]   Lewis, B. and Von Elbe, G. *Combustion, flames, and explosions of gases.* Academic Press, 1987, p. 739 (cit. on p. 85).

[168]   Vanoverberghe, K. P. "Flow, turbulence and combustion of premixed swirling jet flames." PhD thesis. KU Leuven, 2004 (cit. on p. 93).

[169]   Mei, F. "Multiple Modeling of the Singleended Radiant Tubes." In: *Simulation and Optimization of Furnaces and Kilns for Nonferrous Metallurgical Engineering.* Berlin, Heidelberg: Springer Berlin Heidelberg, 2010, pp. 275–296 (cit. on p. 99).

[170]   Ansys. "Enhanced Wall Treatment." In: *Fluent Theory Guide.* 2018. Chap. 4.16.5 (cit. on p. 101).

[171]   Ansys. *Mesh Quality & Advanced Topics - Introduction to ANSYS Meshing.* 2015 (cit. on p. 101).

[172]   Nogenmyr, K. J. et al. "Effects of confinement on premixed turbulent swirling flame using large Eddy simulation." In: *Combustion Theory and Modelling* 17.6 (2013), pp. 1003–1019 (cit. on p. 104).

[173]   Rhew, R. D. and Parker, P. A. *A Parametric Geometry Computational Fluid Dynamics (CFD) Study Utilizing Design of Experiments (DOE).* Tech. rep. Hampton, Virginia: NASA Langley Research Center, 2007 (cit. on pp. 123, 124).

[174]   Seok, W. et al. "Application of the Design of Experiments and Computational Fluid Dynamics to Bow Design Improvement." In: *Journal of Marine Science and Engineering* 7.7 (July 2019), p. 226 (cit. on p. 123).

[175]   Lopez-Arcos, J. I. et al. "Improve the product design process, with CFD and DOE approach." In: *International Conference on Industrial Engineering and Operations Management.* Bogota, Colombia, 2017 (cit. on p. 123).

[176]   Tsioumanis, N. et al. "Flow processes in a radiant tube burner: Isothermal flow." In: *Fuel* 87.1 (Jan. 2008), pp. 103–111 (cit. on pp. 135, 138, 139, 163).

[177] Tsioumanis, N. et al. "Flow processes in a radiant tube burner: Combusting flow." In: *Energy Conversion and Management* 52.7 (2011), pp. 2667–2675 (cit. on pp. 135, 136, 163).

[178] Special Metals Corporation. *Inconel Alloy 600*. 2008 (cit. on p. 141).

[179] Gumen, V. et al. "High-temperature thermal conductivity of ceramic fibers." In: *Journal of Materials Engineering and Performance* 10.4 (2001), pp. 475–478 (cit. on p. 141).

[180] Munro, R. G. "Material properties of a sintered α-SiC." In: *Journal of Physical and Chemical Reference Data* 26.5 (1997), pp. 1195–1203 (cit. on p. 141).

[181] Webb, B. W. et al. "SLW modeling of radiation transfer in comprehensive combustion predictions." In: *Combustion Science and Technology* 190.8 (Aug. 2018), pp. 1392–1408 (cit. on p. 148).

[182] Yaws, C. L. *Yaws' Handbook of Thermodynamic and Physical Properties of Chemical Compounds*. Knovel, 2012 (cit. on p. 148).

[183] Özışık, M. N. *Heat transfer : a basic approach*. McGraw-Hill, 1985, p. 780 (cit. on p. 148).

[184] Jones, J. M. et al. "A compilation of data on the radiant emissivity of some materials at high temperatures." In: *Journal of the Energy Institute* 92.3 (June 2019), pp. 523–534 (cit. on p. 148).

[185] Pollhammer, W. et al. "Modeling of a walking beam furnace using CFD-methods." In: *Energy Procedia*. Vol. 120. Elsevier Ltd, 2017, pp. 477–483 (cit. on p. 148).

[186] Tang, G. et al. "Modeling of steel slab reheating process in a walking beam reheating furnace." In: *ASME Heat Transfer Summer Conference*. Vol. 2. American Society of Mechanical Engineers, 2016 (cit. on p. 148).

[187] Cogent Power. *Typical Properties Grain Oriented Electrical Steel* (cit. on p. 148).

[188] Frederick, M. et al. "Impact of Precessing Vortex Core Dynamics on Shear Layer Response in a Swirling Jet." In: *Journal of Engineering for Gas Turbines and Power* 140.6 (June 2018) (cit. on p. 156).